Coherent Few-Body Physics

Yaakov Yudkin
Department of Physics

Ph.D. Thesis

Submitted to the Senate of Bar-Ilan University

Ramat-Gan, Israel June 2023

This work was carried out under the supervision of

Prof. Lev Khaykovich

Department of Physics,
Bar-Ilan University.

Acknowledgments

I would like to express my deep and honest gratitude to my supervisor Prof. Lev Khaykovich. He is not afraid of "getting his hands dirty" in the lab or staying until late at night. Leading by example and with unlimited patience, he has taught me how to be a precise experimental physicist with enough confidence to tackle difficult and fundamental theoretical problems.

During my PhD I spent seven months at UIBK, Innsbruck, Austria. Besides being grateful to Lev for letting me go, I must thank Prof. Rudolf Grimm who welcomed me with open arms and from whom I learned a lot of physical intuition. I am also grateful to Dr. Emil Kirilov, Rudi's staff scientist, who showed me confidence by giving me increasingly difficult projects to work on. Lastly I thank the entire ultracold atoms team for a great time. I thank the Erasmus+ program and the Austria-Israel Academic Network Innsbruck (AIANI), and in particular Marion Webster and Verena Tanzer, for providing a scholarship and taking care of us while we were there.

I was meant to go for a second academic stay abroad and was awarded the Chauteaubriand fellowship to go to LKB in Paris, France. Due to the stay being delayed by COVID and then my son being born we had to cancel the trip. I would like to thank (and say sorry to) Prof. Frederic Chevy whose group I was supposed to join.

During my PhD I had the privilege to talk to, discuss with and learn from multiple gifted theoretical collaborators. I would like to thank all of them: Prof. Jose P. D'Incao, Prof. Chris H. Greene and Prof. Emer. Paul S. Julienne.

Last, but definitely not least, I thank my lovely and loving wife Hadar. After all, she was the one who had to endure my late nights in the lab. She has always been a source of inspiration and motivation for me.

Contents

List of Figures

Abstract

Experimental and theoretical few-body physics in ultracold-atoms have provided many insights over the last few decades.

On the experimental side, the superb control of the two-body s-wave scattering length via Feshbach resonances has enabled the creation of strongly interacting systems and the observation of large, loosely bound states. The Efimov trimer stands out as a particularly interesting halo molecule, for one, since it has no classical analogue. It has been measured via incoherent and inelastic collisions across a variety of atomic species and Feshbach resonances. The culminating, overwhelming result was that, for broad resonances, the van der Waals tail, common to all neutral atom collisions, accounts for universal laws of nature. On the other hand, Efimov trimers near narrow resonances are dominated by the resonance strength. However in bosonic lithium (^{7}Li), which features intermediate and narrow resonances, many of the observations are unusual and are collectively denoted the "lithium few-body puzzle".

On the theoretical side, increasingly complex multi-channel models are being developed to account for the convoluted nature of few-body collisions. While full coupled-channels have proven to be extraordinarily accurate for alkaline two-body collisions, a similar calculation for the three boson problem would need more computational power than currently available. Simplified models are therefore inevitable.

This Thesis marks considerable progress on both fronts.

On the experimental side we explore the first excited Efimov state of ^{7}Li in the vicinity of the dimer-atom threshold. Our observations add to the few-body puzzle. To access this demanding regime we have developed a protocol with which a superposition of dimers and trimers is created from a thermal gas. Namely, the atoms are subjected to a temporally short, and therefore spectrally broad, radio-frequency-pulse bridging the energy difference from the free atom continuum to both the dimer and trimer. A double pulse sequence allows extraction of the relative phase gained during the intermediate free evolution time, which comprises an accurate measurement of trimer energy with respect to the dimer energy. We thus observe the trimer via its coherent evolution and interference with the dimer. This marks a paradigm shift in the field of few-body physics. Instead of detecting a loosely bound

state as a loss feature, i.e. detecting its absence, we successfully leverage coherent evolution and observe the trimer before it decays. For too long, in the field of few-body physics, coherence remained an unexploited quantum resource. We have applied the experimental protocol at various values of the scattering length and observe the trimer approaching the dimer-atom threshold. Surprisingly, instead of a gradual approach and merger we see the trimer level crossing into the continuum. After the crossing, the trimer is found to form a long-lived bound state – not a scattering resonance – even though it is embedded in a continuum of its constituents.

On the theoretical side, inspired by the level structure of lithium, and in particular by the scattering channel used in the experiment, we have developed two completing models. The first is for overlapping Feshbach resonances while the second incorporates near-degenerate continua. They are desigend to be as simple and straightforward as possible while capturing the essential microscopic physics of resonantly enhanced interactions. We use these models to explore the effects of either a nearby resonance or continuum on the observable two- and three-body physics. In the case of overlapping resonances, we find dimer-dimer level repulsion and that the Efimov features are pushed away from unitarity. The latter is in quantitative agreement with an observation of the ^{6}Li-Cs-Cs trimer. A near degenerate continuum causes the dimer to be shallower than expected from the resonance strength parameter. In addition, contrarily to overlapping resonances, a near-degenerate continuum does not affect the end points of the Efimov spectrum but changes its functional form instead. Combined, the two models take the main contributions to the asymptotic wave function into account. Thus, any two- or three-body feature that is not predicted by either model is probably due to the short-range details of the interatomic potential.

Chapter 1

Introduction and Motivation

Several decades ago, few-body physics and quantum scattering were limited to the field of nuclear physics. Slowly, atomic and molecular beams began entering the stage, thus expanding the range of application. However, all the above experimental systems suffer from a crucial drawback, namely that the interaction strength is given by nature. The pairwise interaction of nuclei, atoms or molecules had to be treated as a constant of nature. Scientists had to wait for the advent of cold atoms and the discovery of magnetic Feshbach resonances until the interaction, in the form of the s-wave scattering length, could be changed over several orders of magnitude and precisely adjusted in the lab.

Shortly after the invention of the laser it became clear that the macroscopic population of a single photonic state can be used to cool gas-phase atoms and molecules at low pressure to very low temperatures [1–3]. An additional push towards even lower temperatures and higher densities was provided by evaporative cooling which led to the creation of the, then elusive but now quite standard, Bose-Einstein condensate in the lab [4, 5]. The field of research that emerged – ultracold atoms and quantum gases – is a cornerstone of modern experimental physics [6]. Today, the family of cold atomic species [7] includes almost all alkalis and earth-alkalis as well as meta-stable noble gas atoms [8] and dipolar lanthanides [9]). The vast range of applications include quantum computation [10, 11] and simulation [12]. Due to the high degree of control provided by the cold-atom platform, many aspects of many-body physics, such as lattices [13, 14], the BEC-BCS crossover [15], many-body localization [16], impurities [17] and magnetism [18] have been explored. Their strong coupling to the electromagnetic field of an optical cavity has enabled experiments in cavity QED [19]. Further, the high sensitivity of ultracold gases has been leveraged for quantum metrology [20, 21], atomic clocks [22] and the search for physics beyond the standard model [23]. Particularly relevant to this Thesis, the immense tunability of the interaction strength has led to various studies of scattering processes and their associated loosely bound states [24, 25]. The latter are

also used to create ground state diatomic molecules from single atoms and explore quantum chemistry [26].

1.1 Scattering at Low Temperatures

In the following a few relevant topics in few-body physics are covered with a special emphasis on the toolbox provided by cold atom systems. To this end, we consider identical bosons with mass m interacting via a short-range, two-body (central) potential $V(r)$, where r is the distance between the two particles.

The initial (and final) state of a scattering process is two distant atoms, such that their energy is purely kinetic. For alkali atoms, this distance is typically given by the van der Waals length r_{vdW}, which is related to the C_6 coefficient of the r^{-6} tail of the potential. Since the scattering potential $V(r)$ is central, the relative orbital angular momentum is a good quantum number (it is conserved throughout the process) and one may write the wave function as a partial wave expansion:

$$\psi(\vec{r}) = \sum_{l=0}^{\infty} \frac{f_l(r)}{r} P_l(\cos\theta), \tag{1.1}$$

where P_l is the l-th Legendre polynomial. The radial part of the wave function $f_l(r)$ has a, in general complicated, potential-dependent structure at short distances, but beyond the reach of the potential it takes the form

$$f_l(r) \sim \sin(kr - l\pi/2 + \delta_l). \tag{1.2}$$

The beauty of this expression is that all the "mess" that is present at short distances is encapsulated by the phase shift δ_l of the asymptotic wave function. In the absence of a potential, $\delta_l = 0$ for all l while, if $\delta_l = \pi/2$ for a specific l, the interaction is said to be resonant[1] in the l-th partial wave.

The realm of cold and ultracold atoms is entered as the kinetic energy $\sim k^2$ reaches the limit $kr_{vdW} \ll 1$. In this limit, all $\delta_{l>0} = 0$ vanish, such that only the s-wave (the $l = 0$ partial wave) contributes to the scattering process. Its scattering phase shift takes the form

$$\delta_0 \sim -\arctan(ka), \tag{1.3}$$

where a is the scattering length, and the scattering cross-section is

$$\sigma = \frac{4\pi}{k^2} \sin^2 \delta_0. \tag{1.4}$$

[1] The resonant condition $\delta_l = \pi/2$ is to be understood modulo π.

Resonant s-wave scattering, also known as the unitary limit, is obtained when $\delta_0 = \pi/2 \to |ka| \gg 1$ which implies $|a| \gg r_{vdW}$. We note that a can be either positive or negative, corresponding to repulsive or attractive interactions, respectively.

Unfortunately, for the overwhelming majority of interactions found in nature $|a| \sim r_{vdW}$. As an exception we mention ground state He-4 which can be studied in molecular beam experiments. Luckily, as already eluded to above, the enormous tunability of cold atom systems includes exact control of the scattering length.

In momentum space, the $l = 0$ scattering amplitude $f_0(k)$ is equal to the negative scattering length in the limit $k \to 0$: $f_0(0) = -a$. For finite k, $f_0^{-1}(k)$ is expanded to second order in k (first order in energy) as

$$\frac{1}{f(k)} = -\frac{1}{a} - ik + \frac{r_e k^2}{2}, \tag{1.5}$$

where r_e is the effective range. This form of $f_0(k)$, which is known as the effective range expansion, makes the optical theorem $\mathrm{Im}^{-1}(f_0) = -k$ obvious. Whether or not the expansion to second order is necessary is determined by the value r_e, or $R^\star = -r_e/2$, compared to r_{vdW} .

1.2 Feshbach Resonance

In general, the scattering length is on the order of the potential range. However, if by chance the interaction potential features a bound state close to its continuum threshold or behind a barrier (e.g. the centrifugal barrier for $l > 0$), the scattering process takes a relatively long time (i.e. the atoms dwell at short inter-particle separations for an increased period of time) thus increasing the scattering phase shift. This situation is called a shape resonance – the shape of the potential gives rise to a scattering resonance.

1.2.1 Mechanism

In cold atom systems it is not a shape resonance but a so-called Feshbach resonance that gives rise to a large (and tunable) phase shift. The key is to consider multiple interaction potentials. Two identical atoms can interact via their combined electronic singlet or triplet. In general, the singlet potential is much deeper and features far more bound states than the triplet potential but we care only about the most loosely bound one. While two distant atoms are generally in a super position of singlet and triplet, we will consider them to be a pure triplet for simplicity. For specificity we consider the energy hierarchy shown in Fig. 1.1. The triplet potential is an open channel and denoted $V_\mathrm{o}(r)$ in Fig. 1.1(a). The singlet potential has a

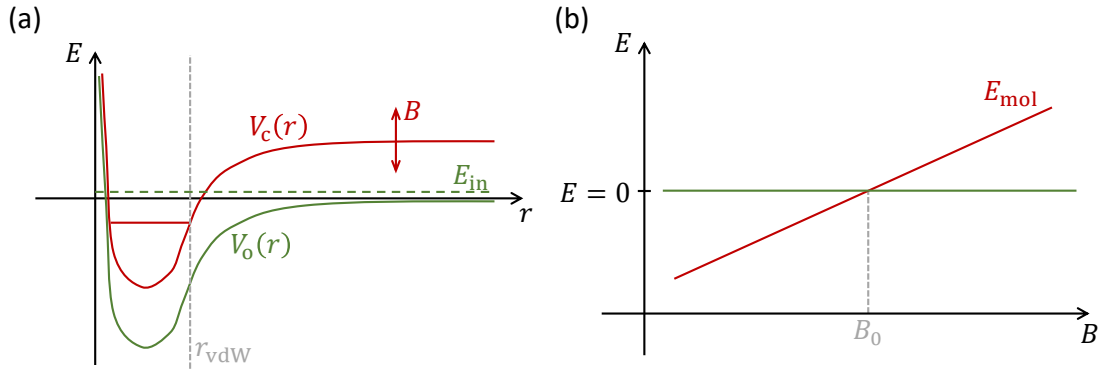

Figure 1.1: Illustration of the mechanism of a Feshbach resonance. (a) The closed channel $V_c(r)$, together with its bound state which is confined to $r < r_{vdW}$, can be tuned in and out of resonance with the incoming energy E_{in} of two particles in the open channel $V_o(r)$ by varying an external magnetic field B. (b) In the two-channel model one forgets about the r-dependence of the potentials and considers the crossing of a discrete energy level (E_{mol}) and a continuum.

larger threshold energy and is therefore energetically inaccessible [closed channel, $V_c(r)$]. Since the singlet has no net magnetic moment it is indifferent to an externally applied magnetic field B. The triplet potential, on the other hand, can be shifted up and down along the energy axis. In effect, one shifts $V_c(r)$ with respect to $V_o(r)$ as illustrated in Fig. 1.1(a). There thus exists a specific value B_0, at which the triplet threshold is degenerate with the most loosely bound state of the singlet. The hyperfine interaction provides a coupling between the two potentials meaning that the singlet bound state acts equivalently to the bound state of a shape resonance.

1.2.2 Phenomenology

In the vicinity of a Feshbach resonance the magnetic field dependence of the scattering length is parametrized as

$$a = a_{bg}\left(1 - \frac{\Delta B}{B - B_{res}}\right), \tag{1.6}$$

where ΔB is the magnetic width of the resonance and a_{bg} is the value of a far from resonance. Due to the coupling between the open and closed channels the resonance position B_{res}, i.e. the value of the magnetic field at which $|a| \to \infty$, does not coincide with B_0.

The quantity $a_{bg} \times \Delta B$ is indicative of the resonance strength. It is related to other quantities, such as $R^\star$ and the dimensionless s_{res}, which also characterize the strength of a resonance. In general, if the coupling between the singlet and triplet potential is large (small), the resonance is called broad (narrow), such that $a_{bg} \times \Delta B$

is large (small), $R^\star$ is small (large) with respect to r_{vdW} and $s_{res} \gg 1$ ($s_{res} \ll 1$). The effective range expansion of Eq. (1.5) is thus relevant for narrow resonances.

The most loosely bound, negative-energy eigenstate of the combined singlet-triplet system is called the Feshbach dimer. It is bound only for $a > 0$ and, in the limit $a \gg r_{vdW}$, has a binding energy of

$$E_D = -\frac{\hbar^2}{ma^2} \tag{1.7}$$

in case of a broad resonance, and

$$E_D = -\frac{\hbar^2}{4mR^{\star 2}} \left(\sqrt{1 + 4\frac{R^\star}{a}} - 1 \right)^2 \tag{1.8}$$

in case of a narrow resonance. Note that the latter reduces to the former in the limit $a \gg R^\star$.

1.2.3 Simple Two-Channel Model

The physics described above can be derived within the framework of a simple two-channel model. The two channels refer to (1) the open (entrance) channel in which the particles are free, i.e. in the triplet potential at distances $r \gg r_{vdW}$, and (2) the closed channel, which corresponds to the (approximately point-like) molecule of the singlet potential [Fig. 1.1(b)]. In effect, we are taking the limit $r_{vdW} \to 0$, such that the triplet (singlet) potential is identical to the open (closed) channel of the two-channel model. We will introduce the Hamiltonian and present analytic expressions for a, $R^\star$ and E_D that result from solving the two-body problem. A more detailed derivation can be found in the Appendix of Chapter 4. Since $R^\star$ is naturally extracted from the model, and since $R^\star \gg r_{vdW}$ is always satisfied given that $r_{vdW} \to 0$, the model is particularly well-suited for narrow resonances.

The model has a naturally occurring UV divergence which is fixed by introducing a high momentum cut-off k_c: All $\int d^3k$ appearing in the following are evaluated in a sphere of radius k_c. The cut-off is then used to renormalize all system parameters and physical observables, rendering them dimensionless.

The Hamiltonian is $\hat{H} = \hat{H}_0 + \hat{H}_{\text{int}}$, where

$$\hat{H}_0 = \int \frac{d^3k}{(2\pi)^3} \left[\frac{\hbar^2 k^2}{2m} \hat{a}^\dagger_{\vec{k}} \hat{a}_{\vec{k}} + \left(E_{\text{mol}} + \frac{\hbar^2 k^2}{4m} \right) \hat{b}^\dagger_{\vec{k}} \hat{b}_{\vec{k}} \right] \tag{1.9}$$

entails an open and a closed channels and

$$\hat{H}_{\text{int}} = \Lambda \int \frac{d^3k}{(2\pi)^3} \int \frac{d^3q}{(2\pi)^3} \left[\hat{b}^\dagger_{\vec{k}} \hat{a}_{\vec{q}+\frac{\vec{k}}{2}} \hat{a}_{-\vec{q}+\frac{\vec{k}}{2}} + \hat{a}^\dagger_{-\vec{q}+\frac{\vec{k}}{2}} \hat{a}^\dagger_{\vec{q}+\frac{\vec{k}}{2}} \hat{b}_{\vec{k}} \right] \tag{1.10}$$

couples them with coupling constant Λ. Here, $\hat{a}_{\vec{k}}$ ($\hat{b}_{\vec{k}}$) annihilates an atom (a molecule) with momentum $\hbar\vec{k}$ and mass m ($2m$) in the open (closed) channel and $\hat{a}^\dagger_{\vec{k}}$ ($\hat{b}^\dagger_{\vec{k}}$) is its Hermitian conjugate. As illustrated in Fig. 1.1(b), the bare molecular binding energy E_{mol} (i.e. the energy detuning) is controlled by an externally applied magnetic field B via $E_{\mathrm{mol}} = \mu(B_0 - B)$, where μ is the molecules magnetic moment with respect to the open channel and B_0 is the bare resonance position. The free parameters of the system are Λ and B_0.

To compute two-body observables the following wave function is used in the Schrödinger equation:

$$|\psi_{2B}\rangle = \beta\hat{b}^\dagger_{\vec{k}=0}|0\rangle + \int \frac{d^3k}{(2\pi)^3}\alpha_{\vec{k}}\hat{a}^\dagger_{\vec{k}}\hat{a}^\dagger_{-\vec{k}}|0\rangle. \tag{1.11}$$

This center-of-mass superpostion of two free atoms and one bare molecule is the most general wave function for a two-body system and therefore a suitable Ansatz.

After solving $(\hat{H} - E)|\psi_{2B}\rangle$ for $E > 0$ and one extracts the renormalized scattering length $\tilde{a} = k_c a$

$$\tilde{a} = -\frac{1}{2\pi}\frac{\tilde{\Lambda}^2}{\tilde{\mu}\,(B_0 - B) - \frac{\tilde{\Lambda}^2}{\pi^2}} \tag{1.12}$$

and the renormalized effective range $\tilde{r}_e = k_c r_e$

$$\tilde{r}_e = -\frac{4\pi}{\tilde{\Lambda}^2}. \tag{1.13}$$

In addition one obtains

$$\tilde{R}^\star = -\frac{\tilde{r}_e}{2} = \frac{2\pi}{\tilde{\Lambda}^2}. \tag{1.14}$$

By denoting

$$B_{\mathrm{res}} = B_0 - \frac{\tilde{\Lambda}^2}{\tilde{\mu}\pi^2}, \quad \tilde{\Delta} = \frac{\tilde{\Lambda}^2}{2\pi\tilde{\mu}}, \tag{1.15}$$

the scattering length may be written in the familiar form

$$\tilde{a} = \frac{\tilde{\Delta}}{B - B_{\mathrm{res}}}. \tag{1.16}$$

The expression for B_{res} demonstrates that the actual resonance position is shifted away from the bare resonance position B_0 by the coupling to the open channel. The expression for $\tilde{\Delta}$ shows that a narrow resonance arises from weakly coupled channels as eluded to above. Furthermore, by substituting the expression for $\tilde{R}^\star$ in $\tilde{\Delta}$ we find the connection

$$\Delta = \frac{\hbar^2}{m\mu R^\star} \tag{1.17}$$

between the resonance width $\Delta = \tilde{\Delta}/k_c$ and $R^\star$. Note that, here, the cut-off can-

celled. This equation illustrates that a narrow resonance is related to a large $R^\star$.

Comparison of $a\,(B)$ in Eq. (1.16) to the phenomenological expression in Eq. (1.6) shows that the two-channel model does not reproduce $a_{\rm bg}$. In fact, the width parameter Δ is related to the magnetic width ΔB via $\Delta = a_{\rm bg} \times \Delta B$. In the two-channel model discussed here, $a_{\rm bg} \to 0$ and $\Delta B \to \infty$, such that their product is finite. It is possible to extend the model to include background scattering. To this end the Hamiltonian is supplemented with the term

$$\hat{H}_{\rm bg} = \Lambda_{\rm bg} \int \frac{d^3p}{(2\pi)^3} \int \frac{d^3k}{(2\pi)^3} \int \frac{d^3q}{(2\pi)^3} \hat{a}^\dagger_{\vec{p}+\frac{\vec{k}}{2}} \hat{a}^\dagger_{-\vec{p}+\frac{\vec{k}}{2}} \hat{a}_{\vec{q}+\frac{\vec{k}}{2}} \hat{a}_{-\vec{q}+\frac{\vec{k}}{2}}, \tag{1.18}$$

which describes a (momentum exchanging) scattering event between two particles in the open channel.

The solution of $(\hat{H} - E)|\psi_{2B}\rangle$ for $E < 0$ leads to the bound state solution, i.e. the dimer binding energy $E_D = -\hbar^2\lambda_D^2/m$. For the binding wave number λ_D one finds

$$\tilde{\lambda}_D = \frac{\tilde{\mu}}{2}\left[\sqrt{\tilde{\Delta}^2 - 4\,(B - B_{\rm res})\,/\tilde{\mu}} - \tilde{\Delta}\right]. \tag{1.19}$$

Using the solution for $\tilde{a}$ and $\tilde{R}^\star$ one obtains

$$\lambda_D = \frac{\sqrt{1 + 4\frac{R^\star}{a}} - 1}{2R^\star} \tag{1.20}$$

which is identical to the narrow resonance dimer in Eq. (1.8). Equipped with E_D the coefficients of the two-body wave function $|\psi_{2B}\rangle$ [see Eq. (1.11)] may be computed. In particular, for the populations $P_{\rm open} = \int d^3k|\alpha(k)|^2$ and $P_{\rm closed} = |\beta|^2$, which satisfy $P_{\rm open} + P_{\rm closed} = 1$, one finds:

$$P_{\rm open} = \frac{1}{2\sqrt{1 + 4R^\star/a} - 1}. \tag{1.21}$$

Just below the Feshbach resonance, i.e. for $E_D \to 0^-$ and $R^\star/a \to 0^+$, a linear expansion in $R^\star/a$ gives $P_{\rm open} \approx 1 - 4R^\star/a$. Thus, the open-channel population decreases very quickly as the scattering length is tuned away from resonance. In this sense, a narrow Feshbach resonance is closed-channel dominated.

We have shown that the bare parameters Λ and B_0 are directly connected to two-body observables such as the scattering length, effective range and dimer binding energy. For a given atomic species and scattering channel one must fix the bare parameters such that the observables are reproduced as well as possible. Incidentally, the set (Λ, B_0) is fully determined by $(R^\star, B_{\rm res})$ or $(\Delta, B_{\rm res})$.

1.2.4 Early Experiments

Shortly after the first realizations of a BEC in ^{23}Na [27] and ^{87}Rb [28] two Feshbach resonances were observed in ^{23}Na [29] and three in the ^{87}Rb-^{40}K mixture [30]. They were found by monitoring inelastic losses as a function of the magnetic field which is resonantly enhanced near B_{res}. Thereafter, resonances were observed in almost all alkali atoms, including isotopes of Li, K, Rb, and Cs, and various mixtures thereof [31]. In addition to inelastic loss spectroscopy, Feshbach resonances can be found by locating the zero crossing $B_{\text{res}} + \Delta B$ via a minimum in elastic scattering. The latter is found by applying evaporative cooling at various values of the magnetic field. At $B_{\text{res}} + \Delta B$ the cooling ceases to be efficient at the (relatively high) temperature at which s-wave scattering becomes dominant [32].

Another way to find and characterize Feshbach resonances is via the loosely bound dimer. To this end one must measure the binding energy as a function of the magnetic field and extract the parameters of either Eq. (1.7) or (1.8) from a fit. The straight forward way to measure E_D is via radio-frequency (rf) association or dissociation. For the association protocol one parks the magnetic field on the $a > 0$ side of the resonance, applies a rf-field of variable frequency ω_{rf} and counts the number of remaining atoms. The latter is minimal if the conversion efficiency is maximal, i.e. for $\hbar\omega_{\text{rf}} = |E_D|$ [33–35]. For the dissociation protocol one first creates dimers by ramping across the resonance from $a < 0$ to a desired value of $a > 0$ and blows away the free atoms with resonant light. One then attempts to dissociate the dimers with an rf-field. Here, the number of free atoms is maximal if $\hbar\omega_{\text{rf}} = |E_D|$ [36].

There exists an alternative measurement of E_D which is especially relevant to this Thesis because it exploits the coherence between dimers and free atoms. Coherent association of dimers is achieved by sweeping over the Feshbach resonance from $a < 0$ to $a > 0$. After a variable evolution time one sweeps back to $a < 0$, thus causing the associated dimers to dissociate and interfere with the free atoms. This allows measurement of the phase difference which is proportional to the binding energy [37–41].

1.2.5 Recent Experiments

In no way is the observation of a Feshbach resonance considered old and boring physics. The systems in which they are found are becoming more and more exotic and complex. For example, magnetic lanthanide atoms were found to have a dense and chaotic spectrum of resonances [42] with up to several tens per Gauss [43]. Resonances were also found between alkali and closed-shell atoms [44] and between atoms and ground state molecules [45]. More recently, resonances between ground

state molecules were measured [46]. Slightly more exotic, hybrid ion-atom systems could be pushed towards low enough temperatures to observe pure s-wave resonances between alkali atoms and a single ion [47].

1.3 Efimov Effect

After discussing two-body physics and Feshbach resonances in particular we now turn to a system made up of three particles with pairwise, resonantly enhanced interactions. The reader is also referred to the numerous well-written review articles written on the subject [24, 48–51].

1.3.1 Hyper Spherical Treatment

The goal is to solve the three-body Schrödinger equation

$$\left[-\sum_{i=1}^{3}\frac{\hbar^2}{2m}\nabla_i^2+\sum_{i<j}V\left(r_{ij}\right)-E\right]\Psi\left(\vec{r}_1,\vec{r}_2,\vec{r}_3\right)=0, \tag{1.22}$$

where $r_{ij}=|\vec{r}_i-\vec{r}_j|$ is the distance between the i-th and j-th atom. One way to do so is to forget about $V(r_{ij})$ altogether and use the Bethe-Peierls boundary condition

$$\frac{\partial\ln\left(r_{ij}\Psi\right)}{\partial r_{ij}}=-\frac{1}{a} \tag{1.23}$$

instead, which guarantees the correct asymptotic form of the two-body wave function: $\sim\left(r^{-1}-a^{-1}\right)$ for $r\gg r_{vdW}$. The boundary condition assumes that the two-body potential describes a zero-range contact interaction.

Due to bosonic exchange symmetry the three-body wave function can be decomposed into three pairs: $\Psi=\chi\left(12,3\right)+\chi\left(23,1\right)+\chi\left(31,2\right)$, where in each $\chi\left(ij,k\right)$ the third particle (k) is considered with respect to the center of mass of the first two (ij). It is thus sufficient to solve Eq. (1.22) for one χ-component. To this end it is convenient to use a set of coordinates known as hyper-spherical coordinates (R,ϖ) which include the hyper-radius

$$R^2=\frac{2}{3}\left(r_{12}^2+r_{23}^2+r_{31}^2\right) \tag{1.24}$$

and five hyper-angles collectively denoted ϖ. The former can be viewed as the overall size of the three-body system while the latter determine their relative orientation. When using the Bethe-Peierls condition in Eq. (1.23) the wave function $\Psi\left(R,\varpi\right)=\Psi\left(R,\alpha\right)$ depends on only one hyper-angle which we denote α. The Schrödinger

equation takes the form

$$\left[-\frac{\partial^2}{\partial R^2}-\frac{1}{R}\frac{\partial}{\partial R}-\frac{1}{R^2}\frac{\partial^2}{\partial\alpha^2}-k^2\right]\chi_0\left(R,\alpha\right)=0 \tag{1.25}$$

and the boundary condition, for $\alpha\to 0$, is

$$\left[\frac{\partial}{\partial\alpha}\chi_0\left(R,\alpha\right)\right]_{\alpha\to 0}+\frac{8}{\sqrt{3}}\chi_0\left(R,\frac{\pi}{3}\right)=-\frac{R}{a}\chi_0\left(R,0\right), \tag{1.26}$$

where $\chi=\chi_0/\left(R^2\cos\alpha\sin\alpha\right)$ and the eigen energy was written as $E=\hbar^2k^2/m$.

In the limit $|a|\to\infty$ the right-hand-side of Eq. (1.26) vanishes such that the problem becomes separable: $\chi_0\left(R,\alpha\right)=F\left(R\right)\Phi\left(\alpha\right)$. Hence, one may solve the hyper-angular part for constant R and use the obtained energies as R-dependent potentials

$$U_n\left(R\right)=\frac{s_n^2-1/4}{R^2}. \tag{1.27}$$

The value of s_n is the solution of the transcendental equation

$$-s_n\cos\left(\frac{\pi}{2}s_n\right)+\frac{8}{\sqrt{3}}\sin\left(\frac{\pi}{6}s_n\right)=0. \tag{1.28}$$

At this point the Schrödinger equation takes the simple form

$$\left[-\frac{\partial^2}{\partial R^2}+U_n\left(R\right)-k^2\right]\sqrt{R}F_n\left(R\right)=0. \tag{1.29}$$

Except for one, all solution of Eq. (1.28) are real and their square larger than $1/4$. Only $s_0=i\times 1.00624$, i.e. $s_0^2<0$, leads to an attractive three-body potential which supports bound states. This situation should be contrasted to the non-interacting three-body problem where $s_n=2\left(n+1\right)$ is real for all n and therefore always repulsive. However, since the potential $\sim R^{-2}$ scales the same as the kinetic term ($\sim\partial^2/\partial R^2$), the Schrödinger equation is scale invariant and admits a solution at any energy – the spectrum is *not* bounded from below. To prevent this unphysical artefact of the zero-range two-body potential one introduces a low-R cut-off R_0, essentially forcing the three-body system to be $>R_0$. The radial wave function of the Efimov trimer bound state is then

$$F_0\left(R\right)\sim\cos\left(|s_0|\ln\frac{R}{R_0}\right). \tag{1.30}$$

While the low-R cut-off breaks the (continuous) scale invariance $R\to\lambda R$ (for arbitrary λ) it still permits a discrete scale invariance $R\to\lambda_0^nR$ with $\lambda_0=e^{\pi/|s_0|}$ and $n\in\mathbb{N}$. Thus, if the ground state solution has energy $E_0<0$, a bound state with $E=E_0/\lambda_0^{2n}$ (for any n) is also a valid solution. In conclusion, the potential $U_0(R)$

together with the cut-off R_0 give rise to an infinite ladder of log-periodic bound states.

1.3.2 Efimov Universality

The low-R cut-off R_0 defines the length and energy scale of the three-body problem and is a possible representation of the three-body parameter. A more convenient option is to define the three-body parameter via physical observables that are related to the microscopic R_0. As such, the most common choice is $a_-^{(0)}$, i.e. the value of the scattering length at which the ground state trimer (whose spectrum is determined by R_0) vanishes at the three-body scattering threshold. Other options include the binding wave number at unitarity $\kappa_\star^{(0)}$, the value $a_\star^{(0)}$ of the scattering length at which the trimer dissociates into a dimer and a free atom and the value $a_+^{(0)}$ of the scattering length at which the three-body recombination exhibits a minimum due to destructive interference of two different decay channels. Given the value of any of these in the ground state $n = 0$, for the n-th excited state they are given via

$$a_i^{(n)} = \lambda_0^n a_i^{(0)}, \quad \kappa_\star^{(n)} = \kappa_\star^{(0)}/\lambda_0^n \tag{1.31}$$

where $i = \{-, \star, +\}$. The binding energy $E_T^{(n)} = \hbar^2 \left(\kappa^{(n)}\right)^2/m$ of the n-th excited state is found by solving

$$\frac{E_T^{(n)}}{E_D} = \tan^2 \xi, \quad \kappa^{(n)} = \frac{\kappa_\star^{(n)}}{h(\xi)\cos\xi}, \tag{1.32}$$

where $h(\xi) = e^{\Delta(\xi)/2|s_0|}$, and $\Delta(\xi)$ is a piecewise function given by

$$\Delta(\xi) = \begin{cases} -0.825 - 0.05z - 0.77z^2 + 1.26z^3 - 0.37z^4 & \xi \in \left[-\pi, -\frac{5}{8}\pi\right] \\ 2.11y + 1.96y^2 + 1.38y^3 & \xi \in \left[-\frac{5}{8}\pi, -\frac{3}{8}\pi\right] \\ 6.027 - 9.64x + 3.14x^2 & \xi \in \left[-\frac{3}{8}\pi, -\frac{\pi}{4}\right] \end{cases} \tag{1.33}$$

Here, $z = \xi + \pi$, $y = \xi + \pi/2$ and $x = \sqrt{-\xi - \pi/4}$. The angle ξ takes values from $-\pi$ to $-\pi/4$, corresponding to the spectrum from the free-atom continuum ($-\pi$) to the atom-dimer continuum ($-\pi/4$) in the κ-a^{-1} plane.

It is apparent that the Efimov spectrum is fully determined by the three-body parameter. The ground and all excited states have the same functional form and differ only by a multiplicative constant. In addition the various features across the Feshbach resonance are related:

$$a_-^{(n)} = -1.50763/\kappa_\star^{(n)}, \quad a_+^{(n)} = 0.32/\kappa_\star^{(n)}, \quad a_*^{(n)} = 0.0707645/\kappa_\star^{(n)}. \tag{1.34}$$

All the above is part of what is known as the Efimov universality and is the result of the underlying zero-range two-body interaction.

1.3.3 Efimov-van der Waals Universality

While the three-body parameter is arbitrary in the zero-range theory, finite range theories, and in particular the van der Waals tail of the two-body potential, constrain $a_-^{(0)}$ to $\sim -8.9\, r_{vdW}$ [52, 53].

If the two-body potential $V(r_{ij})$ in Eq. (1.22) is not zero-range but has, e.g., a van der Waals tail, the boundary condition (1.23) cannot be used. As before, one separates the wave function into a hyper-radial and a hyper-angular part, but unlike before, one obtains several hyper-radial potentials $U_\nu(R)$ which are coupled via non-adiabatic coupling matrices $\hat{W}_{\nu\nu'}(R)$. The zero-range limit is obtained by neglecting all couplings. However, in the presence of finite-range interactions, the couplings give rise to a diagonal three-body potential that approaches Eq. (1.27) at $R \gg r_{vdW}$ but features a repulsive barrier at $R \approx 2r_{vdW}$ [52–54]. Thus, the low-R cut-off, i.e. the three-body parameter, is not arbitrary as initially assumed but fully determined by the van der Waals length of the two-body interaction.

1.3.4 Two-Channel Model Treatment

In the two-body sector, a two-channel model was introduced to reproduce the phenomenology of a narrow Feshbach resonance with utmost simplicity. To complement the single-channel discussion of Efimov physics above, which is valid for broad resonances (there was no parameter similar to $R^\star$), we here apply the two-channel Hamiltonian [see Eqs. (1.9) and (1.10)] to the three-body sector and explore the formation of Efimov trimers. It is worth emphasizing, again, that the model's bare parameters are fixed in the two-body sector by fitting them to the experimentally observed scattering length and/or dimer binding energy. When going to the three-body sector, no additional parameter is introduced and thus the Efimov spectrum does not have a three-body parameter. The trimers are fully constrained by the underlying pairwise interactions. In fact, we shal see that $R^\star$ plays the role of the three-body parameter in the sense that it gives an absolute scale for the binding energy.

To find the binding energy of Efimov trimers we search for a negative energy solution $E = -\hbar^2\lambda_T^2/m$, where $\lambda_T > \max(0, \lambda_D)$, of the Schrödinger equation $(\hat{H} - E)|\psi_{3B}\rangle$ with

$$|\psi_{3B}\rangle = \int \frac{d^3k}{(2\pi)^3} \beta_{\vec{k}} \hat{b}^\dagger_{\vec{k}} \hat{a}^\dagger_{-\vec{k}} |0\rangle + \int \frac{d^3k}{(2\pi)^3} \int \frac{d^3q}{(2\pi)^3} \alpha_{\vec{k},\vec{q}} \hat{a}^\dagger_{\vec{q}+\frac{\vec{k}}{2}} \hat{a}^\dagger_{-\vec{q}+\frac{\vec{k}}{2}} \hat{a}^\dagger_{-\vec{k}} |0\rangle. \tag{1.35}$$

Also here we work in the center-of-mass frame and have chosen $\vec{k}$ and $\vec{q}$ to be a set of Jacobi momenta. After renormalizing with respect to k_c, the expressions for $\tilde{a}$ and $\tilde{R}^\star$, in Eqs. (1.16) and (1.14) respectively, are substituted and one obtains

$$\left[\sqrt{\frac{3k^2}{4}+\lambda_T^2}-\frac{1}{a}+R^\star\left(\frac{3k^2}{4}+\lambda_T^2\right)\right]\psi(k) - \frac{2}{\pi}\int_0^\infty dq \ln\left(\frac{k^2+kq+q^2+\lambda_T^2}{k^2-kq+q^2+\lambda_T^2}\right)\psi(q)=0, \quad (1.36)$$

where $\psi(k) = k\beta_k$ and all factors of k_c have cancelled. We have eliminated the magnetic field dependence (via the substitution of a) and can directly compute the scattering length dependence of λ_T. We note that all lengths (k^{-1}, q^{-1}, λ_T^{-1}, a) can be expressed in units of $R^\star$ such that the latter disappears from the equation. Hence, the Efimov spectrum resulting from the two-channel model, i.e. the Efimov spectrum of a narrow Feshbach resonance, is universal with respect to $R^\star$.

To solve Eq. (1.36) it is convenient to switch variables via

$$k=\frac{2}{\sqrt{3}}\lambda_T\sinh(\xi), \quad q=\frac{2}{\sqrt{3}}\lambda_T\sinh(\xi') \quad (1.37)$$

and rescale $\psi(k)\to\psi(k)/\cosh(\xi)$. If we limit ourselves to odd solutions for $\psi(k)$ the lower integration limit may be extended to $-\infty$ provided we divide the entire integral by 2. By introducing $\int d\xi'\delta(\xi-\xi')$ in the first term it is included into the integral. One finally finds

$$\int_{-\infty}^{\infty} d\xi' \mathcal{M}_{\lambda_T}(\xi,\xi')\,\psi(\xi')=0 \quad (1.38)$$

with $\psi(\xi)$ an odd function of ξ and

$$\mathcal{M}_{\lambda_T}(\xi,\xi')=\delta(\xi-\xi')\left[1-\frac{1}{a\lambda_T\cosh\xi'}+R^\star\lambda_T\cosh\xi'\right] - \frac{4}{\sqrt{3}\pi}\ln\left(\frac{e^{2(\xi-\xi')}+e^{\xi-\xi'}+1}{e^{2(\xi-\xi')}-e^{\xi-\xi'}+1}\right). \quad (1.39)$$

A non-trivial solution is obtained for

$$\det\mathcal{M}_{\lambda_T}(\xi,\xi')=0, \quad (1.40)$$

which constitutes a closed equation for λ_T and can be solved numerically by discretizing ξ and ξ'. One searches for the value $\lambda_T=\lambda_T^{(\mathrm{sol})}$ for which $\det\mathcal{M}_{\lambda_T}(\xi,\xi')$ changes sign as λ_T is varied through $\lambda_T^{(\mathrm{sol})}$. Note that many solutions $\lambda_T^{(\mathrm{sol})}$ exist for a given a and $R^\star$. To verify ones solution, the obtained value $\lambda_T^{(\mathrm{sol})}$ is plugged back

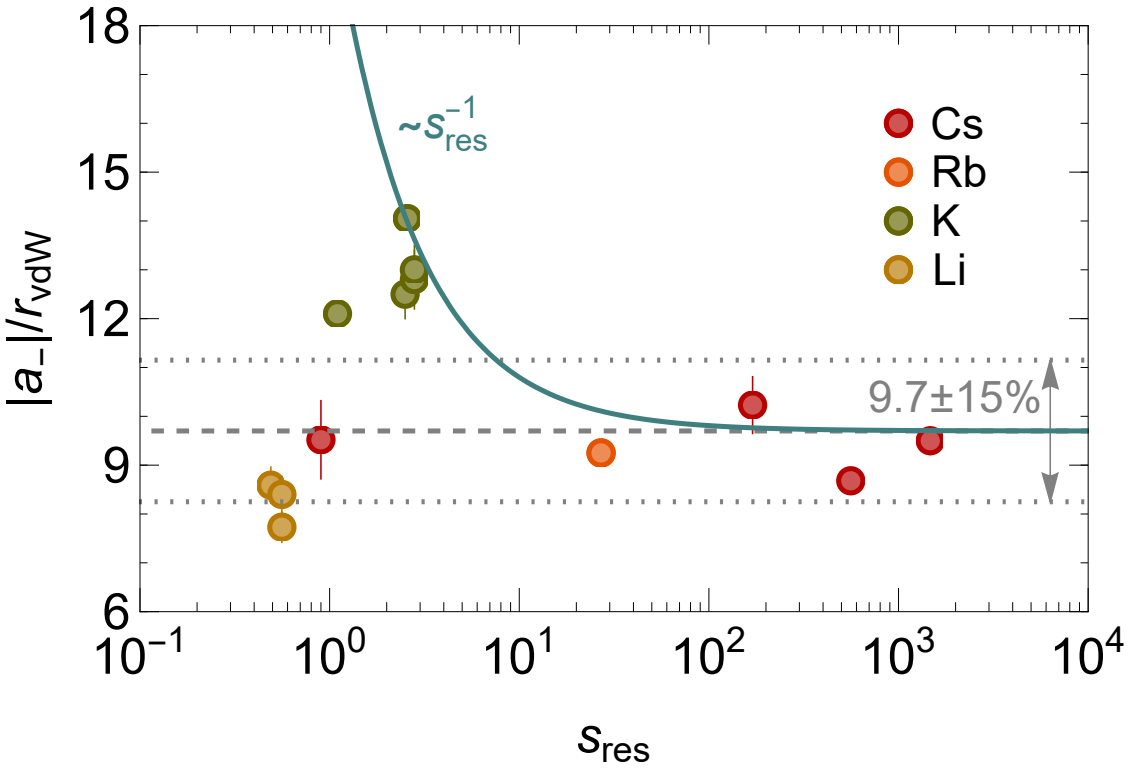

Figure 1.2: The experimental mean $a_-^{(0)}/r_{vdw} = -9.7$ and a $\pm 15\%$ interval are shown together with the various experiments conducted [55–63]. The blue line shows the result of the two-channel model for narrow resonances with an artificially added offset to fit the experimental mean. We note that the measurements in ^{7}Li satisfy the Efimov-van der Waals universality even though the resonances are narrow.

into $\mathcal{M}_{\lambda_T=\lambda_T^{(\mathrm{sol})}}(\xi,\xi')$ and its eigen values and eigenfunctions $\psi(\xi)$ are computed. One of the eigenvalues must be equal to zero (within machine precision) and its associated eigen function must be odd (odd number of nodes). The value of $\lambda_T^{(\mathrm{sol})}$ for which $\psi(\xi)$ has one node is the ground state. If $\psi(\xi)$ has three nodes it is the first excited state and so on.

1.3.5 Efimov-van der Waals Universality – Revisited

According to the two-channel model treatment, the Efimov spectrum is universal with respect to $R^\star$. This implies that, e.g., the point $a_-^{(0)}$, in units of $R^\star$, is a universal number: $R^\star/a_-^{(0)} = -0.091$. Hence, for narrow resonances, where $R^\star \gg r_{vdW}$, the strength of the resonance, and not the range of the two-body potential, determines the position of $a_-^{(0)}$. The Efimov-van der Waals universality is not expected to hold for narrow resonances (see Fig. 1.2).

1.3.6 Experimental Evidence

In cold-atom experiments, the ensemble of atoms is typically pumped into the lowest hyperfine and Zeeman state which is energetically separated from all other states by a (at times minimal) magnetic field. A diatomic collision can therefore not lead to a release energy from a spin flip – the collisions are always elastic. Moreover, energy can also not be released by forming a bound state because energy and momentum cannot be conserved simultaneously. Hence, the lowest order inelastic collision process is three-body recombination in which two atoms form a bound state and a third particle carries away the excess energy. Near a Feshbach resonance, the (universal) Feshbach dimer is the most likely bound state to be formed. In this case, the rate K_3 at which the three-body recombination process happens depends on the fourth power of the scattering length, so $K_3 \sim a^4$, and thus increases quickly as the Feshbach resonance is approached [48].

The standard experimental method to observe an Efimov trimer involves monitoring the loss of atoms while approaching $a \to \infty$ from $a < 0$. As one reaches the value of $a_-^{(0)}$, three-body recombination is resonantly enhanced beyond the $\sim a^4$ background. The first such successful measurement was done with ^{133}Cs atoms [55] and was repeated thereafter in a variety of atomic species [56–61, 63] including a recent high-precision measurement [62]. The notorious difficulty of the experiment stems from the fact Efimov physics is manifested close to a Feshbach resonance, where K_3 is already large. In addition, the atomic ensemble must be extremely cold and dilute, even for typical cold atoms. Observing not just the ground state at $a_-^{(0)}$, but the excited state $a_-^{(1)} = \lambda_0 a_-^{(0)}$ thus took another couple of years [64] and the second excited state remains elusive in homo-nuclear systems. The latter was possible in the highly mass-imbalanced system of ^{6}Li-^{133}Cs where the value of λ_0 is ~ 5 times smaller [65, 66].

The plethora of experimental $a_-^{(0)}$-values obtained in numerous atomic species and at a variety of Feshbach resonances led to the realization that the ratio $a_-^{(0)}/r_{vdW}$ is not arbitrary. On the contrary, most measurements were within 15% of -9.7. The theoretical value -8.9 [52, 53] mentioned above was found following the experimental discovery. A summary of the experiments is shown in Fig. 1.2 together with the broad and narrow resonance theories.

A similar experimental approach can be taken on the $a > 0$ side of the resonance to find $a_\star^{(0)}$, provided one prepares a mixture of atoms and dimers [67, 68]. We also mention the presence of minor resonances due to the presence of a four-body bound state associated to the Efimov trimer [69].

The downside of observing Efimov trimers via three-body recombination is that only the extreme points, i.e. the points at which the trimer dissociates into free

atoms or a dimer and an atom, are accessible. It is not possible to measure the binding energy as a function of scattering length or magnetic field. The solution is to create the trimer via rf-association similar to what was done with Feshbach dimers [70, 71]. A nice feature of this method on the $a > 0$ side, is that both the dimer and trimer can be observed, the former providing a means of calibration.

In this Thesis we develop and refine a new method for observing Efimov trimers.

Finally, in passing we mention a set of experiments conducted, not in cold atomic ensembles, but ^{4}He atomic beams. In this experimental system the scattering length is not tunable, however it is naturally large. In fact, if is so large that two Efimov states exist and they were successfully observed[2] [72].

1.4 Efimov Physics in Bosonic Lithium

The ground state of ^{7}Li has a hyperfine structure splitting of 803.5 MHz. At zero magnetic field the lower (higher) $F = 1$ ($F = 2$) state is three-(five-)fold degenerate. Our work is conducted at large magnetic fields, where the total angular momentum F is no longer a good quantum number, but the projection of the electronic angular momentum m_J is (see Fig. 1.3). Stable ultracold atomic gases can be prepared in either the lowest (a) or second lowest (b) spin state [73, 74]. Both feature an intermediate strength Feshbach resonance, with s_{res} slightly below unity, and the bb-channel has an additional narrow resonance (the one at lower field). All three arise due to the coupling to a hyper-fine split bare molecule which is a spin singlet and therefore magnetic field independent (see Fig. 1.3).

Efimov features have been measured in both spin channels and the two were shown to be overwhelmingly similar [73]. However, although the Feshbach resonances are not broad, they follow the Efimov-van der Waals universality (Fig. 1.2). A theoretical explanation remains to be found. In addition, rf-association was used to map out parts of the bb-channel Efimov spectrum for positive scattering lengths [71]. One might assume, that, since the Efimov-van der Waals universality is obeyed, the Efimov spectrum behaves according to a broad resonance. This would suggest using the measured value of a_- and the universal spectrum in Eq. (1.32) to reproduce the measured spectrum. The fact that it fails teaches us that trimer does not comply to the physics of a broad resonance after all. These observations are collectively known as the "lithium few-body puzzle".

[2] Technically, only the excited state has Efimovian character – see the discussion in e.g. [50].

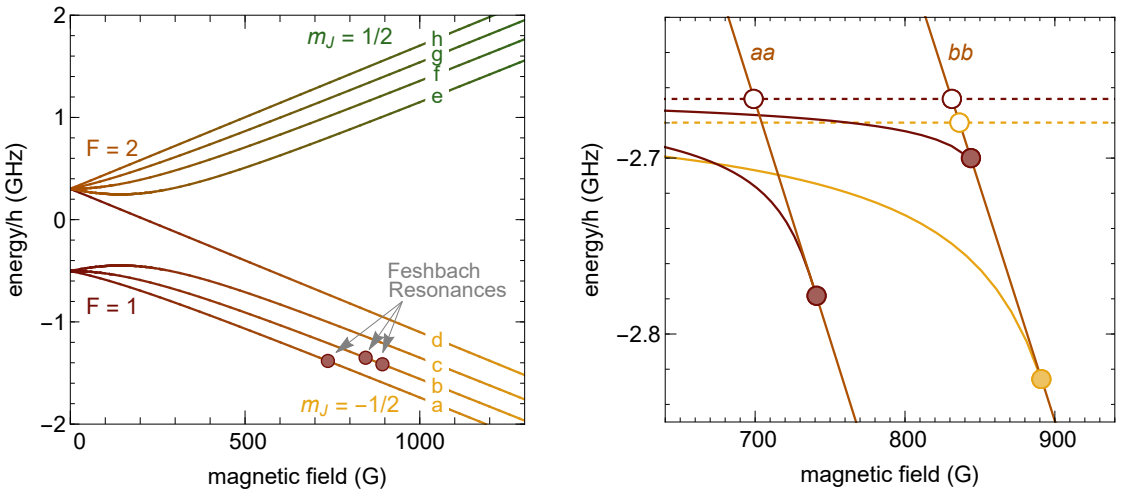

Figure 1.3: Left: The energy levels of the $2S_{1/2}$ ground state of ^{7}Li are shown as a function of magnetic field. The level labels used in the text are indicated, as well as the positions of the Feshbach resonances in the two lowest channels. Right: The molecular and atomic levels of ^{7}Li for the two lowest spin configurations are plotted. The dashed lines are the (singlet) bare molecules which couple to the atomic channels labeled *aa* and *bb*. The bare and real resonance positions are indicated by open and full circles, respectively.

1.5 Outlook – Where is Few-Body Physics in Cold Atoms Headed

1.5.1 Coherence in Few-Body Systems

From the perspective of this Thesis, the most exciting development in few-body physics is the realization that coherence can be leveraged to measure physical observables.

Coherence is the hidden resource of quantum mechanics. While various probabilistic properties of quantum mechanics have classical analogues e.g. in statistical ensembles, coherence is a wave phenomenon and therefore purely quantum for massive particles.

Many research avenues, including various subfields of cold-atoms, such as many-body simulation, quantum metrology and quantum computing, have been taking advantage of this for several decades. In recent years it was realized that also few-body experiments can be designed to leverage this quantum advantage. Prime examples are this Thesis and the observation of the wave function of the ^{4}He dimer in an atomic beam [75]. A recent, across-platform conference[3] dedicated to coherence in few-body system shows the current popularity of the topic.

[3] https://www.weizmann.ac.il/conferences/FBC2023/

1.5.2 Evidence of Few-Body Correlations in Many-Body Processes

One of the major applications of cold-atoms is simulating many-body physics. It is, of course, natural to assume that macroscopic many-body phenomena originate from microscopic interactions [76, 77]. It turns out that there is a quantitative measure, known as Tan's contact parameter [78, 79], that relates many-body observables to few-body observables. Namely, the tail of the momentum distribution of a unitary gas (many-body) is related to the probability of finding two atoms nearby (few-body). Thermodynamically, the two-body contact is the change of the internal energy due to a small modification of the scattering length. In addition to being generalized to reduced dimensions [80] and spin-full gases [81], this concept was observed in a variety of experiments [59, 82–85].

1.5.3 From Few to Many

How many is many?

In relation to the few-body correlations in many-body systems, one may wonder when a system changes from few to many. Probably the most pragmatic approach is to build a many-body system from the bottom up [86]. Although the transition from few to many, somewhat reasonably, does not happen abruptly at a certain exact number, the answer seems to be surprisingly few in both one [87] an two dimensional systems [86, 88, 89].

1.6 This Thesis – Overview

The main actor in this Thesis is the DITRIS – the DImer TRImer Superposition. Early on in my PhD we discovered that we can create a superposition of Feshbach dimers and Efimov trimers by applying very short, and therefore spectrally broad, rf pulses. The number of DITRIS states that are associated from an initial cloud of free atoms is intrinsically small such that the experiment is very prone to various fluctuations (the signal-to-noise ratio just above one). In Chapter 2 we present the first measurement of the DITRIS after we managed to eliminate the major noise sources in the lab.

The large potential of the DITRIS was clear from the beginning: It is a highly accurate tool for measuring the Efimov trimer's binding energy in the so-far inaccessible regime around $a_\star^{(1)}$. This can deepen our understanding of the "lithium few-body puzzle". Moreover, the regime in question was, and still is, the subject of theoretical discrepancies. Namely, different theories predicted contradicting threshold behaviors of the trimer. Does it merge with the atom-dimer continuum or is

there an avoided crossing? Equipped with the proof-of-principle from Chapter 2 we set out to measure the regime in question and found that the trimer does not merge with the atom-dimer continuum (Chapter 3). Further theoretical investigation, which we conducted together with our collaborators, showed that the trimer doesn't go through an avoided crossing either. Instead, the trimer crosses the continuum threshold but remains a long-lived bound state above the threshold. While the experiment is indifferent to the sign of the energy, the numerically computed three-body potentials give a strong argument for the crossing scenario.

Our initial guess was that the crossing is the result of the asymptotic behavior of the spin-channel used in the experiment. It features both an overlapping resonance and a near-degenerate continuum. We developed two simple three-channel models which are generalizations of the two-channel model presented above. In the first, an additional closed molecular channel is added to produce a second, overlapping resonance (Chapter 4). The second has an atomic channel slightly detuned from the open channel and allows spin-exchange interactions (Chapter 5). While both models modify the Efimov spectrum with respect to the two-channel model, they both predict merger between the trimer and the atom-dimer continuum and we conclude that the main contributions to the asymptotic wave function are not responsible for the crossing. Moreover, since we exhaustively investigated the leading contributions we concluded that the reason for the avoided crossing should be explored in the short-range details. This was an important input to the theory we, primarily our collaborators, eventually came up with. In fact, the crossing can be reproduced by a two-channel model using exact two-body potentials in the hyperspherical treatment. It is crucial, however, not to neglect non-adiabatic coupling terms. According to the results, a crossing of the trimer into the continuum happens for a small window of resonance strengths and the resonance used in the experiment lies quite central in that window.

The main remaining open question addresses the nature of the bound state embedded in the continuum above the atom-dimer threshold. Naively one would expect an energy level that is embedded in a continuum to be a scattering resonance but not a long-lived bound state. This assumption is also supported by the theory which, albeit agreeing with the energy level crossing into the continuum, predicts a vanishingly short life time. The experiment shows an inverse lifetime much smaller than the energy but, due to the low signal-to-noise ratio, does not allow its quantitative measurement. The next step, which is elaborated in Chapter 6, is to design a new experimental protocol that drastically increases the signal. Measuring the lifetime as a function of various parameters, first and foremost the binding energy, will shed light on the mystery of the long lifetime.

In this Thesis I was able to develop a new experimental method and apply it to

an unexplored and controversial regime, where I discovered an unexpected feature. Furthermore, I explored various potential explanations and didactically ruled out wrong attempts to finally, with the help of collaborators, converge on a working theory. Finally, I have mapped out the next steps of the DITRIS endeavor.

Chapter 2

Article 1: Coherent Superposition of Feshbach Dimers and Efimov Trimers

Yaakov Yudkin, Roy Elbaz, P. Giannakeas, Chris H. Greene and Lev Khaykovich

Physical Review Letters

Volume 122, Page 200402, May 2019

Coherent Superposition of Feshbach Dimers and Efimov Trimers

Yaakov Yudkin,[1] Roy Elbaz,[1] P. Giannakeas,[2] Chris H. Greene,[3] and Lev Khaykovich[1]
[1]Department of Physics, QUEST Center and Institute of Nanotechnology and Advanced Materials, Bar-Ilan University, Ramat-Gan 5290002, Israel
[2]Max Planck Institute for the Physics of Complex Systems, Nöthnitzer Strasse 38, 01187 Dresden, Germany
[3]Department of Physics and Astronomy, Purdue University, West Lafayette, Indiana 47907, USA

(Received 11 March 2019; published 24 May 2019)

A powerful experimental technique to study Efimov physics at positive scattering lengths is demonstrated. We use the Feshbach dimers as a local reference for Efimov trimers by creating a coherent superposition of both states. Measurement of its coherent evolution provides information on the binding energy of the trimers with unprecedented precision and yields access to previously inaccessible parameters of the system such as the Efimov trimers' lifetime and the elastic processes between atoms and the constituents of the superposition state. We develop a comprehensive data analysis suitable for noisy experimental data that confirms the trustworthiness of our demonstration.

DOI: 10.1103/PhysRevLett.122.200402

In few-body physics, the laws of quantum mechanics allow formation of loosely bound states which possess a variety of universal properties [1] and which have been intensively explored with ultracold atoms in recent years [2–4]. In the two-body domain, weakly bound dimers are now routinely used for the characterization of Feshbach resonances [5] and for the production of ultracold molecules in their ro-vibrational ground state [6]. In the three-body domain, the captivating subject of Efimov physics has been explored in a variety of atomic systems [7–17]. But, interestingly, experimental techniques used in these explorations have been essentially limited to the study of interatomic inelastic processes, such as three-body recombination. Such an approach is best suited for the region of negative scattering lengths ($a < 0$), where trimers can be associated from the three atom continuum. In contrast, for positive scattering lengths ($a > 0$) the presence of dimers shifts the recombination loss features into the atom-dimer continuum and Efimov resonances remain inaccessible for direct observation.

One of the central results of experimental research reveals an intriguing universality in the absolute position of the Efimov resonance across diverse open-channel-dominated Feshbach resonances [14,18–20]. The Efimov resonance's position is determined by the three-body parameter (3BP) which had generally been accepted to be nonuniversal. However, following experimental evidence, it was shown that its universality stems from the fact that atoms interact through a van der Waals potential which suppresses the probability to find the particles at short distances from each other [21–26]. The breakdown of this universality has been predicted [27–29] and confirmed [17] to occur only near closed-channel-dominated Feshbach resonances.

The Efimov-van der Waals universality is well established for $a < 0$. However, for $a > 0$ the presence of an atom-dimer continuum obscures the situation. The way the dimers are created in experiments poses challenges to the preparation of an initial atom-dimer mixture with a significant population of dimers. Among the various laser-cooled bosonic species only cesium allowed the preparation of a suitable atom-dimer mixture through a rather sophisticated protocol [30,31]. In other bosonic species Efimov resonances have been studied only indirectly by means of an avalanche mechanism [9,11,32–35] which is currently questioned [31,35,36]. From the theory side, the universality of the 3BP is predicted to weaken for $a > 0$ [37–41]. Moreover, it predicts that the first excited Efimov level avoids merging with the atom-dimer continuum due to various finite range effects [40]. Despite continuous theoretical interest, experimental progress is hindered due to inherent limitations of the currently available experimental techniques.

In a few previous experiments a limited range of the first excited Efimov energy level has been probed by rf association [33,42,43]. The signature of production of Efimov trimers was revealed by loss resonances which did not permit measuring their lifetime. In addition, the finite resolution of the method prevented exploration of the vicinity of the atom-dimer resonance [33]. Although in a recent experiment the lifetime of the Efimov trimer has been measured directly, the applied method prevented access to spectroscopic information and required a rather significant initial population of trimers [44].

This Letter demonstrates a new experimental approach to study the physics of Efimov trimers at $a > 0$. As illustrated in Fig. 1, we utilize a short and strong pulse of magnetic field modulation which is broad enough to create a coherent

superposition state of Feshbach dimers and Efimov trimers. After a variable time of its coherent evolution we apply a second pulse to observe the accumulated phase difference between the two constituents of the superposition state. The resulting oscillations reveal the Efimov trimer energy level with nearly tenfold improvement in precision and much higher resolution limit compared to the previously applied experimental method [33]. Even more importantly, we observe the decay of the coherent oscillations which can be related to different decoherence mechanisms such as the trimers' lifetime and the elastic atom-dimer and/or atom-trimer collision rates. Note, finally, that we benefit from the fourfold interferometric enhancement of the signal and demonstrate high sensitivity in probing a small population of trimers.

The experiment is performed on ^{7}Li atoms, polarized in the $|F = 1, m_F = 0\rangle$ state and evaporatively cooled to a temperature of $T \approx 1.5$ μK in a crossed-beam optical trap in the vicinity of a Feshbach resonance [45]. The magnetic field bias is set to 880.25 G which corresponds to a scattering length of $\sim 300 a_0$ and a Feshbach dimer binding energy of $E_d = -h \times 6$ MHz [see Fig. 1(a)] [46]. According to an earlier study described in Ref. [33], the first excited Efimov trimer energy level is predicted to be just $\sim$100 kHz below E_d, i.e., $E_t - E_d \approx -h \times 100$ kHz, where E_t is the energy of the trimer state. In Ref. [33], $E_t - E_d$ was measured in the region of 0.5 MHz $< E_d/h <$ 4 MHz by means of loss spectroscopy. The frequency dependent magnetic field modulation was applied for tens to hundreds of milliseconds, and the induced atom loss resonances were related to the positions of dimer and trimer energy levels. The accessible region of the trimer's binding energies was constrained by the finite resolution limit to be $\gtrsim$110 kHz. Thus, our current measurement probes the region which was out of reach for the previous experimental technique.

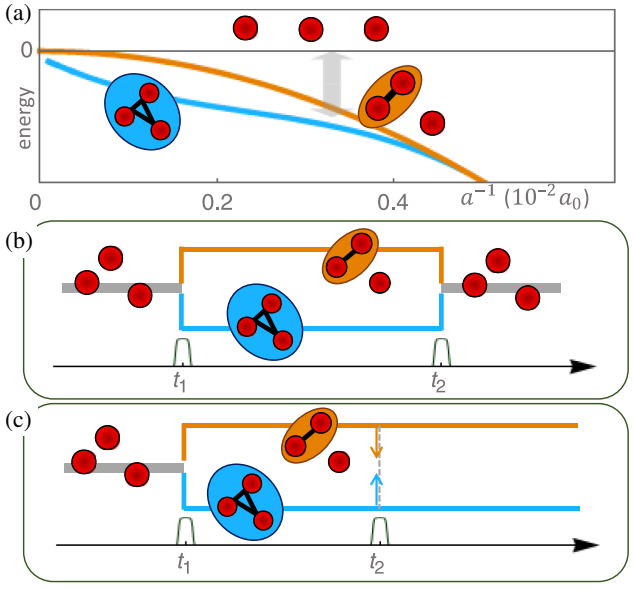

FIG. 1. Illustration of the energy levels and of the interferometer. (a) Dimer (orange) and trimer (blue) energy levels (not to scale) are shown schematically as a function of the inverse scattering length. The grey arrow indicates the parameter regime of our work and illustrates the effect of the modulation pulse. (b), (c) Two pulse sequence results in constructive (b) or destructive (c) interference.

The concept of the interferometer relies on a clear separation of energy scales in the system: $E_d \gg E_t - E_d > k_B T$. The first step of the interferometer, shown in Figs. 1(b) and 1(c), is the beam splitter at time t_1. The bias field is modulated at $\nu_m = 6$ MHz for a FWHM duration of $\tau_m = 10$ μs by a single auxiliary coil. The modulation amplitude at the atom position is $b \approx 1.5$ G [45]. The Fourier transform limited bandwidth of the pulse is 100 kHz at FWHM which allows us to address both (dimer and trimer) energy levels simultaneously while covering the full thermal distribution of the free-atom continuum ($\sim$30 kHz for $T \approx 1.5$ μK). The pulse projects the three-atom continuum to a coherent superposition state of a dimer + free atom and a trimer, denoted hereafter as DITRIS (dimer-trimer superposition) state. The system then evolves freely for a variable time $t \gg \tau_m$ during which the two constituents of the DITRIS accumulate a relative phase difference of $\phi(t) = (E_t - E_d)t/\hbar$, assuming that the energy of the free atom in the dimer + atom pathway is negligible (see the discussion of the results below). At time $t_2 = t_1 + t$ an identical modulation pulse projects the two paths back to free atoms and serves as an output port of the interferometer. When $\phi(t) = 2\pi n$, where $n \in \mathbb{Z}$, constructive interference between the two paths projects the three atoms into the three-atom continuum as shown in Fig. 1(b). In contrast, Fig. 1(c) represents the case where $\phi(t) = \pi(2n + 1)$ when destructive interference suppresses dissociation of the bound states. This produces a time dependent periodic variation in the number of free atoms with a peak-to-peak amplitude proportional to N_D, where N_D is the number of DITRIS states produced by the first pulse. This two-path interferometer picture neglects the contribution of the third path where the three atoms remain in the three-atom continuum. However, due to our experimental conditions ($E_d \gg E_t - E_d$) this channel contributes oscillations at $\sim E_d/h$ which are averaged to zero in the range of interest, namely $(E_t - E_d)/h$ [45].

The results of our interferometer at the output port are shown in Fig. 2, where we measure the number of free atoms, $N(t)$, as a function of the free evolution time t. Each point represents the mean of 2–8 individual measurements. It is evident from the data that the signal-to-noise ratio (SNR) is small. We, hence, begin the analysis with the data for short evolution times [80 μs $< t <$ 220 μs; Fig. 2(a)], where the oscillations can be visually appreciated. Assuming constant amplitude oscillations, we apply three different analyses: (i) a fast Fourier transform (FFT), (ii) a

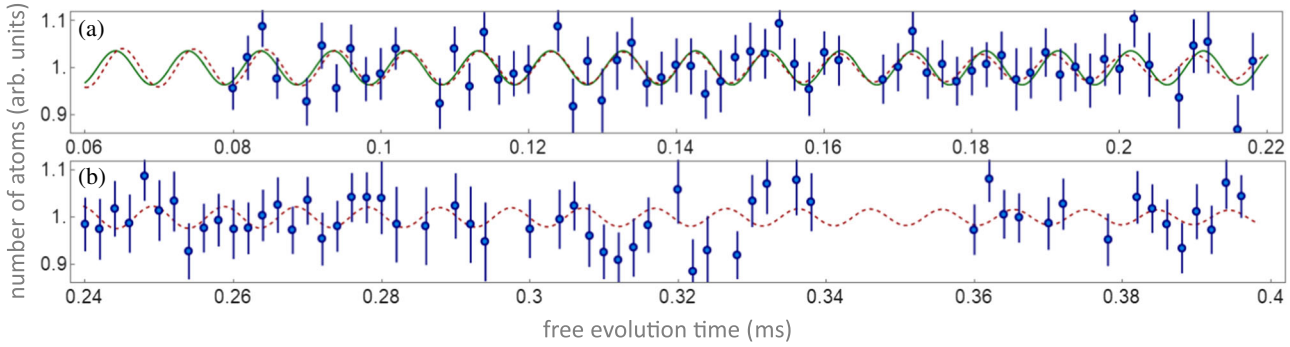

FIG. 2. Observation of oscillations. The number of free atoms N after the interferometer sequence is measured as a function of the free evolution time t. Each data point is the average of 2–8 measurements and the error bar is 1σ of the mean error. (a) Data for $t \in [80, 220]$ μs. Green line indicates the best fit to a cosine Eq. (1). (b) Data for $t \in [240, 400]$ μs. Red dashed line in (a) and (b) indicates (one and the same) best fit to a damped cosine Eq. (2).

two-paramter fit to the cosine function, and (iii) a three-parameter fit to the cosine function:

$$\frac{N(t)}{N_0} = 1 + A\cos(2\pi\nu t + \varphi), \tag{1}$$

where N_0 is the initial number of atoms in the trap. In (ii), the two fitting parameters are the amplitude A and the phase φ, while in (iii) the frequency ν becomes the third fitting parameter.

We verify that in case of small SNR, the most stringent test for the claim that an oscillation frequency has been observed in the experiment is provided by the three-parameter fit, and, therefore, only this analysis is discussed below [45]. The fitting algorithm is applied to the experimental results using a variety of initial conditions. In particular, the initial frequency is scanned very densely in the relevant frequency range. However, the fitting algorithm converges only to a limited number of frequencies, all of which are shown in Fig. 3(I). Among all the converged frequencies, only $\nu^\star = 102.9(8)$ kHz [47] has a distinguishable amplitude $A^\star = 0.036(7)$, while all other $A(\nu)$ are smaller and similar to each other [see Fig. 3(I)(a)]. This provides the first evidence that a single, dominant frequency can be indicated in the data. In fact, a naturally defined SNR $= A^\star/\bar{A}$, where $\bar{A}$ is the mean value of $A(\nu)$ excluding A^*, is found to be SNR $= 2.79(55)$. The second evidence for the presence of a dominant frequency is the coincidence of global minima in errors obtained for all three fitting parameters at $\nu^\star$ [see Figs. 3(I)(c)–(e)].

The reported SNR is small mainly due to the small signal that we are detecting (see discussion below), and it poses an obvious question: What is the likelihood for one to observe a similar peak with the same frequency analysis for a randomly generated noisy data? This is exactly the question where the full strength of the three-parameter fit method is revealed [45]. We perform a likelihood analysis with 1000 fake sequences of $N(t)$ with the same sampling frequency and length as in Fig. 2(a) generated from a random Gaussian distribution with the same standard deviation as in our experimental data. We then apply our frequency analysis for each sequence and look for events with a SNR larger than 1σ below the experimental SNR and a central frequency within the expected interval of [90, 110] kHz. The likelihood analysis results in zero such events. Only when the SNR threshold is lowered to 2.1 (1.25σ below the experimental SNR) does the first false positive occur. Hence the probability of our result being wrong is $0.21 \times 0.001 = 2 \times 10^{-4}$ (0.21 is the probability of getting a result $\geq 1.25\sigma$). This sufficiently negligible probability together with the fact that no oscillations were detected when only a single pulse was applied [45] allows us to fully trust our results.

To see the duration of the coherent oscillations, the experiment is repeated for longer free evolution times. In Fig. 2(b) the data points for t between 240 and 400 μs are shown, and the corresponding three-parameter fit analysis is in Fig. 3(II). Since we observe no dominant contribution at any frequency we conclude that the oscillations are below the detection limit and, thus, we detect the decay of the signal. Next, the entire data set ($t \in [80, 400]$) is analyzed by fitting it to a damped cosine curve:

$$\frac{N(t)}{N_0} = 1 + Ae^{-t/\tau}\cos\left[t\sqrt{(2\pi\nu)^2 + \tau^{-2}} + \varphi\right]. \tag{2}$$

This analysis is performed in two steps. First, a fit with four free parameters (A, τ, ν, and φ) is executed in the vicinity of the earlier derived values of some of them ($A^\star$, $\nu^\star$, and $\varphi^\star$). The fit converges and yields $\tau = 331(297)$ μs which allows us to put an upper bound of $\sim$630 μs for the detected decay time. The three-parameter fit analysis is then repeated for the entire data set using Eq. (2) and keeping $\tau = 331$ μs fixed. The result, shown in Fig. 4, agrees with the previous one [Fig. 3(I)] for the central frequency $\nu^\star$ (within the errors) and has a slightly reduced SNR $= 2.41(49)$. The

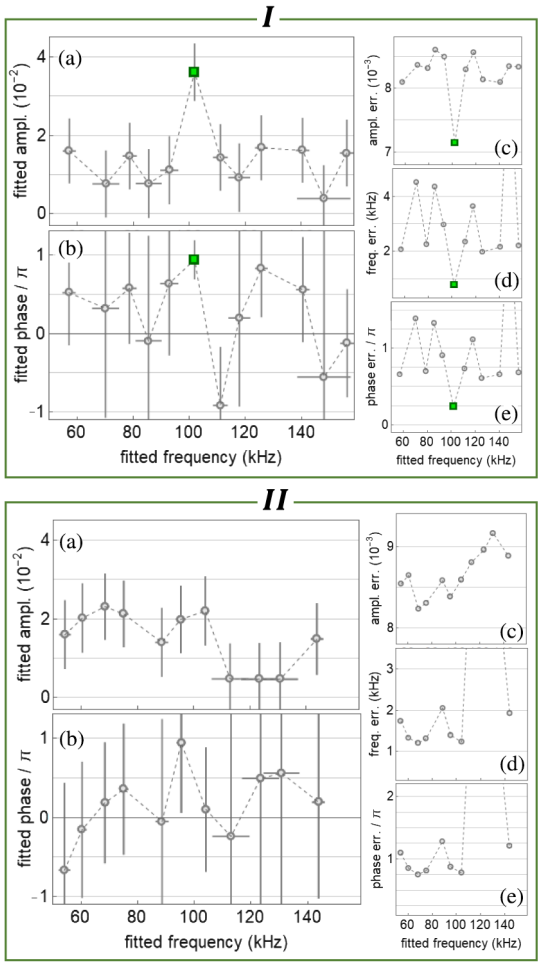

FIG. 3. Data analysis using three free parameters. I. The results of a three-parameter fit using the data of Fig. 2(a) and Eq. (1): (a) $A(\nu)$ and (b) $\varphi(\nu)$. Error bars are 1σ fitting uncertainties and they are also depicted in (c)–(e) as a function of ν. Parameters indicated by the green square are used for the green fit in Fig. 2(a). II. Same as (I) for the data of Fig. 2(b).

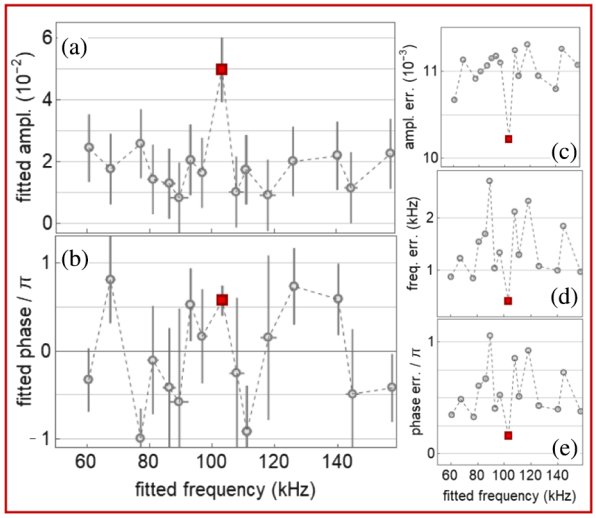

FIG. 4. Data analysis using three free parameters and a damped cosine. Same as Fig. 3, but for the entire data set [Figs. 2(a) and 2(b)] and using Eq. (2) for the fit. Parameters indicated by the red square are used for the red (dashed) fit in Fig. 2.

phase of the oscillations at $\nu^\star$ is measured to be $\varphi^\star = 0.57(16)\pi$, which is consistent with $N(t=0) = N_0$.

Extrapolating the damped oscillations to $t = 0$ we obtain an initial peak-to-peak signal of $2A = 0.10(1) \times N_0 \approx 3000$ atoms, where $N_0 \approx 3 \times 10^4$ is the initial number of atoms before the first pulse is applied. This implies that $\sim 3000/4 = 750$ atoms participate in the creation of $\sim 750/3 = 250$ DITRIS states [45]. For our experimental parameters, a trimer-excluding theory predicts the conversion of $\sim 0.018 \times N_0 \approx 540$ atoms into ~ 270 dimers after the first pulse [48]. This provides an upper bound for DITRIS states that can be created in our system in agreement with the observed results. Thus, the theory confirms the small signal in Fig. 2, and we fully benefit from the interferometric enhancement to obtain this level of sensitivity.

We now discuss the decay of the coherent oscillations, which can be caused by different mechanisms. The first is related to the finite thermal energy of the "spectator" atom in a dimer + atom path of the interferometer. However, this scenario, if it were relevant, would cause a significantly faster decay as the thermal energy has a ~30 kHz bandwidth. Therefore, experimental results signify a certain narrowing mechanism which currently remains unclear. This question deserves special attention, which we plan to provide in a future combined experimental and theoretical effort. On the other hand, this result opens up the opportunity to study other sources of decoherence.

The other two mechanisms indicate access to new observables, that were inaccessible in previous experiments. In the first, molecules are lost due to the finite lifetime of the trimers (T_1 time). As trimers naturally have a shorter lifetime than the dimers, the contribution of the finite lifetime of the dimers can be safely excluded from consideration. In the second mechanism (T_2 time) coherence is lost due to elastic collisions between the constituents of the DITRIS states and the free atoms. Our reported result sets an upper bound on both times. Future experiments should be able to determine which of the above is the dominant mechanism by analyzing the density dependence of the decoherence time τ. The T_1 time is density independent while the T_2 time decreases for higher densities.

The observed decoherence is probably caused by the finite lifetime of the trimers (which seems to be longer than the previously observed lifetime in a gas of ^{85}Rb atoms [44]). However, closer to the Efimov resonance the atom-dimer elastic collisional cross section increases by several orders of magnitude and might become the dominant mechanism for decoherence. Future experiments should allow investigation of this aspect of Efimov physics which

is currently totally absent from the list of available experimental observables.

In conclusion, we demonstrate the creation of a superposition state of Efimov trimers and Feshbach dimers. The newly developed data analysis, consistency in the fitting parameters, and vanishingly small level of failure in the likelihood analysis prove that the interference signal between the constituents of the superposition state observed in the experiment is real. We thus measure the energy of the trimer bound state with high precision and give an upper bound for decoherence processes. The main difficulty, namely the small SNR, needs to be improved for future applications. First, by increasing the stability of the sample preparation and the detection we expect to reduce the noise by a factor of ∼2. Second, by using a denser sample improving the signal by a factor of ∼2 is feasible.

An interesting question for future research is the identification of the exact mechanism responsible for the decoherence. Another extension of our work consists of repeating the interferometer sequence at different values of the bias field (different scattering lengths) to explore the elastic collisions channel and to identify the position of the Efimov resonance, and whether it even exists. Applying the interferometer to other accessible sublevels of lithium atoms and other atomic species should clarify and deepen our understanding of finite range corrections to the Efimov physics at positive scattering lengths.

Y. Y. and L. K. acknowledge fruitful discussions with N. Navon. This research was supported in part by the Israel Science Foundation (Grant No. 1340/16), the United States-Israel Binational Science Foundation (BSF, Grant No. 2012504), and by NSF Grant No. PHY-1607180. The numerical calculations have been performed using NSF XSEDE Resource Allocation No. TG-PHY150003.

[1] E. Braaten and H.-W. Hammer, Phys. Rep. **428**, 259 (2006).
[2] C. H. Greene, P. Giannakeas, and J. Pérez-Ríos, Rev. Mod. Phys. **89**, 035006 (2017).
[3] P. Naidon and S. Endo, Rep. Prog. Phys. **80**, 056001 (2017).
[4] J. P. D'Incao, J. Phys. B **51**, 043001 (2018).
[5] C. Chin, R. Grimm, P. Julienne, and E. Tiesinga, Rev. Mod. Phys. **82**, 1225 (2010).
[6] J. L. Bohn, A. M. Rey, and J. Ye, Science **357**, 1002 (2017).
[7] T. Kraemer, M. Mark, P. Waldburger, J. G. Danzl, C. Chin, B. Engeser, A. D. Lange, K. Pilch, A. Jaakkola, H.-C. Nägerl, and R. Grimm, Nature (London) **440**, 315 (2006).
[8] A. N. Wenz, T. Lompe, T. B. Ottenstein, F. Serwane, G. Zurn, and S. Jochim, Phys. Rev. A **80**, 040702(R) (2009).
[9] M. Zaccanti, B. Deissler, C. D'Errico, M. Fattori, M. Jona-Lasinio, S. Müller, G. Roati, M. Inguscio, and G. Modugno, Nat. Phys. **5**, 586 (2009).
[10] N. Gross, Z. Shotan, S. Kokkelmans, and L. Khaykovich, Phys. Rev. Lett. **103**, 163202 (2009).
[11] S. E. Pollack, D. Dries, and R. G. Hulet, Science **326**, 1683 (2009).
[12] F. Ferlaino, S. Knoop, M. Berninger, W. Harm, J. P. D'Incao, H.-C. Nägerl, and R. Grimm, Phys. Rev. Lett. **102**, 140401 (2009).
[13] A. Zenesini, B. Huang, M. Berninger, S. Besler, H.-C. Nägerl, F. Ferlaino, R. Grimm, C. H. Greene, and J. von Stecher, New J. Phys. **15**, 043040 (2013).
[14] R. J. Wild, P. Makotyn, J. M. Pino, E. A. Cornell, and D. S. Jin, Phys. Rev. Lett. **108**, 145305 (2012).
[15] S.-K. Tung, K. Jiménez-García, J. Johansen, C. V. Parker, and C. Chin, Phys. Rev. Lett. **113**, 240402 (2014).
[16] R. Pires, J. Ulmanis, S. Häfner, M. Repp, A. Arias, E. D. Kuhnle, and M. Weidemüller, Phys. Rev. Lett. **112**, 250404 (2014).
[17] J. Johansen, B. J. DeSalvo, K. Patel, and C. Chin, Nat. Phys. **13**, 731 (2017).
[18] M. Berninger, A. Zenesini, B. Huang, W. Harm, H.-C. Nägerl, F. Ferlaino, R. Grimm, P. S. Julienne, and J. M. Hutson, Phys. Rev. Lett. **107**, 120401 (2011).
[19] N. Gross, Z. Shotan, S. Kokkelmans, and L. Khaykovich, Phys. Rev. Lett. **105**, 103203 (2010).
[20] S. Roy, M. Landini, A. Trenkwalder, G. Semeghini, G. Spagnolli, A. Simoni, M. Fattori, M. Inguscio, and G. Modugno, Phys. Rev. Lett. **111**, 053202 (2013).
[21] J. Wang, J. P. D'Incao, B. D. Esry, and C. H. Greene, Phys. Rev. Lett. **108**, 263001 (2012).
[22] Y. Wang, J. Wang, J. P. D'Incao, and C. H. Greene, Phys. Rev. Lett. **109**, 243201 (2012).
[23] R. Schmidt, S. P. Rath, and W. Zwerger, Eur. Phys. J. B **85**, 386 (2012).
[24] P. Naidon, S. Endo, and M. Ueda, Phys. Rev. Lett. **112**, 105301 (2014).
[25] D. Blume, Few-Body Syst. **56**, 859 (2015).
[26] C. Langmack, R. Schmidt, and W. Zwerger, Phys. Rev. A **97**, 033623 (2018).
[27] D. S. Petrov, Phys. Rev. Lett. **93**, 143201 (2004).
[28] A. O. Gogolin, C. Mora, and R. Egger, Phys. Rev. Lett. **100**, 140404 (2008).
[29] P. K. Sorensen, D. V. Fedorov, A. S. Jensen, and N. T. Zinner, Phys. Rev. A **86**, 052516 (2012).
[30] S. Knoop, F. Ferlaino, M. Berninger, M. Mark, H.-C. Nägerl, and R. Grimm, Nat. Phys. **5**, 227 (2009).
[31] A. Zenesini, B. Huang, M. Berninger, H.-C. Nägerl, F. Ferlaino, and R. Grimm, Phys. Rev. A **90**, 022704 (2014).
[32] P. Dyke, S. E. Pollack, and R. G. Hulet, Phys. Rev. A **88**, 023625 (2013).
[33] O. Machtey, Z. Shotan, N. Gross, and L. Khaykovich, Phys. Rev. Lett. **108**, 210406 (2012).
[34] O. Machtey, D. A. Kessler, and L. Khaykovich, Phys. Rev. Lett. **108**, 130403 (2012).
[35] M.-G. Hu, R. S. Bloom, D. S. Jin, and J. M. Goldwin, Phys. Rev. A **90**, 013619 (2014).
[36] C. Langmack, D. H. Smith, and E. Braaten, Phys. Rev. A **86**, 022718 (2012).
[37] A. Kievsky and M. Gattobigio, Phys. Rev. A **87**, 052719 (2013).
[38] C. Ji, E. Braaten, D. R. Phillips, and L. Platter, Phys. Rev. A **92**, 030702(R) (2015).
[39] P. Giannakeas and C. H. Greene, Few-Body Syst. **58**, 20 (2017).

[40] P. M. A. Mestrom, J. Wang, C. H. Greene, and J. P. D'Incao, Phys. Rev. A **95**, 032707 (2017).
[41] P. M. A. Mestrom, T. Secker, R. M. Kroeze, and S. J. J. M. F. Kokkelmans, Phys. Rev. A **99**, 012702 (2019).
[42] T. Lompe, T. B. Ottenstein, F. Serwane, A. Wenz, G. Zürn, and S. Jochim, Science **330**, 940 (2010).
[43] S. Nakajima, M. Horikoshi, T. Mukaiyama, P. Naidon, and M. Ueda, Phys. Rev. Lett. **106**, 143201 (2011).
[44] C. E. Klauss, X. Xie, C. Lopez-Abadia, J. P. D'Incao, Z. Hadzibabic, D. S. Jin, and E. A. Cornell, Phys. Rev. Lett. **119**, 143401 (2017).
[45] See Supplementary Material at http://link.aps.org/supplemental/10.1103/PhysRevLett.122.200402 for the experiment details, the interferometer principles, and the thorough discussion of the three methods applied for the data analysis, including the likelihood analysis.
[46] N. Gross, Z. Shotan, O. Machtey, S. Kokkelmans, and L. Khaykovich, C.R. Phys. **12**, 4 (2011).
[47] All errors reported in brackets are the 1σ fitting errors.
[48] P. Giannakeas, L. Khaykovich, J.-M. Rost, and C. H. Greene, arXiv:1903.01389.

Supplementary Material: Coherent Superposition of Feshbach Dimers and Efimov Trimers

Yaakov Yudkin[1], Roy Elbaz[1], P. Giannakeas[2], Chris H. Greene[3], and Lev Khaykovich[1]
[1]*Department of Physics, QUEST Center and Institute of Nanotechnology and Advanced Materials, Bar-Ilan University, Ramat-Gan 5290002, Israel*
[2]*Max Planck Institute for the Physics of Complex Systems, Nöthnitzer Strasse 38, 01187 Dresden, Germany and*
[3]*Department of Physics and Astronomy, Purdue University, West Lafayette, Indiana 47907, USA*
(Dated: May 16, 2019)

I. EXPERIMENTAL DETAILS

A. Sample preparation

A far off-resonance (wavelength 1080 nm) crossed-beam optical trap (OT) is loaded directly from a compressed magneto-optical trap. By ramping down the intensity of the OT the atomic cloud is evaporatively cooled in the vicinity of a narrow Feshbach resonance [46] and the magnetic field is then ramped up to the vicinity of a broad Feshbach resonance located at 893.7 G. In the final state the trapping frequencies of the radially symmetric trap are $(\omega_r, \omega_z) \approx 2\pi \times (1500, 60)$ Hz in the radial and axial directions respectively. The atoms have a peak density of $n_0 \approx 5 \times 10^{12}$ cm^{-3}, a temperature of $T \approx 1.5$ μK and a s-wave scattering length of $a \approx 300 a_0$, corresponding to a bias field of 880.25 G. The interferometer experiment is performed at this point.

B. Setting the magnetic field

The bias field $\bar{B}$ and modulation frequency ν_m have to be such that the dimer/trimer production is maximal. We set the modulation frequency to $\nu_m = 6$ MHz for all the data presented in this letter (see next subsection) and find the resonance of $\bar{B}$ spectroscopically. To this end we use a 1 ms long pulse and measure the number of remaining atoms as a function of $\bar{B}$. At a certain bias magnetic field a loss of $\sim 50\%$ of the atoms is observed caused by inelastic collisions between the associated molecules and the remaining atoms. We associate this feature with the field where the maximal production efficiency of molecules is obtained. We observe slight variations of the field on the pulse intensity [48] but not on the pulse duration. In virtue of their close vicinity, E_d and E_t are unresolved in this experiment [34].

C. Field modulation

The essence of our experiment is the short (10 μs) and strong (1.5 G) modulation of the bias field at high modulation frequency which serves as beam-splitters of the interferometer. This pulse is generated by a home-built resonance LC-circuit, where the inductance (L) is provided by the auxiliary coil itself. An arbitrary function generator creates a square pulse with a single polarity. It is amplified by a digital amplifier (peak current 1.7 A) and injected into the LC-circuit which serves as a filter for the resonance frequency. The result is a high amplitude, sinusoidal modulation of the magnetic field. The rise time of the modulation amplitude is 4μs and the FWHM of the pulse is 10μs.

D. Data acquisition

After the second pulse of the interferometer experiment, the atoms are counted following a 350 μs time-of-flight (TOF) by absorption imaging, whose frequency is tuned such that only free atoms are detected (dimers and trimers are out of resonance with the detection light). Hence the interference is seen by plotting the number of atoms N versus free evolution time t. To obtain the data we run many, partially overlapping sequences of 40 μs (e.g. $t \in [120, 160]$ μs) and 60 μs (e.g. $t \in [80, 140]$ μs) making sure that the system remains stabilized in-between sequences. In each sequence, the experiment is repeated several times and averaged for each t. We observe a slight change in the mean atom number (offset of the oscillations) from sequence to sequence. Thus, each sequence is normalized to its offset. The sequences are then stitched together, where the mean value is taken for overlapping regions.

We have verified that no oscillations are detectable when using solely one pulse (on a 80 μs long sequence, $2-4$ measurements per point) and when the magnetic field is off-resonance (40 μs sequence) for short evolution times. We stress again, that in the long sequence for long evolution times [Fig. 2(b) of main text] also no oscillations are detectable. In addition, at very long evolution times ($400 \leq t \leq 1000$ μs), which we probed in several 40 μs intervals, an oscillating signal also remains undetectable.

II. INTERFEROMETER CONSIDERATIONS

Here we refine the meaning of the DITRIS (see main text) by deriving its wave function based on the three-

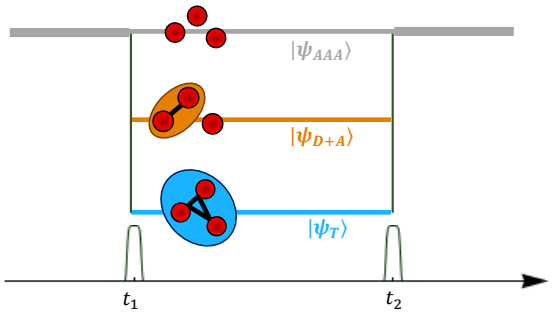

FIG. S1. **Illustration of the 3-particle wave function.**

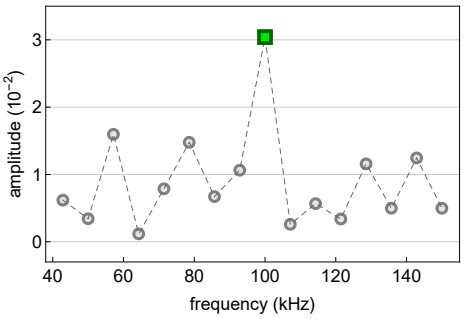

FIG. S2. **FFT of data presented in Fig. 2(a) of the main text.**

atom Hilbert space illustrated in Fig. S1.

Initially the three atoms are free: $|\psi_i\rangle = |\psi_{AAA}\rangle$. The first pulse (at time $t_1 = 0$) projects this state into a superposition of free atoms ($|\psi_{AAA}\rangle$), a dimer + atom ($|\psi_{D+A}\rangle$) and a trimer ($|\psi_T\rangle$):

$$|\psi(t_1)\rangle = A|\psi_{AAA}\rangle + B|\psi_{D+A}\rangle + C|\psi_T\rangle, \qquad (1)$$

where A, B, C are the probability amplitudes for the conversion. We neglect the contribution of dimers which are not in the superposition state and assume $B \approx C$ which, in fact, is the DITRIS association amplitude. During the free evolution time $t = t_2 - t_1$ the $|\psi_{D+A}\rangle$ and the $|\psi_T\rangle$ terms gain relative phases of $e^{-i\omega_{DA}t}$ and $e^{-i\omega_T t}$ respectively. The second pulse (at time t_2) projects the two bound states back into the free atom continuum, i.e. $|\psi_{D+A}\rangle \to |\psi_{AAA}\rangle$ and $|\psi_T\rangle \to |\psi_{AAA}\rangle$, such that after the pulse the three particle system is described by

$$|\psi_f\rangle = \left(A + Be^{-i\omega_{DA}t} + Be^{-i\omega_T t}\right)|\psi_{AAA}\rangle. \qquad (2)$$

The probability of detecting all three atoms is given by the square of the coefficient. Extracting a common phase factor of $e^{-i\omega_{DA}t}$ and keeping among the interference terms only those with slow varying phase $e^{-i(\omega_T-\omega_{DA})t}$ we get:

$$P = A^2 + 2B^2\left[1 + \cos(\omega t)\right], \qquad (3)$$

where $\omega = \omega_T - \omega_{DA}$. The first term is the offset (or background) of the oscillation signal. The second term, which has a peak-to-peak modulation of $4B^2$, is proportional to the detected oscillation signal and demonstrates the factor 4 enhancement of the DITRIS signal exploited in the experiment. To estimate the number of DITRIS states associated in the experiment, we must divide the detected peak-to-peak modulation in number of atoms by $4\times 3 = 12$, because, in addition to the interferometric enhancement, there are three atoms in each DITRIS state. As stated in the main text, we find that $3000/12 \approx 250$ such superposition states are created.

III. DATA ANALYSIS

A. Analysis (i): FFT

In addition to the three-parameter fitting procedure described in the main text, the time-domain oscillation signal is analyzed using a numerical fast-Fourier-transform (FFT) and is shown to have the same qualitative behavior. In Fig. S2 the FFT of the interval $t \in [80, 220]$ μs [the data in Fig. 2(a) of the main text] is shown. The δ-like feature obtained has a signal-to-noise ratio of SNR = 3.57 and is centered at $\nu^\star = 100$ kHz. Since FFT is model-independent and since the peak appears at the expected frequency value these observations are a convincing indication of a single dominant frequency contribution. Due to our limited sample size ($N_s = 70$), the width of each bin is $\nu_s/N_s \approx 7.1$ kHz, where $\nu_s = 500$ kHz is the sampling frequency. The fitting procedures are therefore more accurate than the FFT in the determination of the oscillation frequency.

B. Analysis (ii): two-parameters fit

Here, a second alternative to the three-parameters fit is considered. The cosine function in Eq. (1) of the main text is fitted to the experimental data while holding the frequency ν fixed and using the amplitude A and the phase φ as fitting parameters. This procedure is repeated for various values of $\nu \in [50, 150]$ kHz. In Fig. S3(I) the fitted amplitude (a) and phase (b) are plotted versus ν together with the 1σ fitting error (c,d). As the frequency is fixed no fitting error is associated with it. The FWHM of the obtained distribution is ~ 5 kHz in agreement with the FFT analysis, as expected. This can be considered an upper limit of the determined frequency uncertainty, derived from the finite length of the detected signals. Then, the two-parameter fit is applied to the second time interval [Fig. S3(II)] and, using Eq. (2) of the main text with fixed $\tau = 331$ μs, to the entire data set (Fig. S4).

Table. I summarizes the results of all three methods.

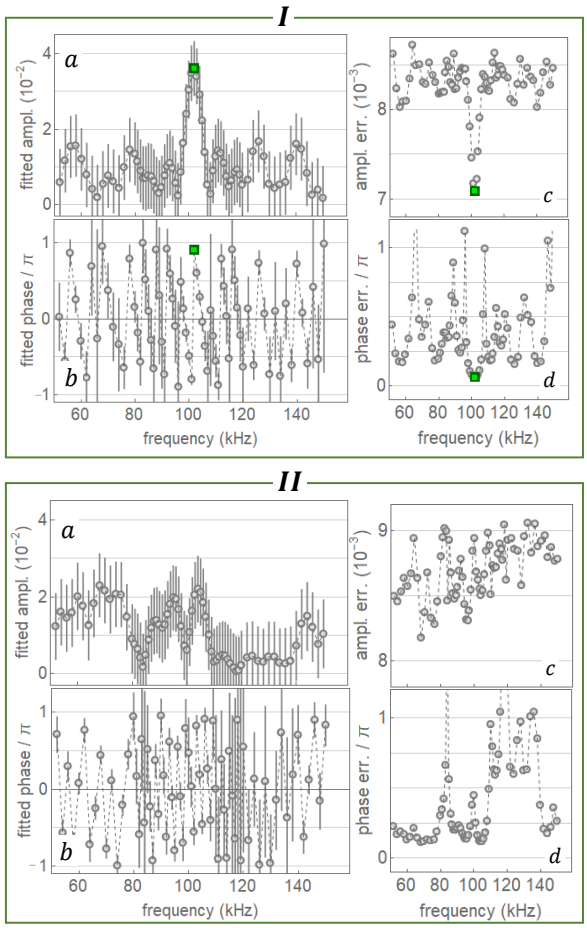

FIG. S3. **Data analysis using two free parameters and a constant-amplitude cosine. I.** For the data in Fig. 2(a) of the main text, the fitted amplitude $A(\nu)$ (**a**) and phase $\varphi(\nu)$ (**b**) are shown as a function of the fixed frequency. Subplots (**c**) and (**d**) are their respective 1σ fitting error. The best fit is indicated by the green square. **II.** Same as (**I**) for the data in Fig. 2(b) of the main text.

	constant cosine				decaying cosine			
	ν	$\Delta\nu$	SNR	Δ(SNR)	ν	$\Delta\nu$	SNR	Δ(SNR)
(i) FFT	100	7.1	3.57	-	-	-	-	-
(ii) 2 par	102	-	3.43	0.67	103	-	3.66	0.75
(iii) 3 par	101.9	0.8	2.79	0.55	103.2	0.4	2.41	0.49

TABLE I. **Observed frequency ν [kHz] and SNR for the various analyses.**

C. Comparison of analyses

As an illustrative example we apply all three analysis methods to a pure cosine with unity amplitude and zero phase: $\cos(2\pi\nu_p t)$ with $\nu_p = 100$ kHz, with the same sample length and sampling frequency as our experimental data and as the fake signals used in the likelihood analysis. The result of a Fourier transform is, of course, known analytically in this case (convolution of a δ- with a sinc-function). In Fig. S5(a) one sees that the two-parameter fit is the closest to the analytic Fourier transform curve. While the FFT captures the minima of $A(\nu)$, the three-parameter fit converges towards the local maxima. This illustrates that the three-parameters fit method is the most robust because its SNR is the lowest. In other words, it is the most sensitive measure for the strongest frequency components which are present in the signal and, as a consequence, it poses the most stringent test (see also likelihood analysis in the next section). The $\varphi(\nu)$ plot in Fig. S5(b) shows that $\varphi^\star = 0$ is correctly obtained at ν_p by all three methods; note though, that if the ratio ν_s/N_s of the FFT would not lead to a point at this frequency, this information would be lost. Therefore, either one of the two fitting methods is needed to correctly identify the phase. Figs. S5(c,d,e) also affirm that the fitting error is minimal for ν_p for all fitting parameters. As a side remark, we mention that the FFT becomes more problematic if ν_p lies towards the center of a frequency bin. It is well-known that a FFT analysis is best suited for large sample sizes – a fact illustrated here.

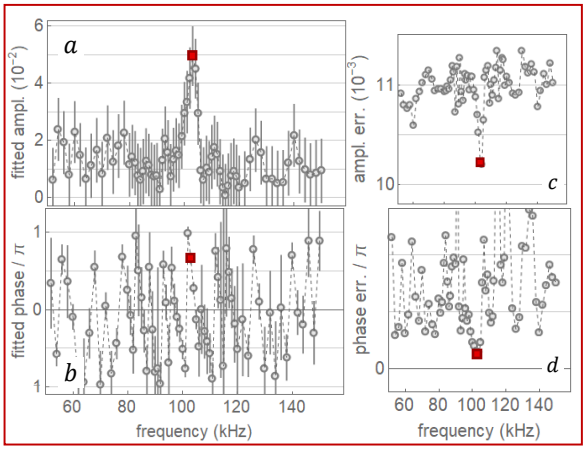

FIG. S4. **Data analysis using two free parameters and a damped cosine.** Same as Fig. S3, but for the entire data set [Fig. 2(a+b) in main text] and using the damped cosine function. The best fit is indicated by the red square.

D. Likelihood analysis

As the SNR of the experimental data is small the natural question that we have to answer is: what is the probability of finding a similar peak in random data (with the same standard deviation of noise) by applying our analyses. As we have already mentioned, the most stringent test of this question is provided by the three-parameter fit, reflecting the reason why only this method is discussed in the main text. It emphasizes the true strongest frequency components over the entire signal by searching

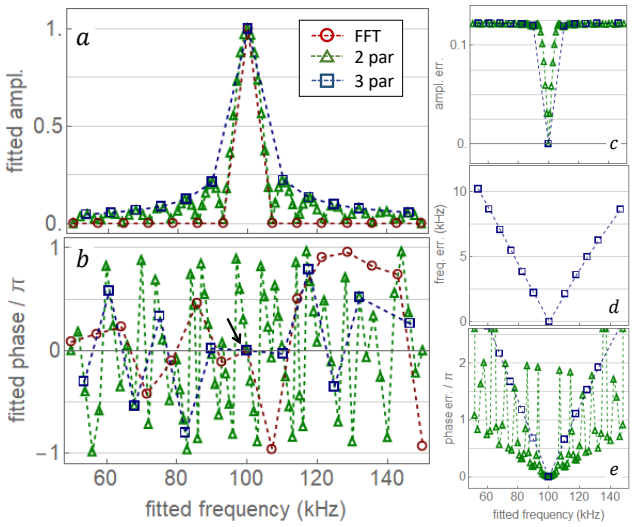

FIG. S5. **Comparison of all analysis methods for a pure cosine. a,b.** Results of the FFT (red circle), two-parameter (green triangle) and three-parameter fit (blue square) applied to a pure cosine function. **c,d,e.** 1σ fitting errors for the relevant analyses.

for a local minimum of all three parameters. If the frequency is fixed, as in two-parameter fit, more local minima will potentially be discovered in any type of noisy signal. We illustrate this idea by performing the following likelihood analysis.

After generating 1000 fake signals all three analysis methods are conducted. Each fake signal has the same length and sampling frequency as the real data and is drawn from a random Gaussian distribution with a standard deviation equal to the mean atom number standard deviation of the real data shown in Fig. 2(a) of the main text (0.038). Then the analyses are conducted for each fake signal and we look for the events that show a SNR larger than that of the experiment (Table I) for any dominant frequency over the entire frequency range $[50, 150]$ kHz. For methods (i), (ii) and (iii) we find 1, 1 and 0 such events respectively. In addition, the two false positives are for different fake signals, i.e. there is no overlap (in contrast to the experimental data where all three analyses agree with each other). If we lower the threshold to SNR $-\,\Delta$(SNR), thus allowing for more false events (however suppressed by a factor of 0.32), 20, 60 and 1 events are identified respectively (still no overlap). It is now evident that the most stringent test for false events is provided by the three-parameters fit method. Note, that to count the false positives for the FFT analysis we use the 1σ error of method (ii), because the FFT method does not yield an error estimation (see Table I). Narrowing the frequency range to the expected interval $[90, 110]$ kHz reduces the number of false positives to 3, 6 and 0 respectively. If the threshold is lowered further to SNR $-\,2\Delta$(SNR) (suppression factor of 0.05) 15 overlapped fake signals are misinterpreted by all three methods. Even in this case the overall probability to obtain a false positive is 7.5×10^{-4}.

Chapter 3

Article 2: Reshaped three-body interactions and the observation of an Efimov state in the continuum

Yaakov Yudkin, Roy Elbaz, Jose P. D'Incao, Paul S. Julienne and Lev Khaykovich

Nature Communications

Volume 15, Page 2127, March 2024

nature communications

Article

https://doi.org/10.1038/s41467-024-46353-1

Reshaped three-body interactions and the observation of an Efimov state in the continuum

Received: 23 July 2023

Accepted: 23 February 2024

Published online: 08 March 2024

Check for updates

Yaakov Yudkin[1] ✉, Roy Elbaz[1], José P. D'Incao[2,3] ✉, Paul S. Julienne[4] & Lev Khaykovich[1] ✉

Efimov trimers are exotic three-body quantum states that emerge from the different types of three-body continua in the vicinity of two-atom Feshbach resonances. In particular, as the strength of the interaction is decreased to a critical point, an Efimov state merges into the atom-dimer threshold and eventually dissociates into an unbound atom-dimer pair. Here we explore the Efimov state in the vicinity of this critical point using coherent few-body spectroscopy in ^{7}Li atoms using a narrow two-body Feshbach resonance. Contrary to the expectation, we find that the ^{7}Li Efimov trimer does not immediately dissociate when passing the threshold, and survives as a metastable state embedded in the atom-dimer continuum. We identify this behavior with a universal phenomenon related to the emergence of a repulsive interaction in the atom-dimer channel which reshapes the three-body interactions in any system characterized by a narrow Feshbach resonance. Specifically, our results shed light on the nature of ^{7}Li Efimov states and provide a path to understand various puzzling phenomena associated with them.

The unique ability to fine-tune the interaction between ultracold atoms has led to the realization of a number of quantum phenomena[1], among which the Efimov effect has become a quantum workhorse that allows for the exploration of some of the deepest issues of universal few-body physics[2–5]. Near a magnetic field dependent Feshbach resonance, the strength of the interatomic interaction is characterized by the s-wave scattering length a, which can assume arbitrarily large values compared to the characteristic range of the interactions, i.e., the van der Walls length $r_{\rm vdW} = (mC_6/\hbar^2)^{1/4}/2$, where m is the atomic mass, and C_6 is the dispersion coefficient. However, not all Feshbach resonances are the same. The intricate nature of the hyperfine interactions in alkali-metal atoms allows for different couplings between the open channel and the corresponding closed channel carrying the Feshbach state. As such, a resonance is said to be broad (narrow) in case of a strong (weak) coupling and is characterized by the dimensionless strength parameter $s_{\rm res} \gg 1$ ($s_{\rm res} \ll 1$)[1].

Regardless of the strength of the Feshbach resonance, the Efimov effect occurs at $|a| \to \infty$ due to the formation of an induced long-range three-body interaction of the form $-1/R^2$, where R is the hyperradius[5] providing the overall size of the system. This interaction gives rise to a log-periodic series of bound Efimov states whose absolute position is determined by the short-range three-body physics (Fig. 1)[2–5]. In the case of a broad resonance, the three-body potential supporting Efimov states features a universal repulsive wall near $R \approx 2r_{\rm vdW}$ thus preventing the atoms from probing small hyperradii. In fact, this repulsive wall is the hallmark characterizing the van der Waals (vdW) universality, according to which the ground Efimov state dissociates into the three-atom continuum at $a_-^{(0)} \approx -9.73 r_{\rm vdW}$[6,7]. This was observed across

[1]Department of Physics, QUEST Center and Institute of Nanotechnology and Advanced Materials, Bar-Ilan University, Ramat-Gan 5290002, Israel. [2]JILA, University of Colorado and NIST, Boulder, CO 80309-0440, USA. [3]Department of Physics, University of Colorado, Boulder, CO 80309-0440, USA. [4]Joint Quantum Institute (JQI), University of Maryland and NIST, College Park, MD 20742, USA. ✉e-mail: yaakov.yudkin@gmail.com; jpdincao@jila.colorado.edu; lev.khaykovich@biu.ac.il

https://doi.org/10.1038/s41467-024-46353-1

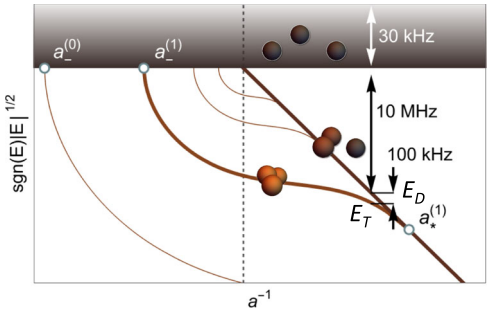

Fig. 1 | Efimov spectrum and energy scales. Schematic illustration of the Efimov scenario (universal theory) in the vicinity of a Feshbach resonance. The horizontal axis is the inverse scattering length a^{-1}, and the dashed vertical line corresponds to the position of the Feshbach resonance ($|a| = \infty$). The vertical axis indicates the wavenumber corresponding to the three-atom continuum (gray region) and the discrete spectrum of Efimov trimers (solid curved lines). The straight solid line originating at the Feshbach resonance position corresponds to the universal dimer state. The extreme points of the trimers' spectrum are labeled to indicate Efimov resonances and the first excited Efimov state is highlighted. The energy scales relevant to this work are indicated and are specific to the 894 G resonance in ^{7}Li.

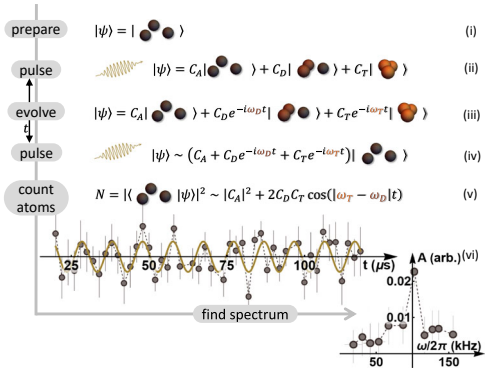

Fig. 2 | Experimental double pulse sequence. (i) Initial state of the three-atom continuum. (ii) A first rf pulse transfers a fraction of the initial state to dimer and trimer bound states creating a superposition state. (iii) As the wave function evolves, each constituent gains a phase proportional to its binding energy. (iv) A second rf pulse mixes the states. For simplicity, only the free-atom part is depicted. (v) Using absorption imaging, the number of free atoms is measured. (vi) An example of a measured signal as a function of free evolution time and its three-parameter fit. The signal has a large background term ($|C_A|^2$), fast oscillating terms (not shown) and a term that oscillates at $\omega = |E_T - E_D|/\hbar$. The latter is extracted via a three-parameter fit, where A indicates the amplitude.

several different Feshbach resonances in ^{133}Cs and ^{85}Rb[8,9]. For narrow resonances, however, this result is expected to be modified as yet another length scale emerges, namely $r_\star = 2\bar{a}/s_{\rm res} \approx 1.912 r_{\rm vdW}/s_{\rm res}$. Since now $r_\star > r_{\rm vdW}$, three-body observables are expected to depend on $r_\star$ (or equivalently, $s_{\rm res}$) rather than $r_{\rm vdW}$ alone[10–16]. Indeed, for intermediate resonances ($s_{\rm res} \gtrsim 1$) deviations from the Efimov-van der Waals universality were already confirmed in recent precision measurements and calculations[17–22]. For ^{7}Li atoms, although the Feshbach resonances are narrower than those above, experimental observations of a_- are consistent with the vdW universality, thus challenging our understanding of universality.

Here, we show that as the resonance becomes narrower, the three-body interaction is reshaped with respect to that of a broad resonance (in any atomic species). While the universal repulsive wall near $R \approx 2r_{\rm vdW}$ disappears, the system also develops an additional potential barrier ranging from $R \approx 4r_{\rm vdW}$ to a distance proportional to $r_\star$, leading to a double-well structure absent for broad resonances. Specifically, we experimentally explore the energy spectrum using coherent spectroscopy in the vicinity of the atom-dimer threshold for ^{7}Li atoms polarized in the $|F = 1, m_F = 0\rangle$ state, which features a Feshbach resonance at 894 G with $s_{\rm res} \approx 0.493$, and observe an Efimov state above the atom-dimer threshold. This provides strong evidence of the reshaping for the three-body interactions for narrow resonances, and further elucidates some of the mechanisms leading to other puzzeling observations with ^{7}Li atoms[23–26].

Results and discussion

The DITRIS interferometer

In contrast to traditional cold-atom few-body experiments, which utilize inelastic losses to uncover Efimov features[27–30], we perform high-resolution coherent spectroscopy of the Efimov state on the $a > 0$ side of the Feshbach resonance. Following the proof-of-principle demonstration of ref. 31, we generate a DImer-TRImer Superposition (DITRIS) state by rf association and let it evolve in time. The accumulated relative phase between its constituents is then measured in an interferometer-like sequence. The method works best in the region around $a_\star^{(1)}$ –the value of a at which the Efimov state merges with the atom-dimer threshold–where there is a clear separation of energy scales (Fig. 1). The difference between the trimer and dimer bound states must be smaller than their depth below the three-atom continuum on the one hand but larger than the temperature of the latter on the other. In this energy regime the straightforward measurement combining rf association and loss-spectroscopy fails due to rf power broadening[30]. Our procedure thus goes beyond the existing methods. As a second condition, the rf pulse must be short enough in time such that it is Fourier broadened beyond the trimer-dimer energy difference $|E_T - E_D|$. When three atoms are subjected to such a broadband rf pulse they have the option to either form a dimer while one atom remains free or a trimer. This effectively creates a superposition of the two chemically different bound states.

The double pulse sequence is illustrated in Fig. 2. The first pulse generates DITRIS states from a fraction of a gas of free atoms. Then, following the accumulation of a relative phase according to their binding energies, the second pulse attempts to dissociate them. The dimer and trimer pathways interfere, and one observes oscillations in the number of free atoms as a function of the free evolution time. The frequency of the oscillations is proportional to $|E_T - E_D|$. The DITRIS method is thus a measurement of the trimer binding energy with respect to the atom-dimer continuum. The two requirements (separation of energies and short, Fourier-broadened pulses) set the lower and upper limits of detectable $|E_T - E_D|$. It lies between the temperature of the free-atom continuum and the pulse bandwidth, respectively (see Methods). In this regime the conversion efficiency is limited by the pulse duration, i.e. it is not saturated by the phase space density argument[32], and therefore remains low, such that $|C_A| \gg |C_D|, |C_T|$ (see Fig. 2). As a result, the oscillations appear as a small signal on top of a large background. However, making the pulses longer would decrease the upper detection limit and is therefore not favorable. To faithfully extract the main frequency contribution, we use a Fourier transform-inspired three-parameter fit (for details, see Supplementary Note 2 and 3 as well as ref. 31). As is typical for frequency measurements, the accuracy increases for longer measurements. The free evolution time is thus varied over a wide range of values (up to ~100 μs) limited only by the coherence time of the superposition state (see Methods).

Trimer spectroscopy

Having established a reliable tool for measuring $|E_T - E_D|$ we apply the double pulse sequence for various values of the magnetic field (scattering length) with the goal of finding the point at which $E_T \to E_D$. In Fig. 3a, measurements from the DITRIS interferometer (filled circles) are represented together with the data from the previous incoherent rf association spectroscopy (open circles)[30]. At large scattering lengths,

https://doi.org/10.1038/s41467-024-46353-1

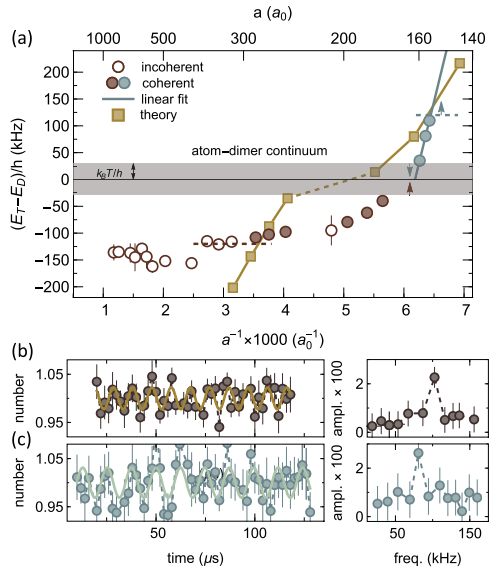

Fig. 3 | Trimer energy from experiment and theory. a The values of $(E_T - E_D)/h$ obtained from the double pulse sequence (filled circles) are shown together with data from rf association followed by loss (open circles)[30] as a function of inverse scattering length multiplied by 1000. For the former, the errorbars (1σ fitting error) are smaller than the point size and so are all scattering length errorbars (see Methods). The horizontal shaded region and dashed lines show the respective lower and upper detection limits of the DITRIS interferometer. The numerical results (filled squares) for $(E_T - E_D)/h < 0$ were obtained from the methodology used in refs. 39,40 while the results for $(E_T - E_D)/h > 0$ are those extracted from Fig. 5. Being treated differently, the two regions are connected by a dashed line. **b**, **c** On the left panel—examples of the experimental signal (number of atoms as a function of the time between pulses). Each point is the average of 10–20 measurements and the errorbars show the standard deviation. On the right panel—results of the three-parameter fit applied to the corresponding signals which clearly indicate the presence of dominant frequencies. The horizontal (smaller than point size) and vertical errorbars are 1σ fitting errors. (For further details see Supplementary Note 2 and ref. 31). **b** For data below the threshold, at $a = 265a_0$, and **c** for data above the threshold, at $a = 156a_0$. The experimental signal and three-parameter fit for the remaining points are shown in Supplementary Fig. 3. Note that the experimental data predict the crossing of the threshold somewhere between 177 a_0 and 160 a_0.

the Efimov state is relatively deeply bound, $(E_T - E_D)/h \lesssim -100$ kHz, and our new measurements agree with those obtained from incoherent spectroscopy[30]. However, as the scattering length decreases and the Efimov state becomes more weakly bound, instead of the expected gradual approach towards the atom-dimer continuum[2–5], a sharp turn in the energy is observed. Subsequently, the experimental signal disappears for energies below the lower detection limit [see arrows in the shaded region in Fig. 3a). The latter is set by the temperature via $|E_T - E_D|/h \lesssim k_BT/h \approx 30$ kHz, due to the loss of coherence amplitude[33] (see also Supplementary Note 2). Most surprisingly, however, meaningful frequencies reemerge when the scattering length is further decreased (gray circles in Fig. 3a). The Efimov state binding energy quickly changes away from the threshold again and becomes undetectable above the higher frequency detection limit set by the pulse bandwidth [see the upper gray dashed line in Fig. 3a) leading to measurements with no dominant frequency contribution (gray arrow) (see Supplementary Fig. 3). Figure 3a also shows our theoretical results for the energies of the ^{7}Li Efimov state (squares). These results, along with the physical interpretation of the phenomena controlling the observations, are discussed later in the text.

Experimentally we are only sensitive to the absolute value of the energy difference, which leads to two equally plausible scenarios: the trimer either crosses into or bounces off the atom-dimer continuum. Although the latter scenario has been indicated in the literature to occur for broad resonances[34,35], our numerical simulations for ^{7}Li instead show that the Efimov trimer crosses the atom-dimer continuum threshold due to a reshape of the three-body interaction potential associated with the narrow character of its Feshbach resonance (see discussion below).

We emphasize that the trimer remains in a metastable state well inside the atom-dimer continuum. This is demonstrated in Fig. 3b, c, where two-time sequences of the DITRIS interferometer are compared. In Fig. 3b, we show a signal obtained below the threshold and in Fig. 3c one from above it. Both signals are similar, and no observable decay is detected within the first 100 μs, covering up to 10 full oscillations. Although a thorough investigation of the trimer lifetime with the DITRIS interferometer is beyond the scope of this work, it is clear from these signals that the coherence time exceeds the expected lifetime of the Efimov trimer. (Our numerical simulations estimate the lifetime of the trimer state within the experimental range to be around 10–20 μs.) Interestingly, a recent theoretical study (performed for broad resonances) has provided a possible interpretation of such unusually large coherence times[33], with coherence still being observed for times as long as twice the lifetime of the Efimov state. Although this result does not fully explain the experimentally observed coherence times, our analysis below demonstrates fundamental differences between the three-body physics for broad and narrow resonances as ^{7}Li, which can potentially lead to substantial modifications of the coherence times.

Finally, we argue the implausibility of attributing the nonzero signal from the DITRIS interferometer above the threshold to any molecular state other than the Efimov state. Although one cannot completely rule out that a non-universal (non-Efimovian) trimer state exists by accident in the same energy region in which our observations are performed, this coincidence is very unlikely. In particular, the region in phase space (above the threshold) that we explore experimentally is extremely narrow, covering only a few a_0 in scattering length and only a few tens of kHz in energy. Moreover, for DITRIS interferometry to provide a detectable signal, it is necessary for all states involved in the problem to be extraordinarily large. Near the region where we observe the crossing, the dimer state itself should be ~$160a_0$, and the trimer should be comparable to or even greater than that. On the other hand, a non-Efimovian accidental state could only originate from short-range physics and would be $\lesssim r_{vdW} = 32a_0$ for ^{7}Li. For such small states, the coupling between them and the initial atomic state (with a size comparable to the average interatomic distance, i.e., ~10^4a_0 for our case) would be extraordinarily small due to the poor Frank-Condon factor, and the DITRIS interferometer would be inefficient. As a result, since we know that the only weakly bound dimer state is the Feshbach dimer, it is reasonable to accept that the only trimer that can overlap well with both the dimer and the initial atomic state is an Efimov state.

Theory and numerical simulations

In order to better understand the nature of the ^{7}Li Efimov trimer near the atom-dimer threshold, we have performed numerical calculations using the adiabatic hyperspherical representation (see Methods). In the following, we first present a two-channel interaction model with variable s_{res}. This model gives insight into the crucial difference between broad and narrow resonances in the context of three-body Efimov interactions. Building upon the physical picture that emerges from the two-channel model, we then develop a multichannel theory using realistic ^{7}Li two-body potentials. This latter model qualitatively reproduces the trimer's crossing of the atom-dimer threshold, thus verifying the experimental observations. We note that while necessary approximations in our theoretical model hinder quantitative agreement with the experiment, our findings clearly identify the physical mechanism controlling the experimental observations.

https://doi.org/10.1038/s41467-024-46353-1

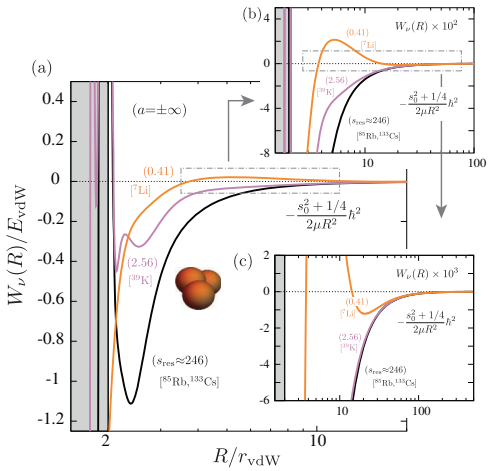

Fig. 4 | Reshape of three-body interactions for narrow resonances. a Effective potentials, $W_\nu(R)$, for the relevant channel supporting an infinity of Efimov states for different values of $s_{\rm res}$ in units of $E_{\rm vdW}=\hbar^2/mr_{\rm vdW}^2$. As $s_{\rm res}$ evolves from the regime of broad ($s_{\rm res}\gg1$) to narrow ($s_{\rm res}\ll1$) resonances a repulsive interaction emerges for $R\gtrsim 4r_{\rm vdW}$ and extends up to $R\approx 3r_\star$, where $r_\star\approx 1.912r_{\rm vdW}/s_{\rm res}$. The double-well structure of the three-body interaction for narrow resonances allows for trimer states to exist above the atom-dimer continuum for finite values of $a>0$ as shape resonances. **b** 100-fold zoom of the dot-dashed box in **a**. Likewise, **c** shows a 10-fold zoom of the dot-dashed box in **b**. For more values of $s_{\rm res}$ see Supplementary Fig. 5.

Three-body interactions near narrow resonances

The two-channel model we use for the interatomic interaction contains the proper van der Waals physics and a set of parameters chosen to produce a Feshbach resonance with the ^{7}Li background scattering length, $a_{\rm bg}\approx -25a_0$[36], but variable values for $s_{\rm res}$ (see Supplementary Note 4). In the adiabatic hyperspherical representation, a great deal of physical insight can be obtained from the hyperspherical effective potentials $W_\nu(R)$, which are solutions of the adiabatic Hamiltonian at fixed values of the hyperradius R. In Fig. 4 (see also Supplementary Fig. 5), we show the effective potentials relevant for Efimov physics at $a=\pm\infty$ and various values of $s_{\rm res}$ between 0.41 and 246, thus covering the broad, intermediate and narrow resonance regimes. Asymptotically, all potentials approach the universal form $-(s_0^2+1/4)\hbar^2/2\mu R^2$ with $s_0\approx 1.00624$, which supports infinitely many Efimov states. However, at shorter distances the potentials are drastically reshaped as the resonance strength enters the narrow resonance regime. (We note that similar results have been found in a recent publication[16]).

For our broadest resonance ($s_{\rm res}\approx 246$), representing atomic species like ^{85}Rb and ^{133}Cs, the effective potential displays the expected universal repulsive wall near $R\approx 2r_{\rm vdW}$ (thick black curve in Fig. 4a), which prevents atoms from probing the small R region representing the hallmark of vdW universality[6,7]. As $s_{\rm res}$ is tuned towards the intermediate ($s_{\rm res}\approx 2.56$, similar to ^{39}K) and narrow ($s_{\rm res}\approx 0.41$, similar to ^{7}Li) resonance regime, the effective potentials are reshaped, and the universal repulsive wall eventually disappears. Remarkably, the three-body potentials develop a repulsive barrier for $R\gtrsim 4r_{\rm vdW}$ (Fig. 4b), which extends up to $R\approx 3r_\star$ (Fig. 4c), as a result of the strong mixing between the open and closed hyperspherical channels (see Supplementary Note 4). Therefore, in the $s_{\rm res}<1$ regime, the effective potentials display a double-well structure, where interactions within the inner well ($R\lesssim 4r_{\rm vdW}$) are dominated by vdW interactions while interactions in the outer well ($R\gtrsim 3r_\star$) are dominated by Efimov physics. For the $s_{\rm res}\approx 0.41$ case, the closest to ^{7}Li ($s_{\rm res}\approx 0.493$), the potential barrier height is found to be ~10 MHz ($0.02E_{\rm vdW}$) at $a=\pm\infty$, i.e. much larger than the range of binding energies found experimentally. Importantly, and relevant to our present experiment, this barrier also persists for finite values of $a>0$ (see Supplementary Note 4).

Multichannel calculations for ^{7}Li

To provide a more quantitative analysis of the effect of the repulsive barrier in the parameter regime of the experiment, we perform additional numerical calculations that characterize the energy of the ^{7}Li Efimov state using a more realistic interaction model based on the methodology developed in refs. 18,19. We note that modifications to this model were made (see Supplementary Note 4) in order to compensate for strong (short-ranged) electronic exchange interactions[37,38]. Yet, our model displays the correct physics at distances $R\gtrsim r_{\rm vdW}$, thus preserving the major features relevant to the central physical question we explore here, i.e., whether the repulsive barrier allows for Efimov states to exist above the atom-dimer threshold.

While our results for $(E_T-E_D)/h<0$ in Fig. 3a were obtained using a methodology that provides a direct characterization of the energy of the Efimov state[39,40], for $(E_T-E_D)/h>0$, the analysis of the near-resonant energy regime in the atom-dimer continuum is much more subtle. However, a convenient way to characterize the existence of the ^{7}Li Efimov state above the atom-dimer threshold is to compare the energy dependence of the ^{7}Li atom-dimer elastic cross-section, σ_{AD}, with that of a system without the barrier, i.e., a system controlled by a broad ($s_{\rm res}=\infty$) Feshbach resonance, σ_{AD}^∞[35]. It is crucial, however, that this comparison is performed when the two physical systems have the same value for the atom-dimer scattering lengths, $a_{AD}=a_{AD}^\infty$, such that both cross-sections converge to the same value, $4\pi|a_{AD}|^2$, as the collision energy vanishes. In this case, if $a_{AD}<0$ and an Efimov state exists above the threshold, the cross-section difference should display the enhancement whenever the collision energy coincides with that of the ^{7}Li Efimov state. In practice, the above procedure is most meaningful in the case of weak inelastic transitions, which has led us to suppress the short-range decay mechanisms in our model. Also, since, in our case, the values of a_{AD} we obtained are only approximately the same (differing by no more than 2%), we define the weighted cross-section difference as

$$\Delta\sigma_{AD}^w(E)=\sigma_{AD}(E)-\frac{|a_{AD}|^2}{|a_{AD}^\infty|^2}\sigma_{AD}^\infty(E), \tag{1}$$

which ensures that the cross-section difference vanishes as the collision energy $E\to 0$. In the above expression, $\sigma_{AD}(E)=\pi|1-S_{AD}(E)|^2/k_{AD}^2$ where S_{AD} is the diagonal S-matrix element associated with the atom-dimer channel and $k_{AD}^2=2m/3E/\hbar^2$, with m being the atomic mass. The results for $\Delta\sigma_{AD}^w$ for various a_{AD} in Fig. 5 clearly show the expected enhanced scattering of ^{7}Li with respect to the broad resonance case thus demonstrating the existence of a ^{7}Li Efimov state above the threshold as a direct consequence of the existence of the repulsive barrier. The energy of the Efimov state is associated with the maximum value of $\Delta\sigma_{AD}^w$ occurring at smaller values of E as $|a_{AD}|$ increases, i.e., when the state approaches the atom-dimer threshold from above, and is displayed in Fig. 3a. We note that simplified, asymptotic models have failed to explain our experimental observations, indicating the importance of van der Waals interactions in order to properly describe the reshape of the three-body interactions[41,42]. Note also that, as shown in Fig. 3a, when $(E_T-E_D)/h<0$, the theory results predict deeper energies close to the Feshbach resonance, which dive faster towards the atom-dimer continuum. We attribute such discrepancies to the simplifications adopted for otherwise nearly intractable, truly multichannel interactions in lithium. Even the most advanced attempt to model these interactions[38] have not reached fully converged results, leading to a significant discrepancy between theory and experiment[24,25] for the spin state considered here. Most importantly, however, is that both our experimental data and theoretical simulations refute the

conventional expectation that an Efimov state simply merges with the atom-dimer continuum for the case of narrow resonances.

In summary, our experimental and theoretical observations of the existence of an Efimov state above the atom-dimer continuum provides strong evidence of a fundamental reshaping of the three-body interactions for narrow resonances. Although our theoretical analysis allows us to point out that this phenomenon is universally valid for narrow Feshbach resonances, much is still needed to fully characterize the ^{7}Li Efimov states, in particular, with respect to their lifetime. The coherence times observed with the DITRIS interferometer are clearly much longer than the estimations of the trimer lifetime obtained from our numerical simulations without coherence. Since we show here that for ^{7}Li atom-dimer collisions are enhanced, this raises the intriguing question on whether the character of the DITRIS superposition state, along with the form of the three-body interaction, can conspire to form more long-lived superposition states in a way that coherence can still be observed at long times[33]. Although some open questions still remain, our current observations provide evidence that Efimov physics at a narrow Feshbach resonance deviates from the expectations from vdW universality, where the Efimov state simply disappears at the atom-dimer threshold.

Successful application of the DITRIS interferomter to coherent spectroscopy of the Efimov energy level, together with a notable demonstration of coherent manipulation of ^{4}He halo dimers by ultrashort laser pulses[43], reveals the great potential of the coherent approach to few-body physics phenomena. Future investigation into the superposition state lifetime, and the extension of the unique capabilities of the DITRIS interferometer to other atomic species and mixtures are expected to greatly advance our understanding of Efimov physics in ultracold atoms.

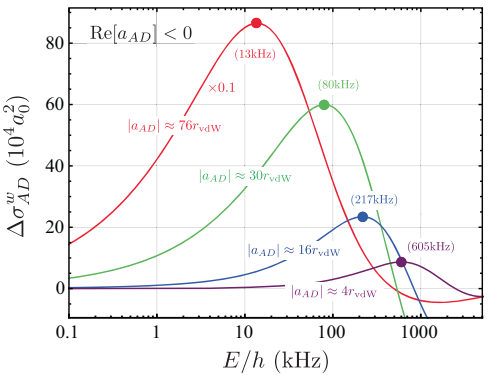

Fig. 5 | Evidence of resonant scattering above atom-dimer threshold. Weighted elastic cross-section difference [Eq. (1)] between ^{7}Li atom-dimer collisions and that of a system controlled by a broad Feshbach resonance for approximately the same value for $|a_{AD}|$ and Re[a_{AD}] < 0. The existence of the repulsive barrier on the entrance atom-dimer channel for ^{7}Li leads to the enhancement of elastic collisions just above the threshold as compared to that without the barrier, indicating the presence of the Efimov state above the atom-dimer threshold and with energy indicated by the closed circles. Note that at higher energies $\Delta\sigma^w_{AD}$<0, most likely due to the fact that $|a_{AD}|$ and $|a^\infty_{AD}|$ are only approximately the same, but also due to other multichannel effects causing modifications on the scattering at such energies.

Methods

Experimental details

Standard laser cooling and evaporation techniques are used to produce a gas of 3×10^4 bosonic lithium atoms at 1.5 μK and an average density of 1.25×10^{12} cm^{-3} in a crossed optical dipole trap. The temperature corresponds to 30 kHz and is our lower detection limit. To image the atoms we use absorption imaging which is sensitive to free atoms only.

At the core of the experiment lies the 10 μs pulse, which is Fourier broadened to address both the dimer and the trimer simultaneously. The duration 10 μs refers to the full-width at half-maximum (FWHM). There is also a (measured) turn-on/turn-off time of $\tau_0 = 4$ μs, which means that the pulse is at its maximal value during $\tau_c = 6$ μs. The experimental rf pulse envelope is modeled as

$$\chi(t) = \begin{cases} \sin^2\left(\frac{\pi}{2}\frac{t+\tau_c/2+\tau_0}{\tau_0}\right) & -\tau_0 - \frac{\tau_c}{2} < t < -\frac{\tau_c}{2} \\ 1 & -\frac{\tau_c}{2} < t < \frac{\tau_c}{2} \\ \sin^2\left(\frac{\pi}{2}\frac{t-\tau_c/2-\tau_0}{\tau_0}\right) & \frac{\tau_c}{2} < t < \frac{\tau_c}{2} + \tau_0 \end{cases} \quad (2)$$

and plotted in Fig. 6. The Fourier transform of $\chi(t)$ is also shown in Fig. 6 in the low-frequency domain. It closely resembles a sinc, the transform of an ideal rectangular pulse, but is slightly broadened. It is FWHM is 117 kHz which is the value we use as our upper detection limit.

The method was refined with respect to the proof-of-principle in ref. 31 mainly by reducing the atom number fluctuations. This was achieved by stabilizing the magnetic field to a relative stability of 5×10^{-5} and by improved statistics (Supplementary Note 2).

Scattering length calibration

In Fig. 3a, the values of $(E_T - E_D)/h$ are shown as a function of inverse scattering length. In the experiment we vary the magnetic field bias to tune the scattering length. The calibration is performed via the dimer binding energy, which is frequently measured during the DITRIS interferometer data accusation. The measurement protocol can be found elsewhere[44]. Finally, the dimer binding energy is related to the scattering length via coupled channel calculations[45]. Given the high accuracy of the dimer binding energy measurement and coupled channels calculations, the scattering length uncertainty is <a_0 in the region explored in the experiment.

DITRIS coherence time

The longest feasible free evolution time is given by the decoherence of the superposition state[31]. The possible relevant parameters are the elastic collision rate and the trimer's intrinsic lifetime. The low signal-to-noise ratio does not permit precise measurement of the decohrence

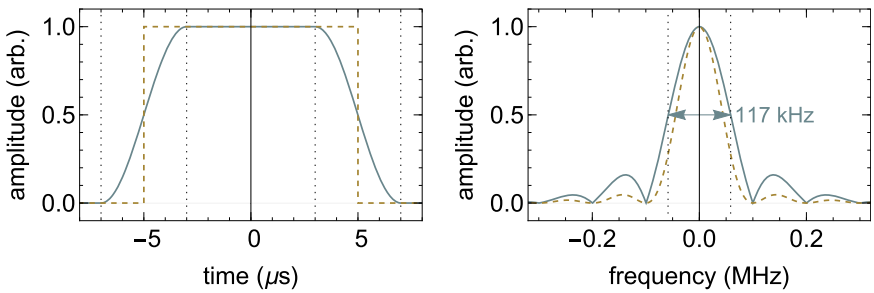

Fig. 6 | Pulse shape and spectrum. The pulse shape of Eq. (2) is compared to a pure square pulse with the same FWHM. The FFT of the former is slightly broader.

time but empirically we do not observe signs of decay for <150 μs. In practice, the three-parameter fit allows neglecting the decay in the data analysis by keeping the range of the evolution time <150 μs.

Theory

The adiabatic hyperspherical representation provides a simple and conceptually clear description of the three-body system in terms of the hyperradius R, characterizing the overall size of the system, and the set of hyperangles, Ω[46]. Bound and scattering properties[47] of the system are determined from solutions of the hyperradial Schrödinger equation:

$$\left[-\frac{\hbar^2}{2\mu}\frac{d^2}{dR^2}+W_\nu(R)-E\right]F_\nu(R)+\sum_{\nu'\neq\nu}W_{\nu\nu'}(R)F_{\nu'}(R)=0. \quad (3)$$

where μ is the three-body reduced mass, E the total energy, W_ν is the hyperspherical effective potentials governing the radial motion and $W_{\nu\nu'}$ the nonadiabatic couplings driving transitions between different channels, characterized by the collective index ν. The hyperspherical effective potentials are defined as

$$W_\nu(R)=U_\nu(R)+\left\langle\Phi_\nu(R;\Omega)\left|\frac{d^2}{dR^2}\right|\Phi_\nu(R;\Omega)\right\rangle, \quad (4)$$

where $U_\nu(R)$, the hyperspherical potentials, and $\Phi_\nu(R;\Omega)$, the channel functions, are solutions of the hyperangular adiabatic equation

$$\hat{H}_{\rm ad}\Phi_\nu(R;\Omega)=U_\nu(R)\Phi_\nu(R;\Omega), \quad (5)$$

obtained at fixed values of R. The adiabatic Hamiltonian contains the hyperangular kinetic energy, as well as all the atomic and interatomic interactions in the system. We explicitly define the terms of the adiabatic Hamiltonian used in our studies in Supplementary Note 4.

Data availability

Two-dimensional raw atomic cloud pictures from all experimental runs are available upon request to Y.Y. or L.K. Source data are provided with this paper.

Code availability

All code supporting the findings of this article and its Supplementary Information will be made available upon request to the authors.

References

1. Chin, C., Grimm, R., Julienne, P. & Tiesinga, E. Feshbach resonances in ultracold gases. *Rev. Mod. Phys.* **82**, 1225 (2010).
2. Braaten, E. & Hammer, H.-W. Universality in few-body systems with large scattering length. *Phys. Rep.* **428**, 259 (2006).
3. Greene, C. H., Giannakeas, P. & Pérez-Ríos, J. Universal few-body physics and cluster formation. *Rev. Mod. Phys.* **89**, 035006 (2017).
4. Naidon, P. & Endo, S. Efimov physics: a review. *Rep. Prog. Phys.* **80**, 056001 (2017).
5. D'Incao, J. P. Few-body physics in resonantly interacting ultracold quantum gases. *J. Phys. B: At. Mol. Opt. Phys.* **51**, 043001 (2018).
6. Wang, J., D'Incao, J. P., Esry, B. D. & Greene, C. H. Origin of three-body parameter universality in Efimov physics. *Phys. Rev. Lett.* **108**, 263001 (2012).
7. Naidon, P., Endo, S. & Ueda, M. Microscopic origin and universality classes of the Efimov three-body parameter. *Phys. Rev. Lett.* **112**, 105301 (2014).
8. Berninger, M. et al. Universality of the three-body parameter for Efimov states in ultracold cesium. *Phys. Rev. Lett.* **107**, 120401 (2011).
9. Wild, R. J., Makotyn, P., Pino, J. M., Cornell, E. A. & Jin, D. S. Measurements of Tan's contact in an atomic Bose-Einstein condensate. *Phys. Rev. Lett.* **108**, 145305 (2012).
10. Petrov, D. S. Three-boson problem near a narrow Feshbach resonance. *Phys. Rev. Lett.* **93**, 143201 (2004).
11. Gogolin, A. O., Mora, C. & Egger, R. Analytical solution of the bosonic three-body problem. *Phys. Rev. Lett.* **100**, 140404 (2008).
12. Wang, Y., D'Incao, J. P. & Esry, B. D. Ultracold three-body collisions near narrow Feshbach resonances. *Phys. Rev. A* **83**, 042710 (2011).
13. Schmidt, R., Rath, S. P. & Zwerger, W. Efimov physics beyond universality. *Eur. Phys. J B* **85**, 386 (2012).
14. Langmack, C., Schmidt, R. & Zwerger, W. Efimov states near a Feshbach resonance and the limits of van der Waals universality at finite background scattering length. *Phys. Rev. A* **97**, 033623 (2018).
15. van de Kraats, J., Ahmed-Braun, D. J. M., Li, J.-L. & Kokkelmans, S. J. J. M. F. Efimovian three-body potential from broad to narrow Feshbach resonances. *Phys. Rev. A* **107**, 023301 (2023).
16. Tempest, K.-M. & Jonsell, S. Multichannel hyperspherical model for Efimov physics with van der Waals interactions controlled by a Feshbach resonance. *Phys. Rev. A* **107**, 053319 (2023).
17. Johansen, J., DeSalvo, B. J., Patel, K. & Chin, C. Testing universality of Efimov physics across broad and narrow Feshbach resonances. *Nat. Phys.* **13**, 731 (2017).
18. Chapurin, R. et al. Precision test of the limits to universality in few-body physics. *Phys. Rev. Lett.* **123**, 233402 (2019).
19. Xie, X. et al. Observation of Efimov universality across a non-universal Feshbach resonance in ^{39}K. *Phys. Rev. Lett.* **125**, 243401 (2020).
20. Secker, T., Li, J.-L., Mestrom, P. M. A. & Kokkelmans, S. J. J. M. F. Multichannel nature of three-body recombination for ultracold ^{39}K. *Phys. Rev. A* **103**, 022825 (2021).
21. Li, A., Yudkin, Y., Julienne, P. S. & Khaykovich, L. Efimov resonance position near a narrow Feshbach resonance in a Li-Cs mixture. *Phys. Rev. A* **105**, 053304 (2022).
22. Etrych, J. et al. Pinpointing Feshbach resonances and testing Efimov universalities in ^{39}K. *Phys. Rev. Res.* **5**, 013174 (2023).
23. Pollack, S. E., Dries, D. & Hulet, R. G. Universality in three- and four-body bound states of ultracold atoms. *Science* **326**, 1683 (2009).
24. Gross, N., Shotan, Z., Kokkelmans, S. & Khaykovich, L. Observation of universality in ultracold ^{7}Li three-body recombination. *Phys. Rev. Lett.* **103**, 163202 (2009).
25. Gross, N., Shotan, Z., Kokkelmans, S. & Khaykovich, L. Nuclear-spin-independent short-range three-body physics in ultracold atoms. *Phys. Rev. Lett.* **105**, 103203 (2010).
26. Dyke, P., Pollack, S. E. & Hulet, R. G. Finite-range corrections near a Feshbach resonance and their role in the Efimov effect. *Phys. Rev. A* **88**, 023625 (2013).
27. Kraemer, T. et al. Evidance for Efimov quantum states in an ultracold gas of caesium atoms. *Nature* **440**, 315–318 (2006).
28. Knoop, S. et al. Observation of an Efimov-like trimer resonance in ultracold atom-dimer scattering. *Nat. Phys.* **5**, 227–230 (2009).
29. Lompe, T. et al. Radio-frequency association of Efimov trimers. *Science* **330**, 940 (2010).
30. Machtey, O., Shotan, Z., Gross, N. & Khaykovich, L. Association of Efimov trimers from a three-atom continuum. *Phys. Rev. Lett.* **108**, 210406 (2012).
31. Yudkin, Y., Elbaz, R., Giannakeas, P., Greene, C. H. & Khaykovich, L. Coherent superposition of Feshbach dimers and Efimov trimers. *Phys. Rev. Lett.* **122**, 200402 (2019).
32. Hodby, E. et al. Production efficiency of ultracold Feshbach molecules in bosonic and fermionic systems. *Phys. Rev. Lett.* **94**, 120402 (2005).

33. Bougas, G., Mistakidis, S. I., Schmelcher, P., Greene, C. H. & Giannakeas, P. Interferometry of Efimov states in thermal gases by modulated magnetic fields. *Phys. Rev. Res.* **5**, 043134 (2023).
34. Wang, Y. & Julienne, P. S. Universal van der Waals physics for three cold atoms near Feshbach resonances. *Nat. Phys.* **10**, 768–773 (2014).
35. Mestrom, P. M. A., Wang, J., Greene, C. H. & D'Incao, J. P. Efimov-van-der Waals universality for ultracold atoms with positive scattering lengths. *Phys. Rev. A* **95**, 032707 (2017).
36. Pollack, S. E. et al. Extreme tunability of interactions in a ^{7}Li Bose-Einstein condensate. *Phys. Rev. Lett.* **102**, 090402 (2009).
37. Li, J.-L., Secker, T., Mestrom, P. M. A. & Kokkelmans, S. J. J. M. F. Strong spin-exchange recombination of three weakly interacting ^{7}Li atoms. *Phys. Rev. Res.* **4**, 023103 (2022).
38. van de Kraats, J., Ahmed-Braun, D. J. M., Li, J.-L. & Kokkelmans, S. J. J. M. F. Emergent inflation of the Efimov spectrum under three-body spin-exchange interactions. *arXiv* https://arxiv.org/abs/2309.13128 (2023).
39. Nielsen, E., Suno, H. & Esry, B. D. Efimov resonances in atom-diatom scattering. *Phys. Rev. A* **66**, 012705 (2002).
40. Goban, A. et al. Emergence of multi-body interactions in a fermionic lattice clock. *Nature* **563**, 369–373 (2018).
41. Yudkin, Y. & Khaykovich, L. Efimov scenario for overlapping narrow Feshbach resonances. *Phys. Rev. A* **103**, 063303 (2021).
42. Yudkin, Y., Julienne, P. S. & Khaykovich, L. Loosely bound few-body states in a spin-1 gas with near-degenerate continua. *Phys. Rev. A* **107**, 053303 (2023).
43. Kunitski, M. et al. Ultrafast manipulation of the weakly bound helium dimer. *Nat. Phys.* **17**, 174–178 (2021).
44. Gross, N., Shotan, Z., Machtey, O., Kokkelmans, S. & Khaykovich, L. Study of Efimov physics in two nuclear-spin sublevels of ^{7}Li. *C.R. Phys.* **12**, 4–12 (2011).
45. Julienne, P. S. & Hutson, J. M. Contrasting the wide Feshbach resonances in ^{6}Li and ^{7}Li. *Phys. Rev. A* **89**, 052715 (2014).
46. Suno, H., Esry, B. D., Greene, C. H. & Burke, J. P. Three-body recombination of cold helium atoms. *Phys. Rev. A* **65**, 042725 (2002).
47. Wang, J., D'Incao, J. P. & Greene, C. H. Numerical study of three-body recombination for systems with many bound states. *Phys. Rev. A* **84**, 052721 (2011).

Acknowledgements

This work is supported by the US National Science Foundation (NSF, Grant no. PHY-2012125 and PHY-2308791), and the US-Israel Binational Science Foundation (BSF, Grant No. 2019795 and No. 2022740). L.K. also acknowledges the Israel Science Foundation (ISF, Grant no. 1543/20) and J.P.D. acknowledges partial support from NASA/JPL (Grant No. 1502690). This work utilized the RMACC Summit supercomputer, which is supported by the National Science Foundation (awards ACI-1532235 and ACI-1532236), the University of Colorado Boulder, and Colorado State University. The authors also acknowledge further support from the NSF grant PHY-1748958 via the Kavli Institute for Theoretical Physics.

Author contributions

Y.Y. and R.E. performed the experiments and analyzed the data. J.P.D. and P.S.J. developed the theoretical models and performed the numerical calculations. L.K. supervised the project. All authors contributed to the discussion of the results and writing of the manuscript.

Competing interests

The authors declare no competing interests.

Additional information

Supplementary information The online version contains supplementary material available at https://doi.org/10.1038/s41467-024-46353-1.

Correspondence and requests for materials should be addressed to Yaakov Yudkin, José P. D'Incao or Lev Khaykovich.

Peer review information *Nature Communications* thanks the anonymous reviewer(s) for their contribution to the peer review of this work. A peer review file is available.

SUPPLEMENTARY INFORMATION
Reshaped Three-Body Interactions and the Observation of an Efimov State in the Continuum

Yaakov Yudkin[1], Roy Elbaz[1], José P. D'Incao[2,3], Paul S. Julienne[4], and Lev Khaykovich[1]
[1]*Department of Physics, QUEST Center and Institute of Nanotechnology and Advanced Materials, Bar-Ilan University, Ramat-Gan 5290002, Israel*
[2]*JILA, University of Colorado and NIST, Boulder, Colorado 80309-0440, USA*
[3]*Department of Physics, University of Colorado, Boulder, Colorado 80309-0440, USA and*
[4]*Joint Quantum Institute (JQI), University of Maryland and NIST, College Park, Maryland 20742, USA*
(Dated: February 19, 2024)

Supplementary Note 1. MAGNETIC MOMENT

The fact that the trimer's nature changes after the crossing is most dominantly shown by looking at the magnetic moment of the trimer before and after the crossing. This is extracted from our data as follows. The slope of a molecules' binding energy, when plotted as a function of the magnetic field, is given by the magnetic moment of the molecule with respect to the free atoms. Since our Feshbach resonance is located at high magnetic fields the electronic spins of the free atoms are almost perfectly polarized (almost $2\mu_B$, where $\mu_B = 1.4$ MHz/G is the Bohr magneton). The magnetic moment of two free atoms for the relevant magnetic fields is $\mu_{AA} = 2.66$ MHz/G while the deeply bound dimer is a pure singlet with zero magnetic moment. The dimer is relatively shallow in this regime but deep enough to show non-universality. We extract its magnetic moment μ_D by performing a derivative of its binding energy E_D: $\mu_D = \mu_{AA} - \partial E_D/\partial B$. Adding the third atom as a free atom (moment $\mu_A = 1.33$ MHz/G) the polarized, three particle, dimer + atom system has $\mu_{DA} = \mu_D + \mu_A$. This is plotted as a function of the inverse scattering length in Supplementary Fig. 1. The magnetic moment of the trimer is $\mu_T = 3\mu_A - \partial E_T/\partial B$. Applying a discrete derivative to our measurement of E_T before it vanishes below the lower detection limit (before the crossing) results in the brown circles in Supplementary Fig. 1. The almost-overlap with μ_{DA} indicates that the trimer is very similar in nature to the dimer + atom system. However, the slope after crossing (see linear fit in Fig. 3 of the main text, the slope is ∓ 171 kHz/G) has a larger magnitude leading to a distinct change in μ_T (blue dot in Supplementary Fig. 1). This change in the magnetic moment provides an additional evidence of the emergence of the trimer as a bound state above the atom-dimer continuum. If μ_T remained unchanged, it would instead indicate the dissociation of the trimer state. We conclude that the nature of the trimer state changes as it emerges from below of the detection limit as a result of the reshape of the three-body interactions leading to the formation of the repulsive barrier near $R \approx 4r_{\mathrm{vdW}}$ (see Fig. 4 of the main text).

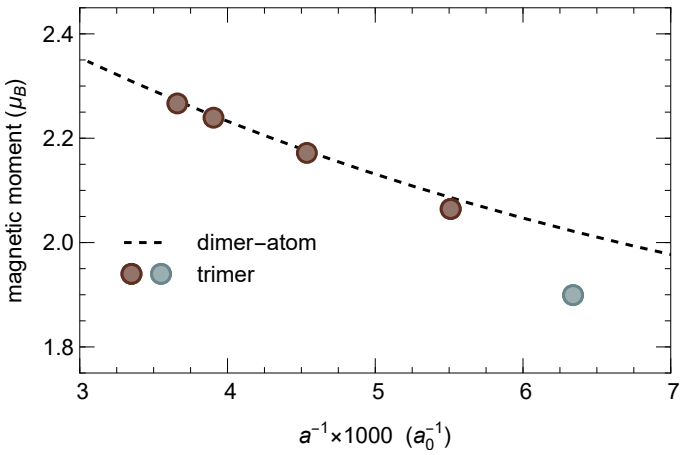

Supplementary Fig. 1. **Magnetic moment.** The magnetic moment of the measured trimer is compared to the dimer + atom complex. The scattering length calibration is discussed in Methods and the errorbars (1σ) are smaller than the point size in both the horizontal and vertical direction.

Supplementary Note 2. DATA ANALYSIS

Here we elaborate on the idea and procedure of the three-parameter fit analysis (3PA) used to extract the dominant frequency contribution from our low-SNR data. Please also refer to the Supplement of Ref. [1], where this method was first introduced.

A. Detailed description of the three-parameter analysis

In order to illustrate our data analysis it is instructive to apply it to a simulated data sequence. Consider a finite-length sinusoidal signal similar to the one shown in the left column of Supplementary Fig. 2(a), for which a 100 μs long pure sine with $\omega/2\pi = 87.5$ kHz was generated. As in our experiment a discrete "measurement" value is taken every 2 μs corresponding to a sampling rate of 500 kHz. In order to determine the frequency we guess a pure oscillatory fitting function:

$$N(t) = A\cos(\omega t + \varphi). \tag{S1}$$

The three fitting parameters are the amplitude A, the frequency ω and the phase φ. Since the frequency is not known a priori we instruct the least-squares algorithm to start its search for a minimum in parameter space $(A, \omega, \varphi) = (1, \omega_0, 0)$, where $\omega_0 \in 2\pi \times [20, 200]$ kHz. For each initial value of ω_0 the algorithm converges to some value for the three parameters (A, ω, φ) in the vicinity of the initial parameters (possibly a local minimum, not necessarily the global minimum) and we record the converged $A(\omega)$, see right column of Supplementary Fig. 2(a). The value of ω at which A is maximal (we denote these values $\omega^\star$ and $A^\star$) is the dominant frequency contribution and the *global* minimum in parameter space. As expected for this pure sine, $\omega^\star/2\pi = 87.5$ kHz is obtained. The trustworthiness of the spectrum

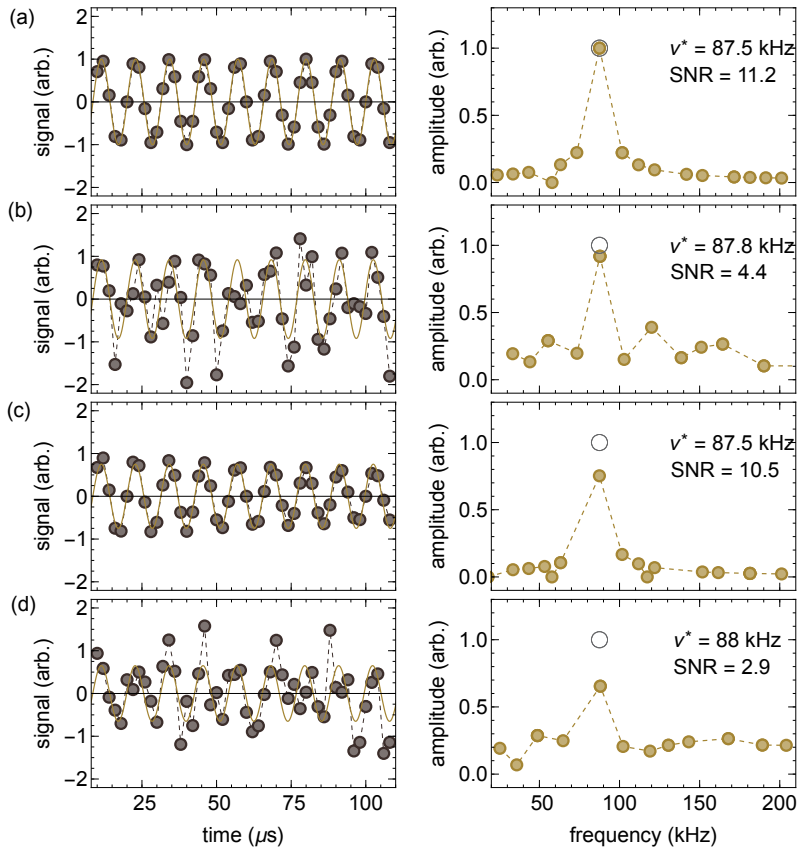

Supplementary Fig. 2. **Three-parameter fit.** The 3PA is applied to four signals to illustrate its working principle. The open circle shows the frequency and amplitude of the pure sine. (a) Pure sine. (b) Noisy sine. (c) Sine with decay. (d) Noisy sine with decay.

is quantified by a signal-to-noise ratio as:

$$\mathrm{SNR} = \frac{A^\star}{\bar{A}}, \tag{S2}$$

where $\bar{A}$ is the mean of all points excluding $A^\star$. For the pure sine, SNR = 11.2. Due to the finite length of the signal, $\bar{A} \neq 0$ and hence the SNR does not diverge as it would for an infinitely long noiseless sine.

We now add white Gaussian noise (WGN) with a standard deviation of 0.5 (half the amplitude) to the pure sine and repeat the procedure in Supplementary Fig. 2(b). Albeit the WGN, the 3PA is able to determine the dominant frequency contribution with an error < 1 kHz (corresponding to the typical errorbar) but with a reduced SNR = 4.4. Note that it is not $A^\star$ that is lowered due to the WGN but $\bar{A}$ which is increased.

The real signal of the DITRIS experiment decays. A decaying sine with characteristic decay time $\tau = 200$ μs is simulated without noise in Supplementary Fig. 2(c). One notes that the obtained $\nu^\star$ is identical to the non-decaying signal of Supplementary Fig. 2(a) although Eq. (S1) was used to determine it, and that the SNR is reduced by less than 10%.

Finally, Supplementary Fig. 2(d) shows a noisy decaying sine representing the real experimental conditions. Despite the fitting function not including the decay and despite the noise, the frequency $\nu^\star$ is found with an error < 1 kHz! Although the SNR is reduced by a factor of ~ 3 with respect to Supplementary Fig. 2(a), the dominant frequency contribution is easy to read off.

B. Alternative analyses

The 3PA is better than a fast Fourier transform (FFT). The main reason for this is the finite sample length. For the signals in Supplementary Fig. 2 the sample length (100 μs) would lead to a frequency resolution of $(100\ \mu\mathrm{s})^{-1} = 10$ kHz (irrelevant of the sampling rate). The accuracy of frequency determination is thus limited to 10 kHz. In our case, where 87.5 kHz is the correct frequency, both the 80 kHz and the 90 kHz point have an amplitude of ~ 0.5, heavily reducing the accuracy and the SNR. The FFT method is very well suited for long samples but not for our relatively short data sets. Nevertheless, see right column of Supplementary Fig. 3, application of a FFT to the experimental signal yields the (approximately) correct dominant frequency distribution.

An alternative to the 3PA is a two-parameter fit analysis (2PA). This involves a fit to Eq. (S1) but using only A and φ as fitting parameters. The frequency is put in by hand and the least-squares algorithm finds the best fitting amplitude and phase for each frequency. Although this method does not suffer from finite resolution, which may be made arbitrarily small, the likelihood analysis, described below, shows its clear disadvantage. In addition, fixing ω does not provide fitting errors for the frequency. The 3PA on the other hand provides a confidence interval for all three parameters.

For completeness and in addition to the 3PA we have analyzed our experimental $N(t)$ with the 2PA and FFT – see Supplementary Fig. 3. Unsurprisingly the same signature is obtained with all three methods.

An illustrative comparison of all three methods (FFT, 2PA and 3PA) can be found in the Supplemental Material of Ref. [1].

C. Likelihood analysis

Here we show that the 3PA is the least likely to be fooled by a false signal. The question we answer here is: For a sample of random numbers, how likely is the 3PA to find a dominant frequency contribution even though none is there (a so-called false-positive)?

To this end we generate 10^4 fake signals, each 100 μs long and sampled at a 500 kHz rate. The random numbers are drawn from a Gaussian random number generator with 0.035 standard deviation (derived from the experimental signals similar to those in Supplementary Fig. 3). We run all three analysis methods on each signal and, as a function of $\mathrm{SNR} = A^\star/\bar{A}$, count the number of false-positives. The result, presented in Supplementary Fig. 4, shows that for $SNR > 1.6$ the 3PA is least likely to be fooled by a false-positive and that for $\mathrm{SNR} > 2.47$ this probability drops below the 10^{-3} level . The other two methods require an SNR of 3.67 (2PA) and 3.59 (FFT) respectively to obtain the same probability.

None of the curves reaches unity for $\mathrm{SNR} \leq 1$ because we only consider frequency values within our physically accessible window 30 kHz $< \omega^\star/2\pi <$ 120 kHz). Especially the FFT finds mainly high frequencies. The lowest experimental SNR value is indicated by the vertical dashed line in Supplementary Fig. 4. Since the false-positive probability of the 3PA is the lowest in this region we consider it as the most reliable method to analyse the data.

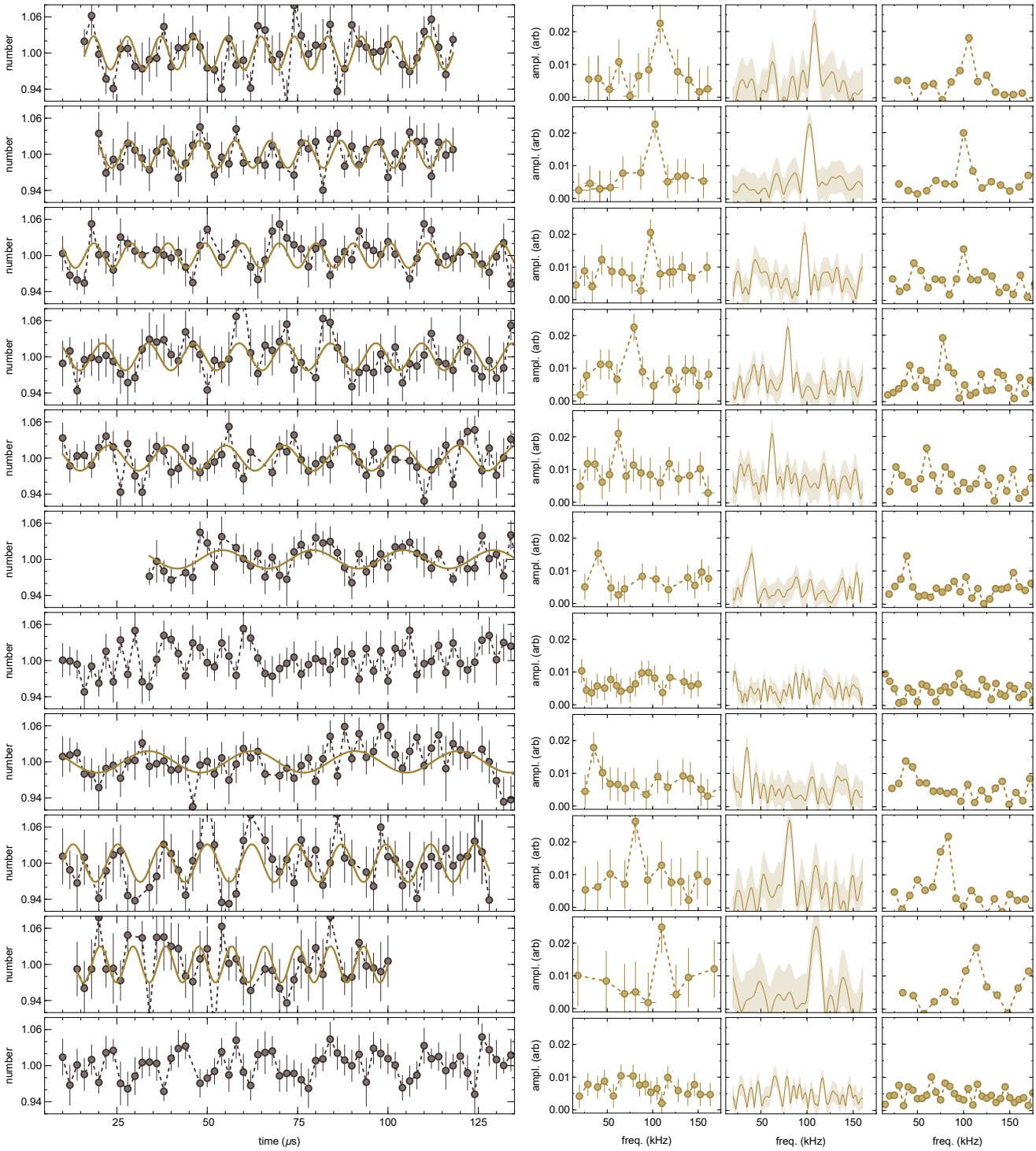

Supplementary Fig. 3. **Measured number of atoms and spectral analysis.** The left column shows the number of atom signal in the double pulse sequence. Each point is the average of 10-20 measurements and the errorbars show the standard deviation. The remaining columns are, from left-to-right, the 3PA, 2PA and FFT of the signals. For the 3PA and 2PA the errorbars and shaded region, respectively, show the 1σ fitting errors. From top-to-bottom the signals were recorded for a scattering length of $a/a_0 = 283$, 265, 248, 197, 185, 176, 164, 160, 157, 156 and 151.

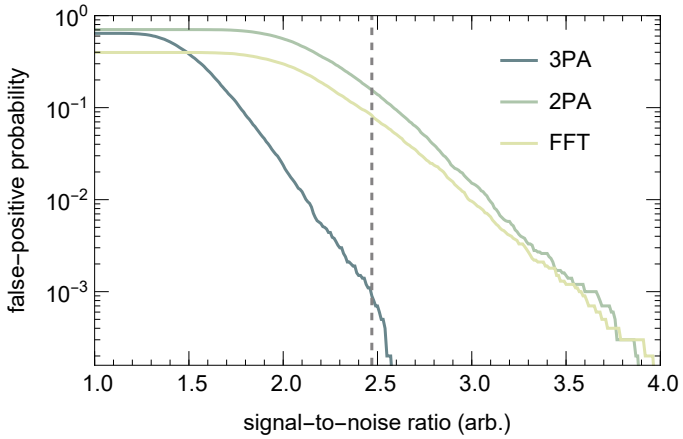

Supplementary Fig. 4. **Likelihood analysis.** The probability of a false-positive is shown as a function of the SNR for the three analysis methods. The vertical dashed line shows the lowest experimental SNR.

Supplementary Note 3. CRAMER-RAO LOWER BOUND

When considering low-SNR sinusoidal data the following question naturally arises: How much could we benefit from increasing the sampling rate at the expense of shortening the sample length? In other words, given a finite number of data points, is it better to spread them out over many oscillations or to sample the first oscillation very densely?

To answer this question we look at the standard signal-processing figure-of-merit called Cramer-Rao lower bound (CRLB) [2]. Consider N samples obtained at times t_n $(n = 1, \ldots, N)$:

$$x_n = A\cos(\omega t_n + \varphi) + w_n(0, \sigma), \tag{S3}$$

where w_n is a Gaussian random number with zero mean and standard deviation σ. The values of A, ω and φ are not known. The CRLB provides a mathematical expression for how well their value may be estimated for a given σ and N. In the following we consider two cases:

- $t_n = (n-1)dt$
- $t_n = (n-1)dt/N$

In the first case, increasing N makes the sample longer but the sampling rate $(1/dt)$ remains constant. For the second option the opposite is the case. To find the CRLB we need the probability distribution function (PDF) of the n-th point:

$$p_n(x_n; A, \omega, \varphi) = \frac{1}{\sqrt{2\pi\sigma^2}} \exp\left[-\frac{(x_n - A\sin(\omega t_n + \varphi))^2}{2\sigma^2}\right]. \tag{S4}$$

The PDF of the entire data set $x = \{x_n\}$ is $p(x; A, \omega, \varphi) = \prod_n p_n$. The CRLB theorem claims that the lower bound for estimating A, ω or φ is given by the inverse of the curvature of $p(x; A, \omega, \varphi)$ in parameter space (spanned by A, ω and φ). The curvature, moreover, is given by the negative of the second log derivative. The lower bound is thus computed in two steps. First we must arrange all second partial derivatives of $\ln[p(x; A, \omega, \varphi)]$ into a matrix known as the Fisher information matrix:

$$\hat{F} = \begin{pmatrix} -\frac{\partial^2 \ln p}{\partial A^2} & -\frac{\partial^2 \ln p}{\partial A \partial \omega} & -\frac{\partial^2 \ln p}{\partial A \partial \varphi} \\ -\frac{\partial^2 \ln p}{\partial \omega \partial A} & -\frac{\partial^2 \ln p}{\partial \omega^2} & -\frac{\partial^2 \ln p}{\partial \omega \partial \varphi} \\ -\frac{\partial^2 \ln p}{\partial \varphi \partial A} & -\frac{\partial^2 \ln p}{\partial \varphi \partial \omega} & -\frac{\partial^2 \ln p}{\partial \varphi^2} \end{pmatrix}. \tag{S5}$$

Note that for any element of $\hat{F}$ that depends explicitly on x_n the expectation value weighted by $p(x; A, \omega, \varphi)$ must be taken. In the second step we compute the inverse matrix and keep the on-diagonal elements. The lower bound variance of the i-th parameter estimation is given by $(\hat{F}^{-1})_{ii}$.

We have numerically computed this value as a function of N in both cases outlined above. The frequency lower bound $\mathrm{var}(\omega) \geq (\hat{F}^{-1})_{22}$ is found to be $\sim 1/N^3$ in the first case (increasing N means increasing sample length) and

only $\sim 1/N$ in the second (increasing N means increasing sampling rate). By increasing the sample length one thus benefits from an additional factor of $1/N$ (note that the variance is the square of the standard error). For frequency estimation it is thus advantageous to sample at a low rate and for a long time.

In our experiment the sample length is ultimately limited by the decay of the signal which is $\sim 300\mu$s [1].

Supplementary Note 4. THREE-BODY INTERACTION MODELS FOR NARROW RESONANCES

The major task in solving the three-body problem in the adiabatic hyperspherical representation is to solve the hyperangular adiabatic equation $\hat{H}_{\rm ad}\Phi_\nu(R;\Omega) = U_\nu(R)\Phi_\nu(R;\Omega)$, at fixed values of R, to determine the potentials U_ν and channel functions Φ_ν, both of which are required for the study of the solutions of Eq. (3) in the Methods section. The adiabatic Hamiltonian $\hat{H}_{\rm ad}$,

$$\hat{H}_{\rm ad} = \frac{\hat{\Lambda}^2(\Omega) + 15/4}{2\mu R^2}\hbar^2 + \hat{V}_T(R,\Omega) + \hat{H}_{\rm at}, \tag{S6}$$

contains the hyperangular kinetic energy via the hyperangular momentum operator [3], $\hat{\Lambda}$, the internal atomic energies, $\hat{H}_{\rm at}$, as well as all the interatomic interactions of the system,

$$\hat{V}_T(R,\Omega) = \hat{V}(r_{12}) + \hat{V}(r_{23}) + \hat{V}(r_{31}), \tag{S7}$$

where r_{ij} is the distance between atoms i and j, and $\hat{V}$ is the corresponding pairwise interaction.

The solutions of the hyperangular adiabatic equation are obtained by expanding the channel functions Φ_ν on the basis of the separated atomic spins $|\sigma\rangle$

$$\Phi_\nu(R;\Omega) = \sum_\sigma \phi_\nu^\sigma(R;\Omega)|\sigma\rangle. \tag{S8}$$

Applying this expansion to the hyperangular adiabatic equation results in a coupled system of equations for the components of ϕ_ν^σ:

$$\left[\frac{\hat{\Lambda}^2(\Omega) + 15/4}{2\mu R^2}\hbar^2 + E_{\rm at}^\sigma - U_\nu(R)\right]\phi_\nu^\sigma(R;\Omega) + \sum_{\sigma'} V_T^{\sigma\sigma'}(R,\Omega)\phi_\nu^{\sigma'}(R;\Omega) = 0, \tag{S9}$$

where $E_{\rm at}^\sigma$ is the sum of the three separated atoms in the $|\sigma\rangle$ spin state.

For our studies on the effect of the resonance width (see Fig. 4 of the main text) we use a simple two-channel model for the interatomic interaction

$$\hat{V}(r) = \begin{pmatrix} v_{\rm bg}(r) & v_{\rm c}(r) \\ v_{\rm c}(r) & v_{\rm bg}(r) \end{pmatrix} \tag{S10}$$

with background interaction, $v_{\rm bg}$, and inter-channel coupling, $v_{\rm c}$, given by

$$v_{\rm bg}(r) = -\frac{C_6}{r^6}\left(1 - \frac{\lambda_{\rm bg}^6}{r^6}\right), \tag{S11}$$

$$v_{\rm c}(r) = A_{\rm c}\exp\left[-\frac{(r-r_{\rm c})}{2w_{\rm c}^2}\right]. \tag{S12}$$

In our calculations we adjust $\lambda_{\rm bg}$ to produce a Feshbach resonance with the ^{7}Li background scattering length, $a_{\rm bg} \approx -25a_0$ [4], set $r_{\rm c} = 0$ and $w_{\rm c} = 0.5r_{\rm vdW}$ and vary $A_{\rm c}$ to produce different values for $s_{\rm res}$. We assume the B-field dependent energy difference between open and closed channels to be given by $\epsilon + \delta\mu B$ where we set $\epsilon = 10E_{\rm vdW}$ and $\delta\mu = 6\times10^{-3}E_{\rm vdW}/$G. In Supplementary Fig. 5 we show the effective potentials relevant for Efimov physics at $a = \pm\infty$ and various values of $s_{\rm res}$ between 0.13 and 246, thus covering both the broad and narrow resonance regimes.

For our more quantitative studies of ^{7}Li, the spin states and corresponding separated atomic energies are determined by the hyperfine interactions. We assumed the interatomic interactions to be given in terms of the singlet, $V_{S=0}$, and triplet, $V_{S=1}$, potentials:

$$\hat{V}(r) = \sum_{SM_S} |SM_S\rangle V_S(r)\langle SM_S|. \tag{S13}$$

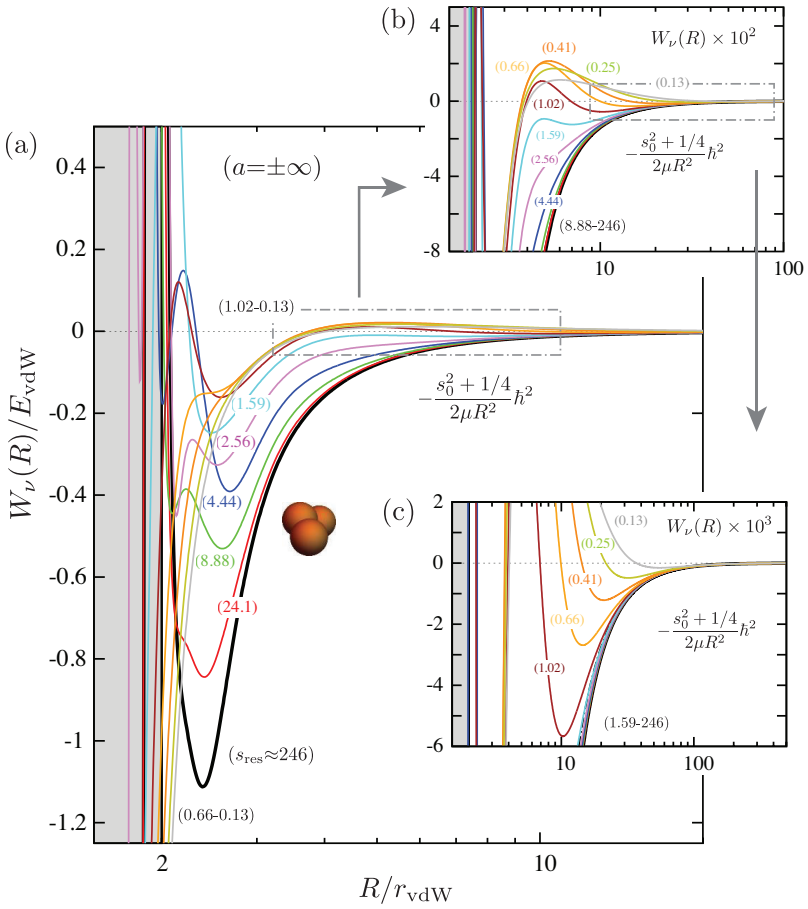

Supplementary Fig. 5. **Reshape of three-body interactions for narrow resonances.** (**a**) Effective potentials, $W(R)$, for the relevant channel supporting an infinity of Efimov states for different values of $s_{\rm res}$ in units of $E_{\rm vdW}=\hbar^2/mr_{\rm vdW}^2$. (**b**) and (**c**) Enhanced views of $W(R)$ illustrating their properties for different values of $s_{\rm res}$: As $s_{\rm res}$ evolves from the regime of broad ($s_{\rm res}\gg 1$) to narrow $s_{\rm res}\ll 1$ resonances a repulsive interaction emerges for $R\gtrsim 4r_{\rm vdW}$ and extending up to $R\approx 3r_*$, where $r_*\approx 1.912r_{\rm vdW}/s_{\rm res}$. The double-well structure of the three-body interaction for narrow resonances allows for trimer states to exist above the atom-dimer continuum for finite values of $a>0$ as shape resonances.

Within our approach, a key approximation is that we introduce a λ_S^6/r^{12} repulsive interaction to the *ab initio* singlet and triplet ^{7}Li Born-Oppenheimer potentials from Ref. [5] in order to restrict the diatomic molecular states to a manageable number (about 100 instead of 1000s) for our three-body calculations. By adjusting the values of λ to produce the correct values for the singlet and triplet scattering lengths [5], this model accurately describes the relevant Feshbach resonances for atoms in the $|F=1,m_F=0\rangle$ hyperfine state. In Supplementary Fig. 6 we show the hyperspherical effective potentials for ^{7}Li demonstrating the existence of the repulsive barrier for both obtained for $a=\pm\infty$ (dashed lines) and $a\approx 5.7r_{\rm vdW}$ (solid lines).

The three-body spin function used in our calculations follows the spectator atom approximation, where two atoms are allowed to interact via spin states satisfying $m_{F_1}+m_{F_2}=0$ while the third atom remains in the $|F_3=1,m_{F_3}=0\rangle$ state. Although this approximation has been shown to be enough to describe the experimental results for ^{39}K [6, 7], this is not the case for ^{7}Li when it comes to reproducing the position of the Efimov resonance in recombination experiments [8]. This result is most likely due to the presence of strong electronic spin exchange for ^{7}Li atoms [9, 10], which would require a larger spin basis to accurately describe the ^{7}Li interactions. Here, in order to set our model to produce results compatible with these observations we introduce a fictitious three-body interaction of the form

$$V_{\rm ex}(R)=-A_{\rm ex}R^\lambda {\rm Exp}[-R/\beta], \tag{S14}$$

where we set $\lambda=5$ and $\beta=0.2r_{\rm vdW}$ and tune $A_{\rm ex}$ to fit the position of the $a<0$ Efimov resonance of Ref. [8]. While this approach leads to an atom-dimer Efimov resonance for $a>0$ with energies comparable to those observed here for ^{7}Li, the calculated lifetimes are on the order of 10s of μs. For our simulations shown in Fig. 5 of the main text, we

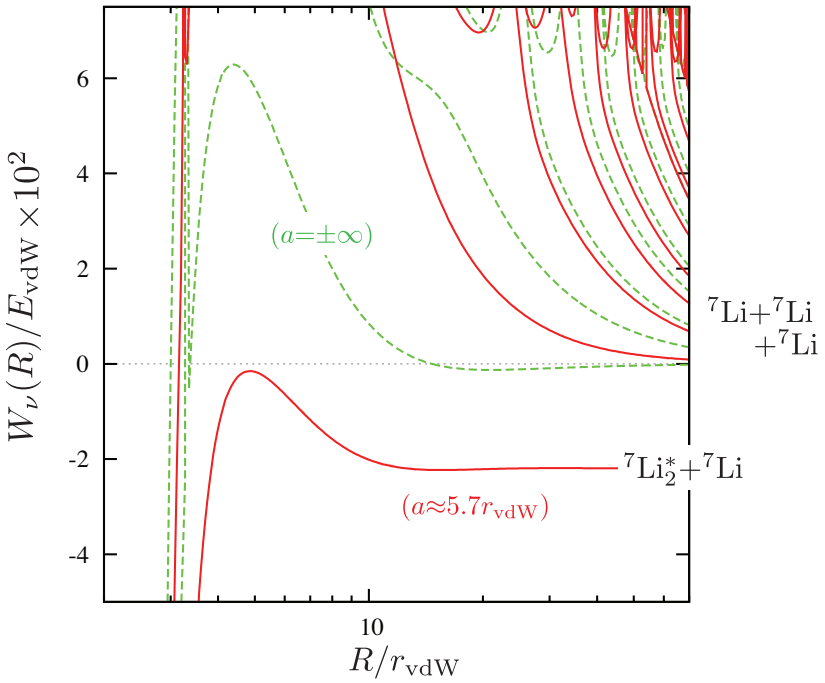

Supplementary Fig. 6. **Effective potentials for ^{7}Li atoms,** in van der Waals units of length, $r_{\rm vdW}$, and energy, $E_{\rm vdW}{=}\hbar^2/mr_{\rm vdW}^2$. Potentials where $W(R){>}0$ for $R{\gg}r_{\rm vdW}$ correspond to three-body continuum channels while potentials where $W(R){<}0$ for $R{\gg}r_{\rm vdW}$ describe atom-dimer channels. Dashed and solid lines represent the potentials for $a=\pm\infty$ and $a\approx5.7r_{\rm vdW}$, respectively.

have turned off non-adiabatic coupling between deeply-bound molecular states in order to set a lifetime comparable to the experiments.

SUPPLEMENTARY REFERENCES

[1] Yudkin, Y., Elbaz, R., Giannakeas, P., Greene, C. H. & Khaykovich, L. Coherent superposition of Feshbach dimers and Efimov trimers. *Phys. Rev. Lett.* **122**, 200402 (2019).

[2] Kay, S. M. *Fundamentals of Statistical Signal Processing: Estimation Theory* (Prentice Hall PTR, Upper Saddle River, New Jersey, 1993).

[3] Suno, H., Esry, B. D., Greene, C. H. & Burke, J. P. Three-body recombination of cold helium atoms. *Phys. Rev. A* **65**, 042725 (2002).

[4] Pollack, S. E. *et al.* Extreme tunability of interactions in a ^{7}Li Bose-Einstein condensate. *Phys. Rev. Lett.* **102**, 090402 (2009).

[5] Julienne, P. S. & Hutson, J. M. Contrasting the wide Feshbach resonances in ^{6}Li and ^{7}Li. *Phys. Rev. A* **89**, 052715 (2014). URL https://link.aps.org/doi/10.1103/PhysRevA.89.052715.

[6] Chapurin, R. *et al.* Precision test of the limits to universality in few-body physics. *Phys. Rev. Lett.* **123**, 233402 (2019).

[7] Xie, X. *et al.* Observation of Efimov universality across a non-universal Feshbach resonance in ^{39}K. *Phys. Rev. Lett.* **125**, 243401 (2020).

[8] Gross, N., Shotan, Z., Kokkelmans, S. & Khaykovich, L. Nuclear-spin-independent short-range three-body physics in ultracold atoms. *Phys. Rev. Lett.* **105**, 103203 (2010).

[9] Li, J.-L., Secker, T., Mestrom, P. M. A. & Kokkelmans, S. J. J. M. F. Strong spin-exchange recombination of three weakly interacting ^{7}Li atoms. *Phys. Rev. Res.* **4**, 023103 (2022). URL https://link.aps.org/doi/10.1103/PhysRevResearch.4.023103.

[10] van de Kraats, J., Ahmed-Braun, D. J. M., Li, J.-L. & Kokkelmans, S. J. J. M. F. Emergent inflation of the Efimov spectrum under three-body spin-exchange interactions. *arXiv:2309.13128* (2023).

Chapter 4

Article 3: Efimov scenario for overlapping narrow Feshbach resonances

Yaakov Yudkin and Lev Khaykovich

Physical Review A

Volume 103, Page 063303, June 2021

Efimov scenario for overlapping narrow Feshbach resonances

Yaakov Yudkin and Lev Khaykovich
Department of Physics, QUEST Center and Institute of Nanotechnology and Advanced Materials, Bar-Ilan University, Ramat-Gan 5290002, Israel

(Received 3 March 2021; revised 25 May 2021; accepted 25 May 2021; published 7 June 2021)

While Efimov physics in ultracold atoms is usually modeled with an isolated Feshbach resonance, many real world resonances appear in close vicinity to each other and are therefore overlapping. Here we derive a realistic model based on the mutual coupling of an open channel and two closed molecular channels while neglecting short-range physics as permitted by the narrow character of the considered resonances. The model is applied to three distinct scenarios with experimental relevance. We show that the effect of overlapping resonances is manifested most strikingly at a narrow resonance in whose vicinity there is a slightly narrower one. In this system the Efimov ground state extends not only over the scattering length zero crossing between the two resonances but also over the pole of the second resonance to finally meet the dissociation threshold below it. In the opposite scenario, when a narrow resonance is considered in the vicinity of a slightly broader one, we observe that the Efimov features are pushed to lower binding energies and smaller scattering lengths by a significant factor facilitating their experimental investigation. Both scenarios are compared with the case of two narrow resonances which are far enough away from each other to be effectively decoupled. In this case the two-channel model results are recovered. Finally, we analyze the rich excitation spectrum of the system and construct and explain its nodal pattern.

DOI: 10.1103/PhysRevA.103.063303

I. INTRODUCTION

Tunability of the s-wave scattering length a via a magnetic Feshbach resonance is at the heart of recent studies of few-body physics in ultracold atoms [1–3]. Conceptually, a Feshbach resonance can be understood within a simple two-channel model: it occurs when incoming atoms in an open channel are coupled to an almost degenerate bound state in a closed channel [4]. Loosely speaking, one differentiates between two types of Feshbach resonances quantified by the dimensionless resonance strength parameter s_{res}. A broad resonance ($s_{\mathrm{res}} \gg 1$) arises from a strong coupling to the bound state. The scattering amplitude is largely dominated by a, which is on the order of the van der Waals length r_{vdW} (the range of the interaction potential) away from collisional resonances. On the contrary, a narrow resonance ($s_{\mathrm{res}} \ll 1$) arises from a weak coupling. In this case the effective range r_e, in addition to a, determines the scattering amplitude at a given magnetic field. As a new length scale associated with the narrow resonance one defines $R^\star = -r_e(B_{\mathrm{res}})/2 > 0$, where $r_e(B_{\mathrm{res}})$ is the value of r_e at the resonance position ($|a| \to \infty$). $R^\star$ is related to s_{res} via $R^\star = \bar{a}/s_{\mathrm{res}}$ where $\bar{a} = [4\pi/\Gamma(1/4)^2]r_{vdW}$ is the mean scattering length [4]. Thus, for a broad (narrow) resonance $R^\star \ll r_{vdw}$ ($R^\star \gg r_{vdw}$) is satisfied [5].

It is clear, however, that the description of a real-world scattering system, which in general is a multichannel problem, within the framework of a two-channel model is an approximation and should be applied with caution. It is worth noting that nearly all atomic species used in experiments exhibit multiple, often overlapping, Feshbach resonances. Extreme examples include recently studied cold molecules with their complex internal structure [6] and heavy lanthanide species where a dense and chaotic spectrum of Feshbach resonances has been reported [7].

Ironically, simple analytical or semi-analytical expressions have been developed to describe the scattering length with great precision even in the case of a diverging number of scattering channels [8–10]. This has lured few-body physics treatments to consider an isolated Feshbach resonance a good approximation for calculating various properties of few-body systems such as the energy levels of Efimov trimers [11]. The latter, which is the main focus of this paper, form in a system with three atoms when the pairwise interactions exceed the relevant length scale, so $a \gg r_{vdW}$ ($a \gg R^\star$) for a broad (narrow) resonance. Efimov physics has been studied extensively in the recent decade, theoretically and experimentally [1–3], in the vicinity of both isolated broad [12–15] and, more recently, narrow Feshbach resonances [16–19]. Many of these studies were performed in the vicinity of overlapping resonances [12–17], but the theoretical treatment rarely goes beyond an isolated resonance. For a few exception see Refs. [20,21].

Recent efforts to fully incorporate the multichannel character of two-body interactions suggest properly including the hyperfine structure of the real atomic system [18,19,22]. Although this is arguably the most comprehensive approach, it comes at the expense of heavy numerical calculations and the absence of direct relations between the microscopic parameters of the theory and the macroscopic experimental

observables. Here, in contrast, we consider the simplest way to deal with a consequence of the multichannel character of two-body interactions, namely, the existence of two *overlapping* Feshbach resonances. We generalize the two-channel model, which is suitable for isolated narrow Feshbach resonances [23], to two overlapping resonances by including a second closed channel with an independently tunable bound state. For completeness an intermolecular coupling between the two closed channels is incorporated. We develop a protocol to fix all model parameters in the two-body sector and compute the Efimov spectrum without any adjustable parameters. In the three-body sector we identify unique features related to the addition of a second closed channel and discuss their experimental implications.

The paper is organized as follows. We begin in Sec. II by examining the expected phenomenology of the three-channel model. In Sec. III we state the three-channel model Hamiltonian and derive equations for the scattering amplitude, dimer binding energy, and trimer binding energy. The model is applied to three distinct systems in Sec. IV and their experimental relevance is addressed. The model's bare parameters are further discussed in Sec. V and the trimer eigenfunctions are analyzed in Sec. VI. We conclude in Sec. VII with possible extensions of the three-channel model.

II. PHENOMENOLOGY OF THREE-CHANNEL MODEL

The two-channel model is very successful at reproducing the basic phenomenology of a narrow and isolated Feshbach resonance. It captures both the two- and the three-body sector [23]. In its most fundamental form one considers a featureless open channel (i.e., no background scattering) and, coupled to it, a closed (molecular) channel detuned from the open channel by a magnetic-field-dependent binding energy. For completeness, this model is reviewed in Appendix A. It has been applied to various aspects of bosonic [24–28] and fermionic [29–34] scenarios and may be generalized to include background scattering in the open channel [35] and to hetero-nuclear systems [36,37].

Here we take a different route and generalize the model to three channels by adding a second molecular channel. The coupling of the two molecular channels to the free-atom continuum gives rise to two scattering resonances and two two-body bound states which we call dimers. Note the distinction between a molecular state, which is a bare state of the (noninteracting) Hamiltonian, and a dimer, which is the two-body bound eigenstate of the full Hamiltonian. In the three-body sector, which is schematically illustrated in Fig. 1, there are three types of continua. In addition to the free-atom continuum there are two different dimer-atom continua—one above each dimer. Around each of the resonances and below the respective dimers we expect three-body bound states, i.e., Efimov trimers. Note though that only the trimers associated with the higher resonance (higher magnetic field, $B_2^{(\mathrm{res})}$ in Fig. 1) are true bound states. The $B_1^{(\mathrm{res})}$ trimers coexist with a continuum of dimer-atom states and are therefore not stable bound states. The question of their existence depends on their lifetime and they might be manifested as dimer-atom collision resonances [30]. This subject, however, is beyond the scope of the present discussion in which only true bound states are considered.

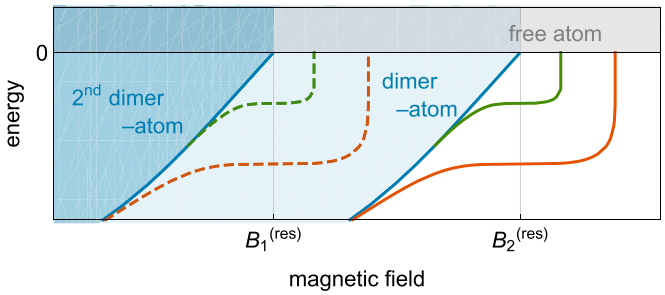

FIG. 1. Schematic representation of the three-body sector of overlapping resonances. The two resonance positions are labeled $B_1^{(\mathrm{res})}$ and $B_2^{(\mathrm{res})}$. The binding energies of the dimers (blue curves) as well as the ground (orange) and excited (green) state trimers are plotted. The regions of the free-atom continuum (gray, positive energy) and the two dimer-atom continua (shades of blue) are indicated. The trimers associated with $B_1^{(\mathrm{res})}$ are embedded in the dimer-atom continuum due to the resonance at $B_2^{(\mathrm{res})}$.

III. DERIVATION OF THREE-CHANNEL MODEL

The following three-channel Hamiltonian is the most general extension of the two-channel model. We use it to formulate equations for the scattering amplitude and the dimer binding energy (two-body sector). We examine the two-body sector and relate the bare parameters to physical observables before moving on to the three-body sector where the equation for Efimov bound states is presented and discussed.

A. Three-channel Hamiltonian

The full Hamiltonian of the three-channel model is $\hat{H} = \hat{H}_0 + \hat{H}_{\mathrm{int}}$, where $\hat{H}_{\mathrm{int}} = \hat{H}_1 + \hat{H}_2 + \hat{H}_{12}$. The first term is the bare Hamiltonian of all three channels

$$\hat{H}_0 = \int \frac{d^3k}{(2\pi)^3}\left[\frac{\hbar^2k^2}{2m}\hat{a}^\dagger_{\vec{k}}\hat{a}_{\vec{k}} + \left(E_{b,1} + \frac{\hbar^2k^2}{4m}\right)\hat{b}^\dagger_{\vec{k}}\hat{b}_{\vec{k}} + \left(E_{b,2} + \frac{\hbar^2k^2}{4m}\right)\hat{c}^\dagger_{\vec{k}}\hat{c}_{\vec{k}}\right], \tag{1}$$

where $\hat{a}_{\vec{k}}$ annihilates free particles and $\hat{b}_{\vec{k}}$ ($\hat{c}_{\vec{k}}$) annihilates molecules in the first (second) molecular channel with bare molecular energy $E_{b,1}$ ($E_{b,2}$). We assume the latter to be an affine function of the magnetic field: $E_{b,i} = \mu_i(B_i - B)$, where μ_i is the magnetic moment of the ith molecular channel with respect to the free-atom continuum and B_i is the bare resonance position. Without loss of generality we assume $B_1 < B_2$. Both molecular channels are coupled to the open channel via

$$\hat{H}_1 = \Lambda_1 \int \frac{d^3k}{(2\pi)^3}\int \frac{d^3q}{(2\pi)^3}\left[\hat{b}^\dagger_{\vec{k}}\hat{a}_{\vec{q}+\frac{\vec{k}}{2}}\hat{a}_{-\vec{q}+\frac{\vec{k}}{2}} + \hat{a}^\dagger_{-\vec{q}+\frac{\vec{k}}{2}}\hat{a}^\dagger_{\vec{q}+\frac{\vec{k}}{2}}\hat{b}_{\vec{k}}\right], \tag{2}$$

and

$$\hat{H}_2 = \Lambda_2 \int \frac{d^3k}{(2\pi)^3}\int \frac{d^3q}{(2\pi)^3}\left[\hat{c}^\dagger_{\vec{k}}\hat{a}_{\vec{q}+\frac{\vec{k}}{2}}\hat{a}_{-\vec{q}+\frac{\vec{k}}{2}} + \hat{a}^\dagger_{-\vec{q}+\frac{\vec{k}}{2}}\hat{a}^\dagger_{\vec{q}+\frac{\vec{k}}{2}}\hat{c}_{\vec{k}}\right]. \tag{3}$$

In addition, the two molecular channels are coupled to each other via

$$\hat{H}_{12} = \Lambda_{12} \int \frac{d^3k}{(2\pi)^3} [\hat{c}^\dagger_{\vec{k}} \hat{b}_{\vec{k}} + \hat{b}^\dagger_{\vec{k}} \hat{c}_{\vec{k}}]. \tag{4}$$

The Hamiltonian thus has five bare parameters, namely, the bare resonance positions B_1 and B_2, and the coupling constants Λ_1, Λ_2, and Λ_{12}. Since background scattering in the open channel is not included in the model, we expect it to work for systems with vanishingly small background scattering length a_{bg}.

B. Two-body observables: Scattering length, effective range, and binding energy

To describe the two-body sector we solve the Schrödinger equation $(\hat{H} - E)|\psi_{2B}\rangle = 0$ with the most general two-body ansatz in the center-of-mass frame:

$$|\psi_{2B}\rangle = \gamma \hat{c}^\dagger_{\vec{k}=0}|0\rangle + \beta \hat{b}^\dagger_{\vec{k}=0}|0\rangle + \int \frac{d^3k}{(2\pi)^3} \alpha_{\vec{k}} \hat{a}^\dagger_{\frac{\vec{k}}{2}} \hat{a}^\dagger_{-\frac{\vec{k}}{2}}|0\rangle. \tag{5}$$

In the following, all quantities are renormalized with respect to a naturally arising momentum cutoff k_c and its associated energy $E_c = \hbar^2 k_c^2/m$. For clarity, a dimensionful quantity x is denoted $\tilde{x}$ after it is renormalized and dimensionless, for example, the renormalized scattering length a (dimensionful) is denoted $\tilde{a}$ (dimensionless) and they are related via $\tilde{a} = k_c a$. However, dimensions of magnetic field are not renormalized. The molecular magnetic moment μ_i (dimensions of energy per unit magnetic field: J/G) is renormalized to $\tilde{\mu}_i = \mu_i/E_c$ which has dimensions of 1/G.

For positive energy $E = \hbar^2 k_0^2/m > 0$ the Schrödinger equation leads to two coupled equations for the molecular amplitudes β and γ:

$$\begin{aligned}&\big(\tilde{\mu}_1(B_1 - B) - \tilde{k}_0^2\big)\tilde{\beta} + 2\tilde{\Lambda}_1 + \tilde{\Lambda}_{12}\tilde{\gamma} \\ &\quad - \frac{\tilde{\Lambda}_1}{\pi^2}\left(1 - \frac{i\pi}{2}\tilde{k}_0\right)(\tilde{\Lambda}_1\tilde{\beta} + \tilde{\Lambda}_2\tilde{\gamma}) = 0,\end{aligned} \tag{6a}$$

$$\begin{aligned}&\big(\tilde{\mu}_2(B_2 - B) - \tilde{k}_0^2\big)\tilde{\gamma} + 2\tilde{\Lambda}_2 + \tilde{\Lambda}_{12}\tilde{\beta} \\ &\quad - \frac{\tilde{\Lambda}_2}{\pi^2}\left(1 - \frac{i\pi}{2}\tilde{k}_0\right)(\tilde{\Lambda}_1\tilde{\beta} + \tilde{\Lambda}_2\tilde{\gamma}) = 0,\end{aligned} \tag{6b}$$

with which the scattering amplitude

$$\tilde{f}_{k_0} = -\frac{\tilde{\Lambda}_1\tilde{\beta} + \tilde{\Lambda}_2\tilde{\gamma}}{4\pi} \tag{7}$$

is computed. The resulting expression is expanded to second order in $\tilde{k}_0$ and compared with the effective range expansion $\tilde{f}_{k_0}^{-1} = -\tilde{a}^{-1} - i\tilde{k}_0 + \tilde{r}_e\tilde{k}_0^2/2$ to find $\tilde{a}$ and $\tilde{r}_e$.

If instead of the scattering states ($E > 0$) we search for a bound-state solution $E = -\hbar^2\lambda_D^2/m < 0$ ($\lambda_D > 0$), the following equations are obtained for the binding wave number of the dimer $\tilde{\lambda}_D$ and the ratio $\chi = \tilde{\beta}/\tilde{\gamma}$:

$$\big(\tilde{\mu}_1(B_1 - B) + \tilde{\lambda}_D^2\big)\chi + \tilde{\Lambda}_{12} - \frac{\tilde{\Lambda}_1}{\pi^2}\left(1 - \tilde{\lambda}_D\frac{\pi}{2}\right)(\tilde{\Lambda}_1\chi + \tilde{\Lambda}_2) = 0, \tag{8a}$$

$$\big(\tilde{\mu}_2(B_2 - B) + \tilde{\lambda}_D^2\big) + \tilde{\Lambda}_{12}\chi - \frac{\tilde{\Lambda}_2}{\pi^2}\left(1 - \tilde{\lambda}_D\frac{\pi}{2}\right)(\tilde{\Lambda}_1\chi + \tilde{\Lambda}_2) = 0. \tag{8b}$$

By eliminating χ, the two coupled Eqs. (8) can be written as a fourth-order polynomial equation in $\tilde{\lambda}_D$. Depending on the value of B, it can have two, one, or zero positive solutions. The values of B at which the number of solutions changes coincides with the resonance positions $a \to \pm\infty$ which we denote $B_i^{(\mathrm{res})}$.

Details on the derivation of Eqs. (6)–(8) can be found in Appendix B 1.

C. Relating the bare parameters to observables

Eliminating the amplitudes $\tilde{\beta}$ and $\tilde{\gamma}$ from Eqs. (6) with $\tilde{k}_0 = 0$, one finds an analytic expression for $\tilde{a} = -\tilde{f}_{k_0=0} = (\tilde{\Lambda}_1\tilde{\beta} + \tilde{\Lambda}_2\tilde{\gamma})|_{k_0=0}/4\pi$ which can be parametrized as

$$\tilde{a}(B) = \frac{\tilde{\Delta}_1}{B_1^{(\mathrm{res})} - B} + \frac{\tilde{\Delta}_2}{B_2^{(\mathrm{res})} - B}, \tag{9}$$

where the resonance widths $\tilde{\Delta}_i$ and the positions $B_i^{(\mathrm{res})}$ (for $i = 1, 2$) are observable parameters [38]. This parametrization is also obtained in the context of multichannel quantum-defect theory [9] (see Appendix B 3) and, therefore, generic. Analytic expressions relating the four observable and five bare parameters are given in Appendix B 2. As expected, the observable parameters do not depend on the absolute position of the bare resonances but only on the difference $B_1 - B_2$, except for $B_i^{(\mathrm{res})}$ which also depend additively on the mean $(B_1 + B_2)/2$ for positioning. Because there is one more bare parameter than there are observable parameters there is an apparent redundancy in the model. Indeed, keeping the observable parameters fixed, one can, for example, find a set of parameters $(\tilde{\Lambda}_1, \tilde{\Lambda}_2, B_1, B_2)$ for a variety of $\tilde{\Lambda}_{12}$ values without altering the scattering amplitude, the dimer binding energy, or the trimer binding energy. This is further discussed in Sec. V below.

D. Three-body sector: Efimov trimers

Here the main result of this paper, the equation for the trimer binding energy in the three-channel model, is stated. Details of the derivation can be found in Appendix B 4. In short, the trimer binding energy $E_T = -\hbar^2\lambda_T^2/m$, with $\lambda_T > \max(0, \lambda_D)$, is the eigenvalue associated with the three-body wave function:

$$\begin{aligned}|\psi_{3B}\rangle = &\int \frac{d^3k}{(2\pi)^3} \gamma_{\vec{k}} \hat{c}^\dagger_{\vec{k}} \hat{a}^\dagger_{-\vec{k}}|0\rangle + \int \frac{d^3k}{(2\pi)^3} \beta_{\vec{k}} \hat{b}^\dagger_{\vec{k}} \hat{a}^\dagger_{-\vec{k}}|0\rangle \\ &+ \int \frac{d^3k}{(2\pi)^3} \int \frac{d^3q}{(2\pi)^3} \alpha_{\vec{k},\vec{q}} \hat{a}^\dagger_{\vec{q}+\frac{\vec{k}}{2}} \hat{a}^\dagger_{-\vec{q}+\frac{\vec{k}}{2}} \hat{a}^\dagger_{-\vec{k}}|0\rangle.\end{aligned} \tag{10}$$

Hence one must solve the Schrödinger equation $(\hat{H} - E_T)|\psi_{3B}\rangle = 0$ to arrive at a closed equation for λ_T. The condition

$\lambda_T > \max(0, \lambda_D)$ implies that only trimers associated with the higher resonance are properly determined by the following equations. In between the two dimers, where Efimov trimers associated with the lower resonance are expected (see Fig. 1), a solution for any value of λ_T exists due to the dimer-atom continuum. It is not possible to distinguish between the dimer-atom and the trimer state since both are of the form (10) [39].

Direct substitution of $|\psi_{3B}\rangle$ into $(\hat{H} - E_T)|\psi_{3B}\rangle = 0$ leads to three coupled integral equations which are reduced to two by eliminating the free particle amplitude $\alpha_{\vec{k},\vec{q}}$. It is then convenient to write the two remaining three-body scattering amplitudes as a vector $\psi(k) = (\beta_k, \gamma_k)^T$ and put the coefficients in a 2×2 matrix $\mathcal{M}_{\lambda_T}(k, q)$ that depends on λ_T. The Schrödinger equation thus takes the form $\int_0^\infty dq \mathcal{M}_{\lambda_T}(k, q)\psi(q) = 0$ and a nontrivial solution is obtained for $\det \mathcal{M}_{\lambda_T}(k, q) = 0$. After renormalizing with respect to the momentum cutoff and using the practical substitution $k = (2/\sqrt{3})\lambda_T \sinh\xi$, the Schrödinger equation can be written as

$$\int_{-\infty}^{\infty} d\xi \mathcal{M}_{\lambda_T}(\xi, \xi')\psi(\xi') = 0. \tag{11}$$

The lower integration limit was extended to $-\infty$ by demanding that both $\tilde{\beta}_\xi$ and $\tilde{\gamma}_\xi$ be odd functions of ξ. The vector $\psi(\xi)$ is now defined as $\psi(\xi) = (\tilde{\beta}_\xi, \tilde{\gamma}_\xi)^T$ and the matrix elements are

$$(\mathcal{M}_{\lambda_T})_{ij} = [(f_i(\xi') - h(\xi'))\delta_{ij} + h(\xi') - \tilde{\Lambda}_i\tilde{\Lambda}_j g(\xi')]\,\delta(\xi - \xi') - \tilde{\Lambda}_i\tilde{\Lambda}_j L(\xi, \xi'), \tag{12}$$

where we have defined

$$f_i(\xi) = \tilde{\lambda}_T \cosh\xi + \frac{\tilde{\mu}_i}{\tilde{\lambda}_T \cosh\xi}(B_i - B), \tag{13a}$$

$$g(\xi) = \frac{1}{\pi^2}\left(\frac{1}{\tilde{\lambda}_T \cosh\xi} - \frac{\pi}{2}\right), \tag{13b}$$

$$h(\xi) = \frac{\tilde{\Lambda}_{12}}{\tilde{\lambda}_T \cosh\xi}, \tag{13c}$$

$$L(\xi, \xi') = \frac{2}{\sqrt{3}\pi^2} \ln\left(\frac{e^{2(\xi-\xi')} + e^{\xi-\xi'} + 1}{e^{2(\xi-\xi')} - e^{\xi-\xi'} + 1}\right). \tag{13d}$$

The requirement of a vanishing determinant:

$$\det \mathcal{M}_{\lambda_T}(\xi, \xi') = 0, \tag{14}$$

is a closed equation for λ_T. Depending on the magnetic field there are many values $\lambda_T = \lambda_T^{(\mathrm{sol})}$ for which Eq. (14) is satisfied. To single out the physical solutions corresponding to three-body bound states one must compute the zero-eigenvalue eigenfunction $\psi(\xi)$ of $\mathcal{M}_{\lambda_T^{(\mathrm{sol})}}$ in accordance with Eq. (11) and determine $\tilde{\beta}_\xi$ and $\tilde{\gamma}_\xi$. The mathematical solution $\lambda_T^{(\mathrm{sol})}$ is physically relevant only if both are odd functions of ξ. In addition, the number of nodes in $\tilde{\beta}_\xi$ and $\tilde{\gamma}_\xi$ allows the assignment of $\lambda_T^{(\mathrm{sol})}$ to the ground or an excited Efimov state (see Sec. VI).

TABLE I. Parameters of the three model systems.

Type	NB	NN	BN
Δ_1/a_0 (G)	150	150	1000
Δ_2/a_0 (G)	1000	150	150
$B_1 - B_2^{(\mathrm{res})}$ (G)	−39.3857	−23.7856	−54.0702
$B_2 - B_2^{(\mathrm{res})}$ (G)	−17.22	−5.76371	−2.53547
$\tilde{\Lambda}_1$	2.02991	0.776438	2.29268
$\tilde{\Lambda}_2$	1.21692	0.926494	0.587429
$\tilde{\Lambda}_{12}$	0.1	0.1	0.1

IV. APPLICATION TO MODEL SYSTEMS

A. Definitions

To illustrate the three-channel model we choose a model atom whose molecular bound states are pure spin singlets and consider high magnetic fields such that the Zeeman shift is linear to a good approximation. The value of the magnetic moment is thus $\mu_1 = \mu_2 = -2\mu_B$, where $\mu_B = 1.4$ MHz/G is the Bohr magneton. The momentum cutoff is somewhat arbitrarily fixed to $k_c = 0.05/a_0$ but, as discussed in Sec. V, the results are indifferent to variations in k_c. All lengths are calculated in units of the Bohr radius a_0 and all energies in units of $E_0 = \hbar^2/ma_0^2$, where m is the atomic mass. Three scenarios are considered: $\Delta_1 \ll \Delta_2$ (denoted NB), $\Delta_1 = \Delta_2$ (NN), and $\Delta_1 \gg \Delta_2$ (BN)—see Table I. The distance between the two resonances is identical in all three scenarios; we choose $B_2^{(\mathrm{res})} - B_1^{(\mathrm{res})} = 20$ G, so the only difference between the models is the width. In the NN scenario, as will be shown, $B_2^{(\mathrm{res})} - B_1^{(\mathrm{res})}$ is too large for the two resonances to be considered overlapping. We therefore expect the results of the three-channel model to be in good agreement with those of the two-channel model, i.e., the additional channel has no influence on the two- and three-channel observables. This system is used as a sanity check for our three-channel model. In the NB (BN) scenario the higher (lower) resonance is broadened to make them overlapping. (Alternatively, one could keep $\Delta_1 = \Delta_2$ constant and decrease $B_2^{(\mathrm{res})} - B_1^{(\mathrm{res})}$ to generate overlap.) Because the three-channel model allows for the determination of the higher-resonance trimers only, both the case NB and BN are considered. In each scenario we ask the question: How does the resonance at $B_1^{(\mathrm{res})}$ influence the Efimov spectrum around $B_2^{(\mathrm{res})}$?

B. Two-body sector

From the analytic equations in Appendix B 2 we find the bare parameters for each model (Table I). Here, because of the redundancy in the number of bare parameters, we fix $\tilde{\Lambda}_{12} = 0.1$. Other options and their consequences are discussed in Secs. V and VI.

We use the two-body equations to compute the scattering lengths, effective ranges, and dimer binding energies of the three scenarios. The results are compared with an individual treatment of the resonances with the two-channel model (Fig. 2). As expected, the two-channel model is a good approximation only in the direct vicinity of the resonance. The three-channel model introduces three important additions: (1) The scattering length is forced to cross $a = 0$ in between the

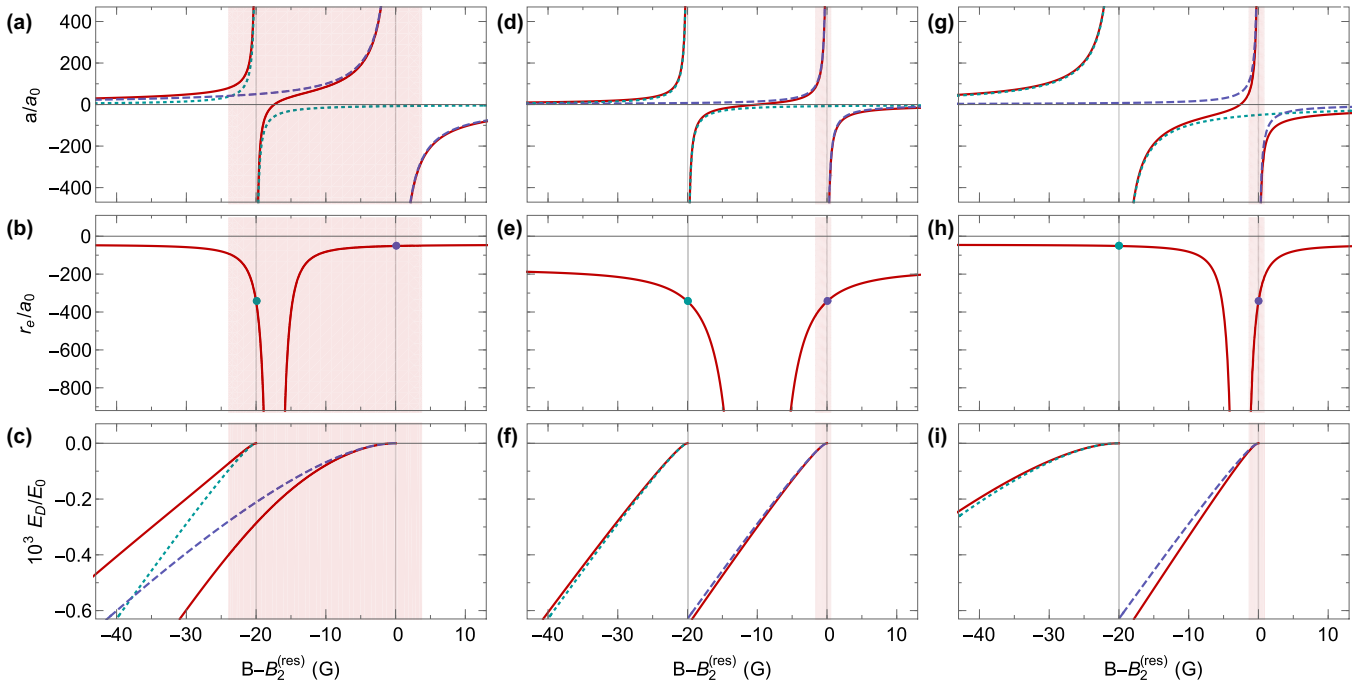

FIG. 2. Two-body sector. The (a), (d), (g) scattering length, (b), (e), (h) effective range, and (c), (f), (i) dimer binding energy for the (a)–(c) NB, (d)–(f) NN, and (g)–(h) BN scenarios are shown. The three-channel model (solid curves) is compared with the two-channel model applied to the lower (dotted) and higher (dashed) resonance. In panels (b), (e), and (h), the two-channel value of the effective range is represented by a point because of its lack of B dependence. The gray vertical lines indicate the resonance positions $B_1^{(\mathrm{res})}$ and $B_2^{(\mathrm{res})}$, and the shaded region shows the extent of the ground-state Efimov trimer $B_\star^{(0)} < B < B_-^{(0)}$ associated with $B_2^{(\mathrm{res})}$.

two resonances, close to the narrower one. According to the two-channel model this never happens (for zero background scattering length). (2) While in the two-channel model, the effective range is constant across the Feshbach resonance; it develops a magnetic-field dependence in the three-channel model. In particular, at $a = 0$, $r_e \to -\infty$. (3) Finally, unlike the two independent dimer energy levels arising from an individual treatment of the two resonances with the two-channel model, level repulsion naturally arises in the three-channel model. We stress at this point that the level repulsion is not due to $\tilde{\Lambda}_{12}$ but is intrinsic to the model and also happens for $\tilde{\Lambda}_{12} = 0$. The physical origin of the repulsion in this case is the second-order coupling through the continuum via $\hat{H}_1$ and $\hat{H}_2$. Changing $\tilde{\Lambda}_{12}$ (and accordingly also $\tilde{\Lambda}_1$ and $\tilde{\Lambda}_2$, see Sec. V) tunes the relative strength of the two.

The NN scenario in Figs. 2(d)–2(f) is hardly affected by the additional channel. In particular, the two dimers are nearly identical in both treatments. As mentioned above, this is the consequence of $B_2^{(\mathrm{res})} - B_1^{(\mathrm{res})}$ being large compared with $\Delta_1 = \Delta_2$, and the resonances cannot be considered properly overlapping. The three-channel model thus reproduces the results of the two-channel model in the limit of nonoverlapping resonances. Nevertheless, all three additions of the three-channel model, however small, are appreciable.

In the NB scenario, on the other hand, extensive repulsion of the two dimers is visible [Figs. 2(a)–2(c)]. The two-channel-model dimers are not coupled and intersect each other at a binding energy of $-0.57\times10^{-3}E_0$. The mutual coupling introduced in the three-channel model leads to an avoided crossing, strongly altering their functional form. This is in stark contrast to the two-channel model already at the two-body level.

Finally, to a lesser extent, this repulsion can also be seen in the BN scenario; Figs. 2(g)–2(i). The effect is much weaker because the two-channel-model dimers do not cross. In addition, a scattering length zero-crossing and its associated effective range divergence are introduced relatively close to the narrow resonance due to the neighboring broader resonance.

We note that the scattering length zero crossing could also be obtained in the two-channel model by using a nonzero background scattering length to account for the lower resonance. Although the magnetic-field regime, for which the two- and three-channel scattering length agree, would be extended, it would remain limited to the vicinity of the resonance. The use of a nonzero background scattering length also raises the question of how to define it. Does one prefer a larger regime of agreement or a perfect overlap at the zero crossing? Using the lower resonance explicitly avoids these questions, automatically takes into account the background generated by the nearby resonance and, most importantly, makes it magnetic-field dependent.

A more general model than we are presenting here would include both resonances and, in addition, a background scattering which arises from scattering in the open channel—not another closed channel.

C. Three-body sector

Here we solve the three-body equations for the three scenarios. In each case we compute the ground and first-excited

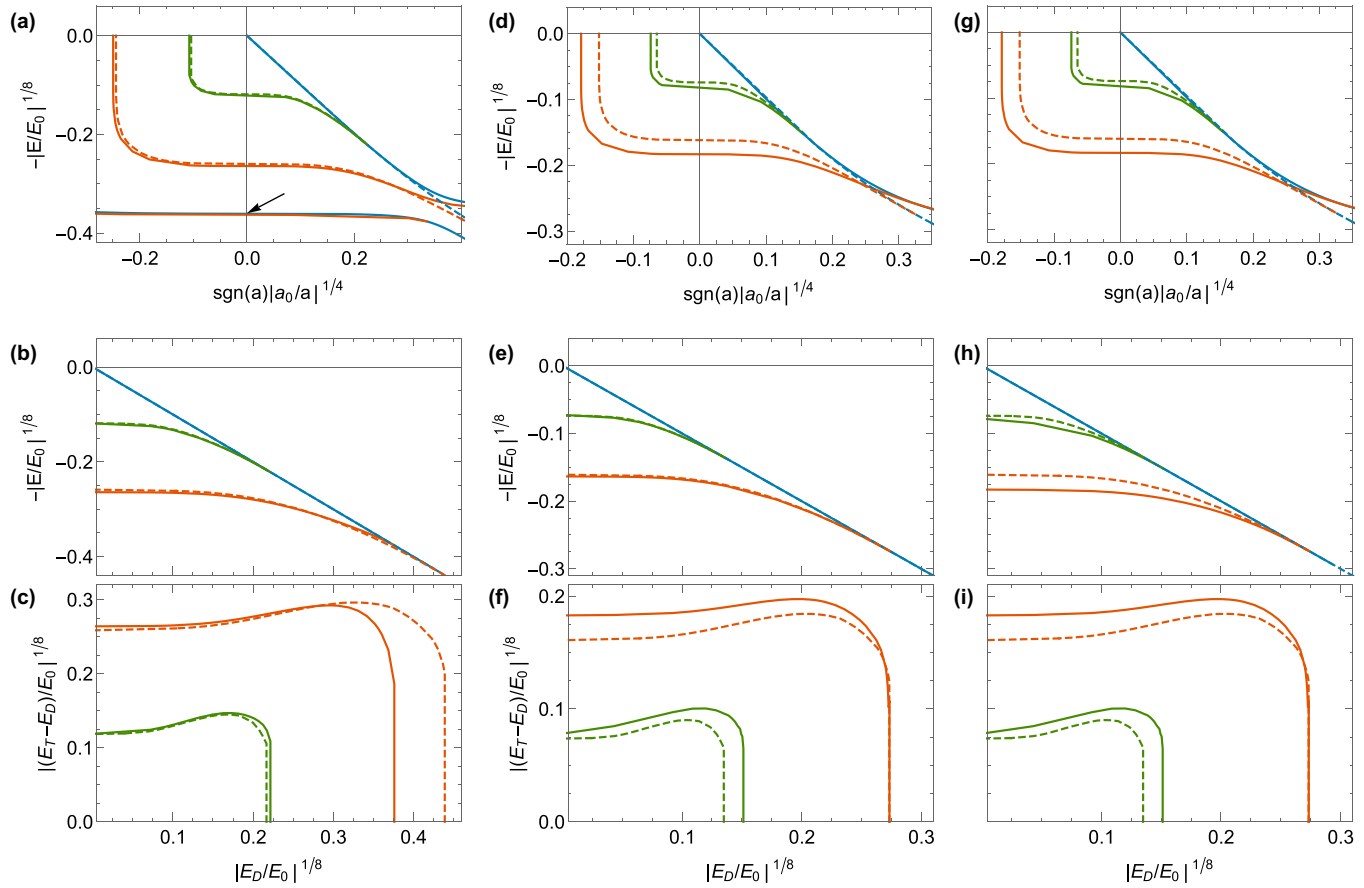

FIG. 3. Three-body sector. The dimer (blue, upper curve), ground-state trimer (orange, lower curve), and excited-state trimer (green, middle curve) are plotted as a function of (a), (d), (g) the inverse scattering length and, for $a > 0$, (b), (e), (h) the dimer binding energy. The difference between the trimer and the dimer is shown in panels (c), (f), (i). As in Fig. 2 the three columns correspond to the (a)–(c) NB, (d)–(f) NN, and (g)–(i) BN scenario. The three-channel model (solid curves) is compared with the two-channel model (dashed). The arrow in panel (a) indicates where the lower resonance $B_1^{(\mathrm{res})}$ is crossed.

Efimov state around $B_2^{(\mathrm{res})}$. They are plotted in Fig. 3 as a function of inverse scattering length and as a function of dimer binding energy. The three-channel model is compared with the solution obtained from an isolated resonance according to the two-channel model. We denote the scattering length value at which the nth trimer (starting from the ground state $n = 0$) crosses the free-atom continuum by $a_-^{(n)}$ and the value at which it merges with the dimer-atom continuum by $a_\star^{(n)}$. The corresponding magnetic-field values are denoted $B_-^{(n)}$ and $B_\star^{(n)}$, respectively. To put the extent of the Efimov spectrum in context, Fig. 2 highlights the region $B_\star^{(0)} < B < B_-^{(0)}$ for the three scenarios.

As in the two-body sector, the NN scenario is hardly affected by the additional molecule, demonstrating again that the three-channel model reduces to the two-channel model for large $B_2^{(\mathrm{res})} - B_1^{(\mathrm{res})}$ and small $\Delta_{1,2}$ [Figs. 3(d)–3(f)]. The three-channel trimers almost overlap with the two-channel trimers, although they are pushed to slightly deeper binding energies.

For smaller $B_2^{(\mathrm{res})} - B_1^{(\mathrm{res})}$ the overlap grows and the deepening effect increases. As a real-world example one may consider the *bb* channel of ^{39}K, which features two very close resonances ($B_2^{(\mathrm{res})} - B_1^{(\mathrm{res})} = 6.8$ G) of comparable widths. Indeed, the Δ parameters are within 10%–15% of $\Delta_1/a_0 = \Delta_2/a_0 = 150$ G while $B_2^{(\mathrm{res})} - B_1^{(\mathrm{res})}$ is a factor of ≈3 smaller than in our NN scenario. Experiments have shown deviations from the prediction of the two-channel model [16]. In fact, $a_-^{(0)}$ was found to be at a lower scattering-length value than predicted, in agreement with the general trend pointed out by the three-channel model. Using coupled-channels values for the experimentally relevant parameters [40] the three-channel model predicts $a_-^{(0)} \approx -6030a_0$. This corresponds to a shift of ≈8% with respect to the two-channel-model value $a_-^{(0)} \approx -6550a_0$. The reported experimental value is $a_-^{(0)} \approx -1000a_0$. A quantitative comparison to the experiment is, however, inconvenient since the measurements, as pointed out in Ref. [16], are accompanied by large uncertainties which arise mainly from the fact that the functional form of the experimental results disagree with the known theoretical models. Thus, the level of understanding of these results have yet to reach a level which would allow a meaningful comparison with the three-channel model.

In the NB scenario, the most striking difference is that the ground-state trimer extends from $B_-^{(0)} > B_2^{(\mathrm{res})}$ to $B_\star^{(0)} < B_1^{(\mathrm{res})}$ [see shaded region in Figs. 2(a)–2(c)], i.e., it merges with the atom-dimer continuum after passing through the scattering

length zero-crossing and the pole of the lower resonance. This is manifested by E_D and $E_T^{(0)}$ exiting the plot in Fig. 3(a) through $1/a \to \infty$, reentering from $1/a \to -\infty$, crossing $1/a = 0$ again due to the lower resonance [see arrow in Fig. 3(a)] to finally merge in the $a > 0$ region. Note that the Efimov trimer remains bound even though the scattering length vanishes. The two-channel model cannot possibly capture this effect due to the absence of the second molecular channel, even if one would include a nonzero background scattering length. In fact, the background scattering length induced by the second resonance obviously diverges at *its* pole. This strong magnetic-field dependence makes the extension of the two-channel model by any finite (constant) background scattering length ineffective. In addition, although the three-channel trimer is slightly more deeply bound than the two-channel trimer for most of the spectrum, as they approach $a_\star^{(0)}$ the two cross and the three-channel trimer merges at a larger scattering length [Figs. 3(b) and 3(c)]. The effect on the excited trimer is very similar to the NN scenario.

A real-world example for the NB scenario is the *bb* channel in ^{7}Li. It features two resonances with $R_1^\star = 722a_0$ ($s_{\mathrm{res},1} = 0.0411$), $R_2^\star = 60a_0$ ($s_{\mathrm{res},2} = 0.493$), and $B_2^{(\mathrm{res})} - B_1^{(\mathrm{res})} = 48.4$ G [9,41,42]. Indeed, the three-channel model is very good in the two-body sector. It reproduces the scattering length, effective range and dimer binding energies better than the individual two-channel-model treatments (see Appendix C). However, the three-body sector is unexpectedly dominated by finite-range corrections despite both resonances having $s_{\mathrm{res}} < 1$ [43]. The reason for this behavior is currently unknown and considered an open question in few-body physics [44,45]. This puzzle is beyond the reach of our simplified model, which neglects all van der Waals physics.

The trimer in the BN scenario is pushed to lower energies by an appreciable amount, as shown in Fig. 3(g). In particular, the Efimov resonance at $a_-^{(0)}$ is shifted from $R_\star/a_-^{(0)} = -0.092$ in the two-channel model [31] to $R_\star/a_-^{(0)} = -0.174$. This factor of ≈ 2 reduction in the absolute value of $a_-^{(0)}$ works in favor of the experimental demonstration of Efimov physics in the vicinity of narrow resonances, as it relaxes severe magnetic-field stability requirements necessary for experimental exploration of narrow Feshbach resonances [17]. On the $a > 0$ side one notes that $a_\star^{(0)}$ is unaltered but the excited state $a_\star^{(1)}$ is [see Figs. 3(h) and 3(i)]. In addition, away from $a_\star^{(n)}$ ($n = 0, 1$), both states are pushed to deeper binding energies and reach maximal deviation from the two-channel model at the resonance position where $E_D \to 0$. We note that, in this particular scenario, a two-channel model which includes a nonzero background scattering length would be in better agreement with the three-channel results. However, we expect the three-channel model to be superior because it naturally includes the magnetic-field dependence of the background scattering length. It also removes the unavoidable ambiguity of choosing a certain background scattering length in the improved two-channel model.

For the BN scenario we mention the *aa* channel of the heteronuclear ^{6}Li -Cs system as a real-world example. Its two resonances have $s_{\mathrm{res},1} = 0.66$ and $s_{\mathrm{res},2} = 0.05$ and their distance is $B_2^{(\mathrm{res})} - B_1^{(\mathrm{res})} = 49.9$ G. In fact, this is the only system to date where Efimov resonances near a truly narrow Feshbach resonance (i.e., for a resonance with $s_{\mathrm{res}} \ll 1$ as opposed to $s_{\mathrm{res}} \lesssim 1$) were measured [17]. The experimental value of $a_-^{(1)}$ associated with the $B_2^{(\mathrm{res})}$ trimers was found to be significantly lower than that predicted by two-channel theory. Quantitative analysis of this system with the three-channel model requires extension of the latter to the heteronuclear case.

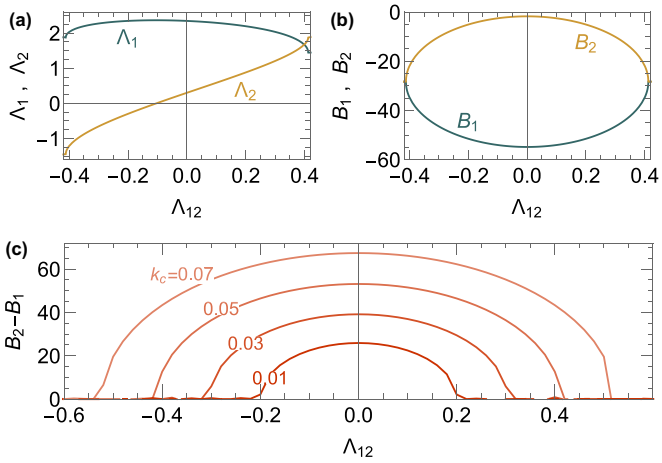

FIG. 4. Dependence of (a) $\tilde{\Lambda}_1$ and $\tilde{\Lambda}_2$ and of (b) B_1 and B_2 (with respect to $B_2^{(\mathrm{res})}$) on $\tilde{\Lambda}_{12}$ for fixed k_c and observable parameters. (c) Dependence of $B_2 - B_1$ on $\tilde{\Lambda}_{12}$ for various values of k_c as indicated (in units of $1/a_0$) and fixed observable parameters.

V. DISCUSSION OF FREE BARE PARAMETER

As mentioned in Sec. III C (see also Appendix B 2) there are four observable parameters, namely $\{B_1^{(\mathrm{res})}, B_2^{(\mathrm{res})}, \Delta_1, \Delta_2\}$, related to the five bare parameters $\{B_1, B_2, \tilde{\Lambda}_1, \tilde{\Lambda}_2, \tilde{\Lambda}_{12}\}$ of the model. Hence, one of the latter is free to choose. We emphasize though, that as long as the observable parameters are fixed and therefore constrain the bare parameters to change in a mutually dependent manner, all two- and three-body observables (such as scattering length and binding energies) remain the same.

For illustration, in what follows, we treat $\tilde{\Lambda}_{12}$ as the free parameter and fix the observable parameters to those of the BN scenario. The $\tilde{\Lambda}_{12}$ dependence of the other four bare parameters is shown in Figs. 4(a) and 4(b) for fixed cutoff $k_c = 0.05/a_0$. As $|\tilde{\Lambda}_{12}|$ increases, the bare resonance position difference $B_2 - B_1$ decreases towards 0. Beyond the point where $B_2 - B_1 = 0$, no solution exists for the analytic equations of Appendix B 2. Therefore, there is a maximal value $\tilde{\Lambda}_{12}^{\max}$ which the intermolecular coupling constant can assume.

Although $\tilde{\Lambda}_{12}$ may in principle be chosen anywhere in the range $-\tilde{\Lambda}_{12}^{\max} < \tilde{\Lambda}_{12} < \tilde{\Lambda}_{12}^{\max}$, additional physical inputs can constrain $\tilde{\Lambda}_{12}$. For example, the absolute position of B_1, B_2 or their relative position $B_2 - B_1$ introduces a fifth condition on the bare parameters. Alternatively, one may wish to maintain $|\tilde{\Lambda}_1| > |\tilde{\Lambda}_2|$, as is the case in the two-channel model. See, for example, the case of the *bb* channel of ^{7}Li considered in Appendix C.

Figure 4(c) shows the relative position $B_2 - B_1$ as a function of $\tilde{\Lambda}_{12}$ for various values of k_c. The value of $\tilde{\Lambda}_{12}^{\max}$ increases together with k_c and so does the range of B_1 and

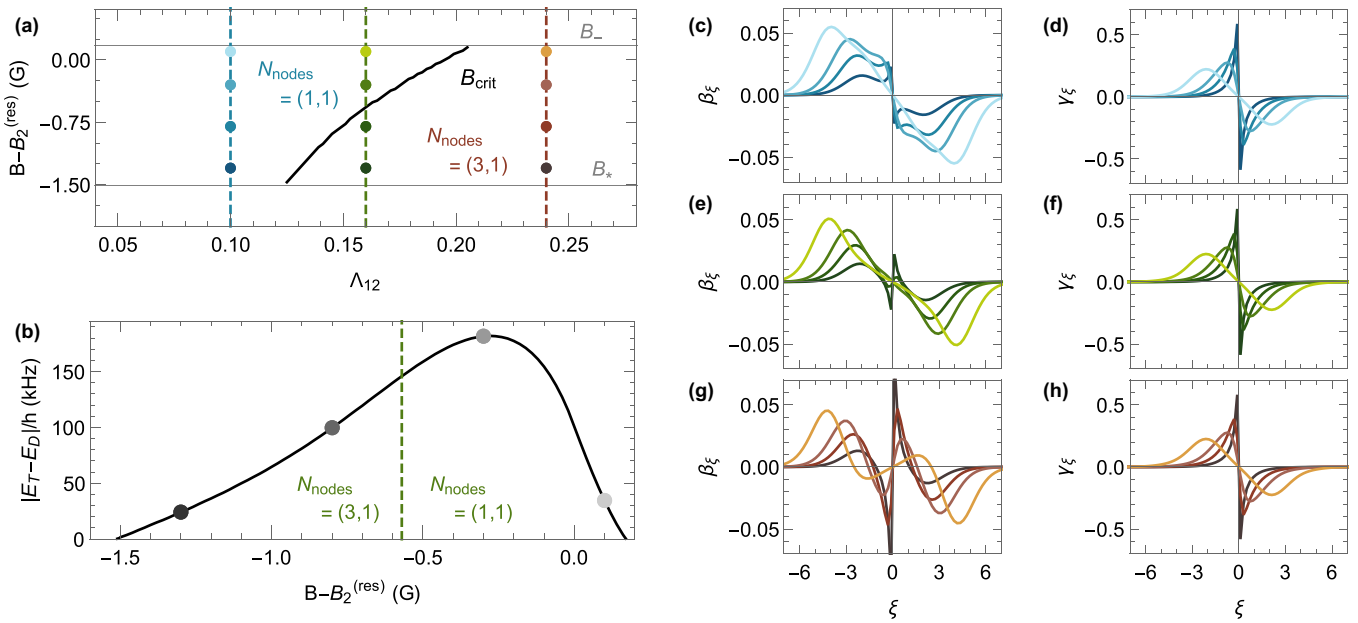

FIG. 5. (a) Nodal pattern of the BN scenario ground state. Above and to the left of the black line, which is given by Eq. (16), $\tilde{\beta}_\xi$ has one node such that $N_{\text{nodes}} = (1, 1)$. Below and to the right $N_{\text{nodes}} = (3, 1)$. (b) Plot of the ground state Efimov energy with respect to the dimer-atom (for $B < B_2^{(\text{res})}$) and free-atom (for $B > B_2^{(\text{res})}$) continuum. The dashed line indicates the transition from $N_{\text{nodes}} = (3, 1)$ to $(1, 1)$ in the case of $\tilde{\Lambda}_{12} = 0.16$. (c), (e), (g) Plot of $\tilde{\beta}_\xi$ and (d), (f), (h) of $\tilde{\gamma}_\xi$ for the three values of $\tilde{\Lambda}_{12}$ and the four values of B indicated by the points in panel (a). The points in panel (b) also indicate the values of B.

B_2. Physically, k_c should be chosen on the order of the inverse potential range, i.e., $k_c \sim 1/r_{vdW}$. Variations have no influence on the two- and three-body observables though. Also here, additional physical inputs of a real system may further constrain the value of k_c.

VI. TRIMER EIGENFUNCTIONS

The matrix $\mathcal{M}_{\lambda_T^{(\text{sol})}}(\xi, \xi')$, with $\lambda_T^{(\text{sol})}$ a solution of Eq. (14), has one vanishing eigenvalue in accordance with Eq. (11). We compute the corresponding eigenfunction $\psi_0(\xi)$ satisfying $\int d\xi' \mathcal{M}_{\lambda_T^{(\text{sol})}}(\xi, \xi')\psi_0(\xi') = 0$ and extract the amplitudes of $\psi_0(\xi) = (\tilde{\beta}_\xi, \tilde{\gamma}_\xi)^T$. Recall that the amplitudes that correspond to a physical bound state are odd functions of ξ (odd number of nodes), which implies that they vanish at $\xi = 0$. Solutions of Eq. (14) that lead to an even zero-eigenvalue eigenfunction are discarded on this basis.

For specificity, the following discussion focuses on the ground state of the BN scenario, whose binding energy is shown in Fig. 5(b), but the conclusions are general. The amplitudes $\tilde{\beta}_\xi$ and $\tilde{\gamma}_\xi$ for the three values $\tilde{\Lambda}_{12} = 0.1$, 0.16, and 0.24 are shown in Figs. 5(c) and 5(d), 5(e) and 5(f), and 5(g) and 5(h), respectively. While $\tilde{\gamma}_\xi$ is insusceptible and has a single node (at $\xi = 0$), the form of $\tilde{\beta}_\xi$, whose amplitude is an order of magnitude smaller, is sensitive to changes in $\tilde{\Lambda}_{12}$. Figures 5(c), 5(e), and 5(g) shows how the number of nodes changes from one to three as $\tilde{\Lambda}_{12}$ is increased. For certain values of $\tilde{\Lambda}_{12}$, see Figs. 5(b) and 5(e), the number of nodes depends on the position within the spectrum. There is a critical magnetic-field value B_{crit} above (below) which $\tilde{\beta}_\xi$ has one (three) nodes. Moreover, B_{crit} depends on $\tilde{\Lambda}_{12}$ and therefore gives rise to the nodal pattern represented in Fig. 5(a). For convenience we denote $N_{\text{nodes}} = (\text{number of nodes in } \tilde{\beta}_\xi, \text{ number of nodes in } \tilde{\gamma}_\xi)$ such that $N_{\text{nodes}} = (1, 1)$ to the left of the black curve and $N_{\text{nodes}} = (3, 1)$ to the right.

The number of nodes in a wave function is indicative of the excitedness of the state. For example, in the two-channel model (see Appendix A), since only odd wave functions are allowed, the nth state (starting at the ground state $n = 0$) has $2n + 1$ nodes. In the three-channel model, $\tilde{\gamma}_\xi$, which is the dominant molecule-atom amplitude for the $B_2^{(\text{res})}$ trimers, follows this rule. The secondary molecule-atom amplitude $\tilde{\beta}_\xi$, on the other hand, may have $2n + 1$ or $2(n + 1) + 1$ nodes, signifying it as being in the nth or $(n + 1)$st state. As we will show, this is the result of two competing processes whose amplitudes are proportional to Λ_1 and $\Lambda_{12}\Lambda_2$. This could serve as an experimental indicator for the value of Λ_{12}.

To find an equation for the $\tilde{\Lambda}_{12}$-dependent B_{crit} we consider the ratio $\chi_\xi = \tilde{\beta}_\xi/\tilde{\gamma}_\xi$. At $\xi = 0$, where both amplitudes have a node, χ_ξ remains finite. It vanishes only if $\tilde{\beta}_\xi$ has a node while $\tilde{\gamma}_\xi$ does not and is thus indicative of the excess number of nodes in $\tilde{\beta}_\xi$. Switching back to k via $k = (2/\sqrt{3})\lambda_T \sinh\xi$, the following expression for χ_k can be readily derived (see Appendix B 5):

$$\chi_k = \frac{\tilde{\Lambda}_1\left[\frac{3}{4}\tilde{k}^2 + \tilde{\lambda}_T^2 + \tilde{\mu}_2(B_2 - B)\right] - \tilde{\Lambda}_2\tilde{\Lambda}_{12}}{\tilde{\Lambda}_2\left[\frac{3}{4}\tilde{k}^2 + \tilde{\lambda}_T^2 + \tilde{\mu}_1(B_1 - B)\right] - \tilde{\Lambda}_1\tilde{\Lambda}_{12}}. \tag{15}$$

This function features one zero crossing for $\text{Re}\{k\} \geqslant 0$ (and another for $\text{Re}\{k\} \leqslant 0$) if

$$\Lambda_1 < \frac{\Lambda_2\Lambda_{12}}{|E_T| + E_{b,2}}, \tag{16}$$

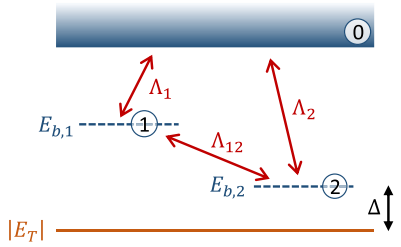

FIG. 6. Analogy of the three-channel model to a three-level system. The circled numbers are the quantum optics energy levels. Here, the two-photon detuning is $\Delta = |E_T| + E_{b,2}$.

and none otherwise. If Eq. (16) is satisfied, the eigenfunctions correspond to $N_{\text{nodes}} = (3, 1)$; if not, to (1, 1).

To give meaning to the inequality we rearrange the channels as depicted in Fig. 6 and draw the analogy to a three-level system in quantum optics. While the left-hand-side of Eq. (16) is analogous to the Rabi frequency for the direct (one-photon) transition from level 0 to 1, the right-hand side is the equivalent of the effective Rabi frequency for the indirect (two-photon) transition via level 2. Thus, the inequality states that the extra node in β_k (for $k > 0$) is the result of the indirect coupling strength surpassing the direct one.

For a given $\tilde{\Lambda}_{12}$, inequality (16) is solved for B_{crit} and displayed in Fig. 5(a). For the case $\tilde{\Lambda}_{12} = 0.16$ we find $B_{\text{crit}} - B_2^{(\text{res})} = -0.57$ G as indicated in Fig. 5(b).

VII. CONCLUSIONS

We have developed a simple three-channel theory of overlapping Feshbach resonances and show that the Efimov spectrum can be substantially altered in this scenario. Experimental observations that are in disaccord with the isolated resonance theory can be revisited with the three-channel model (e.g., ^{6}Li -Cs). Moreover, given the demanding requirements for measuring Efimov resonances in the vicinity of a truly narrow resonance, our treatment allows identification of the favorable structure of Feshbach resonances.

The model can be generalized to fermionic systems [29] and $\hat{H}_0$ can be extended to include background scattering, as was done for the two-channel model [35]. In addition to three-body bound states one may analyze low-energy atom-dimer and three-atom scattering [30,39] as well as four-body bound states associated with Efimov trimers [36]. Although cumbersome, one can speculate of an extension to N-channel theory for $N - 1 > 2$ overlapping Feshbach resonances to describe possible few-body states in even more complex scenarios.

ACKNOWLEDGMENTS

We acknowledge fruitful discussions with F. Chevy, J.P. D'Incao and P.S. Julienne. This research was supported in part by the Israel Science Foundation (Grant No. 1543/20) and by a grant from the United States-Israel Binational Science Foundation (BSF), Jerusalem, Israel, and the United States National Science Foundation.

APPENDIX A: REVIEW OF THE TWO-CHANNEL MODEL

Here the two-channel model is reiterated in a slightly different approach than usual. In particular, the momentum cutoff is used for renormalization purposes; see Eq. (A9) below. Following the introduction of the Hamiltonian we show that the model provides analytic expressions for all two-body observables. Thereafter, an integral equation for the three-body bound states is derived.

1. Two-channel Hamiltonian

We start from the Hamiltonian $\hat{H} = \hat{H}_0 + \hat{H}_{\text{int}}$, where

$$\hat{H}_0 = \int \frac{d^3k}{(2\pi)^3}\left[\frac{\hbar^2k^2}{2m}\hat{a}^\dagger_{\vec{k}}\hat{a}_{\vec{k}} + \left(E_b + \frac{\hbar^2k^2}{4m}\right)\hat{b}^\dagger_{\vec{k}}\hat{b}_{\vec{k}}\right] \tag{A1}$$

entails an open and a closed channel and

$$\hat{H}_{\text{int}} = \Lambda \int \frac{d^3k}{(2\pi)^3}\int \frac{d^3q}{(2\pi)^3}[\hat{b}^\dagger_{\vec{k}}\hat{a}_{\vec{q}+\frac{\vec{k}}{2}}\hat{a}_{-\vec{q}+\frac{\vec{k}}{2}} + \hat{a}^\dagger_{-\vec{q}+\frac{\vec{k}}{2}}\hat{a}^\dagger_{\vec{q}+\frac{\vec{k}}{2}}\hat{b}_{\vec{k}}] \tag{A2}$$

couples them with coupling constant Λ. Here, $\hat{a}_{\vec{k}}$ ($\hat{b}_{\vec{k}}$) annihilates an atom (a molecule) with momentum $\hbar\vec{k}$ and mass m ($2m$) in the open (closed) channel and $\hat{a}^\dagger_{\vec{k}}$ ($\hat{b}^\dagger_{\vec{k}}$) is its Hermitian conjugate. The bare molecular binding energy E_b is assumed to be an affine function of an externally applied magnetic field B: $E_b = \mu(B_0 - B)$, where μ is the molecules magnetic moment with respect to the open channel and B_0 is the bare resonance position. The free parameters of the system are thus Λ and B_0.

2. Two-body observables: Scattering length, effective range, and binding energy

To compute two-body observables, the following wave function is used in the Schrödinger equation $(\hat{H} - E)|\psi_{2B}\rangle$:

$$|\psi_{2B}\rangle = \beta\hat{b}^\dagger_{\vec{k}=0}|0\rangle + \int \frac{d^3k}{(2\pi)^3}\alpha_{\vec{k}}\hat{a}^\dagger_{\vec{k}}\hat{a}^\dagger_{-\vec{k}}|0\rangle. \tag{A3}$$

This center-of-mass superposition of two free atoms and one bare molecule is the most general wave function for a two-body system and therefore a suitable ansatz. The two coupled equations

$$\left(\frac{\hbar^2k^2}{m} - E\right)\alpha_{\vec{k}} + \Lambda\beta = 0, \tag{A4a}$$

$$(E_b - E)\beta + 2\Lambda\int \frac{d^3q}{(2\pi)^3}\alpha_{\vec{q}} = 0 \tag{A4b}$$

are obtained. Comparison of the open-channel coefficient $\alpha_{\vec{k}}$, as obtained from the first equation for $E = \hbar^2k_0^2/m > 0$, with the scattering Green's function

$$G_{\text{scat}}(k, k_0) = (2\pi)^3\delta(\vec{k} - \vec{k}_0) + \frac{4\pi f_{k_0}}{k^2 - k_0^2 - i\eta}, \tag{A5}$$

implies that the scattering amplitude is given via

$$f_{k_0} = -\frac{m\Lambda\beta}{4\pi\hbar^2}. \tag{A6}$$

Next, $\alpha_{\vec{k}}$ is plugged into the second equation and, exploiting the spherical symmetry of s-wave scattering $\alpha_{\vec{k}} = \alpha_k$, one finds an equation for the molecular amplitude β:

$$\left[\mu(B_0 - B) - \frac{\hbar^2 k_0^2}{m}\right]\beta + 2\Lambda - \frac{m\Lambda^2}{\pi^2\hbar^2}\left(k_c - \frac{i\pi}{2}k_0\right)\beta = 0. \tag{A7}$$

Here a high-momentum cutoff k_c was introduced during the computation of the radial integral to avoid a divergence. If instead of $E > 0$ one searches for a bound-state solution $E = -\hbar^2\lambda_D^2/m < 0$ (with $\lambda_D > 0$), the same procedure leads to

$$\left[\mu(B_0 - B) + \frac{\hbar^2\lambda_D^2}{m}\right] - \frac{m\Lambda^2}{\pi^2\hbar^2}\left(k_c - \lambda_D\frac{\pi}{2}\right) = 0, \tag{A8}$$

where β conveniently canceled. To get rid off the momentum cutoff we renormalize the model parameters according to

$$\tilde{\Lambda} = \frac{\Lambda k_c^{3/2}}{E_c}, \quad \tilde{\mu} = \frac{\mu}{E_c}, \quad \tilde{\beta} = \beta k_c^{3/2}, \tag{A9}$$

where $E_c = \hbar^2 k_c^2/m$. In addition, the scattering and binding wave numbers are renormalized as $\tilde{k}_0 = k_0/k_c$ and $\tilde{\lambda}_D = \lambda_D/k_c$. With this, Eqs. (A7) and (A8) become

$$\left(\tilde{\mu}(B_0 - B) - \tilde{k}_0^2\right)\tilde{\beta} + 2\tilde{\Lambda} - \frac{\tilde{\Lambda}^2}{\pi^2}\left(1 - \frac{i\pi}{2}\tilde{k}_0\right)\tilde{\beta} = 0, \tag{A10}$$

and

$$\left(\tilde{\mu}(B_0 - B) + \tilde{\lambda}_D^2\right) - \frac{\tilde{\Lambda}^2}{\pi^2}\left(1 - \tilde{\lambda}_D\frac{\pi}{2}\right) = 0, \tag{A11}$$

and the normalized scattering amplitude $\tilde{f}_{k_0} = k_c f_{k_0}$ is

$$\tilde{f}_{k_0} = \frac{\tilde{\Lambda}\tilde{\beta}}{4\pi}. \tag{A12}$$

By solving Eq. (A10) for $\tilde{\beta}$ and comparing $\tilde{f}_{\tilde{k}_0}$ to the known low-energy expansion

$$\frac{1}{\tilde{f}_{\tilde{k}_0}} = -\frac{1}{\tilde{a}} - i\tilde{k}_0 + \frac{\tilde{r}_e\tilde{k}_0^2}{2}, \tag{A13}$$

where $\tilde{a} = k_c a$ and $\tilde{r}_e = k_c r_e$ are the renormalized scattering length and effective range, respectively, one finds

$$\tilde{a} = -\frac{1}{2\pi}\frac{\tilde{\Lambda}^2}{\tilde{\mu}(B_0 - B) - \frac{\tilde{\Lambda}^2}{\pi^2}} \tag{A14}$$

and

$$\tilde{r}_e = -\frac{4\pi}{\tilde{\Lambda}^2}. \tag{A15}$$

We note that the effective range is field independent. By denoting

$$B_{\mathrm{res}} = B_0 - \frac{\tilde{\Lambda}^2}{\tilde{\mu}\pi^2}, \quad \tilde{\Delta} = \frac{\tilde{\Lambda}^2}{2\pi\tilde{\mu}}, \tag{A16}$$

the scattering length may be written in the familiar form

$$\tilde{a} = \frac{\tilde{\Delta}}{B - B_{\mathrm{res}}}. \tag{A17}$$

Here, Δ is defined with the opposite sign with respect to Eq. (9). We note that this expression, which is faithfully reproduced, is far more general than the two-channel model [9].

The expression for B_{res} demonstrates that the actual resonance position is shifted away from the bare resonance position B_0 by the coupling to the open channel. Furthermore, the expression for $\tilde{\Delta}$ shows that a narrow resonance arises from weakly coupled channels as eluded to in the introduction. From Eq. (A11) and the condition $\tilde{\lambda}_D > 0$ the dimer binding wave number is found to be

$$\tilde{\lambda}_D = \frac{\tilde{\mu}}{2}[\sqrt{\tilde{\Delta}^2 - 4(B - B_{\mathrm{res}})/\tilde{\mu}} - \tilde{\Delta}]. \tag{A18}$$

Using the solution for $\tilde{a}$ and $\tilde{R}^\star = -\tilde{r}_e/2$ the well-known narrow-resonance dimer formula

$$\lambda_D = \frac{\sqrt{1 + 4\frac{R^\star}{a}} - 1}{2R^\star} \tag{A19}$$

is obtained. Also this equation is far more general than the simple two-channel model. Finally we note the connection

$$\Delta = \frac{\hbar^2}{m\mu R^\star} \tag{A20}$$

between the resonance width $\Delta = \tilde{\Delta}/k_c$ and $R^\star$. This equation illustrates that a narrow resonance is related to a large $R^\star$.

We have shown that the bare parameters Λ and B_0 are directly connected to two-body observables such as the scattering length, effective range and dimer binding energy. For a given atomic species and scattering channel one must fix the bare parameters such that the observables are reproduced as well as possible. Incidentally, the set (Λ, B_0) is fully determined by $(R^\star, B_{\mathrm{res}})$ or $(\Delta, B_{\mathrm{res}})$.

3. Three-body sector: Efimov trimers

Having fixed the bare parameters in the two-body sector we move on to the three-body sector with no more adjustable parameters. To find the binding energy of Efimov trimers we search for a negative-energy solution $E = -\hbar^2\lambda_T^2/m$, where $\lambda_T > \max(0, \lambda_D)$, of the Schrödinger equation $(\hat{H} - E)|\psi_{3B}\rangle$ with

$$|\psi_{3B}\rangle = \int \frac{d^3k}{(2\pi)^3}\beta_{\vec{k}}\hat{b}_{\vec{k}}^\dagger\hat{a}_{-\vec{k}}^\dagger|0\rangle + \int \frac{d^3k}{(2\pi)^3}\int \frac{d^3q}{(2\pi)^3}\alpha_{\vec{k},\vec{q}}\hat{a}_{\vec{q}+\frac{\vec{k}}{2}}^\dagger\hat{a}_{-\vec{q}+\frac{\vec{k}}{2}}^\dagger\hat{a}_{-\vec{k}}^\dagger|0\rangle. \tag{A21}$$

Also, here we work in the center-of-mass frame and have chosen $\vec{k}$ and $\vec{q}$ to be a set of Jacobi momenta. The Schrödinger equation leads to the coupled equations

$$\left(\frac{\hbar^2 q^2}{m} + \frac{3}{4}\frac{\hbar^2 k^2}{m} - E\right)\alpha_{\vec{k},\vec{q}} + \Lambda\beta_{\vec{k}} = 0, \tag{A22}$$

$$\left(\frac{3}{4}\frac{\hbar^2 k^2}{m} + E_b - E\right)\beta_{\vec{k}} + 2\Lambda\int \frac{d^3q}{(2\pi)^3}\left(\alpha_{\vec{k},\vec{q}} + 2\alpha_{\vec{q}-\frac{\vec{k}}{2},-\vec{q}-\frac{3\vec{k}}{4}}\right) = 0. \tag{A23}$$

One eliminates $\alpha_{\vec{k},\vec{q}}$ from the first and plugs it into the second, upon which the first integral is computed by introducing a momentum cutoff k_c as in the two-body sector. After renormalizing with respect to k_c, the expressions for $\tilde{a}$ and $\tilde{R}^\star$ are

substituted and one obtains

$$\left[\sqrt{\frac{3k^2}{4}+\lambda_T^2}-\frac{1}{a}+R^\star\left(\frac{3k^2}{4}+\lambda_T^2\right)\right]\psi(k) - \frac{2}{\pi}\int_0^\infty dq\ln\left(\frac{k^2+kq+q^2+\lambda_T^2}{k^2-kq+q^2+\lambda_T^2}\right)\psi(q)=0, \quad \text{(A24)}$$

where $\psi(k)=k\beta_k$ and all factors of k_c have canceled. We have eliminated the magnetic-field dependence (via the substitution of a) and can directly compute the scattering length dependence of λ_T. We stress that the parameter $R^\star=-r_e/2$ was fixed in the two-body sector [see Eq. (A15)]. To solve Eq. (A24) we first switch variables via

$$k=\frac{2}{\sqrt{3}}\lambda_T\sinh(\xi), \quad q=\frac{2}{\sqrt{3}}\lambda_T\sinh(\xi'), \quad \text{(A25)}$$

and rescale $\psi(k)\to\psi(k)/\cosh(\xi)$. If we limit ourselves to odd solutions $\psi(k)$, the lower integration limit may be extended to $-\infty$ provided we divide the entire integral by two. One obtains

$$\left[1-\frac{1}{a\lambda_T\cosh\xi}+R^\star\lambda_T\cosh\xi\right]\psi(\xi) - \frac{4}{\sqrt{3}\pi}\int_{-\infty}^\infty d\xi'\ln\left(\frac{e^{2(\xi-\xi')}+e^{\xi-\xi'}+1}{e^{2(\xi-\xi')}-e^{\xi-\xi'}+1}\right)\psi(\xi')=0. \quad \text{(A26)}$$

By introducing $\int d\xi'\delta(\xi-\xi')$ in the first term it is included into the integral. One finally finds

$$\int_{-\infty}^\infty d\xi'\mathcal{M}_{\lambda_T}(\xi,\xi')\psi(\xi')=0, \quad \text{(A27)}$$

with $\psi(\xi)$ an odd function of ξ and

$$\mathcal{M}_{\lambda_T}(\xi,\xi')=\delta(\xi-\xi')\left[1-\frac{1}{a\lambda_T\cosh\xi'}+R^\star\lambda_T\cosh\xi'\right] - \frac{4}{\sqrt{3}\pi}\ln\left(\frac{e^{2(\xi-\xi')}+e^{\xi-\xi'}+1}{e^{2(\xi-\xi')}-e^{\xi-\xi'}+1}\right). \quad \text{(A28)}$$

A nontrivial solution is obtained for $\det\mathcal{M}_{\lambda_T}(\xi,\xi')=0$ which constitutes a closed equation for λ_T and can be solved numerically by discretizing ξ and ξ'. One searches for the value $\lambda_T=\lambda_T^{(\mathrm{sol})}$ for which $\det\mathcal{M}_{\lambda_T}(\xi,\xi')$ changes sign as λ_T is varied through $\lambda_T^{(\mathrm{sol})}$. Note that many solutions $\lambda_T^{(\mathrm{sol})}$ exist for a given a and $R^\star$. To verify one solution, the obtained value $\lambda_T^{(\mathrm{sol})}$ is plugged back into $\mathcal{M}_{\lambda_T=\lambda_T^{(\mathrm{sol})}}(\xi,\xi')$ and its eigenvalues and eigenfunctions $\psi(\xi)$ are computed. One of the eigenvalues must be equal to zero (within machine precision) and its associated eigenfunction must be odd (odd number of nodes). The value of $\lambda_T^{(\mathrm{sol})}$ for which $\psi(\xi)$ has one node is the ground state. If $\psi(\xi)$ has three nodes it is the first-excited state and so on. This formalism was used to produce the dashed curves in Fig. 3.

APPENDIX B: DETAILS OF THE DERIVATION OF THE THREE-CHANNEL MODEL

1. Two-body sector

After plugging the two-body wave function (5) into the Schrödinger equation one obtains the following system of coupled equations:

$$\left(\frac{\hbar^2k^2}{m}-E\right)\alpha_{\vec{k}}+\Lambda_1\beta+\Lambda_2\gamma=0, \quad \text{(B1a)}$$

$$(E_{b,1}-E)\beta+2\Lambda_1\int\frac{d^3q}{(2\pi)^3}\alpha_{\vec{q}}+\Lambda_{12}\gamma=0, \quad \text{(B1b)}$$

$$(E_{b,2}-E)\gamma+2\Lambda_2\int\frac{d^3q}{(2\pi)^3}\alpha_{\vec{q}}+\Lambda_{12}\beta=0. \quad \text{(B1c)}$$

From the expression for $\alpha_{\vec{k}}$ as determined from the first equation with $E=\hbar^2k_0^2/m$ and the scattering problem's Green's function [Eq. (A5)], one finds the scattering amplitude to be

$$f_{k_0}=-\frac{m}{4\pi\hbar^2}(\Lambda_1\beta+\Lambda_2\gamma). \quad \text{(B2)}$$

Then, by plugging $\alpha_{\vec{k}}$ into the second and third equation one obtains Eqs. (6) for $E=\hbar^2k_0^2/m>0$, and Eqs. (8) for $E=\hbar^2\lambda_D^2/m<0$. When solving the integrals in the second and third equation of (B1) one must introduce a high momentum cutoff k_c to prevent the divergence with respect to which the various parameters, amplitudes, and variables are renormalized. Note that Eqs. (6) and (8) are the analog of Eqs. (A10) and (A11) in the two-channel model.

2. Relating the bare parameters to observable parameters

In terms of the bare parameters, the observable parameters are given via

$$\tilde{\Delta}_1=-\frac{L_s^2}{4\pi}+\frac{L_d^2(B_1-B_2)+L_p^4}{4\pi R_1}, \quad \text{(B3a)}$$

$$\tilde{\Delta}_2=-\frac{L_s^2}{4\pi}-\frac{L_d^2(B_1-B_2)+L_p^4}{4\pi R_1}, \quad \text{(B3b)}$$

$$B_1^{(\mathrm{res})}=\frac{B_1+B_2}{2}-\frac{L_s^2}{2\pi^2}-\frac{R_2}{2\pi^2}, \quad \text{(B3c)}$$

$$B_2^{(\mathrm{res})}=\frac{B_1+B_2}{2}-\frac{L_s^2}{2\pi^2}+\frac{R_2}{2\pi^2}, \quad \text{(B3d)}$$

where we have defined

$$R_1=\left\{2(L_1L_2-2\pi^2L_{12})^2+2L_1^2L_2^2-4\pi^4L_{12}^2+\left[\pi^2(B_1-B_2)-\left(L_1^2-L_2^2\right)\right]^2\right\}^{1/2}, \quad \text{(B4a)}$$

$$R_2=\left\{4\pi^4L_{12}^2-8\pi^2L_1L_2L_{12}+L_s^4-2L_d^2(B_1-B_2)+\pi^4(B_1-B_2)^2\right\}^{1/2} \quad \text{(B4b)}$$

as well as $L_s^2=L_1^2+L_2^2$, $L_d^2=\pi^2(L_1^2-L_2^2)$, and $L_p^4=4\pi^2L_1L_2L_{12}-2L_1^2L_2^2-L_1^4-L_2^4$. The L parameters correspond to the Λ parameters scaled by the magnetic moment, so $L_1=\tilde{\Lambda}_1/\sqrt{\tilde{\mu}_1}$, $L_2=\tilde{\Lambda}_2/\sqrt{\tilde{\mu}_2}$, and $L_{12}=\tilde{\Lambda}_{12}/\sqrt{\tilde{\mu}_1\tilde{\mu}_2}$.

Note that the functions produce $\tilde{\Delta}_1$ and $\tilde{\Delta}_2$ which are related to Δ_1 and Δ_2 in Table I via $\tilde{\Delta}_1/k_c=\Delta_1$ and $\tilde{\Delta}_2/k_c=\Delta_2$, respectively. Hence, k_c must be fixed before solving the equations for the bare parameters.

3. Relation of Eq. (9) to Eq. (26) in Ref. [9]

For the case of two resonances and vanishing background scattering, Eq. (26) of Ref. [9] can be written as

$$a(B) = \frac{\Delta_1(B_2 - B) + \Delta_2(B_1 + B)}{(B_1 - B)(B_2 - B) + (B_1 - B)\delta B_2 + (B_2 - B)\delta B_1}. \tag{B5}$$

To obtain this form one must take $a_{bg} \to 0$ and $\Delta_1 \to \infty$, $\Delta_2 \to \infty$ while keeping their product (which we call Δ_1 and Δ_2, respectively) finite. Furthermore, our expression for the scattering length can be written in the form

$$a(B) = \frac{-\frac{L_1^2}{2\pi}(B_2 - B) - \frac{L_2^2}{2\pi}(B_1 - B) + \frac{L_1 L_2 L_{12}^4}{\pi}}{(B_1 - B)(B_2 - B) - \frac{L_2^2}{\pi^2}(B_1 - B) - \frac{L_1^2}{\pi^2}(B_2 - B) + 2\frac{L_1 L_2 L_{12}}{\pi^2} - L_{12}^2}. \tag{B6}$$

For $L_{12} = 0$ one recognizes the same combinations of $(B_i - B)$ in the two expressions. Our model is thus consistent with the previously used framework of multichannel quantum-defect theory. Note that the apparent connection between Δ_i and δB_i suggested by comparison of the two equations does not exist in Ref. [9]. This is due to the presence of the van der Waals potential in Ref. [9]; see Eq. (22) there.

4. Three-body sector

From the Schrödinger equation $(\hat{H} - E_T)|\psi_{3B}\rangle = 0$, where $|\psi_{3B}\rangle$ is given in Eq. (10), one obtains three coupled integral equations:

$$\left(\frac{\hbar^2 q^2}{m} + \frac{3}{4}\frac{\hbar^2 k^2}{m} - E_T\right)\alpha_{\vec{k},\vec{q}} + \Lambda_1 \beta_{\vec{k}} + \Lambda_2 \gamma_{\vec{k}} = 0, \tag{B7a}$$

$$\left(\frac{3}{4}\frac{\hbar^2 k^2}{m} + E_{b,1} - E_T\right)\beta_{\vec{k}} + \Lambda_{12}\gamma_{\vec{k}} + 2\Lambda_1 \int \frac{d^3 q}{(2\pi)^3}\left[\alpha_{\vec{k},\vec{q}} + 2\alpha_{\vec{q}-\frac{\vec{k}}{2},-\frac{\vec{q}}{2}-\frac{3\vec{k}}{4}}\right] = 0, \tag{B7b}$$

$$\left(\frac{3}{4}\frac{\hbar^2 k^2}{m} + E_{b,2} - E_T\right)\gamma_{\vec{k}} + \Lambda_{12}\beta_{\vec{k}} + 2\Lambda_2 \int \frac{d^3 q}{(2\pi)^3}\left[\alpha_{\vec{k},\vec{q}} + 2\alpha_{\vec{q}-\frac{\vec{k}}{2},-\frac{\vec{q}}{2}-\frac{3\vec{k}}{4}}\right] = 0. \tag{B7c}$$

The free-particle amplitude $\alpha_{\vec{k},\vec{q}}$ is eliminated from the first equation and plugged into the second and third equations. The first of the two integrals can be solved as in the two-body sector by introducing a high-momentum cutoff k_c with which the coupling constants are renormalized according to $\tilde{\Lambda}_1 = \Lambda_1 k_c^{3/2}/E_c$, $\tilde{\Lambda}_2 = \Lambda_2 k_c^{3/2}/E_c$, and $\tilde{\Lambda}_{12} = \Lambda_{12}, E_c$, and the amplitudes according to $\tilde{\beta} = \beta k_c^{3/2}$ and $\tilde{\gamma} = \gamma k_c^{3/2}$. The renormalized magnetic moment is $\tilde{\mu}_i = \mu_i/E_c$ and all momenta are $\tilde{k} = k/k_c$. In addition one uses the s-wave property that $\beta_{\vec{k}} = \beta_k$ and $\gamma_{\vec{k}} = \gamma_k$ are spherically symmetric. The equations are then

$$\begin{aligned} 0 = &\left(\frac{3}{4}\tilde{k}^2 + \tilde{\lambda}_T^2 + \tilde{\mu}_1(B_1 - B)\right)\tilde{\beta}_k + \tilde{\Lambda}_{12}\tilde{\gamma}_k - \frac{\tilde{\Lambda}_1}{\pi^2}\left(1 - \frac{\pi}{2}\sqrt{\frac{3}{4}\tilde{k}^2 + \tilde{\lambda}_T^2}\right)(\tilde{\Lambda}_1\tilde{\beta}_k + \tilde{\Lambda}_2\tilde{\gamma}_k) \\ &- \frac{\tilde{\Lambda}_1}{\pi^2}\int_0^\infty d\tilde{q}\,\frac{\tilde{q}}{\tilde{k}}\ln\left(\frac{\tilde{q}^2 + \tilde{q}\tilde{k} + \tilde{k}^2 + \tilde{\lambda}_T^2}{\tilde{q}^2 - \tilde{q}\tilde{k} + \tilde{k}^2 + \tilde{\lambda}_T^2}\right)(\tilde{\Lambda}_1\tilde{\beta}_q + \tilde{\Lambda}_2\tilde{\gamma}_q), \end{aligned} \tag{B8a}$$

$$\begin{aligned} 0 = &\left(\frac{3}{4}\tilde{k}^2 + \tilde{\lambda}_T^2 + \tilde{\mu}_2(B_2 - B)\right)\tilde{\gamma}_k + \tilde{\Lambda}_{12}\tilde{\beta}_k - \frac{\tilde{\Lambda}_2}{\pi^2}\left(1 - \frac{\pi}{2}\sqrt{\frac{3}{4}\tilde{k}^2 + \tilde{\lambda}_T^2}\right)(\tilde{\Lambda}_1\tilde{\beta}_k + \tilde{\Lambda}_2\tilde{\gamma}_k) \\ &- \frac{\tilde{\Lambda}_2}{\pi^2}\int_0^\infty d\tilde{q}\,\frac{\tilde{q}}{\tilde{k}}\ln\left(\frac{\tilde{q}^2 + \tilde{q}\tilde{k} + \tilde{k}^2 + \tilde{\lambda}_T^2}{\tilde{q}^2 - \tilde{q}\tilde{k} + \tilde{k}^2 + \tilde{\lambda}_T^2}\right)(\tilde{\Lambda}_1\tilde{\beta}_q + \tilde{\Lambda}_2\tilde{\gamma}_q). \end{aligned} \tag{B8b}$$

From here one proceeds equivalent to the two-channel model. The amplitudes are rescaled according to $\tilde{\beta}_k \to \tilde{\beta}_k/\tilde{k}$ and $\tilde{\gamma}_k \to \tilde{\gamma}_k/\tilde{k}$. We then switch from $(\tilde{k}, \tilde{q})$ to (ξ, ξ') using Eq. (A25) and rescale once more according to $\tilde{\beta}_\xi \to \tilde{\beta}_\xi/\cosh\xi$ and $\tilde{\gamma}_\xi \to \tilde{\gamma}_\xi/\cosh\xi$. Finally, the lower integration limit is extended to $-\infty$ and the integral divided by two. The amplitudes must thus be odd functions of ξ. One obtains

$$\int_{-\infty}^{\infty} d\xi'\left[\left\{F_1(\xi')\delta(\xi - \xi') - \tilde{\Lambda}_1^2 L(\xi, \xi')\right\}\tilde{\beta}_{\xi'} + \left\{H(\xi')\delta(\xi - \xi') - \tilde{\Lambda}_1\tilde{\Lambda}_2 L(\xi, \xi')\right\}\tilde{\gamma}_{\xi'}\right] = 0, \tag{B9a}$$

$$\int_{-\infty}^{\infty} d\xi'\left[\left\{H(\xi')\delta(\xi - \xi') - \tilde{\Lambda}_1\tilde{\Lambda}_2 L(\xi, \xi')\right\}\tilde{\beta}_{\xi'} + \left\{F_2(\xi')\delta(\xi - \xi') - \tilde{\Lambda}_2^2 L(\xi, \xi')\right\}\tilde{\gamma}_{\xi'}\right] = 0, \tag{B9b}$$

where

$$\begin{aligned} F_i(\xi) &= f_i(\xi) - \tilde{\Lambda}_i^2 g(\xi), \\ H(\xi) &= h(\xi) - \tilde{\Lambda}_1\tilde{\Lambda}_2 g(\xi). \end{aligned} \tag{B10a}$$

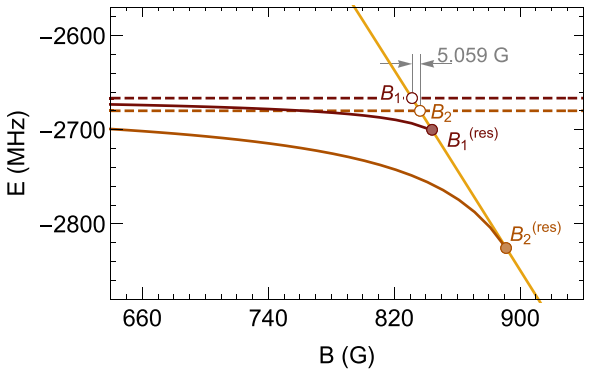

FIG. 7. Magnetic-field dependence of the three relevant channels as obtained from coupled-channels calculations. The free atoms (yellow) experience a linear Zeeman shift. The bare molecules (dashed light and dark brown) are spin singlets and thus are magnetic-field independent. The interaction terms of the three-channel model give rise to the physical dimers (solid light and dark brown).

As discussed in the main text, these two coupled integral equations can be written in matrix form and the condition of vanishing determinant gives a closed equation for λ_T. To solve Eq. (14), each block $\mathcal{M}_{ij}$ is written as a $n \times n$ matrix by discretizing ξ and ξ' in the interval $[-\xi_m, \xi_m]$ and step size $d\xi = 2\xi_m/(n-1)$. The total matrix thus has dimensions $2n \times 2n$ and its determinant is found numerically. In Fig. 3, we used $\xi_m = 10.02$ (to avoid the singularity at $\xi = 0$) and $n = 50$.

5. Equation for eigenfunction ratio

The first and second equations of (B8) are multiplied by $\tilde{\Lambda}_2$ and $\tilde{\Lambda}_1$, respectively. Subtracting the second from the first then gives

$$\left[\tilde{\Lambda}_2\left(\frac{3}{4}\tilde{k}^2 + \tilde{\lambda}_T^2 + \tilde{\mu}_1(B_1 - B)\right) - \tilde{\Lambda}_1\tilde{\Lambda}_{12}\right]\tilde{\beta}_k$$
$$= \left[\tilde{\Lambda}_1\left(\frac{3}{4}\tilde{k}^2 + \tilde{\lambda}_T^2 + \tilde{\mu}_2(B_2 - B)\right) - \tilde{\Lambda}_2\tilde{\Lambda}_{12}\right]\tilde{\gamma}_k, \quad \text{(B11)}$$

which leads directly to expression (15) for the ratio $\chi_k = \tilde{\beta}_k/\tilde{\gamma}_k$. Looking for zero crossings at positive k, so $\chi_k = 0$ for $k \geqslant 0$, leads to condition (16).

APPENDIX C: TWO-BODY SECTOR OF THE *bb*-CHANNEL OF ^{7}Li

Here the two-body sector equations of the three-channel model are applied to the *bb*-channel of ^{7}Li. Figure 7 shows coupled-channels calculations of the relevant energy levels (channels). Both bare molecular states are spin singlets and therefore have no magnetic moment, i.e., they are magnetic-field independent. Since the two resonances occur at high magnetic field, the Zeeman shift is linear in the region of interest. The two free atoms are essentially a spin triplet and have a combined magnetic moment of $\mu = -2.66$ MHz/G, which is close to $-2\mu_B$ of a full triplet, where $\mu_B = 1.4$ MHz/G is the Bohr magneton.

We note that the coupled-channels data shown in Fig. 7 illustrate the ingredients and phenomenology of the three-channel model. The two closed channels of $\hat{H}_0$ (straight dashed lines) intersect the open channel (straight yellow line) with relative slope $\mu = \mu_1 = \mu_2$ at the bare resonance positions B_i. The energy differences between the two dashed and the yellow solid line are the bare binding energies $E_{b,i}$ and are negative for $B < B_i$. The atom-molecule couplings $\hat{H}_i$ and the intermolecular coupling $\hat{H}_{12}$ shift the actual resonance position to lower energies and higher magnetic fields and alter the dimer binding energy, as illustrated.

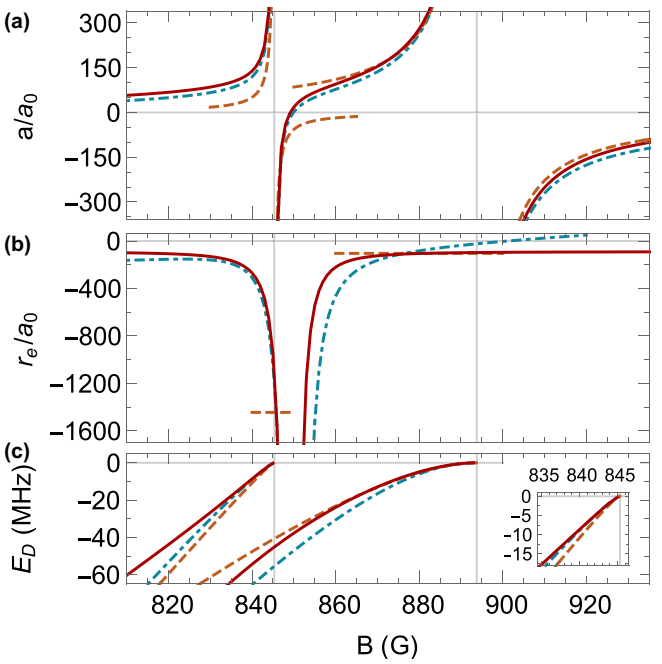

FIG. 8. The (a) scattering length, (b) effective range, and (c) dimer binding energy of the *bb*-channel in ^{7}Li as obtained from the three-channel model are compared with the exact coupled-channels result and the individual two-channel model treatments.

We go through the following three steps to fix the bare parameters. (1) Fitting Eq. (9) to coupled-channels data of the scattering length gives $(B_1^{(\mathrm{res})}, B_2^{(\mathrm{res})}) = (845.3, 893.7)$ G, which are in perfect agreement with the coupled-channels resonance positions, and $(\Delta_1, \Delta_2)/a_0 = (342.37, 3996.93)$ G. (2) To approximately satisfy $k_c \sim 1/r_{vdW}$ we choose $k_c = 1/(60a_0)$. (3) Using $B_2 - B_1 = 5.029$ G (Fig. 7) as the additional constraint (as suggested in Sec. V) and the analytic expressions from Appendix B 2 we find $(\tilde{\Lambda}_1, \tilde{\Lambda}_2, \tilde{\Lambda}_{12}) = (0.561, 2.849, 0.243)$ and $(B_1, B_2) = (844, 849.1)$ G.

The computed scattering length, effective range, and dimer binding energy are shown in Fig. 8. The coupled-channels scattering length is consistently below the three-channel result. This is to be expected since the coupled-channels calculation includes background scattering in the open channel and the shift agrees with its magnitude $a_{bg} = -18.42a_0$. The two-channel model captures the scattering length only in a small window around the resonance positions which is by-far narrower than the resonance widths ΔB. Moreover, since both resonances are treated individually, it is not capable of reproducing the zero crossing. The fact that the three-channel model *does* capture the zero crossing can be appreciated by looking at the effective range. In Fig. 8(b) the effective range

is seen to diverge at the scattering length zero crossing for both the coupled-channels and three-channel calculations. According to the two-channel model, however, the effective range is magnetic-field independent and agrees with the three-channel model only at the resonance positions. The difference of the coupled-channels effective range at the higher resonance is due to van der Waals physics [46,47] not taken into account by either of the models. Finally, Fig. 8(c) and its inset show also that the dimer binding energy is captured better by an overlapping resonance theory then by an individual treatment, especially in the shallow-binding regime. At larger binding energy the intermolecular coupling manifests itself as level repulsion. However, as discussed in Sec. V, the level repulsion is not related to the numerical value assigned to $\tilde{\Lambda}_{12}$—which here was constrained by $B_2 - B_1 = 5.029$ G—but to the intrinsic cross talk of the two dimers.

[1] C. H. Greene, P. Giannakeas, and J. Pérez-Ríos, Universal few-body physics and cluster formation, Rev. Mod. Phys. **89**, 035006 (2017).

[2] P. Naidon and S. Endo, Efimov physics: A review, Rep. Prog. Phys. **80**, 056001 (2017).

[3] J. P. D'Incao, Few-body physics in resonantly interacting ultracold quantum gases, J. Phys. B: At. Mol. Opt. Phys. **51**, 043001 (2018).

[4] C. Chin, R. Grimm, P. Julienne, and E. Tiesinga, Feshbach resonances in ultracold gases, Rev. Mod. Phys. **82**, 1225 (2010).

[5] The meaning of "broad" and "narrow" in the classification of Feshbach resonances refers to the value of $s_{\rm res}$. It is not equivalent to the parameter ΔB in $a = a_{bg}[1 - \Delta B/(B - B_0)]$ which is usually termed "resonance width" and signifies the distance (in units of magnetic field) between the resonance position B_0 and the zero crossing. The $s_{\rm res}$ parameter is more general; in addition to ΔB it also depends on a_{bg} whose value determines the position of the zero crossing. In fact, up to numerical coefficients on the order of unity and factors of $\hbar$ and mass, $s_{\rm res}$ is proportional to $a_{bg} r_{vdW} \mu \Delta B$ [4].

[6] H. Yang, D.-C. Zhang, L. Liu, Y.-X. Liu, J. Nan, B. Zhao, and J.-W. Pan, Observation of magnetically tunable Feshbach resonances in ultracold ^{23}N ^{40}K + ^{40}K collisions, Science **363**, 261 (2019).

[7] A. Frisch, M. Mark, K. Aikawa, F. Ferlaino, J. L. Bohn, C. Makrides, A. Petrov, and S. Kotochigova, Quantum chaos in ultracold collisions of gas-phase erbium atoms, Nature (London) **507**, 475 (2014).

[8] A. D. Lange, K. Pilch, A. Prantner, F. Ferlaino, B. Engeser, H.-C. Nägerl, R. Grimm, and C. Chin, Determination of atomic scattering lengths from measurements of molecular binding energies near Feshbach resonances, Phys. Rev. A **79**, 013622 (2009).

[9] K. Jachymski and P. S. Julienne, Analytical model of overlapping Feshbach resonances, Phys. Rev. A **88**, 052701 (2013).

[10] N. P. Mehta, K. R. A. Hazzard, and C. Ticknor, Model for scattering with proliferating resonances: Many coupled square wells, Phys. Rev. A **98**, 062703 (2018).

[11] V. Efimov, Energy levels arising from resonant two-body forces in a three-body system, Phys. Lett. B **33**, 563 (1970).

[12] N. Gross, Z. Shotan, S. J. J. M. F. Kokkelmans, and L. Khaykovich, Observation of Universality in Ultracold ^{7}Li Three-Body Recombination, Phys. Rev. Lett. **103**, 163202 (2009).

[13] M. Berninger, A. Zenesini, B. Huang, W. Harm, H. C. Nägerl, F. Ferlaino, R. Grimm, P. Julienne, and J. Hutson, Universality of the Three-Body Parameter for Efimov States in Ultracold Cesium, Phys. Rev. Lett. **107**, 120401 (2011).

[14] S.-K. Tung, K. Jiménez-García, J. Johansen, C. Parker, and C. Chin, Geometric Scaling of Efimov States in a ^{6}Li - ^{133}Cs Mixture, Phys. Rev. Lett. **113**, 240402 (2014).

[15] R. Pires, J. Ulmanis, S. Häfner, M. Repp, A. Arias, E. D. Kuhnle, and M. Weidemüller, Observation of Efimov Resonances in A Mixture with Extreme Mass Imbalance, Phys. Rev. Lett. **112**, 250404 (2014).

[16] S. Roy, M. Landini, A. Trenkwalder, G. Semeghini, G. Spagnolli, A. Simoni, M. Fattori, M. Inguscio, and G. Modugno, Test of the Universality of the Three-Body Efimov Parameter at Narrow Feshbach Resonances, Phys. Rev. Lett. **111**, 053202 (2013).

[17] J. Johansen, B. J. DeSalvo, K. Patel, and C. Chin, Testing universality of Efimov physics across broad and narrow Feshbach resonances, Nat. Phys. **13**, 731 (2017).

[18] R. Chapurin, X. Xie, M. J. Van de Graaff, J. S. Popowski, J. P. D'Incao, P. S. Julienne, J. Ye, and E. A. Cornell, Precision Test of the Limits to Universality in Few-Body Physics, Phys. Rev. Lett. **123**, 233402 (2019).

[19] X. Xie, M. J. Van de Graaff, R. Chapurin, M. D. Frye, J. M. Hutson, J. P. D'Incao, P. S. Julienne, J. Ye, and E. A. Cornell, Observation of Efimov Universality Across a Non-Universal Feshbach Resonance in 39K, Phys. Rev. Lett. **125**, 243401 (2020).

[20] Y. Wang and P. S. Julienne, Universal van der Waals physics for three cold atoms near Feshbach resonances, Nat. Phys. **10**, 768 (2014).

[21] K. Kato, Y. Wang, J. Kobayashi, P. S. Julienne, and S. Inouye, Isotopic Shift of Atom-Dimer Efimov Resonances in K-Rb Mixtures: Critical Effect of Multichannel Feshbach Physics, Phys. Rev. Lett. **118**, 163401 (2017).

[22] T. Secker, D. J. M. Ahmed-Braun, P. M. A. Mestrom, and S. J. J. M. F. Kokkelmans, Multichannel effects in the Efimov regime from broad to narrow Feshbach resonances, Phys. Rev. A **103**, 052805 (2021).

[23] D. S. Petrov, Three-Boson Problem Near a Narrow Feshbach Resonance, Phys. Rev. Lett. **93**, 143201 (2004).

[24] A. O. Gogolin, C. Mora, and R. Egger, Analytical Solution of the Bosonic Three-Body Problem, Phys. Rev. Lett. **100**, 140404 (2008).

[25] L. Pricoupenko, Crossover in the Efimov spectrum, Phys. Rev. A **82**, 043633 (2010).

[26] M. Jona-Lasino and L. Pricoupenko, Three Resonant Ultracold Bosons: Off-Resonance Effects, Phys. Rev. Lett. **104**, 023201 (2010).

[27] L. Pricoupenko and M. Jona-Lasinio, Ultracold bosons in the vicinity of a narrow resonance: Shallow dimer and recombination, Phys. Rev. A **84**, 062712 (2011).

[28] J. Levinsen, M. M. Parish, and G. M. Bruun, Impurity in a Bose-Einstein Condensation and the Efimov Effect, Phys. Rev. Lett. **115**, 125302 (2015).

[29] Y. Castin, Basic theory tools for degenerate Fermi gases, in *Ultra-Cold Fermi Gases, Proceedings of the Enrico Fermi Varenna School on Fermi Gases*, edited by S. M. Inguscio and W. Ketterle (2006).

[30] M. Jona-Lasinio, L. Pricoupenko, and Y. Castin, Three fully polarized fermions close to a p-wave Feshbach resonance, Phys. Rev. A **77**, 043611 (2008).

[31] Y. Nishida, New Type of Crossover Physics in Three-Component Fermi Gases, Phys. Rev. Lett. **109**, 240401 (2012).

[32] Y. Nishida, Polaronic Atom-Trimer Continuity in Three-Component Fermi Gases, Phys. Rev. Lett. **114**, 115302 (2015).

[33] W. Yi and X. Cui, Polarons in ultracold Fermi superfluids, Phys. Rev. A **92**, 013620 (2015).

[34] M. Pierce, X. Leyronas, and F. Chevy, Few-Versus Many-Body Physics of an Impurity Immersed in a Superfluid of Spin 1/2 Attractive Fermions, Phys. Rev. Lett. **123**, 080403 (2019).

[35] F. Werner, L. Tarruell, and Y. Castin, Number of closed-channel molecules in the BEC-BCS crossover, Eur. Phys. J. B **68**, 401 (2009).

[36] Y. Castin, Ch. Mora, and L. Pricoupenko, Four-Body Efimov Effect for Three Fermions and a Lighter Particle, Phys. Rev. Lett. **105**, 223201 (2010).

[37] Ch. Mora, Y. Castin, and L. Pricoupenko, Integral equations for the four-body problem, C. R. Phys. **12**, 71 (2011).

[38] Since our model does not include background scattering (so $a_{bg} = 0$) the formula $a = a_{bg}[1 - \Delta B/(B - B_0)]$, or its extension to multiple resonances [9], is not applicable. The correct single-resonance formula is $a = a_{bg}\Delta B/(B - B_0)$, where $a_{bg} \to 0$ and $\Delta B \to \infty$ while their product $\Delta = a_{bg}\Delta B$ remains constant. Thus, the width parameter Δ has dimensions of magnetic field times length and the renormalized $\tilde{\Delta} = k_c\Delta$ is in units of magnetic field.

[39] The trimers that are associated with the resonance at $B_1^{(\mathrm{res})}$ and embedded in the dimer-atom continuum of the dimer associated with the resonance at $B_2^{(\mathrm{res})}$ are manifested as scattering resonances between a $B_2^{(\mathrm{res})}$ dimer and a free atom. It should therefore be possible to find them in a scheme similar to the computation of the three-body recombination rate at $E > 0$ in which $a_-^{(n)}$ shows up as a resonance [30].

[40] P. S. Julienne (private communication).

[41] N. Gross, Z. Shotan, O. Machtey, S. J. J. M. F. Kokkelmans, and L. Khaykovich, Study of Efimov physics in two nuclear-spin sublevels of ^{7}Li, C. R. Phys. **12**, 4 (2011).

[42] P. S. Julienne and J. M. Hutson, Contrasting the wide Feshbach resonances in ^{6}Li and ^{7}Li, Phys. Rev. A **89**, 052715 (2014).

[43] O. Machtey, Z. Shotan, N. Gross, and L. Khaykovich, Association of Efimov Trimers from a Three-Atom Continuum, Phys. Rev. Lett. **108**, 210406 (2012).

[44] R. Schmidt, S. P. Rath, and W. Zwerger, Efimov physics beyond universality, Eur. Phys. J. B **85**, 386 (2012).

[45] C. Langmack, R. Schmidt, and W. Zwerger, Efimov states near a Feshbach resonance and the limits of van der Waals universality at finite background scattering length, Phys. Rev. A **97**, 033623 (2018).

[46] B. Gao, Analytic description of atomic interaction at ultracold temperatures. II. Scattering around a magnetic Feshbach resonance, Phys. Rev. A **84**, 022706 (2011).

[47] F. Werner and Y. Castin, General relations for quantum gases in two and three dimensions: Two-component fermions, Phys. Rev. A **86**, 013626 (2012).

Chapter 5

Article 4: Loosely bound few-body states in a spin-1 gas with near-degenerate continua

Yaakov Yudkin, Paul Julienne and Lev Khaykovich

Physical Review A

Volume 107, Page 053303, May 2023

Loosely bound few-body states in a spin-1 gas with near-degenerate continua

Yaakov Yudkin,[1] Paul S. Julienne,[2] and Lev Khaykovich[1]
[1]*Department of Physics, QUEST Center and Institute of Nanotechnology and Advanced Materials, Bar-Ilan University, Ramat-Gan 5290002, Israel*
[2]*Joint Quantum Institute (JQI), University of Maryland and NIST, College Park, Maryland 20742, USA*

(Received 5 January 2023; accepted 18 April 2023; published 2 May 2023)

A distinguishing feature of ultracold collisions of bosonic lithium atoms is the presence of two near-degenerate two-body continua. The influence of such a near degeneracy on the few-body physics in the vicinity of a narrow Feshbach resonance is investigated within the framework of a minimal model with two atomic continua and one closed molecular channel. The model allows analysis of the spin composition of loosely bound dimers and trimers. In the two-body sector the well-established coupled-channel calculation phenomenology of lithium is qualitatively reproduced, and its particularities are emphasized and clarified. In the three-body sector we find that the Efimov trimer energy levels follow a different functional form as compared to a single continuum scenario while the thresholds remain untouched. This three-channel model with two atomic continua complements our earlier developed three-channel model with two molecular channels [Yudkin and Khaykovich, Phys. Rev. A **103**, 063303 (2021)] and suggests that the experimentally observed exotic behavior of the first excited Efimov energy level (Yudkin, Elbaz, and Khaykovich, arXiv:2004.02723) is most probably caused by the short-range details of the interaction potential.

DOI: 10.1103/PhysRevA.107.053303

I. INTRODUCTION

Two decades of experiments with ultracold atoms have stimulated spectacular advance in our understanding of few-body systems. Especially intriguing is scattering in the vicinity of a Feshbach resonance [1], near a so-called singularity, because diverging two-body interactions give rise to a large variety of bound clusters whose properties are universal functions of the scattering length [2–5]. Several experimental and theoretical works were able to establish this universality [6–9].

Apart from the scattering length a, the systems' size and energy length scales are governed by the three-body parameter which, in the case of short-range two-body interaction potentials, succumbs to another type of universality. This Efimov–van der Waals universality relates the three-body parameter to the van der Waals length R_{vdW} of the underlying two-body potential [10–12]. While this holds for broad resonances [13–16], in the vicinity of narrow resonances the three-body parameter was shown to deviate from such universality [17–21].

Although the concept of universality is now well understood, bosonic lithium (^{7}Li) deviates from it in various aspects and continues to puzzle experimentalists and theorists. For one, ^{7}Li satisfies the Efimov–van der Waals universality quite well even though all its resonances are narrow [22]. Further, it was shown that modeling experimental results requires relatively complex multichannel theories [23] with, on occasion, even energetically distant channels [24] and spin-exchange interactions [25] playing a crucial role. In addition, it has been speculated that generic three-body forces must be taken into account to achieve quantitative agreement between experiment and theory [26]. Finally, the spectrum of the trimer was observed to cross into the atom-dimer continuum (or go through an avoided crossing) instead of merging with it [27].

While the typical few-body experiment is conducted with atoms polarized in the absolute ground state (the a-state), in ^{7}Li the second lowest state (b-state; see Fig. 1) was shown to be extraordinarily stable against dipolar relaxation [22]. Bosonic lithium is thus an attractive species for experiments with either spin state or a mixture of both [28]. In particular, it provides an opportunity to compare the few-body physics, e.g., the three-body parameter and the Efimov spectrum, of the two channels [22,29].

In the case of ^{7}Li (and many other species), Feshbach resonances occur at high magnetic fields B, such that $\mu_B B \gg A_{hf}$ (where μ_B is the Bohr magneton and A_{hf} the hyperfine-structure constant) and the Zeeman shift $\sim\mu_B B m_J$ dominates over the hyperfine splitting $\sim A_{hf} m_J m_I$. Here m_J and m_I are the electronic angular momentum (spin + orbital) and nuclear spin projections, respectively, and $m_F = m_J + m_I$ (Fig. 1). Therefore, when considering differences within the $m_J = -1/2$ subset the Zeeman shifts cancel, leaving the hyperfine splitting ($\sim A_{hf}/2$) to dominate. To first order in hyperfine interaction, the differences between the lowest pair (a, b) and the second lowest pair (b, c) are identical such that the two-body bb- and ac-channels are degenerate. To higher order the degeneracy is lifted and amounts to a few tens of MHz. Moreover, the total spin projection of the bb- and ac-channels are identical, which permits energy-conserving spin-exchange coupling between the two. This near degeneracy of a same-spin state in the bb-channel, and its absence in the aa-channel, motivates a comparison of the spin composition of the loosely bound states. Indeed, full two-body

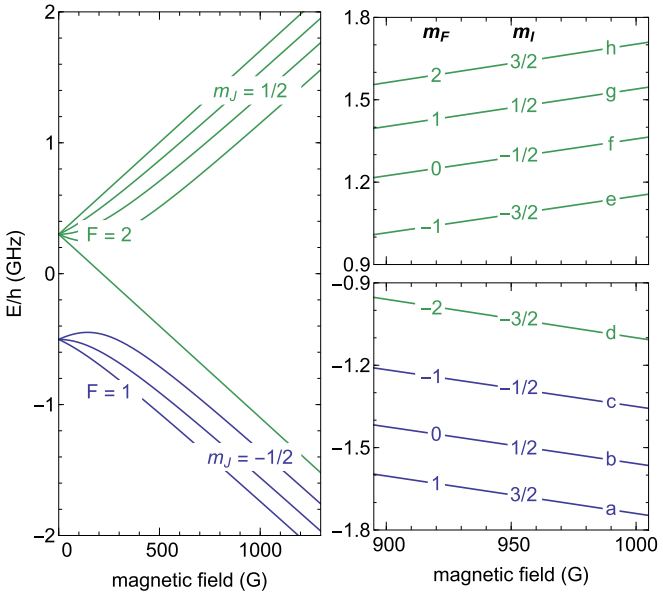

FIG. 1. Plot of the energy of the hyperfine levels of the ^{7}Li $2S_{1/2}$ ground-state vs magnetic field B in gauss. The labels of the levels used throughout this paper are shown.

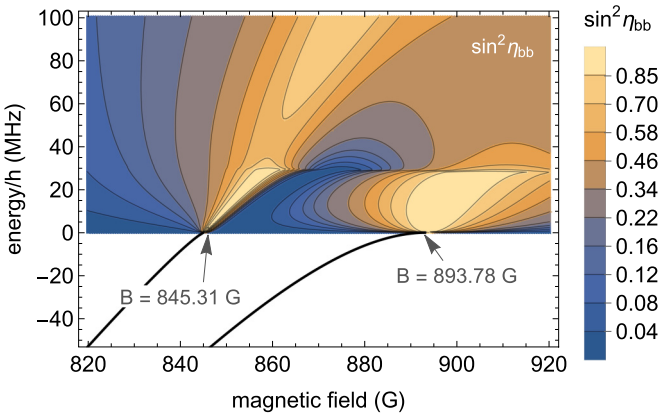

FIG. 2. Coupled-channel calculation for two atoms in the b-state showing $\sin^2\eta_{bb}(E,B)$ for elastic scattering for $E>0$ and the dimer binding energies for $E<0$. Here $E=0$ is the energy of two atoms in the b-state at magnetic field B. At the ac-threshold ($E/h=28$ MHz) the scattering exhibits cusp behavior.

coupled-channel calculations show that the near-threshold bb-eigenstate has a non-negligible ac-population, and we explore its implications here by building a simplified model for the bb-channel [30]. Another strong motivation for the model originates in an effort to understand exotic behavior of the first excited Efimov energy level in the vicinity of the atom-dimer threshold observed in a recent experiment [27]. Although the attempt ultimately fails, it indicates that the solution may be hidden in the short-range details of the interatomic interaction potential.

The paper is organized as follows. First, the two-body sector observables of ^{7}Li are presented in Sec. II and the distinctiveness of the bb-channel, in comparison to the aa-channel, is demonstrated. In Sec. III we introduce a model for the bb-channel which captures the physics with three channels [30]. The two-body scattering and bound state observables of the model are derived in Sec. IV. We compare the results to the standard two-channel model and demonstrate qualitative agreement with full coupled-channel calculations of the aa- and bb-scattering channels of ^{7}Li. In Sec. V we apply the model to the three-body sector and find that the functional form of the trimer's binding energy is altered. Although the thresholds are not affected by the ac-channel, the binding energy is consistently lower than in its absence. After following up with a quick discussion on the lithium few-body puzzle and the implications of the developed model in Sec. VI, we conclude the paper.

Note that together with the previously developed model with one open atomic and two closed molecular channels, used for reproducing overlapping Feshbach resonances [20,31], the current treatment complements the description of the complexity of the bb-channel in ^{7}Li within the well-defined framework of the simplified theory. Thus, a meaningful comparison with the experimental results is performed in Sec. VI.

II. ^{7}Li

The bb-channel features a Feshbach resonance at $B_{\mathrm{res},bb}=893.78(4)$ G and a second, overlapping, much narrower one at 845.31(4) G [32,33]. The former is the resonance of interest, but the effect of the latter cannot be fully ignored. Since it was considered in depth in Ref. [31] we use the conclusions of that work and focus on the additional closed atomic ac-channel here.

Our coupled-channel calculations are based on the molecular potentials determined in Ref. [33] and include all s-wave two-body channels with the same total angular momentum projection M_{tot}, which in this case is just the total spin projection summed over both atoms. Bound or scattering wave functions are written as $|\psi(R)\rangle=\sum_{ij}\phi_{ij}(R)|ij\rangle$, where ij denotes the channel indices specifying all atomic states with the same M_{tot} included in the coupled-channel basis set, and the components ϕ_{ij} reflect closed or open channel boundary conditions depending on the total energy E. Figure 2 shows the energies $E<0$ of the two bound states with $M_F=0$ below the bb-channel threshold and the elastic scattering indicated by $\sin^2\eta_{bb}(E,B)$ for $E>0$ above the threshold, where $\eta_{bb}(E,B)$ is the asymptotic phase shift for the bb-channel. Strong near-unitary elastic scattering persists above threshold as the two bound states emerge into the bb scattering continuum as resonant features, exhibiting cusp behavior at the ac-threshold.

The eight components of the $M_{\mathrm{tot}}=0$ bound state in the bb-channel 9 G below the 893.78 G resonance are shown in Fig. 3(a). In addition to the bb- and ac-channels there are another six two-body channels: ae, bf, cg, dh, eg, and ff (see Fig. 1). Around the resonance position (893.78 G), the ac-channel lies only $(E_{ac}-E_{bb})/h=28$ MHz above the bb-channel threshold (see Fig. 2), whereas the other six atomic channels include at least one $m_J=+1/2$ spin component such that the Zeeman shift makes them energetically very distant from the bb- or ac-channels ($\gtrsim$2 GHz for $B>800$ G). Consequently, the behavior of the wave function components in the latter two channels is quite different than for the other six. First, the spin-exchange interaction

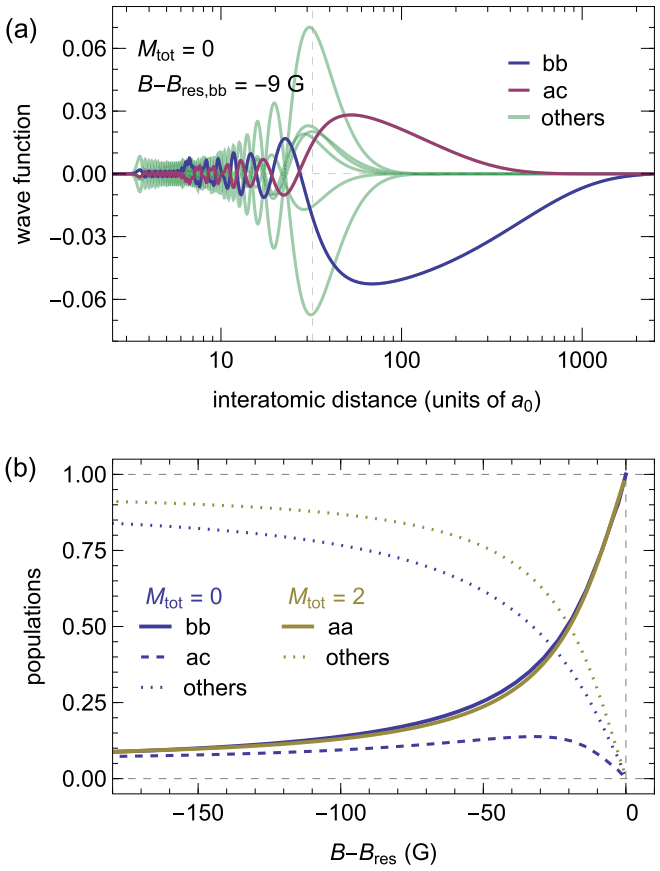

FIG. 3. (a) Wave function components of the dimer bound state close to resonance in the basis of the $M_{tot} = 0$ two-body channels, where $a_0 \approx 0.0529$ nm is one atomic unit of length. The vertical dashed line, where all six energetically distant channels (faint green) are maximal, indicates the van der Waals length $R_{vdW} = 32\ a_0$. Both the *bb*- and the *ac*-components reach far beyond R_{vdW}. Note the logarithmic scale of the horizontal axis. (b) Magnetic field dependence of the populations.

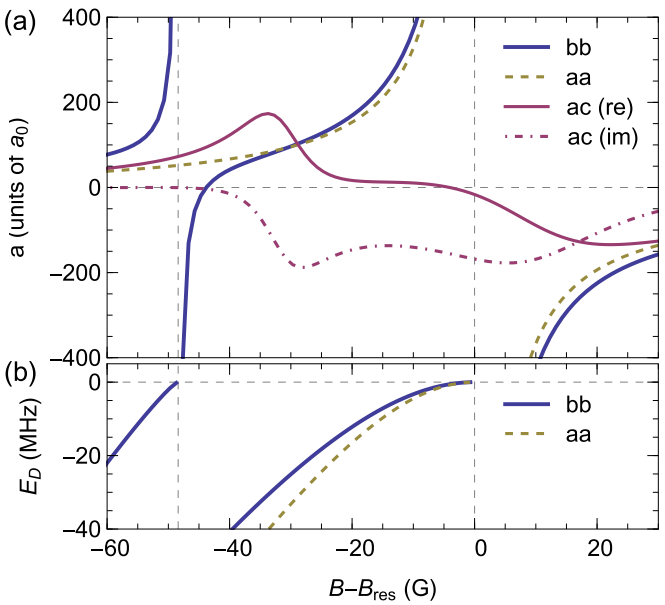

FIG. 4. The magnetic field dependence of the ^{7}Li *bb*- and *aa*-channel (a) scattering lengths and (b) dimer binding energies.

$bb \to ac \to bb$ is relatively strong, suppressed by only a small energy denominator. Furthermore, the *bb*- and *ac*-components can persist to much larger distances than the other six, extending far beyond the van der Waals length (as with a halo dimer) while the remaining six are short ranged, i.e., their amplitude decays quickly outside the van der Waals length R_{vdW}. Since R_{vdW} is the smallest relevant length scale for our problem (we can ignore short-range "chemistry"), it can be thought of as vanishingly small. A diatomic channel that is confined within this range thus resembles a pointlike molecule. As is typical for two-channel models [34,35], also here we categorize the six channels with components confined to short range (order R_{vdW} or less) as "molecular channels" while the two channels with components that extend far beyond R_{vdW} are called "atomic channels." We will use this nomenclature throughout this paper.

In the model in Sec. III for the *bb*-channel we consider both long-range components as separate atomic channels and group all closed channels together [30], thus reducing an eight-channel problem to an effective three-channel model. Utilizing this reduction, the magnetic field dependence of the populations is shown in Fig. 3(b) and discussed below.

In contrast to the eight-channel *bb* case, the *aa*-channel, which features an isolated Feshbach resonance at $B_{res,aa} = 737.69(2)$ G [33], has no near-lying channel with the same spin projection, $M_{tot} = 2$. Hence, all additional four channels (*ag*, *bh*, *fh*, and *gg*) collectively form the molecular channel, thus making the *aa*-channel a good example of the reduction of a homonuclear five-channel case to an effective two-channel model, as described in Ref. [36].

We note that, within the coupled channels framework, the reduction from eight (five) to three (two) channels is more complicated than just grouping together the "molecular channels." In reality, an "atomic channel" can also have a nonzero contribution to the molecular bound state at short range [36].

Comparing the scattering lengths and dimer binding energies of the *aa*- and *bb*-channels demonstrates the effect of a second, near-degenerate continuum. To this end we use full coupled-channel calculations [37] and shift the observables of both channels by their respective resonance position.

It is worth mentioning that the two resonances of the *bb*-channel and the resonance of the *aa*-channel all arise due to different nuclear spin projections of the same bare molecular $\nu = 41$, $J = 0$ bound state in the singlet potential [33]. In addition, since all three resonances are at large magnetic fields, the free atom states have both electron spins down and thus correspond to molecular triplet states. Thus, the differential magnetic moments of the bare molecule in the *bb*- and *aa*-channels are almost the same (within 3%).

The scattering lengths of the *aa*- and *bb*-channels, shown in Fig. 4(a), are overwhelmingly similar. The main difference between the two channels is caused by the additional resonance in the *bb*-channel. Its existence forces a zero crossing, and thus a large gradient, at $B - B_{res,bb} = -44$ G which is absent in the *aa*-channel. We also show the *ac*-scattering length, which is complex because of inelastic collisional loss to the open *bb*-continuum due to strong spin-exchange coupling. Its structure, in particular the double peak of the imaginary part and

the inflection point of the real part, is due to the overlapping nature of the two resonances.

The similarity of the *bb* and *aa* scattering lengths suggests that also the two dimer binding energies are comparable. Moreover, the additional dimer associated with the narrow resonance in the *bb*-channel is expected to make the *bb*-dimer near 893.7 G more deeply bound due to dimer-dimer level repulsion (see Ref. [31], in particular Appendix C therein). However, as seen in Fig. 4(b), the *bb*-channel dimer is considerably shallower than the *aa*-channel dimer and has a somewhat larger universal range where $E_D \sim a^{-2}$ [38].

For the dimer, the populations $0 \leqslant \int |\phi_{ij}(R)|^2 dR \leqslant 1$ of the various channels are shown in Fig. 3(b). While the atomic *bb*- and *aa*-channels have similar behavior, the molecular channels are different. In the *bb* case, the population of the molecular channel (which dominates far from resonance, i.e., at deep dimer binding energies) increases at a slower rate due to the population in the *ac*-channel. The latter reaches a maximal population of ∼14 % at $B - B_{\mathrm{res},bb} = -30$ G and then decays like an atomic channel.

The magnetic field dependence of the spin composition of the *aa*-dimer is typical for a closed-channel-dominated resonance and reproduced by a simple two-channel model with one open atomic and one closed molecular channel [34,39,40]; see also Ref. [36]. In contrast, the unique behavior of the *ac* population marks the appearance of a nontrivial spin composition which we successfully model with a three-channel model (*bb*, *ac*, and a closed molecular channel) in the following. The naturally arising question then concerns the three-body sector: How is the Efimov trimer affected by the proximity of the *ac*-channel and its non-negligible population? Finding an answer within a full coupled-channel model is extremely resource intensive. The straightforward and comprehensive three-channel model introduced here and benchmarked in the two-body sector can be applied to the three-body sector without major complications. In addition, due to the model's simplicity, any deviation from the two-channel model is necessarily caused by the *ac*-channel.

III. MODEL DESCRIPTION

We consider spin-1 particles (i.e., total spin $F = 1$) with spin projections $m_F = 1, 0, -1$ which we label $\sigma = a, b, c = 1, 2, 3$, respectively (lowest three states in Fig. 1). In contrast to other studies of few-body physics in a spinor gas [41,42], we work at large magnetic fields ($\mu_B B \gg A_{hf}$) and with a single, well-defined, entrance spin channel (the *bb*-channel). The model is designed to capture resonant scattering and associated loosely bound states. To this end, we assume, in addition to atomic channels formed from $\sigma = a, b, c$, the presence of diatomic molecular levels with energy detuning $E_{\mathrm{mol},\sigma}$. In cold-atom experiments, $E_{\mathrm{mol},\sigma}$ can be tuned via an external magnetic field. For the closed molecular channels, the index σ indicates the spin flavor not part of the molecule, and has a spin projection of, e.g., $M_F^{(\sigma=3)} = m_F^{(\sigma=1)} + m_F^{(\sigma=2)}$. We are interested in the zero total-spin projection ($M_{\mathrm{tot}} = 0$) two- and three-body systems made up of these particles. Thus, in the two-body sector there are two atomic channels (continua), *bb* and *ac*, which are coupled via a single $M_F = 0$ molecular state (closed channel). For the energies of interest, the atomic *bb*-(*ac*-)channel is open (closed). The three-body sector also features two continua: *bbb* (open) and *abc* (closed). However, a three-body bound state with $M_{\mathrm{tot}} = 0$ can be composed from a diatomic molecule and a supplementary particle in three different ways: (1) a $M_F = 0$ molecule with a $m_F = 0$ atom, (2) a $M_F = +1$ molecule with a $m_F = -1$ atom, and (3) a $M_F = -1$ molecule with a $m_F = 1$ atom.

We proceed by writing the Hamiltonian of the system:

$$\hat{H} = \hat{H}_{\mathrm{atom}} + \hat{H}_{\mathrm{mol}} + \hat{H}_{\mathrm{int}}. \tag{1}$$

The atomic and molecular parts, which are the sum of all three spin flavors, $\hat{H}_{\mathrm{atom/mol}} = \sum_\sigma \hat{H}_{\mathrm{atom/mol},\sigma}$, include kinetic energy and an energy detuning:

$$\hat{H}_{\mathrm{atom},\sigma} = \int \frac{d^3k}{(2\pi)^3}\left(\frac{\hbar^2 k^2}{2m} + E_\sigma\right)\hat{a}^\dagger_{\sigma,\vec{k}}\hat{a}_{\sigma,\vec{k}}, \tag{2}$$

$$\hat{H}_{\mathrm{mol},\sigma} = \int \frac{d^3k}{(2\pi)^3}\left(\frac{\hbar^2 k^2}{4m} + E_{\mathrm{mol},\sigma}\right)\hat{d}^\dagger_{\sigma,\vec{k}}\hat{d}_{\sigma,\vec{k}}. \tag{3}$$

Here $\hat{a}^\dagger_{\sigma,\vec{k}}$ ($\hat{d}^\dagger_{\sigma,\vec{k}}$) creates an atom (a molecule) of type σ, mass m ($2m$) and with energy detuning E_σ ($E_{\mathrm{mol},\sigma}$) and momentum $\hbar\vec{k}$. The molecular detuning $E_{\mathrm{mol},\sigma}$ is tunable and serves as a surrogate for the magnetic field detuning from resonance. The interaction has two parts:

$$\hat{H}_{\mathrm{int}} = \sum_\sigma \hat{H}_{\mathrm{int},\sigma} + \hat{H}_{\mathrm{int},22}. \tag{4}$$

The first takes two atoms different from σ and turns them into a molecule of type σ or vice versa. Written explicitly for $\sigma = 3$ it is

$$\hat{H}_{\mathrm{int},3} = \Lambda_3 \int \frac{d^3q}{(2\pi)^3}\int \frac{d^3k}{(2\pi)^3} \times \left(\hat{d}^\dagger_{3,\vec{q}}\hat{a}_{1,\vec{k}+\frac{\vec{q}}{2}}\hat{a}_{2,-\vec{k}+\frac{\vec{q}}{2}} + \hat{a}^\dagger_{2,-\vec{k}+\frac{\vec{q}}{2}}\hat{a}^\dagger_{1,\vec{k}+\frac{\vec{q}}{2}}\hat{d}_{3,\vec{q}}\right). \tag{5}$$

The second part takes two $\sigma = 2$ atoms to create a $\sigma = 2$ molecule:

$$\hat{H}_{\mathrm{int},22} = \Lambda_{22} \int \frac{d^3q}{(2\pi)^3}\int \frac{d^3k}{(2\pi)^3} \times \left(\hat{d}^\dagger_{2,\vec{q}}\hat{a}_{2,\vec{k}+\frac{\vec{q}}{2}}\hat{a}_{2,-\vec{k}+\frac{\vec{q}}{2}} + \hat{a}^\dagger_{2,-\vec{k}+\frac{\vec{q}}{2}}\hat{a}^\dagger_{2,\vec{k}+\frac{\vec{q}}{2}}\hat{d}_{2,\vec{q}}\right). \tag{6}$$

We stress that the molecule participating in $\hat{H}_{\mathrm{int},22}$ is the same as the one in $\hat{H}_{\mathrm{int},2}$, namely, a molecule with $M_F = 0$ spin projection.

The Hamiltonian in Eq. (1) does not include scattering within the *bb*- or *ac*-channel, given that they are often, and in particular for ^{7}Li, negligible with respect to the resonant scattering considered here. An exception occurs if a zero-energy resonance is present; see, e.g., Ref. [43,44]. Further, direct *bb*-to-*ac* coupling is also not included. A spin exchange of this sort is possible indirectly via the $M_F = 0$ molecule and therefore resonantly enhanced around the Feshbach resonance. The direct coupling is of the same form as background scattering within either of the atomic channels and neglected here for the sake of simplicity.

The Hamiltonian can be viewed as the amalgamation of a homo- and heteronuclear version of the two-channel model, where the synthesis is made by merging the homonuclear

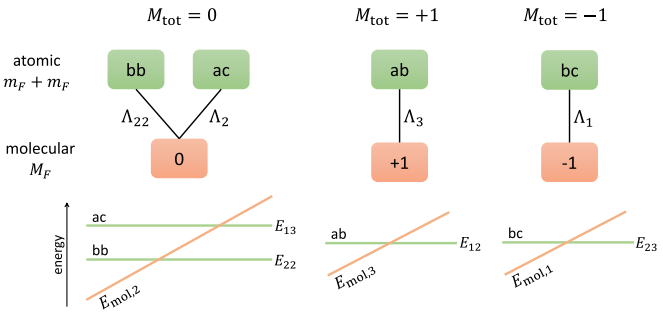

FIG. 5. Depiction of the three possible two-body sectors in $F = 1$. The upper illustration shows the bare states and their coupling via $\hat{H}_{\rm int}$. Below the bare state energy-dependence on the parameter controlling $E_{{\rm mol},\sigma}$ is illustrated.

molecule with the same-spin heteronuclear molecule. The two models are slightly offset by a relative shift in energy. For $\Lambda_\sigma = 0$ ($\Lambda_{22} = 0$) the standard homo-(hetero-)nuclear two-channel model is reobtained, allowing quantitative comparisons in what follows.

IV. TWO-BODY SECTOR

In the $M_{\rm tot} = 0$ two-body sector, the most general two-body wave function is

$$|\psi_0\rangle = \beta_2 \hat{a}^\dagger_{2,\vec{q}=0}|0\rangle + \int \frac{d^3k}{(2\pi)^3}\alpha_{ac}(\vec{k})\hat{a}^\dagger_{3,\vec{k}}\hat{a}^\dagger_{1,-\vec{k}}|0\rangle + \int \frac{d^3k}{(2\pi)^3}\alpha_{bb}(\vec{k})\hat{a}^\dagger_{2,\vec{k}}\hat{a}^\dagger_{2,-\vec{k}}|0\rangle, \tag{7}$$

where we have chosen the center-of-mass reference frame. As is the case in ^{7}Li we choose the energy $E_{22} = 2E_2$ of the bb-channel to be lower than the energy $E_{13} = E_1 + E_3$ of the ac-channel: $E_{13} > E_{22}$. The three bare states are illustrated in Fig. 5 together with the couplings induced by the Hamiltonian. The decoupled homo-(hetero-)nuclear wave function $|\psi_{\rm hom}\rangle$ ($|\psi_{\rm het}\rangle$) is given by plugging in $\alpha_{ac} = 0$ ($\alpha_{bb} = 0$) (Appendix A). In the $M_{\rm tot} = \pm 1$ two-body sectors, $|\psi_{+1}\rangle$ and $|\psi_{-1}\rangle$ are equivalent to $|\psi_{\rm het}\rangle$.

In the following we solve the Schrödinger equation $\hat{H}|\psi_0\rangle = E|\psi_0\rangle$ and obtain expressions for the scattering properties and the associated bound state. Direct substitution of $\hat{H}$ and $|\psi_0\rangle$ into $\hat{H}|\psi_0\rangle = E|\psi_0\rangle$ leads to three coupled equations, one for each bare state projection. The free particle amplitudes are of Lorentzian form [see Eq. (9) below] and thus a three-dimensional integral over them diverges. In order to avoid infinities, a high-momentum cutoff $k_{\rm cutoff}$ must be introduced, which we use to renormalize all of the quantities appearing in $\hat{H}$ and $|\psi_0\rangle$, such that they become dimensionless. For example, the renormalized momentum k is $\tilde{k} = k/k_{\rm cutoff}$, the renormalized molecular amplitude β_2 is $\tilde{\beta}_2 = \beta_2 k^{3/2}_{\rm cutoff}$ and the renormalized coupling constants $\Lambda_{\sigma,22}$ are $\tilde{\Lambda}_{\sigma,22} = \Lambda_{\sigma,22}k^{3/2}_{\rm cutoff}/E_{\rm cutoff}$, where $E_{\rm cutoff} = \hbar^2 k^2_{\rm cutoff}/m$ is the cutoff energy. Note that the atomic amplitudes $\alpha_{\rm ac,bb}$ are already dimensionless and hence do not need renormalizing. After this step, $k_{\rm cutoff}$ no longer appears in the coupled equations. Hernceforth, all dimensionless, renormalized quantities are denoted by a tilde.

TABLE I. The first two rows list the parameters used for Figs. 6–9. The last two rows are the obtained resonance positions and strengths.

	bb (22)	ac (2)	Homo-	Hetero-
$\tilde{\Lambda}$	1	1	1	1
$\tilde{E}_{\rm thr}$	0	0.0004	0	0
$\tilde{E}_{\rm res}$	0.1504	0.1524	0.1013	0.0507
$\tilde{R}^\star$	18.78	–	6.28	12.57

For demonstration, the various two-body observables are considered using the parameters in Table I, and we compare them to those of the homo- and heteronuclear case. We choose the same coupling constants for all models, i.e., $\tilde{\Lambda}_{22} = \tilde{\Lambda}_2 = \tilde{\Lambda}_{\rm hom} = \tilde{\Lambda}_{\rm het}$, to keep the microscopic models identical and thus allowing quantitative comparison. We note that, due to Bose enhancement, the effective coupling of the homonuclear case is $\sqrt{2}$ larger than in the heteronuclear case, leading to the former resonance being broader (Appendix B). The comparison between the $M_{\rm tot} = 0$ model and the homonuclear model is equivalent to comparing the ^{7}Li bb- and aa-channel observables.

A. Scattering properties

Here, for two atoms in the bb-channel with energy $E = E_{22} + E_0$, where $E_0 = \hbar^2 k_0^2/m > 0$ is their relative kinetic energy, we derive an expression for the elastic scattering amplitude $f_{bb\leftarrow bb}(k_0)$. For $E_0 < E_{13}$ the ac-channel is closed, and $bb \to bb$ is the only possible scattering event. However for $E_0 \geqslant E_{13}$ an additional scattering process is energetically allowed, namely, inelastic scattering $bb \to ac$. Hence, the elastic and inelastic scattering processes compete for incoming kinetic energies above the ac threshold and $f_{bb\leftarrow bb}(k_0)$ is reduced with respect to its two-channel model counterpart. Moreover, if $E_0 \geqslant E_{13}$, the ac-channel qualifies as an entrance channel, i.e., it is an energetically open channel. Two atoms in the ac-channel with kinetic energy $E_0 - E_{13}$ can scatter either elastically back into the ac-channel or inelastically to the bb-channel. The most general incident state with kinetic energy $E_0 \geqslant E_{13}$ is thus

$$\left|\psi_0^{(\rm in)}\right\rangle = \alpha^{(\rm in)}_{bb}\hat{a}^\dagger_{2,\vec{k}_0}\hat{a}^\dagger_{2,-\vec{k}_0}|0\rangle + \alpha^{(\rm in)}_{ac}\hat{a}^\dagger_{3,\delta\vec{k}_0}\hat{a}^\dagger_{1,-\delta\vec{k}_0}|0\rangle, \tag{8}$$

where $E_{22} + \hbar^2 k_0^2/m = E_{13} + \hbar^2 \delta k_0^2/m$ with $k_0 = |\vec{k}_0|$ and $\delta k_0 = |\delta\vec{k}_0|$, and the coefficients are normalized according to $|\alpha^{(\rm in)}_{bb}|^2 + |\alpha^{(\rm in)}_{ac}|^2 = 1$. For $0 < E_0 < E_{13}$ the ac-channel coefficient $\alpha^{(\rm in)}_{ac} = 0$ vanishes, such that $\alpha^{(\rm in)}_{bb} = 1$.

In order to find $f_{bb\leftarrow bb}(k_0)$ we use $\hat{H}|\psi_0\rangle = (E_{22} + E_0)|\psi_0\rangle$ to write the bb and ac atomic channel amplitudes $\alpha_{bb}(\tilde{k})$ and $\alpha_{ac}(\tilde{k})$ in terms of the closed molecular amplitude $\tilde{\beta}_2$:

$$\alpha_{bb}(\tilde{k}) = \alpha^{(\rm in)}_{bb}(2\pi)^3\delta(\tilde{k} - \tilde{k}_0) - \frac{\tilde{\Lambda}_{22}\tilde{\beta}_2}{\tilde{k}^2 - \tilde{k}_0^2 - i\eta}, \tag{9a}$$

$$\alpha_{ac}(\tilde{k}) = \alpha^{(\rm in)}_{ac}(2\pi)^3\delta\big(\tilde{k} - \sqrt{\tilde{k}_0^2 - \Delta\tilde{E}}\big) - \frac{\tilde{\Lambda}_2\tilde{\beta}_2}{\tilde{k}^2 - \tilde{k}_0^2 + \Delta\tilde{E} - i\eta}, \tag{9b}$$

where $\Delta\tilde{E} = \tilde{E}_{13} - \tilde{E}_{22} > 0$ is the energy difference of the two atomic channels, $\tilde{k}_0 = k_0/k_{\text{cutoff}}$ is the incident momentum in the *bb*-channel, and $\eta \to 0^+$. From a scattering theory perspective the δ function [45] represents an incoming plane wave, and the second term is the scattered, spherically symmetric, wave [46]. For the waves in α_{bb} the modulus of the k vector is $\tilde{k}_0$ such that both waves exist for any kinetic energy. However, in the case of α_{ac} it is $\sqrt{\tilde{k}_0^2 - \Delta\tilde{E}}$, which is real (i.e., the waves propagate) only if the kinetic energy $\tilde{k}_0^2$ is equal or larger than $\Delta\tilde{E}$. Further, the origin of the scattered wave is twofold. Although all scattering events must go through the molecule due to the connectivity defined by the Hamiltonian (Fig. 5), the molecule can originate from either the *bb* or the *ac* atomic channel. This is made clear by the form of the molecular amplitude, which is given by

$$\tilde{\beta}_2(\tilde{k}_0) = -\frac{1}{D(\tilde{k}_0)}\left[2\tilde{\Lambda}_{22}\alpha_{bb}^{(\text{in})}\Theta(\tilde{k}_0) + \tilde{\Lambda}_2\alpha_{ac}^{(\text{in})}\Theta(\tilde{k}_0 - \sqrt{\Delta\tilde{E}})\right], \tag{10}$$

where

$$D(\tilde{k}_0) = \left(\tilde{E}_{\text{mol},2} - \tilde{E}_{22} - \tilde{k}_0^2\right) - \frac{\tilde{\Lambda}_2^2}{2\pi^2}\left(1 - \frac{\pi}{2}\sqrt{\Delta\tilde{E} - \tilde{k}_0^2}\right) - \frac{\tilde{\Lambda}_{22}^2}{\pi^2}\left(1 - i\frac{\pi}{2}\tilde{k}_0\right). \tag{11}$$

The amplitude of the molecular channel is the sum of two terms corresponding to the two origins. The Heaviside step functions $\Theta(x)$ arise due to the two different continuum thresholds and prevent an influx from the *ac*-channel if it is closed. The factor 2 in the first term is due to Bose enhancement. The scattering amplitude for elastic $bb \to bb$ scattering is thus

$$\tilde{f}_{bb\leftarrow bb}(\tilde{k}_0) = \frac{\tilde{\Lambda}_{22}^2}{2\pi}\frac{\Theta(\tilde{k}_0)}{D(\tilde{k}_0)}, \tag{12}$$

where we have used the scattered wave from α_{bb} and the molecular amplitude term originating from the *bb*-channel. Since the entrance channel is specified to be the *bb*-channel, we have set $\alpha_{bb}^{(\text{in})} = 1$. To derive an expression for the $ac \to ac$ elastic scattering amplitude we consider the kinetic energy $\delta E_0 = \hbar^2(\delta k_0)^2/m > 0$ measured with respect to the *ac*-threshold (the excess energy) and defined via $E = E_{22} + \Delta E + \delta E_0$ or $\tilde{k}_0^2 = \Delta\tilde{E} + \delta\tilde{k}_0^2$. Taking the scattered wave from α_{ac} and the molecular amplitude term originating from the *ac*-channel we find

$$\tilde{f}_{ac\leftarrow ac}(\delta\tilde{k}_0) = \frac{\tilde{\Lambda}_2^2}{4\pi}\frac{\Theta(\delta\tilde{k}_0)}{D\left(\sqrt{\Delta\tilde{E} + \delta\tilde{k}_0^2}\right)}, \tag{13}$$

where $\alpha_{ac}^{(\text{in})} = 1$.

As a first observable we extract the resonance position $\tilde{E}_{\text{res},i}$ ($i = \{bb, ac, \text{hom}, \text{het}\}$), i.e., the value the bare molecular energy $\tilde{E}_{\text{mol},2}$ takes when the scattering length diverges and the condition $\tilde{f}_i^{-1}(\tilde{k}_0 = 0) = 0$ is satisfied (Table I). For degenerate continua, i.e., for $E_{13} = E_{22}$, the *bb*- and *ac*-resonance positions are identical and equal to the sum of the homo- and heteronuclear model. In this case, the relative energy offset of the two two-channel subsystems (homo- and heteronuclear) vanishes and the shifts from the bare resonance positions add linearly. For nonequal thresholds the *ac*-resonance position increases linearly with $|E_{13} - E_{22}|$, while the *bb*-resonance decreases as $\sim\sqrt{E_{13} - E_{22}}$; see Fig. 6(a). An energetically distant but equally coupled *ac*-channel ($\tilde{\Lambda}_{22} = \tilde{\Lambda}_2 = 1$) causes the *bb*-resonance to shift below the homonuclear ($\tilde{\Lambda}_2 = 0$) resonance. However, realistically $\tilde{\Lambda}_2$ should decrease with increasing $|E_{13} - E_{22}|$, since distant energy levels are coupled weaker. In the limit $\tilde{\Lambda}_2 \to 0$, $\tilde{E}_{\text{res},bb}$ approaches the value of $\tilde{E}_{\text{res,hom}}$.

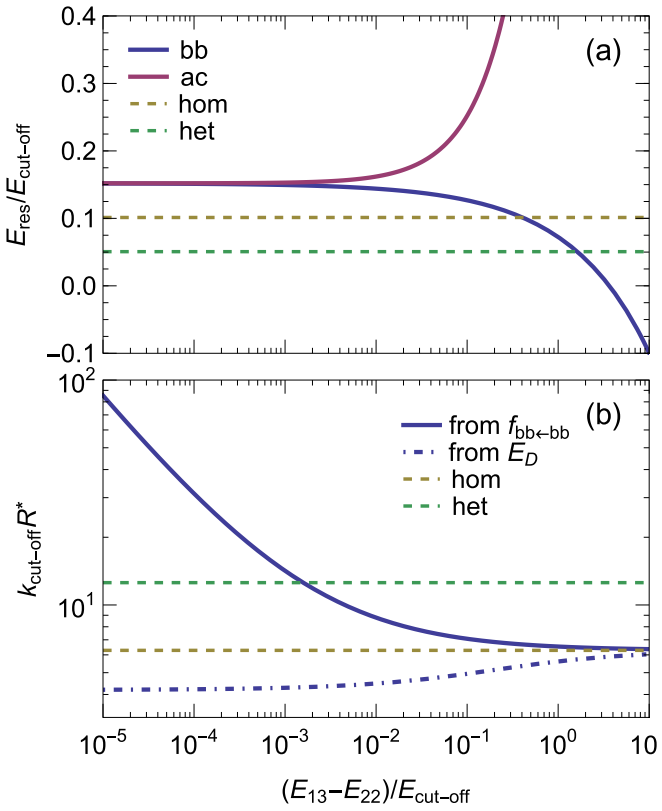

FIG. 6. E_{13} dependence. (a) The *bb*- and *ac*-resonance positions are shown as a function of the energy splitting between the continua. (b) The two possible ways to extract $R_{bb}^\star$ are contrasted. The solid line is Eq. (14). hom = homonuclear, het = heteronuclear.

In the following, the resonance position $E_{\text{res},bb}$ is used to shift the molecular energy axis such that the *bb*-resonance is at the origin.

A contour plot of $0 \leqslant |\tilde{k}_0 \cdot \tilde{f}_{bb\leftarrow bb}(\tilde{k}_0)|^2 \leqslant 1$, which is equivalent to $\sin^2\eta$ [47], demonstrates the effect of the *ac*-threshold embedded in the *bb*-continuum (Fig. 7). As in ^{7}Li (Fig. 2) we observe cusp behavior at the threshold. Compared to the homonuclear two-channel model, the $bb \to bb$ (elastic) scattering is decreased above the *ac*-threshold due to the increase in $bb \to ac$ (inelastic) scattering (Fig. 8).

While the contour plots of Figs. 7 and 8 are instructive, cold-atom experiments usually operate in the $k_0 \to 0$ limit. In this case one may expand the scattering amplitude in powers of k_0 and compare its coefficients to the effective range expansion $[\tilde{f}_{bb\leftarrow bb}(\tilde{k}_0)]^{-1} = -\tilde{a}_{bb}^{-1} - i\tilde{k}_0 + \tilde{r}_{e,bb}\tilde{k}_0^2/2$, thus obtaining expressions for the scattering length $\tilde{a}_{bb}$ [Fig. 9(a)] and effective range $r_{e,bb}$. The latter is related to the parameter $R_{bb}^\star = -r_{e,bb}/2$, which is indicative of the narrowness of a

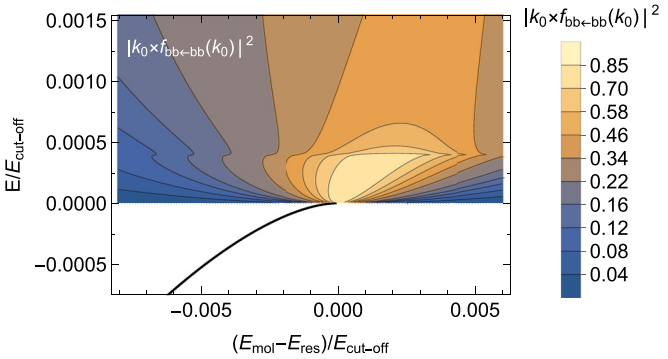

FIG. 7. For $E > 0$, a contour plot of $|\tilde{k}_0 \cdot \tilde{f}_{bb}(\tilde{k}_0)|^2$, as a function of the bare molecular energy $\tilde{E}_{\rm mol}$ (shifted to resonance) and the kinetic energy $\tilde{E}_0$ of two free particles is shown. The dimer binding energy, which vanishes at resonance, is depicted for $E < 0$. These $M_{\rm tot} = 0$ model properties are directly comparable to the full coupled-channel calculations of Fig. 2.

Feshbach resonance (Table I). In Fig. 9(a) we see that a_{bb} is identical to $a_{\rm hom}$, i.e., its width in units of $E_{\rm mol}$ is governed by the bb-channel. However, the seemingly perfect overlap is misleading because, in Fig. 9(a), we shifted both resonances by their respective (different; see Table I) $E_{{\rm res},i}$. More importantly, $R^\star_{bb} > R^\star_{\rm hom}$, indicating that the bb resonance pole strength [48] is increased by the proximity of the additional ac-channel, even beyond $R^\star_{\rm het}$. In fact,

$$\tilde{R}^\star_{bb} = \frac{2\pi}{\tilde{\Lambda}_{22}^2} + \frac{\tilde{\Lambda}_2^2}{4\tilde{\Lambda}_{22}^2}\frac{1}{\sqrt{\tilde{E}_{13} - \tilde{E}_{22}}} \tag{14}$$

is made up of two terms. The first is the contribution from the bb-channel and identical to $\tilde{R}^\star_{\rm hom}$. The second term is inversely proportional to the square root of the energy difference. Thus, the closer the two continua, the stronger the pole. We note that in the limit $\tilde{\Lambda}_2 \to 0$, as well as in the limit $\tilde{E}_{13} \gg \tilde{E}_{22}$, $\tilde{R}^\star_{bb} \to \tilde{R}^\star_{\rm hom}$ as expected.

Turning to the ac-threshold, the scattering length a_{ac}, which is obtained from $\tilde{a}_{ac} = -\tilde{f}_{ac\leftarrow ac}(\delta\tilde{k}_0 = 0)$, is complex [Fig. 9(a)]. At the pole position, Re $a_{ac} = 0$ vanishes and the modulus of Im a_{ac} experiences a maximum. Expanding $f_{ac}(k_0)$ beyond the zeroth order is meaningless because the linear term $\sim k_0$ is not parameter independent as required by the optical theorem.

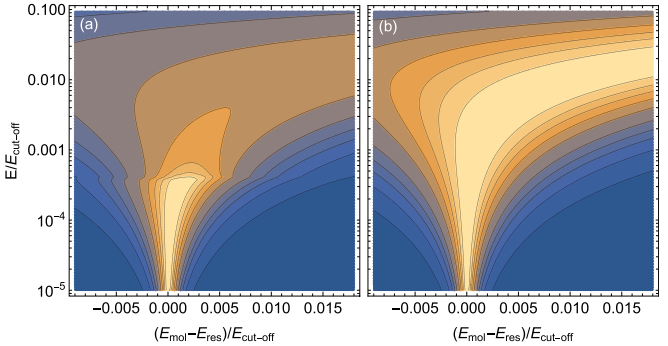

FIG. 8. (a) Contour plot of $|\tilde{k}_0 \cdot \tilde{f}_{bb\leftarrow bb}(\tilde{k}_0)|^2$, as in Fig. 7 but with a logarithmic vertical scale. (b) For comparison, the two-channel homonuclear case is shown. The color scales here and in Figs. 2 and 7 are identical.

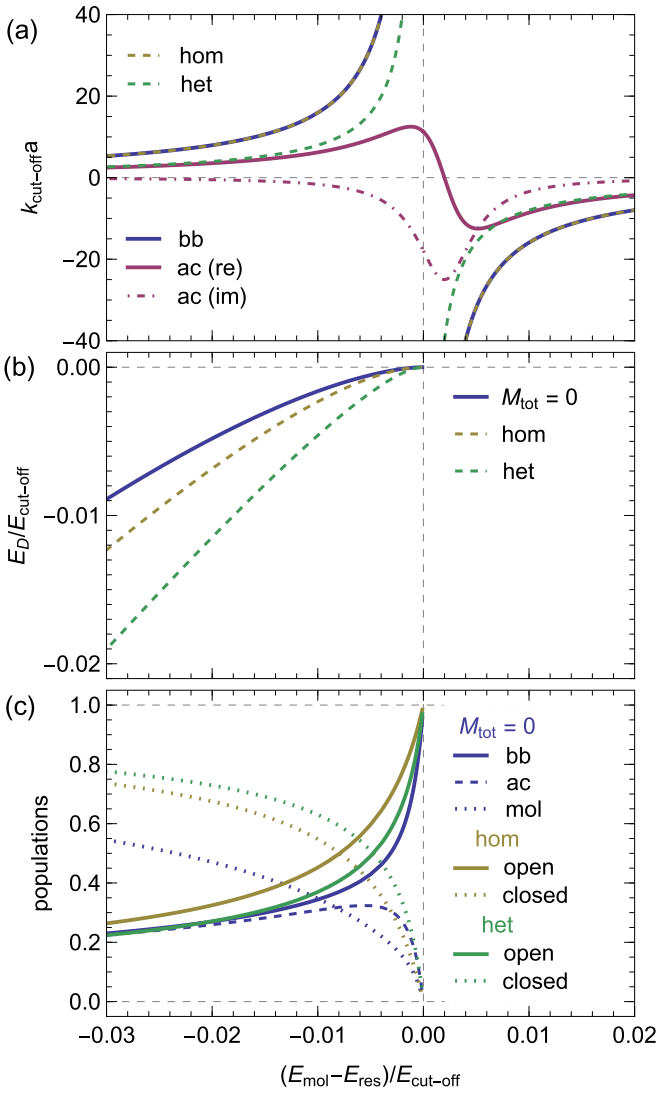

FIG. 9. Two-body sector. (a) Plot of the scattering length $\tilde{a}$ as a function of the bare molecular energy $\tilde{E}_{\rm mol}$. The bb and ac curves are shifted by $\tilde{E}_{{\rm res},bb}$ and hom (het) by $\tilde{E}_{\rm res,hom}$ ($\tilde{E}_{\rm res,het}$). The curves for bb and hom overlap. (b) Plot of the dimer binding energy with respect to the (lower) continuum threshold. (c) For the three models in (b) the open and closed channels populations are contrasted.

B. Binding energy

Now we discuss the negative energy solution of the Schrödinger equation, i.e., the binding energy of the Feshbach dimer. One way of finding it is by looking for poles of the scattering amplitude for $k_0 = i\lambda$, $\lambda > 0$. Alternatively, one may solve the Schrödinger equation with $E_D = E_{22} - \hbar^2\lambda^2/m < E_{22}$ which reduces to solving the following equation:

$$(\tilde{E}_{{\rm mol},2} - \tilde{E}_{22} + \tilde{\lambda}^2) - \frac{\tilde{\Lambda}_2^2}{2\pi^2}\left(1 - \frac{\pi}{2}\sqrt{\Delta\tilde{E} + \tilde{\lambda}^2}\right) - \frac{\tilde{\Lambda}_{22}^2}{\pi^2}\left(1 - \frac{\pi}{2}\tilde{\lambda}\right) = 0. \tag{15}$$

We note that solving the Schrödinger equation for $E_D = E_{13} - \hbar^2\lambda^2/m$ leads to a different solution for λ but the same (observable) binding energy E_D. The additional atomic channel does *not* lead to an additional dimer but instead gives the dimer a mixed *bb* and *ac* spin composition. (This should be contrasted to the three-channel model with two molecular channels [31].) Its numerical solution is compared to the homo- and heteronuclear dimers in Fig. 9(b). Interestingly, although we established above that the presence of the *ac*-channel increases the pole strength (larger $R^\star$), the $M_{\rm tot} = 0$ dimer is shallower than in the homonuclear model and its universal range, where $E_D \sim a^{-2}$, is increased. In fact, the functional form of the homonuclear dimer describes the $M_{\rm tot} = 0$ dimer with $\tilde{\Lambda} = 1.12$ or $\tilde{R}^\star = 4.364$. We conclude that, counterintuitively, the addition of the *ac*-channel increases the pole strength while also increasing the universal range, a correlation that is usually vice versa.

To illustrate this point in a more general setting, Fig. 6(b) contrasts the value of $\tilde{R}^\star_{bb}$ found by expanding the scattering amplitude [Eq. (14)] to the value of $\tilde{R}^\star_{bb}$ obtained from fitting the $M_{\rm tot} = 0$ dimer to the homonuclear dimer. While they become equal at large continua separation, as they approach degeneracy the two values grow apart. We note that $\tilde{R}^\star_{bb}$ extracted from the dimer approaches $\tilde{R}^\star_{\rm hom}\tilde{R}^\star_{\rm het}/(\tilde{R}^\star_{\rm hom} + \tilde{R}^\star_{\rm het})$ for $E_{13} \to E_{22}$ (Appendix C).

Some insight into this counterintuitive behavior may be gained by looking at the populations in the atomic and molecular channels. Given the dimer binding wave number $\lambda > 0$, they are (Appendix E)

$$P_{\rm bb} = \frac{1}{\mathcal{N}}\left(\frac{\tilde{\Lambda}_{22}^2}{8\pi\tilde{\lambda}}\right), \tag{16a}$$

$$P_{\rm ac} = \frac{1}{\mathcal{N}}\left(\frac{\tilde{\Lambda}_2^2}{8\pi\sqrt{\Delta\tilde{E} + \tilde{\lambda}^2}}\right), \tag{16b}$$

$$P_{\rm mol} = \frac{1}{\mathcal{N}}, \tag{16c}$$

where

$$\mathcal{N} = \frac{\tilde{\Lambda}_{22}^2}{8\pi\tilde{\lambda}} + \frac{\tilde{\Lambda}_2^2}{8\pi\sqrt{\Delta\tilde{E} + \tilde{\lambda}^2}} + 1, \tag{17}$$

for the *bb*, *ac*, and molecular channel, respectively. These functions are plotted in Fig. 9(c). Far from resonance, the population of the *ac*-channel behaves like an atomic channel and approaches zero, as the dimer adopts a predominantly closed channel character. Close to resonance, the dimer becomes *bb*-open-channel-dominated and the *ac*-channel population also approaches zero. In between it experiences a maximum as $|E_D - E_{22}| \approx |E_{13} - E_{22}|$. Compared to the open channel populations of the homo- and heteronuclear models, the *bb* population depletes faster, as expected from a stronger pole (larger $R^\star$). However, the molecular channel population increases at a slower rate than the closed channel in both the homo- and heteronuclear models. This is in agreement with the dimer's binding energy being shallower. The missing population is of course found in the *ac*-channel. In other words, the proximity of the *ac*-channel depletes the *bb*-channel faster causing the *bb*-resonance to seem less open-channel dominated (i.e., narrower, larger $R^\star$). But from the point of view of the dimer the atomic channel population is the sum $P_{\rm bb} + P_{\rm ac}$ which implies that the resonance is more open-channel dominated (i.e., larger universal range). It is this duality that gives rise to the (unusual) correlation between the pole strength and the universal range.

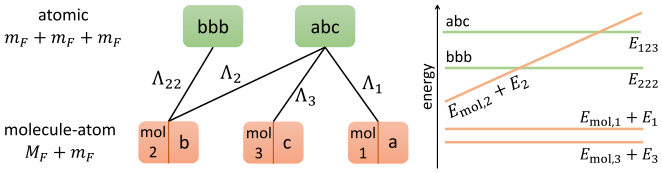

FIG. 10. Depiction of the $M_{\rm tot} = 0$ three-body sector. The illustration on the left shows the bare states and their coupling via $\hat{H}_{\rm int}$. To the right, the bare state energy dependence on the parameter controlling $E_{{\rm mol},\sigma}$ is illustrated.

Contrasting the observables of the $M_{\rm tot} = 0$ model to the homonuclear model is reminiscent of the comparison of the *bb*- and *aa*-channel in ^{7}Li (see Fig. 4). We therefore conclude that the nearby *ac*-channel is responsible for the observed difference. By fitting the model to the coupled-channel scattering length and $R^\star$ of ^{7}Li, the three bare parameters of the model (bare resonance position + two coupling constants) can be found. However, quantitative agreement between the model and the coupled-channel dimer is limited to small binding energies. We observe that the model predicts a less deeply bound dimer (compared to coupled channels) for both channels. We associate this discrepancy to the van der Waals tail of the real interaction potential that is not captured by the model. We do, however, faithfully reproduce the shallowing effect due to *ac*-channel.

V. THREE-BODY SECTOR

In a system with three particles and total-spin projection $M_{\rm tot} = 0$ there are two possible spin configurations in the continuum: *bbb* and *abc* [49]. Each pair (*bb*, *ac*, *ab*, *bc*) is coupled to a molecule with a matching spin projection, and, as discussed above, the *bb* and *ac* pairs are coupled via the $M_F = 0$ molecule. The latter is also the link between the two three-body continua (Fig. 10). The most general three-body wave function is

$$\begin{aligned}|\psi_{\rm 3B}\rangle = &\sum_\sigma \int \frac{d^3q}{(2\pi)^3}\beta_\sigma(\vec{q})\hat{d}^\dagger_{\sigma,\vec{q}}\hat{a}^\dagger_{\sigma,-\vec{q}}|0\rangle \\ &+ \int\frac{d^3q}{(2\pi)^3}\int\frac{d^3k}{(2\pi)^3}\alpha_{bbb}(\vec{q},\vec{k})\hat{a}^\dagger_{2,\vec{k}+\frac{\vec{q}}{2}}\hat{a}^\dagger_{2,-\vec{k}+\frac{\vec{q}}{2}}\hat{a}^\dagger_{2,-\vec{q}}|0\rangle \\ &+ \int\frac{d^3q}{(2\pi)^3}\int\frac{d^3k}{(2\pi)^3}\alpha_{abc}(\vec{q},\vec{k})\hat{a}^\dagger_{3,\vec{k}+\frac{\vec{q}}{2}}\hat{a}^\dagger_{1,-\vec{k}+\frac{\vec{q}}{2}}\hat{a}^\dagger_{2,-\vec{q}}|0\rangle.\end{aligned} \tag{18}$$

There are three decoupled two-body subsystems underlying $|\psi_{\rm 3B}\rangle$, namely, $|\psi_0\rangle$ [Eq. (7)], $|\psi_{+1}\rangle$, and $|\psi_{-1}\rangle$ (Fig. 5). In the three-body sector, these decoupled two-body systems become coupled due to the common continuum (Appendix D).

Upon solving $\hat{H}|\psi_{\rm 3B}\rangle = E|\psi_{\rm 3B}\rangle$ with $E = E_{222} - \hbar^2\lambda^2/m$ one obtains three coupled equations for the molecule-atom

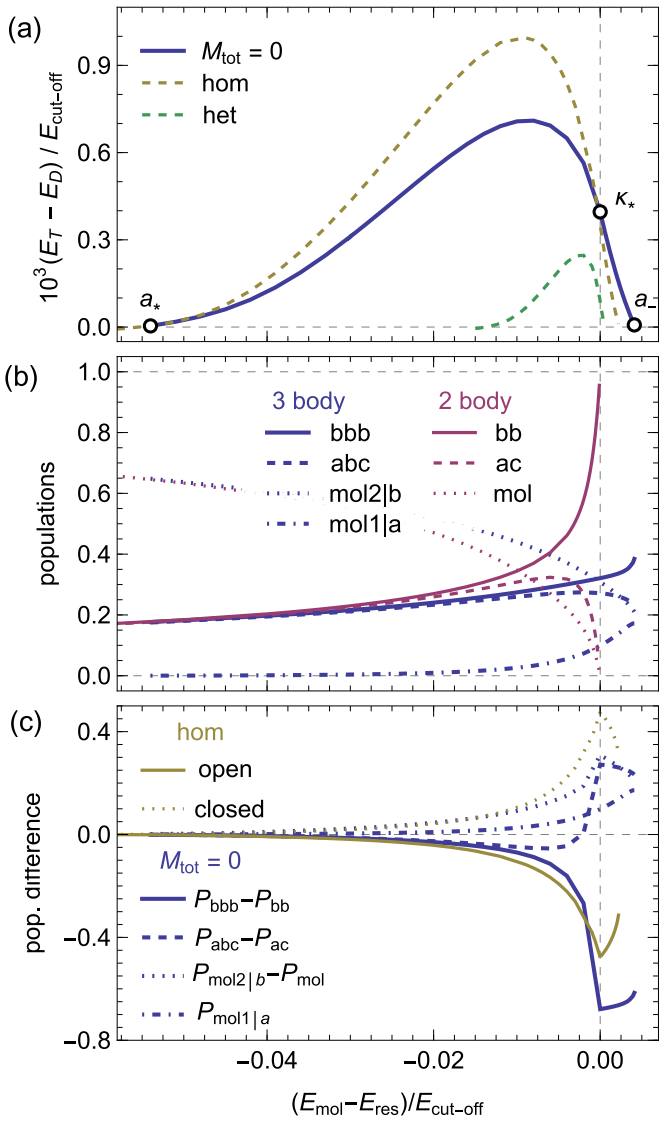

FIG. 11. Three-body sector. (a) Plot of the ground-state trimer binding energy with respect to the dimer, as a function of the bare $M_F = 0$ molecule energy. The large difference between the homo- and heteronuclear trimer is fully explained by Bose enhancement (Appendix B). The positions from which the Efimov features in Table II are extracted are indicated. (b) The populations in the various open and closed channels are shown for the two- and three-body sector of the $bb + ac$ model. (c) The difference between the three- and two-body populations are compared to those of the homonuclear model.

amplitudes $\beta_\sigma(q)$ and the binding wave number λ:

$$[f_\sigma(\tilde{q}) - g_\sigma(\tilde{q})]\tilde{\beta}_\sigma(\tilde{q}) - \delta_{\sigma,2} g_{22}(\tilde{q})\tilde{\beta}_2(\tilde{q}) - \sum_{\sigma' \neq \sigma} \int_0^1 d\tilde{k} L_{\sigma,\sigma'}(\tilde{q},\tilde{k})\tilde{\beta}_{\sigma'}(\tilde{k}) - \delta_{\sigma,2}\int_0^1 d\tilde{k} L_{22}(\tilde{q},\tilde{k})\tilde{\beta}_2(\tilde{k}) = 0. \quad (19)$$

Here we have defined the functions

$$f_\sigma(\tilde{q}) = \left(\frac{3\tilde{q}^2}{4} + \tilde{E}_\sigma + \tilde{E}_{\mathrm{mol},\sigma} - \tilde{E}_{222} + \tilde{\lambda}^2\right), \quad (20a)$$

TABLE II. Top: Parameters used for Fig. 11. $\tilde{E}_{\mathrm{thr}}$ denotes the continuum threshold energy. Bottom: Values of various features of the ground-state Efimov trimer; see Fig. 11(a).

Parameters			
Channel	*bb*	*ac*	*ab*/*bc*
σ	22	2	3/1
$\tilde{\Lambda}$	1	1	1
$\tilde{E}_{\mathrm{thr}}$	0	0.0004	0.0002
$\tilde{E}_{\mathrm{mol}} - \tilde{E}_{\mathrm{res}}$	Vary	–	−0.0008
$\tilde{a}$	Vary	–	100
Features			
	$M_{\mathrm{tot}} = 0$	Homo-	Hetero-
$\tilde{a}_\star$	2.88	2.88	5.77
$R^\star/a_\star$	6.53	2.18	2.18
$\tilde{a}_-$	−37.89	−69.2	−137.2
$R^\star/a_-$	−0.496	−0.091	−0.091
$\tilde{\kappa}_\star$	0.0199	0.0187	0.0094
$R^\star\kappa_\star$	0.374	0.118	0.118

$$g_\sigma(\tilde{q}) = \frac{\tilde{\Lambda}_1^2}{2\pi^2}\left(1 - \frac{\pi}{2}\sqrt{\frac{3\tilde{q}^2}{4} + \tilde{E}_{123} - \tilde{E}_{222} + \tilde{\lambda}^2}\right), \quad (20b)$$

$$g_{22}(\tilde{q}) = \frac{\tilde{\Lambda}_{22}^2}{\pi^2}\left(1 - \frac{\pi}{2}\sqrt{\frac{3\tilde{q}^2}{4} + \tilde{\lambda}^2}\right), \quad (20c)$$

$$L_{\sigma,\sigma'}(\tilde{q},\tilde{k}) = \frac{\tilde{\Lambda}_\sigma \tilde{\Lambda}_{\sigma'}}{4\pi^2} \times \ln\left(\frac{\tilde{k}^2 + \tilde{k}\tilde{q} + \tilde{q}^2 + \tilde{E}_{123} - \tilde{E}_{222} + \tilde{\lambda}^2}{\tilde{k}^2 - \tilde{k}\tilde{q} + \tilde{q}^2 + \tilde{E}_{123} - \tilde{E}_{222} + \tilde{\lambda}^2}\right), \quad (20d)$$

$$L_{22}(\tilde{q},\tilde{k}) = \frac{\tilde{\Lambda}_{22}^2}{\pi^2}\ln\left(\frac{\tilde{k}^2 + \tilde{k}\tilde{q} + \tilde{q}^2 + \tilde{\lambda}^2}{\tilde{k}^2 - \tilde{k}\tilde{q} + \tilde{q}^2 + \tilde{\lambda}^2}\right). \quad (20e)$$

To make the numerical computation of Eqs. (19) more resource effective we set the parameters of $\sigma = 1$ and $\sigma = 3$ to be equal, i.e., $\beta_1 = \beta_3$, $\Lambda_1 = \Lambda_3$, $E_1 = E_3$ and $E_{\mathrm{mol},1} = E_{\mathrm{mol},3}$. This way the three equations in (19) reduce to two (one for $\sigma = 2$ and one for $\sigma = 1$). In addition we fix the value of $E_{\mathrm{mol},1}$ and vary only $E_{\mathrm{mol}} = E_{\mathrm{mol},2}$ as we track the binding energy across the Feshbach resonance. In Fig. 11(a) we show the spectrum of the ground-state trimer, using the parameters in Table II, and we compare it to the homo- and heteronuclear model. In Table II we also extract the usual features of the spectrum, namely, the merging point with the dimer-atom continuum ($a_\star$), the dissociation into the *bbb* continuum (a_-) and the binding wave number at resonance $\kappa_\star$. The results of the two-body sector are used to obtain scattering length values from $\tilde{E}_{\mathrm{mol}}$. We further normalize the features with respect to $R^\star$, such that the high-momentum cutoff cancels and quantitative comparison to experiments is made possible.

The slope near a_- is smaller than in the two-channel models. This, however, is an artifact of varying only $E_{\mathrm{mol},2}$ while keeping the others constant. The same phenomenon is also observed in the pure heteronuclear model.

When comparing the $M_{\rm tot} = 0$ spectrum with that of the homonuclear two-channel model the impact of the *ac*-channel is apparent. Although the extreme points of the spectra (almost) overlap, the trimer formed under near-degenerate continua is bound less deep at its maximum. Thus, the functional form of the spectrum is altered by the presence of the *ac*-channel which suggests that care should be taken in the interpretation of some of the experimental results. For almost two decades, the majority of Efimov-related measurements were conducted at the free atom or atom-dimer threshold with the goal of proving (or disproving) universality. The comparison in Fig. 11(a) shows that the extreme points at their respective continuum thresholds might not suffice to characterize the energy level.

The model is presented here in terms of microscopic parameters such as the coupling constants between the continua and the bare molecules. When dealing with Feshbach resonances in a cold atom experiment one uses observables, such as the resonance width ΔB and the $R^\star$ parameter, to characterize the observed behavior. For this reason, the Efimov features are shown in units of $R^\star$ in Table II. We note that this normalization equates the homo- and heteronuclear model because the Bose enhancement cancels. To demonstrate the consequence of the *ac*-channel consider a given resonance (given $R^\star$). If there is no *ac*-channel one expects the merger with the dimer-atom continuum to be at $a_{\star,\rm hom} = R^\star/2.18$ [50]. However, if one is aware of its presence one anticipates $a_\star = R^\star/6.53 < a_{\star,\rm hom}$ to be a factor ∼3 lower (for the parameters in Table II).

As in the two-body sector, also here we can find the populations of the various three-atomic and molecule-atom channels to explore the spin composition of the trimer (Appendix F). The obtained expressions are accurate in the limit of small population in the $\sigma = 1$ and 3 molecular channel with respect to the $\sigma = 2$ population. This approximation breaks down for $E_{\rm mol} \geqslant E_{\rm res}$, where the latter decreases and approaches 0 at a_-. In fact, at a_- we expect the *bbb*-channel population to approach unity while all others vanish. In Fig. 11(b), where the populations are plotted for the ground-state trimer together with the two-body dimer populations, this property is not reproduced due to the approximation breaking down. At $a_\star$, the trimer populations asymptotically approach the dimer populations indicating the merger of the two energy levels: the trimer dissociates into a dimer and an atom. This is also shown in Fig. 11(c), where the difference between the three- and two-body populations is plotted.

The three-body *bbb* (mol2|*b*) population is smaller (larger) than the two-body *bb* (mol) population in the entire spectrum. The same is true in the homonuclear model. However, comparison of the *abc* and *ac* populations reveals that, as we move from a_- to $a_\star$, the *abc* population is larger (like a molecular channel), then crosses the *ac* population, and finally approaches it from below (like an atomic channel). Thus, close to the free atom (dimer-atom) threshold the *abc*-channel behaves like a molecular (atomic) channel.

Compared to the homonuclear model, the molecular channel of the $M_{\rm tot} = 0$ model is less populated. As in the two-body sector, this is in agreement with its binding energy being smaller.

VI. IMPLICATIONS FOR ^{7}Li TRIMER

Considering the special characteristics of the *bb*-channel of ^{7}Li, namely, overlapping resonances and near-degenerate continua, this near-degenerate continua model and our previous overlapping-resonances model [31] encapsulate the main contributions to the asymptotic scattering wave function. Both are considerably better than the regular two-channel model in the two-body sector and both predict slight alternations to the three-body sector. However, none agree with the unusual features of the trimer. Neither of these minimal models can explain why the three-body parameter is universal despite the resonance being narrow [22] or how the trimer crosses into the dimer-atom continuum [27]. We conclude that the ^{7}Li trimer energy is affected in a major way by the short-range details of the interaction potential whose treatment requires more sophisticated theoretical approaches [26].

VII. CONCLUSION

We have presented a simple and straightforward, but at the same time realistic and successful, model of resonant interactions in the presence of a near-degenerate continuum. The phenomenology of the two-body sector of ^{7}Li is reproduced. Since the interaction potential of the model is hard core (the simplest possible), quantitative agreement is limited. Inclusion of more interaction potential details, such as the van der Waals tail, should improve thereon; however, the physical mechanism causing the behavior of the various observables is clear. In particular, we have shown how a narrow resonance can have an enlarged universal range and how the functional form of the Efimov trimer is altered.

An interesting future aspect to explore is the many-body physics. The extended universal range of the two-body sector could work in favor of exploring universality near a narrow resonance.

A similar configuration was found to be important for the *p*-wave scattering of identical fermions in ^{40}K polarized in the *b*-state [51,52]

ACKNOWLEDGMENTS

We acknowledge fruitful discussions with J. P. D'Incao and S. J. J. M. F. Kokkelmans and members of his research group. This research was supported in part by the Israel Science Foundation (Grant No. 1543/20) and by a grant from the United States–Israel Binational Science Foundation (BSF), Jerusalem, Israel, and the United States National Science Foundation (NSF Award No. 2012125).

APPENDIX A: HETERONUCLEAR TWO-CHANNEL MODEL

The standard two-channel model (one open atomic and one closed molecular channel) can be written for identical bosons (homonuclear) or distinguishable particles (heteronuclear). While the latter is usually applied to a fermionic mixture of different spin states (^{6}Li being a practical example [53]), it may of course be used for any distinguishable particles, such as different-spin bosons.

The heteronuclear two-body wave function, written here for $\sigma = 3$, is

$$|\psi_{\rm het}^{(\sigma=3)}\rangle = \beta_3 \hat{d}^\dagger_{3,\vec{q}=0}|0\rangle + \int \frac{d^3k}{(2\pi)^3}\alpha_3(\vec{k})\hat{a}^\dagger_{1,\vec{k}}\hat{a}^\dagger_{2,-\vec{k}}|0\rangle. \quad \text{(A1)}$$

The Schrödinger equation $\hat{H}|\psi_{\rm het}^{(\sigma=3)}\rangle = E|\psi_{\rm het}^{(\sigma=3)}\rangle$, where $\hat{H}$ is given in Eq. (1), leads to the following two coupled equations:

$$\beta_3(E_{\rm mol,3} - E) + \Lambda_3 \int \frac{d^3k}{(2\pi)^3}\alpha_3(\vec{k}) = 0, \quad \text{(A2a)}$$

$$\alpha_3(\vec{q})\left(\frac{\hbar^2 q^2}{m} + E_{12} - E\right) + \Lambda_3\beta_3 = 0. \quad \text{(A2b)}$$

The second equation shows that the free-particle amplitude $\alpha_\sigma(\vec{q})$ is a Lorentzian of its argument $\vec{q}$, causing the integral in the first equation to diverge linearly in $|\vec{q}|$. To deal with this UV divergence, as mentioned in Sec. IV, a high-momentum cutoff $k_{\rm cutoff}$ is introduced. The Lorentzian form of $\alpha_\sigma(\vec{q})$ agrees with the expected exponential in position space (halo dimer).

In general, Eqs. (A2) lead to three equivalent equations in the two-body sector due to the different coupling constants Λ_σ and molecular and atomic detunings $E_{{\rm mol},\sigma}$ and E_σ. If one assumes, however, that $\Lambda_\sigma = \Lambda$, $E_{{\rm mol},\sigma} = E_{\rm mol}$, and $E_\sigma = 0$ for all σ, the equations of each sector become identical. The scattering amplitude $\tilde{f}(\tilde{k}_0) = -\tilde{\Lambda}\tilde{\beta}(\tilde{k}_0)/4\pi$ is then given by

$$\frac{1}{\tilde{f}(\tilde{k}_0)} = \frac{4\pi\left(\tilde{E}_{\rm mol} - \tilde{k}_0^2\right)}{\tilde{\Lambda}^2} - \frac{2}{\pi}\left[1 - \frac{i\pi}{2}\tilde{k}_0\right], \quad \text{(A3)}$$

and the dimer binding energy $-\tilde{\lambda}^2$ is found by solving

$$(\tilde{E}_{\rm mol} + \tilde{\lambda}^2) - \frac{\tilde{\Lambda}^2}{2\pi^2}\left(1 - \frac{\pi}{2}\tilde{\lambda}\right) = 0. \quad \text{(A4)}$$

In the three-body sector one starts from

$$|\psi_{\rm het}^{(3B)}\rangle = \sum_\sigma \int \frac{d^3q}{(2\pi)^3}\beta_\sigma(\vec{q})\hat{d}^\dagger_{\sigma,\vec{q}}\hat{a}^\dagger_{\sigma,-\vec{q}}|0\rangle + \int \frac{d^3q}{(2\pi)^3} \times \int \frac{d^3k}{(2\pi)^3}\alpha(\vec{q},\vec{k})\hat{a}^\dagger_{3,\vec{k}+\frac{\vec{q}}{2}}\hat{a}^\dagger_{1,-\vec{k}+\frac{\vec{q}}{2}}\hat{a}^\dagger_{2,-\vec{q}}|0\rangle, \quad \text{(A5)}$$

which, in general, leads to three coupled integral equations. Assuming the three two-body subsystems to be identical reduces them to a single equation:

$$\left[\tilde{E}_{\rm mol} + \frac{3\tilde{q}^2}{4} + \tilde{\lambda}^2 - \frac{\tilde{\Lambda}^2}{2\pi^2}\left(1 - \frac{\pi}{2}\sqrt{\frac{3\tilde{q}^2}{4} + \tilde{\lambda}^2}\right)\right]\tilde{\beta}(\tilde{q}) - \frac{\tilde{\Lambda}^2}{2\pi^2}\int_0^1 d\tilde{k}\ln\left(\frac{\tilde{k}^2 + \tilde{k}\tilde{q} + \tilde{q}^2 + \tilde{\lambda}^2}{\tilde{k}^2 - \tilde{k}\tilde{q} + \tilde{q}^2 + \tilde{\lambda}^2}\right)\tilde{\beta}(\tilde{k}) = 0, \quad \text{(A6)}$$

where the trimer binding energy is given by $-\tilde{\lambda}^2$.

For the populations in the open and closed channels of the two- and three-body sectors, see Appendix E.

APPENDIX B: CONTRASTING THE HOMO- AND HETERONUCLEAR TWO-CHANNEL MODELS

The derivation in the homo- and heteronuclear case are equivalent. In particular, the identical two-body sectors assumption is trivial for homonuclear systems. However, when acting with the interaction Hamiltonian $\sim\hat{d}^\dagger\hat{a}\hat{a}$ on the free particle wave function $\sim\hat{a}^\dagger\hat{a}^\dagger|0\rangle$, the homonuclear model allows for two paths for creating a molecule, while in the heteronuclear model there is only one option. This effect is known as Bose enhancement. The two- and three-body equations for the homonuclear model are thus obtained from the heteronuclear equations above by substituting $\tilde{\Lambda} \to \sqrt{2}\tilde{\Lambda}$.

Although Bose enhancement is usually discussed in the context of many-body physics (e.g., the condensation of bosons into a Bose-Einstein condensate), its effect is already apparent at the two-body level and demonstrated beautifully by comparing the homo- and heteronuclear two-channel models. From the above discussion we see that, if $\tilde{\Lambda}_{\rm het} = \tilde{\Lambda}$, then $\tilde{\Lambda}_{\rm hom} = \sqrt{2}\tilde{\Lambda}$, i.e., the effective coupling between the open channel and the closed channel is a factor $\sqrt{2}$ larger for identical bosons. The stronger coupling leads to a broader Feshbach resonance, as compared to the heteronuclear model, with all of its characteristics: larger shift from the bare resonance, smaller $R^\star$, shallower dimer, and slower population increase (decrease) of the closed (open) channel when moving away from resonance.

In the three-body sector, the larger effective coupling leads to a deeper bound trimer and merging features that are farther away from resonance. In fact, if one rescales both axes for the heteronuclear trimer in Fig. 11(a) by a factor of $(\tilde{R}^\star_{\rm het}/\tilde{R}^\star_{\rm hom})^2 = 4$, the two traces are identical.

APPENDIX C: DEGENERACY LIMIT OF $\tilde{R}^\star_{bb}$ FROM E_D

In the main text we noted that, in the limit $E_{13} \to E_{22}$, the value of $\tilde{R}^\star_{bb}$ extracted from the dimer approaches $\tilde{R}^\star_{\rm hom}\tilde{R}^\star_{\rm het}/(\tilde{R}^\star_{\rm hom} + \tilde{R}^\star_{\rm het})$.

To derive this limit we start from Eq. (15) for the dimer binding energy and plug in $E_{13} = E_{22}$. Using $\tilde{R}^\star_{\rm hom} = 2\pi/\tilde{\Lambda}^2_{22}$ and $\tilde{R}^\star_{\rm het} = 4\pi/\tilde{\Lambda}^2_2$ one obtains

$$(\tilde{E}_{\rm mol,2} - \tilde{E}_{22} + \tilde{\lambda}^2) - \frac{2}{\pi}\left(\frac{1}{\tilde{R}^\star_{\rm hom}} + \frac{1}{\tilde{R}^\star_{\rm het}}\right)\left(1 - \frac{\pi}{2}\tilde{\lambda}\right) = 0. \quad \text{(C1)}$$

Comparison with Eq. (A4) leads to the aforementioned expression for $\tilde{R}^\star_{bb}$.

APPENDIX D: FROM THE TWO- TO THE THREE-BODY SECTOR

In the main text we noted that $|\psi_{3B}\rangle$ in Eq. (18) has three different, uncoupled two-body subsystems, as illustrated in Fig. 5. In fact, this effect is true also for the heteronuclear two-channel model, whose three-body wave function, Eq. (A5), has three two-body subsystems of the form of Eq. (A1). To illustrate how to go from the two- to the three-body wave function we introduce the operator

$$\hat{\mathcal{O}}_{\sigma=3}(\vec{q}) = \beta_3(\vec{q})\hat{d}^\dagger_{3,\vec{q}} + \int \frac{d^3k}{(2\pi)^3}\alpha_3(\vec{q},\vec{k})\hat{a}^\dagger_{1,\vec{k}+\frac{\vec{q}}{2}}\hat{a}^\dagger_{2,-\vec{k}+\frac{\vec{q}}{2}}, \quad \text{(D1)}$$

with which Eq. (A1) can be written as

$$\left|\psi_{\rm het}^{(\sigma)}\right\rangle = \hat{\mathcal{O}}_\sigma(\vec{q}=0)|0\rangle. \tag{D2}$$

The operator $\hat{\mathcal{O}}_\sigma(\vec{q})$ creates a two-body system of type σ with center-of-mass momentum $\hbar\vec{q}$. We add a particle of type σ and with momentum $-\hbar\vec{q}$ to $|\psi_{\rm het}^{(\sigma)}\rangle$ and sum over $\sigma = 1, 2, 3$ to obtain

$$\left|\psi_{\rm het}^{(3B)}\right\rangle = \sum_\sigma \int \frac{d^3q}{(2\pi)^3}\hat{\mathcal{O}}_\sigma(\vec{q})\hat{a}^\dagger_{\sigma,-\vec{q}}|0\rangle. \tag{D3}$$

Comparing this expression to Eq. (A5) shows that the β_σ amplitudes are the same in the two- and three-body sector, while the two-body α_σ amplitudes are related to the three-body α amplitude via

$$\begin{aligned}\alpha(\vec{q},\vec{k}) = &\alpha_1\left(\vec{k}-\frac{\vec{q}}{2},-\frac{\vec{k}}{2}-\frac{3\vec{q}}{4}\right) + \alpha_2(\vec{q},\vec{k})\\ &+\alpha_3\left(-\vec{k}-\frac{\vec{q}}{2},-\frac{\vec{k}}{2}+\frac{3\vec{q}}{4}\right).\end{aligned} \tag{D4}$$

In the homonuclear case the identity of the open channel atoms renders the σ index redundant, leading to the conclusion that the three-body α-amplitude is equal to its two-body counterpart with finite center-of-mass momentum.

APPENDIX E: OPEN AND CLOSED CHANNEL POPULATIONS IN THE HOMO- AND HETERONUCLEAR MODEL

We present expressions for the populations of the open and closed channels in the two- and three-body sector of the heteronuclear model using the equal two-body sector assumption.

In the two-body sector the population of the open and closed channels for the dimer is

$$P_{\rm open} = \frac{1}{\mathcal{N}}\int\frac{d^3k}{(2\pi)^3}|\alpha(\vec{k})|^2, \tag{E1a}$$

$$P_{\rm closed} = \frac{1}{\mathcal{N}}|\beta|^2, \tag{E1b}$$

where

$$\mathcal{N} = \int\frac{d^3k}{(2\pi)^3}|\alpha(\vec{k})|^2 + |\beta|^2. \tag{E2}$$

Using the second equation in (A2) one replaces $\alpha(\vec{k})$ for β, which conveniently cancels, to obtain

$$P_{\rm open} = \frac{1}{\mathcal{N}}\left(\frac{\tilde{\Lambda}^2}{8\pi\tilde{\lambda}}\right), \tag{E3a}$$

$$P_{\rm closed} = \frac{1}{\mathcal{N}}, \tag{E3b}$$

and

$$\mathcal{N} = \frac{\tilde{\Lambda}^2}{8\pi\tilde{\lambda}} + 1. \tag{E4}$$

In the three-body sector, similar to the two-body sector, the populations for the trimer are

$$P_{\rm open} = \frac{1}{\mathcal{N}}\int\frac{d^3q}{(2\pi)^3}\int\frac{d^3k}{(2\pi)^3}|\alpha(\vec{q},\vec{k})|^2, \tag{E5a}$$

$$P_{\rm closed} = \frac{1}{\mathcal{N}}\int\frac{d^3q}{(2\pi)^3}|\beta(\vec{q})|^2, \tag{E5b}$$

and $\mathcal{N}$ is the appropriate normalization factor (the sum of both integrals). The free-particle amplitude $\alpha(\vec{q},\vec{k})$ is expressed in terms of the molecule-atom amplitude $\beta(\vec{q})$ via the Schrödinger equation upon which the integral over $\vec{k}$ can be solved. The open channel population thus simplifies to

$$P_{\rm open} = \frac{\tilde{\Lambda}^2}{8\pi\mathcal{N}}\int\frac{d^3\tilde{q}}{(2\pi)^3}\frac{|\beta(\tilde{q})|^2}{\sqrt{3\tilde{q}^2/4+\tilde{\lambda}^2}}. \tag{E6}$$

Having found the trimer binding wave number and its wave function from Eq. (A6), the populations may be computed.

In contrast to the equations presented in Appendix A, here the homonuclear expressions are identical to those of the heteronuclear model. However, when plotted as a function of $E_{\rm mol}$ they differ as described at the end of Appendix B, due to the difference in binding energy.

APPENDIX F: DRIVATION OF THE OPEN- AND CLOSED-CHANNEL POPULATIONS IN THE THREE-BODY SECTOR

According to the three-body wave function in Eq. (18), the open channel populations are (i = bbb, abc)

$$P_i = \frac{1}{\mathcal{N}}\int\frac{d^3q}{(2\pi)^3}\int\frac{d^3k}{(2\pi)^3}|\alpha_i(\vec{q},\vec{k})|^2, \tag{F1}$$

and the closed channel populations are ($\sigma = 1, 2, 3$)

$$P_\sigma = \frac{1}{\mathcal{N}}\int\frac{d^3q}{(2\pi)^3}|\beta_\sigma(\vec{q})|^2. \tag{F2}$$

The normalization constant $\mathcal{N}$ is found from $\sum_i P_i + \sum_\sigma P_\sigma = 1$. From the solution of Eqs. (19) the binding wave number λ and the eigenvectors β_σ are obtained. The closed channel populations are thus readily computed. For the open channel populations we use the Schrödinger equations to express α_i in terms of β_σ, resulting in

$$P_{\rm bbb} = \frac{1}{\mathcal{N}}\int\frac{d^3\tilde{q}}{(2\pi)^3}\int\frac{d^3\tilde{k}}{(2\pi)^3}\left|\frac{\tilde{\Lambda}_{22}\beta_2(\tilde{q})}{\tilde{k}^2+3\tilde{q}^2/4+\tilde{\lambda}^2}\right|^2 \tag{F3}$$

for the *bbb*-open channel. Since $\beta_2(\tilde{q})$ is k-independent the integral over the latter may be computed, and we get

$$P_{\rm bbb} = \frac{\tilde{\Lambda}_{22}^2}{8\pi\mathcal{N}}\int\frac{d^3\tilde{q}}{(2\pi)^3}\frac{|\beta_2(\tilde{q})|^2}{\sqrt{3\tilde{q}^2/4+\tilde{\lambda}^2}}. \tag{F4}$$

For i = abc the substitution leads to

$$\begin{aligned}P_{\rm abc} = &\frac{1}{\mathcal{N}}\int\frac{d^3\tilde{q}}{(2\pi)^3}\int\frac{d^3\tilde{k}}{(2\pi)^3}\\ &\times\left|\frac{\tilde{\Lambda}_1\beta_1\left(\tilde{k}-\frac{\tilde{q}}{2}\right)+\tilde{\Lambda}_2\beta_2\left(\tilde{q}\right)+\tilde{\Lambda}_3\beta_3\left(\tilde{k}+\frac{\tilde{q}}{2}\right)}{\tilde{k}^2+3\tilde{q}^2/4+\tilde{E}_{123}-\tilde{E}_{222}+\tilde{\lambda}^2}\right|^2.\end{aligned} \tag{F5}$$

At this stage we make the simplifying assumption $\beta_{1,3} \ll \beta_2$, which is equivalent to $P_{1,3} \ll P_2$, permitting integration over k:

$$P_{\mathrm{abc}} = \frac{\tilde{\Lambda}_2^2}{8\pi\mathcal{N}} \int \frac{d^3\tilde{q}}{(2\pi)^3} \frac{|\beta_2(\tilde{q})|^2}{\sqrt{3\tilde{q}^2/4 + \tilde{E}_{123} - \tilde{E}_{222} + \tilde{\lambda}^2}}. \quad \text{(F6)}$$

While the expressions for P_{bbb} and P_σ are exact, the expression for P_{abc} is approximate. The approximation breaks down when $P_{1,3} \approx P_2$, which is the case at $E_{\mathrm{mol}} > E_{\mathrm{res}}$ [see Figs. 11(b) and 11(c)]. The populations at a_- are thus not captured well by the expressions derived here.

[1] C. Chin, R. Grimm, P. Julienne, and E. Tiesinga, Feshbach resonances in ultracold gases, Rev. Mod. Phys. **82**, 1225 (2010).

[2] E. Braaten and H.-W. Hammer, Universality in few-body systems with large scattering length, Phys. Rep. **428**, 259 (2006).

[3] P. Naidon and S. Endo, Efimov physics: A review, Rep. Prog. Phys. **80**, 056001 (2017).

[4] C. H. Greene, P. Giannakeas, and J. Pérez-Ríos, Universal few-body physics and cluster formation, Rev. Mod. Phys. **89**, 035006 (2017).

[5] J. P. D'Incao, Few-body physics in resonantly interacting ultracold quantum gases, J. Phys. B: At. Mol. Opt. Phys. **51**, 043001 (2018).

[6] M. Zaccanti, B. Deissler, C. D'Errico, M. Fattori, M. Jona-Lasinio, S. Müller, G. Roati, M. Inguscio, and G. Modugno, Observation of an Efimov spectrum in an atomic system, Nat. Phys. **5**, 586 (2009).

[7] F. Ferlaino, S. Knoop, M. Berninger, W. Harm, J. P. D'Incao, H.-C. Nägerl, and R. Grimm, Evidence for Universal Four-Body States Tied to an Efimov Trimer, Phys. Rev. Lett. **102**, 140401 (2009).

[8] B. Huang, L. A. Sidorenkov, R. Grimm, and J. M. Hutson, Observation of the Second Triatomic Resonance in Efimov's Scenario, Phys. Rev. Lett. **112**, 190401 (2014).

[9] X. Xie, M. J. Van de Graaff, R. Chapurin, M. D. Frye, J. M. Hutson, J. P. D'Incao, P. S. Julienne, J. Ye, and E. A. Cornell, Observation of Efimov Universality Across a Non-Universal Feshbach Resonance in ^{39}K, Phys. Rev. Lett. **125**, 243401 (2020).

[10] M. Berninger, A. Zenesini, B. Huang, W. Harm, H. C. Nägerl, F. Ferlaino, R. Grimm, P. Julienne, and J. Hutson, Universality of the Three-Body Parameter for Efimov States in Ultracold Cesium, Phys. Rev. Lett. **107**, 120401 (2011).

[11] J. Wang, J. P. D'Incao, B. D. Esry, and C. H. Greene, Origin of the Three-Body Parameter Universality in Efimov Physics, Phys. Rev. Lett. **108**, 263001 (2012).

[12] P. Naidon, S. Endo, and M. Ueda, Microscopic Origin and Universality Classes of the Efimov Three-Body Parameter, Phys. Rev. Lett. **112**, 105301 (2014).

[13] R. J. Wild, P. Makotyn, J. M. Pino, E. A. Cornell, and D. S. Jin, Measurements of Tan's Contact in an Atomic Bose-Einstein Condensate, Phys. Rev. Lett. **108**, 145305 (2012).

[14] S.-K. Tung, K. Jiménez-García, J. Johansen, C. Parker, and C. Chin, Geometric Scaling of Efimov States in a ^{6}Li $-$ ^{133}Cs Mixture, Phys. Rev. Lett. **113**, 240402 (2014).

[15] A. Zenesini, B. Huang, M. Berninger, H.-C. Nägerl, F. Ferlaino, and R. Grimm, Resonant atom-dimer collisions in cesium: Testing universality at positive scattering lengths, Phys. Rev. A **90**, 022704 (2014).

[16] R. J. Fletcher, R. Lopes, J. Man, N. Navon, R. P. Smith, M. W. Zwierlein, and Z. Hadzibabic, Two- and three-body contacts in the unitary Bose gas, Science **355**, 377 (2017).

[17] C. Ji, E. Braaten, D. R. Phillips, and L. Platter, Universal relations for range corrections to Efimov features, Phys. Rev. A **92**, 030702(R) (2015).

[18] J. Johansen, B. J. DeSalvo, K. Patel, and C. Chin, Testing universality of Efimov physics across broad and narrow Feshbach resonances, Nat. Phys. **13**, 731 (2017).

[19] R. Chapurin, X. Xie, M. J. Van de Graaff, J. S. Popowski, J. P. D'Incao, P. S. Julienne, J. Ye, and E. A. Cornell, Precision Test of the Limits to Universality in Few-Body Physics, Phys. Rev. Lett. **123**, 233402 (2019).

[20] A. Li, Y. Yudkin, P. S. Julienne, and L. Khaykovich, Efimov resonance position near a narrow Feshbach resonance in a Li-Cs mixture, Phys. Rev. A **105**, 053304 (2022).

[21] J. Etrych, G. Martirosyan, A. Cao, J. A. P. Glidden, L. H. Dogra, J. M. Hutson, Z. Hadzibabic, and C. Eigen, Pinpointing Feshbach resonances and testing Efimov universalities in ^{39}K, Phys. Rev. Res. **5**, 013174 (2023).

[22] N. Gross, Z. Shotan, O. Machtey, S. J. J. M. F. Kokkelmans, and L. Khaykovich, Study of Efimov physics in two nuclear-spin sublevels of ^{7}Li, C. R. Phys. **12**, 4 (2011).

[23] Y. Wang and P. S. Julienne, Universal van der Waals physics for three cold atoms near Feshbach resonances, Nat. Phys. **10**, 768 (2014).

[24] T. Secker, D. J. M. Ahmed-Braun, P. M. A. Mestrom, and S. J. J. M. F. Kokkelmans, Multichannel effects in the Efimov regime from broad to narrow Feshbach resonances, Phys. Rev. A **103**, 052805 (2021).

[25] J.-L. Li, T. Secker, P. M. A. Mestrom, and S. J. J. M. F. Kokkelmans, Strong spin-exchange recombination of three weakly interacting ^{7}Li atoms, Phys. Rev. Res. **4**, 023103 (2022).

[26] J. P. D'Incao (private communication).

[27] Y. Yudkin, R. Elbaz, and L. Khaykovich, Efimov energy level rebounding off the atom-dimer continuum, arXiv:2004.02723.

[28] P. N. Jepsen, Y. K. Lee, I. Dimitrova H. Lin, Y. Margalit, W. W. Ho, and W. Ketterle, Long-lived phantom helix states in Heisenberg quantum magnets, Nat. Phys. **18**, 899 (2022).

[29] N. Gross, Z. Shotan, S. J. J. M. F. Kokkelmans, and L. Khaykovich, Nuclear-Spin-Independent Short-Range Three-Body Physics in Ultracold Atoms, Phys. Rev. Lett. **105**, 103203 (2010).

[30] The "*bb*-channel" refers to two free atoms in the *b*-state. By "scattering in the *bb*-channel" we mean a scattering event for which both the initial and the final state consist of two separated atoms in the *b*-state. However, the intermediate state is a superposition of all $M_{\mathrm{tot}} = 0$ two-body channels. A loosely bound dimer associated with a Feshbach resonance in the *bb*-channel has $M_{\mathrm{tot}} = 0$ spin character and its wave function has projections on multiple channels. At the resonance position the projection on the *bb*-channel approaches unity, and the dimer is thus called the "*bb*-channel dimer." Note the somewhat confusing jargon: Our model of the *bb*-channel, which describes

scattering and dimers in the sense explained above, includes the *bb*-channel (two atoms in the *b*-state), the *ac*-channel, and a closed channel made up of the remaining $M_{\rm tot} = 0$ two-body channels.

[31] Y. Yudkin and L. Khaykovich, Efimov scenario for overlapping narrow Feshbach resonances, Phys. Rev. A **103**, 063303 (2021).

[32] K. Jachymski and P. S. Julienne, Analytical model of overlapping Feshbach resonances, Phys. Rev. A **88**, 052701 (2013).

[33] P. S. Julienne and J. M. Hutson, Contrasting the wide Feshbach resonances in ^{6}Li and ^{7}Li, Phys. Rev. A **89**, 052715 (2014).

[34] D. S. Petrov, Three-Boson Problem near a Narrow Feshbach Resonance, Phys. Rev. Lett. **93**, 143201 (2004).

[35] V. Gurarie and L. Radzihovsky, Resonantly paired fermionic superfluids, Ann. Phys. **322**, 2 (2007).

[36] F. H. Mies, E. Tiesinga, and P. S. Julienne, Manipulation of Feshbach resonances in ultracold atomic collisions using time-dependent magnetic fields, Phys. Rev. A **61**, 022721 (2000).

[37] Throughout this paper coupled-channel calculations were performed using an *s*-wave basis only.

[38] It is possible to produce very similar *aa* and *bb* scattering lengths (except for the region of the narrow resonance) by rescaling the magnetic field axis of the *aa*-channel by a factor of 1.18. In this case, also the two dimers lie on top of each other, suggesting that the two resonances are identical. However, this procedure and conclusion are problematic for at least two reasons. First, due to repulsion from the narrow resonance dimer, if both resonances are identical, the *bb*-dimer should be deeper. The fact that it is not, even after rescaling, points to the shallowing effect of the *ac*-channel. Second, rescaling the magnetic field axis physically means changing the magnetic moment of the bare molecule. However, since the two resonances arise due to the same bare molecule of the singlet potential, such a change is unphysical.

[39] Y. Castin, Basic theory tools for degenerate Fermi gases, in *Ultra-Cold Fermi Gases, Proceedings of the Enrico Fermi Varenna School on Fermi Gases*, edited by C. Salomon, M. Inguscio, and W. Ketterle (IOS Press, Amsterdam, 2007), pp. 289–349.

[40] D. S. Petrov, The few-atom problem, arXiv:1206.5752.

[41] V. E. Colussi, Chris H. Greene, and J. P. D'Incao, Three-Body Physics in Strongly Correlated Spinor Condensates, Phys. Rev. Lett. **113**, 045302 (2014).

[42] P. M. A. Mestrom, J.-L. Li, V. E. Colussi, T. Secker, and S. J. J. M. F. Kokkelmans, Three-body spin mixing in spin-1 Bose-Einstein condensates, Phys. Rev. A **104**, 023321 (2021).

[43] M. Arndt, M. Ben Dahan, D. Guéry-Odelin, M. W. Reynolds, and J. Dalibard, Observation of a Zero-Energy Resonance in Cs-Cs Collisions, Phys. Rev. Lett. **79**, 625 (1997).

[44] E. R. I. Abraham, W. I. McAlexander, J. M. Gerton, R. G. Hulet, R. Côté, and A. Dalgarno, Triplet s-wave resonance in ^{6}Li collisions and scattering lengths of ^{6}Li and ^{7}Li, Phys. Rev. A **55**, R3299 (1997).

[45] In Eqs. (9), the δ functions are intended to be directional. In this sense, $\delta(\tilde{k} - \tilde{k}_0)$ approaches infinity only if the variable $\tilde{k}$ and the incident momentum $\tilde{k}_0$ are identical in both direction and amplitude. The same is true for $\tilde{k}$ and $\sqrt{\tilde{k}_0^2 - \Delta\tilde{E}}$, which is the incident momentum of the *ac*-channel, in $\delta(\tilde{k} - \sqrt{\tilde{k}_0^2 - \Delta\tilde{E}})$. Here the vector symbols were omitted for readability.

[46] The formal textbook solution of the Schrödinger equation for a scattering problem is the Lippmann-Schwinger equation. In fact, Eqs. (9) are the projections of the latter, which in our notion, using Eqs. (1), (7), and (8), reads $|\psi_0\rangle = |\psi_0^{(\rm in)}\rangle + (E - \hat{H}_{\rm atom} - \hat{H}_{\rm mol})^{-1}\hat{H}_{\rm int}|\psi_0\rangle$, onto the *bb*- and *ac*-channels.

[47] The result of the coupled-channel calculations is the scattering matrix S_{ij}, which describes a scattering event from channel i to channel j, e.g., $bb \to bb$ or $bb \to ac$. From S_{ij} one may compute $T_{ij} = \delta_{ij} - S_{ij}$ and $\sin^2\eta_{ij} = |T_{ij}|^2/4$. In the case of *s*-wave scattering, the $i \to i$ scattering amplitude is $f_{ii} = -T_{ii}/2ik$. Thus, $\sin^2\eta_{ii} = |kf_{ii}|^2$ and Fig. 2 is directly comparable to Figs. 7 and 8.

[48] Within the picture of an (atomic) open channel coupled to a (molecular) closed channel the concept of the pole strength can be understood in terms of the coupling strength. Strong coupling gives rise to a broad Feshbach resonance with $R^\star \ll r_{vdW}$ and $s_{res} \gg 1$, while weak coupling gives rise to a narrow Feshbach resonance with $R^\star \gg r_{vdW}$ and $s_{res} \ll 1$. Hence, either $R^\star$ or s_{res} can be used to quantify the pole strength.

[49] As mentioned in the beginning of Sec. III, here we deal with a $F = 1$ spinor gas. However, the ground state of ^{7}Li has both a $F = 1$ and $F = 2$ part (Fig. 1). The energetically low-lying three-body continua consist of three particles with $J = -1/2$. There are three options to form such a continuum: *bbb*, *abc* ($E_{abc} - E_{bbb} = 28$ MHz), and *aad* ($E_{aad} - E_{bbb} = 108$ MHz). The last is neglected because, first, it does not exist in a $F = 1$ spinor gas and, second, because, albeit close, it is almost four times further detuned than the leading-order *abc* contribution.

[50] Y. Nishida, New Type of Crossover Physics in Three-Component Fermi Gases, Phys. Rev. Lett. **109**, 240401 (2012).

[51] D. J. M. Ahmed-Braun, K. G. Jackson, S. Smale, C. J. Dale, B. A. Olsen, S. J. J. M. F. Kokkelmans, P. S. Julienne, and J. H. Thywissen, Probing open- and closed-channel *p*-wave resonances, Phys. Rev. Res. **3**, 033269 (2021).

[52] S. J. J. M. F. Kokkelmans (private communication).

[53] J. H. Huckans, J. R. Williams, E. L. Hazlett, R. W. Stites, and K. M. O'Hara, Three-Body Recombination in a Three-State Fermi Gas with Widely Tunable Interactions, Phys. Rev. Lett. **102**, 165302 (2009).

Chapter 6

Next Step: Measuring the Lifetime of the Superposition State

In the experimental part of this Thesis the precise measurement of the binding energy of an Efimov trimer below and above the atom-dimer threshold was presented. While a lot of understanding was gained from demanding three-body calculations, various aspects remain unexplained. In particular, the longevity and the nature of the trimer above the continuum threshold continue to puzzle. We expect that more experimental input will be able to shed some light. After the binding energy, the next observable of interest is the lifetime of the dimer-trimer superposition. This quantity will provide insight to the trimer's intrinsic lifetime, the coherence time of the superposition and the (in)elastic scattering cross-sections between the constituents of the superposition and the atoms in the background gas.

Unfortunately, the low signal-to-noise ratio intrinsic to the experimental procedure developed and applied in this Thesis, does not allow a quantitative analysis of the lifetime. It is thus necessary to come up with an improved scheme. The idea is to leverage the knowledge of the binding energy, produce a larger signal, and measure it in the absence of the background atoms.

Here we present a roadmap on how we plan to measure the lifetime of the dimer-trimer superposition state. Preparations to implement the scheme are under way in the lab.

6.1 Dipole Trap

First of all, a new optical dipole trap must be built. During the first steps of setting up the new scheme, the 100 W IPG laser that provided the IR light for the dipole

trap used in this Thesis and many previous projects, decided it was time to retire. Subsequently, a new 200 W laser[1] was acquired. While the need to plan and assemble a new beam path is a set-back in time, the break-down comes at a reasonably good time, given the upgrade-desiring previous setup.

The optical setup is shown schematically in Fig. 6.1. The cw high-power output of the laser is focused onto a AOM to split the the beam into a single-beam trap (sODT) and a crossed-beam trap (xODT). The former, derived from the first order of the AOM, is designed to maximize atom number loaded into the dipole trap from MOT. At the atom position, it has a waist of ~ 50 μm, a trap volume of 18.4×10^6 μm^3 and, with 150 W, provides a trap depth of $U_0/k_B = 1.9$ mK. It can be frequency modulated during the CMOT and loading sequence to increase the volume at the expense of slightly decreasing the depth. The zeroth order of the AOM is directed through a second AOM whose first order forms the xODT. This trap is designed to maximize the final state of evaporation and thus the initial conditions for the experiment (large atom number, high density, low temperature). Each beam has a waist of ~ 25 μm such that 15 W of laser power per beam is enough to create a 1.5 mK deep trap. The combined volume of the trap is 15.6×10^3 μm^3.

Both AOMs are amplitude stabilized via a feedback loop. To this end we measure the power in the first order at the backside of an uncoated mirror with a low-noise photo-diode[2]. The photo-current is led through a log-amplifier providing four orders-of-magnitude of dynamical range. This permits accurate control of the power during all evaporation stages and the interferometer sequence.

The goal is to reach $\gtrsim 5 \times 10^4$ atoms at a temperature of $\lesssim 1$ μK. Average densities of $\gtrsim 3 \times 10^{12}$ cm^{-3} should be achievable in the xODT. This corresponds to a phase-space density close to unity, i.e. a quantum gas on the onset of degeneracy. These are ideal conditions for the double pulse sequence comprising the interferometer.

6.2 Interferometer Sequence

For a given magnetic field B, both the dimer binding energy $E_D = -\hbar\omega_D$ and the trimer binding energy $E_T = -\hbar\omega_T$ are known from our work presented in this Thesis (Chap. 3). It is therefore possible to address the two bound states using a long, dual-frequency rf pulse. In principle, this makes Fourier broadening obsolete and the short-pulse limitation is circumvented. However, the finite lifetime of the superposition state ($\lesssim 300$ μs) constrains the realistically feasible pulse lengths to a few tens of μs. A slightly improved conversion efficiency should thus be possible.

[1] IPG Photonics: YLR-200-LP-AC-Y14
[2] Hamamatsu: InGaAs PIN Photodiode, G12180-030A

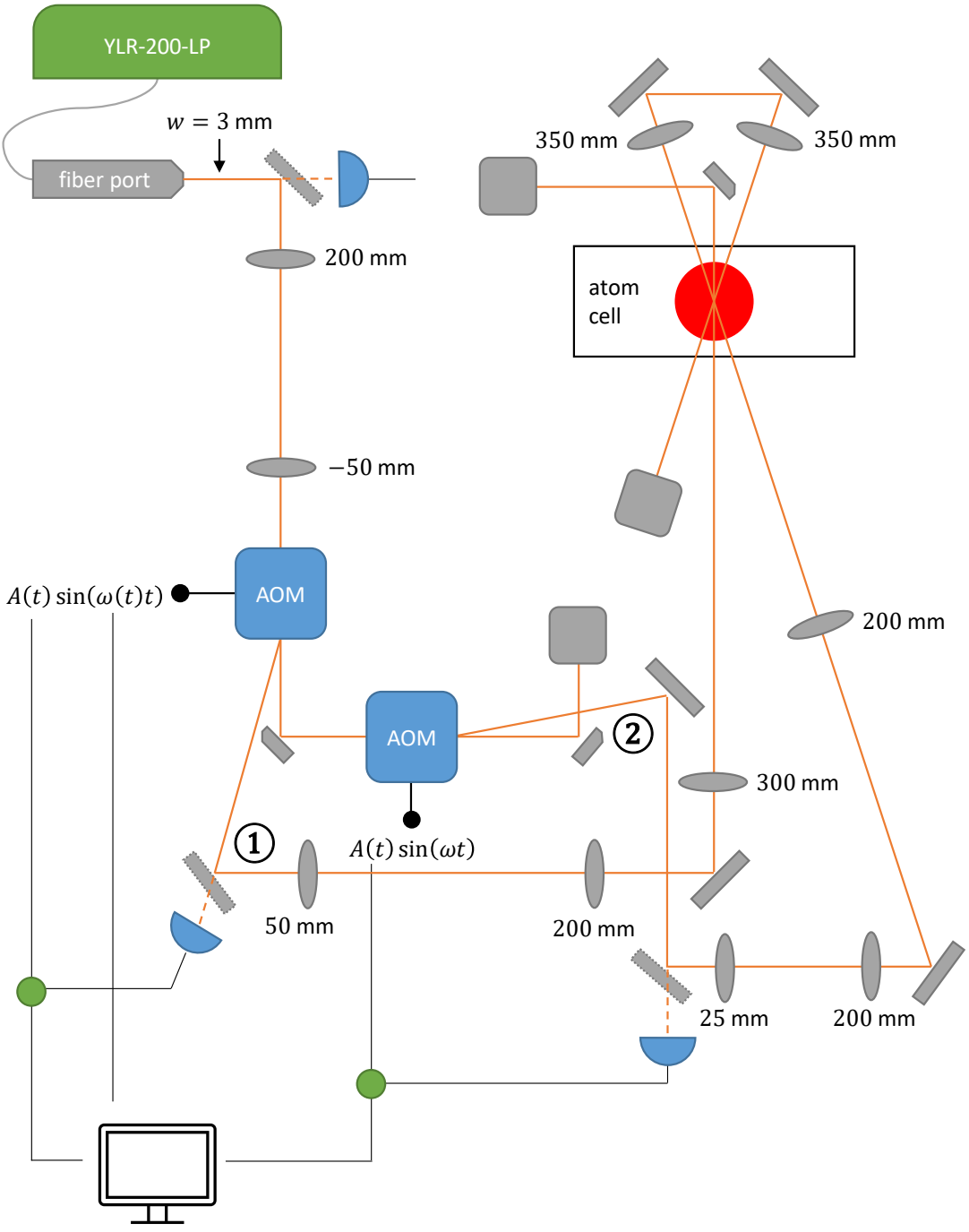

Figure 6.1: Schematic of the new optical dipole trap setup. The numbers (1) and (2) show the sODT and xODT respectively.

While the same pulse could be used to dissociate the bound states and close the interferometer, the interference signal would still have to be extracted from a large, possibly fluctuating, background. There are two alternative possibilities for the second pulse that avoid mixing the signal with the background.

The first option is to dissociate the dimer-trimer superposition onto a different continuum (different spin state). Since the three-body system lives in the zero total spin projection subspace, any three-body continuum with the same total spin projection can be used. With respect to the initial state continuum *bbb* the energetically closest two continua are *abc* ($E_{abc} - E_{bbb} = 28.9$ MHz at 880 G) and *aad* ($E_{aad} - E_{bbb} = 108.2$ MHz at 880 G). All others are > 2 GHz away. Once the signal atoms are in a different continuum the background atoms (in *b*) are blown away with resonant light which can also be used to count them via absorption imaging. In case the *abc* continuum is chosen one also loses 1/3 of the signal atoms. The disadvantage of this option is the instability of more energetic continua. The three-body state *abc* (*aad*) is unstable due to two-body spin-flip interactions $ac \rightarrow bb$ ($ad \rightarrow bc$) while releasing 28.9 MHz (79.3 MHz) in the form of kinetic energy is possible. This is more than enough to expel both atoms from the trap. One must therefore get rid off the background and measure the signal before they are lost. Although this sounds demanding, the low density of the signal atoms decreases the collision rate by $n_{\text{background}}/n_{\text{signal}} \approx 100$ making the task feasable.

The second option is to dissociate the superposition onto the *bbb* continuum (where it is mixed with the background) but to observe the other output port of the interferometer, namely the remaining bound states. To this end one must first quickly blow away the *b*-state atoms without affecting the bound states. Then the dimers (and possibly also the trimer) are dissociated by sweeping over the magnetic field over the Feshbach resonance so that they can be observed as free atoms.

In either case, the number of atoms in the signal is small. We must thus develop an efficient and exact way to count them. This is discussed next.

6.3 Detection

Absorption imaging is a powerful tool for obtaining low-noise images of trapped or expanding cold gases. Since it utilizes resonant light it is state selective and additional background images allow efficient reduction of noise. However, its range of application is limited to samples with $\gtrsim 10^3$ atoms. The number of photons scattered by the atoms is too sparse to obtain a clear signal below this limit. In addition, the destructive nature of absorption imaging limits the exposure time.

One option to solve this problem is to transfer the atoms back into a MOT at the end of the experimental sequence and image them there via their florescence.

Since the atoms remain trapped for a very long time, large exposure times are possible, facilitating low atom number detection. While one looses information on the temperature and spatial extent of the gas, the atom number can be measured with high precision [90–95].

One of the critical parameters is the exposure time, i.e. the time during which the camera collects photons emitted by the atoms. Typically, it is optimized to minimize noise and single-atom uncertainty has been demonstrated [90]. Here, the exposure time mustn't be too long because the MOT itself looses atoms over time.

In our case, however, single-atom sensitivity is not necessary. We estimate that being able to distinguish between 0, 100 and a few 100 to 1000 atoms will be satisfactory. Hence the exposure time can be made much longer – we do not care about the (short) time-scale of single-atom loss. Preliminary experiments on small sample sizes have shown that integration times of several seconds are possible and that we are able to observe down to several 100 atoms. The uncertainty is yet to be determined.

The detection or imaging MOT (IMOT) uses unconventional laser and magnetic field parameters. Because we wish to scatter as many photons as possible the pump laser is tuned very close to (or even on [96]) resonance. In addition, to achieve a favorable the optical density (OD) given the small atom number, the atomic density is increased by using a large magnetic field gradient. We find that using an anti-Helmholtz coil current $\sim 2-3$ times larger for the IMOT compared to the MOT results in a good OD.

Chapter 7

Additional Contributions to Papers

In addition to the papers featured in this Thesis, I contributed to the following three works.

7.1 Efimov resonance position near a narrow Feshbach resonance in a ^{6}Li–^{133}Cs mixture

In this paper [97], headed by Li Ang, the equations derived in Chap. 4 are generalized to a hetero-nuclear mass-imbalanced three-body system. They are applied to the LiCsCs trimer which was explored experimentally and lacked theoretical modelling [98]. In the paper we show quantitative agreement with the experiment.

7.2 Observation of coherent oscillations in association of dimers from a thermal gas of ultracold atoms

The main ingredient to this Thesis is the DITRIS interferometer with which we were able to introduce the concept of coherence into the field of few-body physics. It is not necessary, however, to use a three-body system to do so – two particles suffice. To build a two-body interferometer one must non-adiabatically separate the dressed dimer from the degenerate free-atom state by suddenly applying a strong rf-pulse and reunite them after by a sudden turn-off [99]. In the experiment led by Roy Elbaz [100] we experimentally demonstrated these so-called Stückelberg oscillations.

7.3 Observation of low-field Feshbach resonances between ^{161}Dy and ^{40}K

During my Ph.D. I had the immense privilege to spend seven months in Innsbruck, Austria, and join the research group headed by Prof. Rudolf Grimm[1]. The lab I was part of has built a system that co-traps the fermionic isotopes of dysprosium (^{161}Dy) and potassium (^{40}K) and produces doubly degenerate mixtures. The long-term goal of the system is to observe the exotic and elusive FFLO state [101–103]. An important step towards that goal is the precise characterization of suitable interspecies Feshbach resonances and the formation of Feshbach molecules. The paper which I contributed to [104] investigates numerous low-field resonances, making the increase to high magnetic fields obsolete. In addition, the paper demonstrates the creation of Feshbach molecules and measurement of their binding energy using various methods.

[1] http://ultracold.at/grimm/

Chapter 8

Conclusion

Almost two decades ago, as the measurements of a_- started to accumulate, the Efimov-van der Waals universality became apparent. In fact, the compliance of ^{7}Li was seen as part of the experimental validation. It was soon realized, however, that the narrowness of the involved Feshbach resonances prevents this verification and that a_- should be much larger. The "lithium few-body puzzle" was born.

Several years later the ^{7}Li trimer was directly measured below the dimer-atom threshold via rf-association. Its energy level, as a function of the scattering length, was found to be almost parallel to the dimer-atom threshold, approaching it only very gradually. The "lithium few-body puzzle" was thus extended to the positive side of the Feshbach resonance, where the trimer evidently does not agree with the Efimov universality either.

In this Thesis the puzzle was further explored. After demonstrating the ability to create a superposition of dimers and trimers and designing an interferometer sequence to extract their relative energy, we have measured the trimer below and above the dimer-atom threshold. The realization that it crosses into the continuum and, in particular, the observation that it remains a long-lived bound state is surprising.

Moreover, this Thesis has explored simple models to take into account the leading order contributions to the asymptotic two-body wave function. Specifically, a Hamiltonian that reproduces overlapping Feshbach resonances and a Hamiltonian that accounts for a nearby atomic continuum were proposed and explored. Since neither are able to predict the observed crossing our current best guess is that the short-range details of the two-body interaction potentials are of major importance.

The "lithium few-body puzzle" seems to be far from solved, although important clues on potential solutions are beginning to surface. On the experimental side we have presented a road-map on how to accurately measure the trimer lifetime. This additional observable will be helpful for deciphering the puzzle. On the theoretical side more comlicated models than the ones presented here will be necessary. To this

end we have established fruitful collaborations with renowned theoretical physicists.

Bibliography

[1] William D. Phillips. "Nobel Lecture: Laser cooling and trapping of neutral atoms". In: *Rev. Mod. Phys.* 70 (3 1998), pp. 721–741. DOI: 10.1103/RevModPhys.70.721. URL: https://link.aps.org/doi/10.1103/RevModPhys.70.721.

[2] Claude N. Cohen-Tannoudji. "Nobel Lecture: Manipulating atoms with photons". In: *Rev. Mod. Phys.* 70 (3 1998), pp. 707–719. DOI: 10.1103/RevModPhys.70.707. URL: https://link.aps.org/doi/10.1103/RevModPhys.70.707.

[3] Steven Chu. "Nobel Lecture: The manipulation of neutral particles". In: *Rev. Mod. Phys.* 70 (3 1998), pp. 685–706. DOI: 10.1103/RevModPhys.70.685. URL: https://link.aps.org/doi/10.1103/RevModPhys.70.685.

[4] Wolfgang Ketterle. "Nobel lecture: When atoms behave as waves: Bose-Einstein condensation and the atom laser". In: *Rev. Mod. Phys.* 74 (4 2002), pp. 1131–1151. DOI: 10.1103/RevModPhys.74.1131. URL: https://link.aps.org/doi/10.1103/RevModPhys.74.1131.

[5] E. A. Cornell and C. E. Wieman. "Nobel Lecture: Bose-Einstein condensation in a dilute gas, the first 70 years and some recent experiments". In: *Rev. Mod. Phys.* 74 (3 2002), pp. 875–893. DOI: 10.1103/RevModPhys.74.875. URL: https://link.aps.org/doi/10.1103/RevModPhys.74.875.

[6] C. Cohen-Tannoudji and D. Guery-Odelin. *Advances in Atomic Physics: An Overview*. World Scientific, 2011.

[7] F. Schreck and K. van Druten. "Laser cooling for quantum gases". In: *Nat. Phys.* 17 (2021), 1296—1304. DOI: 10.1038/s41567-021-01379-w. URL: https://doi.org/10.1038/s41567-021-01379-w.

[8] Wim Vassen, Claude Cohen-Tannoudji, Michele Leduc, Denis Boiron, Christoph I. Westbrook, Andrew Truscott, Ken Baldwin, Gerhard Birkl, Pablo Cancio, and Marek Trippenbach. "Cold and trapped metastable noble gases". In: *Rev. Mod. Phys.* 84 (1 2012), pp. 175–210. DOI: 10.1103/RevModPhys.84.175. URL: https://link.aps.org/doi/10.1103/RevModPhys.84.175.

[9] Lauriane Chomaz, Igor Ferrier-Barbut, Francesca Ferlaino, Bruno Laburthe-Tolra, Benjamin L. Lev, and Tilman Pfau. "Dipolar physics: A review of experiments with magnetic quantum gases". In: *arXiv* (2022), p. 2201.02672. URL: https://doi.org/10.48550/arXiv.2201.02672.

[10] M. Saffman, T. G. Walker, and K. Mølmer. "Quantum information with Rydberg atoms". In: *Rev. Mod. Phys.* 82 (3 2010), pp. 2313–2363. DOI: 10.1103/RevModPhys.82.2313. URL: https://link.aps.org/doi/10.1103/RevModPhys.82.2313.

[11] Loïc Henriet, Lucas Beguin, Adrien Signoles, Thierry Lahaye, Antoine Browaeys, Georges-Olivier Reymond, and Christophe Jurczak. "Quantum computing with neutral atoms". In: *Quantum* 4 (Sept. 2020), p. 327. ISSN: 2521-327X. DOI: 10.22331/q-2020-09-21-327. URL: https://doi.org/10.22331/q-2020-09-21-327.

[12] Immanuel Bloch, Jean Dalibard, and Wilhelm Zwerger. "Many-body physics with ultracold gases". In: *Rev. Mod. Phys.* 80 (3 2008), pp. 885–964. DOI: 10.1103/RevModPhys.80.885. URL: https://link.aps.org/doi/10.1103/RevModPhys.80.885.

[13] Christian Gross and Immanuel Bloch. "Quantum simulations with ultracold atoms in optical lattices". In: *Science* 357.6355 (2017), pp. 995–1001. DOI: 10.1126/science.aal3837. eprint: https://www.science.org/doi/pdf/10.1126/science.aal3837. URL: https://www.science.org/doi/abs/10.1126/science.aal3837.

[14] André Eckardt. "Colloquium: Atomic quantum gases in periodically driven optical lattices". In: *Rev. Mod. Phys.* 89 (1 2017), p. 011004. DOI: 10.1103/RevModPhys.89.011004. URL: https://link.aps.org/doi/10.1103/RevModPhys.89.011004.

[15] Wilhelm Zwerger. *The BCS-BEC Crossover and the Unitary Fermi Gas*. Springer Berlin, Heidelberg, 2012. DOI: 10.1007/978-3-642-21978-8.

[16] Dmitry A. Abanin, Ehud Altman, Immanuel Bloch, and Maksym Serbyn. "Colloquium: Many-body localization, thermalization, and entanglement". In: *Rev. Mod. Phys.* 91 (2 2019), p. 021001. DOI: 10.1103/RevModPhys.91.021001. URL: https://link.aps.org/doi/10.1103/RevModPhys.91.021001.

[17] Pietro Massignan, Matteo Zaccanti, and Georg M Bruun. "Polarons, dressed molecules and itinerant ferromagnetism in ultracold Fermi gases". In: *Reports on Progress in Physics* 77.3 (2014), p. 034401. DOI: 10.1088/0034-4885/77/3/034401. URL: https://doi.org/10.1088/0034-4885/77/3/034401.

[18] Dan M. Stamper-Kurn and Masahito Ueda. "Spinor Bose gases: Symmetries, magnetism, and quantum dynamics". In: *Rev. Mod. Phys.* 85 (3 2013), pp. 1191–1244. DOI: 10.1103/RevModPhys.85.1191. URL: https://link.aps.org/doi/10.1103/RevModPhys.85.1191.

[19] Helmut Ritsch, Peter Domokos, Ferdinand Brennecke, and Tilman Esslinger. "Cold atoms in cavity-generated dynamical optical potentials". In: *Rev. Mod. Phys.* 85 (2 2013), pp. 553–601. DOI: 10.1103/RevModPhys.85.553. URL: https://link.aps.org/doi/10.1103/RevModPhys.85.553.

[20] Alexander D. Cronin, Jörg Schmiedmayer, and David E. Pritchard. "Optics and interferometry with atoms and molecules". In: *Rev. Mod. Phys.* 81 (3 2009), pp. 1051–1129. DOI: 10.1103/RevModPhys.81.1051. URL: https://link.aps.org/doi/10.1103/RevModPhys.81.1051.

[21] Luca Pezzè, Augusto Smerzi, Markus K. Oberthaler, Roman Schmied, and Philipp Treutlein. "Quantum metrology with nonclassical states of atomic ensembles". In: *Rev. Mod. Phys.* 90 (3 2018), p. 035005. DOI: 10.1103/RevModPhys.90.035005. URL: https://link.aps.org/doi/10.1103/RevModPhys.90.035005.

[22] Andrew D. Ludlow, Martin M. Boyd, Jun Ye, E. Peik, and P. O. Schmidt. "Optical atomic clocks". In: *Rev. Mod. Phys.* 87 (2 2015), pp. 637–701. DOI: 10.1103/RevModPhys.87.637. URL: https://link.aps.org/doi/10.1103/RevModPhys.87.637.

[23] M. S. Safronova, D. Budker, D. DeMille, Derek F. Jackson Kimball, A. Derevianko, and Charles W. Clark. "Search for new physics with atoms and molecules". In: *Rev. Mod. Phys.* 90 (2 2018), p. 025008. DOI: 10.1103/RevModPhys.90.025008. URL: https://link.aps.org/doi/10.1103/RevModPhys.90.025008.

[24] Chris H. Greene, P. Giannakeas, and J. Pérez-Ríos. "Universal few-body physics and cluster formation". In: *Rev. Mod. Phys.* 89 (3 2017), p. 035006. DOI: 10.1103/RevModPhys.89.035006. URL: https://link.aps.org/doi/10.1103/RevModPhys.89.035006.

[25] Michał Tomza, Krzysztof Jachymski, Rene Gerritsma, Antonio Negretti, Tommaso Calarco, Zbigniew Idziaszek, and Paul S. Julienne. "Cold hybrid ion-atom systems". In: *Rev. Mod. Phys.* 91 (3 2019), p. 035001. DOI: 10.1103/RevModPhys.91.035001. URL: https://link.aps.org/doi/10.1103/RevModPhys.91.035001.

[26] Lincoln D Carr, David DeMille, Roman V Krems, and Jun Ye. "Cold and ultracold molecules: science, technology and applications". In: *New Journal of Physics* 11.5 (2009), p. 055049. DOI: 10.1088/1367-2630/11/5/055049. URL: https://dx.doi.org/10.1088/1367-2630/11/5/055049.

[27] K. B. Davis, M. O. Mewes, M. R. Andrews, N. J. van Druten, D. S. Durfee, D. M. Kurn, and W. Ketterle. "Bose-Einstein Condensation in a Gas of Sodium Atoms". In: *Phys. Rev. Lett.* 75 (22 1995), pp. 3969–3973. DOI: 10.1103/PhysRevLett.75.3969. URL: https://link.aps.org/doi/10.1103/PhysRevLett.75.3969.

[28] M. H. Anderson, J. R. Ensher, M. R. Matthews, C. E. Wieman, and E. A. Cornell. "Observation of Bose-Einstein Condensation in a Dilute Atomic Vapor". In: *Science* 269.5221 (1995), pp. 198–201. DOI: 10.1126/science.269.5221.198. URL: https://www.science.org/doi/abs/10.1126/science.269.5221.198.

[29] S. Inouye, M. Andrews, J. Stenger, H.-J. Miesner, D. M. Stamper-Kurn, and W. Ketterle. "Observation of Feshbach resonances in a Bose–Einstein condensate". In: *Nature* 392 (1998), 151–154. DOI: 10.1038/32354. URL: https://doi.org/10.1038/32354.

[30] S. Inouye, J. Goldwin, M. L. Olsen, C. Ticknor, J. L. Bohn, and D. S. Jin. "Observation of Heteronuclear Feshbach Resonances in a Mixture of Bosons and Fermions". In: *Phys. Rev. Lett.* 93 (18 2004), p. 183201. DOI: 10.1103/PhysRevLett.93.183201. URL: https://link.aps.org/doi/10.1103/PhysRevLett.93.183201.

[31] Cheng Chin, Rudolf Grimm, Paul Julienne, and Eite Tiesinga. "Feshbach resonances in ultracold gases". In: *Rev. Mod. Phys.* 82 (2 2010), pp. 1225–1286. DOI: 10.1103/RevModPhys.82.1225. URL: https://link.aps.org/doi/10.1103/RevModPhys.82.1225.

[32] S. Jochim, M. Bartenstein, G. Hendl, J. Hecker Denschlag, R. Grimm, A. Mosk, and M. Weidemüller. "Magnetic Field Control of Elastic Scattering in a Cold Gas of Fermionic Lithium Atoms". In: *Phys. Rev. Lett.* 89 (27 2002), p. 273202. DOI: 10.1103/PhysRevLett.89.273202. URL: https://link.aps.org/doi/10.1103/PhysRevLett.89.273202.

[33] S. T. Thompson, E. Hodby, and C. E. Wieman. "Ultracold Molecule Production via a Resonant Oscillating Magnetic Field". In: *Phys. Rev. Lett.* 95 (19 2005), p. 190404. DOI: 10.1103/PhysRevLett.95.190404. URL: https://link.aps.org/doi/10.1103/PhysRevLett.95.190404.

[34] C. Klempt, T. Henninger, O. Topic, M. Scherer, L. Kattner, E. Tiemann, W. Ertmer, and J. J. Arlt. "Radio-frequency association of heteronuclear Feshbach molecules". In: *Phys. Rev. A* 78 (6 2008), p. 061602. DOI: 10.1103/PhysRevA.78.061602. URL: https://link.aps.org/doi/10.1103/PhysRevA.78.061602.

[35] J Ulmanis, S Häfner, R Pires, E D Kuhnle, M Weidemüller, and E Tiemann. "Universality of weakly bound dimers and Efimov trimers close to Li–Cs Feshbach resonances". In: *New Journal of Physics* 17.5 (2015), p. 055009. DOI: 10.1088/1367-2630/17/5/055009. URL: https://dx.doi.org/10.1088/1367-2630/17/5/055009.

[36] M. Bartenstein, A. Altmeyer, S. Riedl, R. Geursen, S. Jochim, C. Chin, J. Hecker Denschlag, R. Grimm, A. Simoni, E. Tiesinga, C. J. Williams, and P. S. Julienne. "Precise Determination of ^{6}Li Cold Collision Parameters by Radio-Frequency Spectroscopy on Weakly Bound Molecules". In: *Phys. Rev. Lett.* 94 (10 2005), p. 103201. DOI: 10.1103/PhysRevLett.94.103201. URL: https://link.aps.org/doi/10.1103/PhysRevLett.94.103201.

[37] Elizabeth A. Donley, Neil R. Claussen, Sarah T. Thompson, and Carl E. Wieman. "Atom–molecule coherence in a Bose–Einstein condensate". In: *Nature* 417.6888 (2002), pp. 529–533. ISSN: 1476-4687. DOI: 10.1038/417529a. URL: https://doi.org/10.1038/417529a.

[38] N. R. Claussen, S. J. J. M. F. Kokkelmans, S. T. Thompson, E. A. Donley, E. Hodby, and C. E. Wieman. "Very-high-precision bound-state spectroscopy near a ^{85}Rb Feshbach resonance". In: *Phys. Rev. A* 67 (6 2003), p. 060701. DOI: 10.1103/PhysRevA.67.060701. URL: https://link.aps.org/doi/10.1103/PhysRevA.67.060701.

[39] K. Winkler, G. Thalhammer, M. Theis, H. Ritsch, R. Grimm, and J. Hecker Denschlag. "Atom-Molecule Dark States in a Bose-Einstein Condensate". In: *Phys. Rev. Lett.* 95 (6 2005), p. 063202. DOI: 10.1103/PhysRevLett.95.063202. URL: https://link.aps.org/doi/10.1103/PhysRevLett.95.063202.

[40] N. Syassen, D. M. Bauer, M. Lettner, D. Dietze, T. Volz, S. Dürr, and G. Rempe. "Atom-Molecule Rabi Oscillations in a Mott Insulator". In: *Phys. Rev. Lett.* 99 (3 2007), p. 033201. DOI: 10.1103/PhysRevLett.99.033201. URL: https://link.aps.org/doi/10.1103/PhysRevLett.99.033201.

[41] M. L. Olsen, J. D. Perreault, T. D. Cumby, and D. S. Jin. "Coherent atom-molecule oscillations in a Bose-Fermi mixture". In: *Phys. Rev. A* 80 (3 2009), p. 030701. DOI: 10.1103/PhysRevA.80.030701. URL: https://link.aps.org/doi/10.1103/PhysRevA.80.030701.

[42] T. Maier, H. Kadau, M. Schmitt, M. Wenzel, I. Ferrier-Barbut, T. Pfau, A. Frisch, S. Baier, K. Aikawa, L. Chomaz, M. J. Mark, F. Ferlaino, C. Makrides, E. Tiesinga, A. Petrov, and S. Kotochigova. "Emergence of Chaotic Scattering in Ultracold Er and Dy". In: *Phys. Rev. X* 5 (4 2015), p. 041029. DOI: 10.1103/PhysRevX.5.041029. URL: https://link.aps.org/doi/10.1103/PhysRevX.5.041029.

[43] A. Frisch, M. Mark, K. Aikawa, F. Ferlaino, J. L. Bohn, C. Makrides, A. Petrov, and S. Kotochigova. "Quantum chaos in ultracold collisions of gas-phase erbium atoms". In: *Nature* 507.7493 (2014), pp. 475–479. DOI: 10.1038/nature13137. URL: https://doi.org/10.1038/nature13137.

[44] V. Barbé, A. Ciamei, B. Pasquiou, L. Reichsöllner, F. Schreck, P. S. Żuchowski, and J. M. Hutson. "Observation of Feshbach resonances between alkali and closed-shell atoms". In: *Nature Physics* 14.9 (2018), pp. 881–884. DOI: 10.1038/s41567-018-0169-x. URL: https://doi.org/10.1038/s41567-018-0169-x.

[45] Huan Yang, De-Chao Zhang, Lan Liu, Ya-Xiong Liu, Jue Nan, Bo Zhao, and Jian-Wei Pan. "Observation of magnetically tunable Feshbach resonances in ultracold ¡sup¿23¡/sup¿Na¡sup¿40¡/sup¿K + ¡sup¿40¡/sup¿K collisions". In: *Science* 363.6424 (2019), pp. 261–264. DOI: 10.1126/science.aau5322. URL: https://www.science.org/doi/abs/10.1126/science.aau5322.

[46] Juliana J. Park, Yu-Kun Lu, Alan O. Jamison, Timur Tscherbul, and Wolfgang Ketterle. "A Feshbach resonance in collisions between ultracold ground state molecules". In: *arXiv* (2022), p. 2208.05557. URL: https://doi.org/10.48550/arXiv.2208.05557.

[47] P. Weckesser, F. Thielemann, D. Wiater, A. Wojciechowska, L. Karpa, K. Jachymski, M. Tomza, T. Walker, and T. Schaetz. "Observation of Feshbach resonances between a single ion and ultracold atoms". In: *Nature* 600.7889 (2021), pp. 429–433. DOI: 10.1038/s41586-021-04112-y. URL: https://doi.org/10.1038/s41586-021-04112-y.

[48] Eric Braaten and H.-W. Hammer. "Universality in few-body systems with large scattering length". In: *Physics Reports* 428.5 (2006), pp. 259–390. ISSN: 0370-1573. DOI: https://doi.org/10.1016/j.physrep.2006.03.001. URL: https://www.sciencedirect.com/science/article/pii/S0370157306000822.

[49] Hans-Werner Hammer and Lucas Platter. "Efimov States in Nuclear and Particle Physics". In: *Annual Review of Nuclear and Particle Science* 60.1 (2010), pp. 207–236. DOI: 10.1146/annurev.nucl.012809.104439. eprint: https://doi.org/10.1146/annurev.nucl.012809.104439. URL: https://doi.org/10.1146/annurev.nucl.012809.104439.

[50] Pascal Naidon and Shimpei Endo. "Efimov physics: a review". In: *Reports on Progress in Physics* 80.5 (2017), p. 056001. DOI: 10.1088/1361-6633/aa50e8. URL: https://doi.org/10.1088/1361-6633/aa50e8.

[51] José P D'Incao. "Few-body physics in resonantly interacting ultracold quantum gases". In: *Journal of Physics B: Atomic, Molecular and Optical Physics* 51.4 (2018), p. 043001. DOI: 10.1088/1361-6455/aaa116. URL: https://doi.org/10.1088/1361-6455/aaa116.

[52] Jia Wang, J. P. D'Incao, B. D. Esry, and Chris H. Greene. "Origin of the Three-Body Parameter Universality in Efimov Physics". In: *Phys. Rev. Lett.* 108 (26 2012), p. 263001. DOI: 10.1103/PhysRevLett.108.263001. URL: https://link.aps.org/doi/10.1103/PhysRevLett.108.263001.

[53] Pascal Naidon, Shimpei Endo, and Masahito Ueda. "Physical origin of the universal three-body parameter in atomic Efimov physics". In: *Phys. Rev. A* 90 (2 2014), p. 022106. DOI: 10.1103/PhysRevA.90.022106. URL: https://link.aps.org/doi/10.1103/PhysRevA.90.022106.

[54] Pascal Naidon, Shimpei Endo, and Masahito Ueda. "Erratum: Physical origin of the universal three-body parameter in atomic Efimov physics [Phys. Rev. A 90, 022106 (2014)]". In: *Phys. Rev. A* 104 (5 2021), p. 059903. DOI: 10.1103/PhysRevA.104.059903. URL: https://link.aps.org/doi/10.1103/PhysRevA.104.059903.

[55] T. Kraemer, M. Mark, P. Waldburger, J. G. Danzl, C. Chin, B. Engeser, A. D. Lange, K. Pilch, A. Jaakkola, H.-C. Nägerl, and R. Grimm. "Evidence for Efimov quantum states in an ultracold gas of caesium atoms". In: *Nature* 440.7082 (2006), pp. 315–318. ISSN: 1476-4687. DOI: 10.1038/nature04626. URL: https://doi.org/10.1038/nature04626.

[56] M. Zaccanti, B. Deissler, C. D'Errico, M. Fattori, M. Jona-Lasinio, S. Müller, G. Roati, M. Inguscio, and G. Modugno. "Observation of an Efimov spectrum in an atomic system". In: *Nature Physics* 5.8 (2009), pp. 586–591. ISSN: 1745-2481. DOI: 10.1038/nphys1334. URL: https://doi.org/10.1038/nphys1334.

[57] Noam Gross, Zav Shotan, Servaas Kokkelmans, and Lev Khaykovich. "Observation of Universality in Ultracold ^{7}Li Three-Body Recombination". In: *Phys. Rev. Lett.* 103 (16 2009), p. 163202. DOI: 10.1103/PhysRevLett.103.163202. URL: https://link.aps.org/doi/10.1103/PhysRevLett.103.163202.

[58] M. Berninger, A. Zenesini, B. Huang, W. Harm, H.-C. Nägerl, F. Ferlaino, R. Grimm, P. S. Julienne, and J. M. Hutson. "Universality of the Three-Body Parameter for Efimov States in Ultracold Cesium". In: *Phys. Rev. Lett.* 107 (12 2011), p. 120401. DOI: 10.1103/PhysRevLett.107.120401. URL: https://link.aps.org/doi/10.1103/PhysRevLett.107.120401.

[59] R. J. Wild, P. Makotyn, J. M. Pino, E. A. Cornell, and D. S. Jin. "Measurements of Tan's Contact in an Atomic Bose-Einstein Condensate". In: *Phys. Rev. Lett.* 108 (14 2012), p. 145305. DOI: 10.1103/PhysRevLett.108.145305. URL: https://link.aps.org/doi/10.1103/PhysRevLett.108.145305.

[60] P. Dyke, S. E. Pollack, and R. G. Hulet. "Finite-range corrections near a Feshbach resonance and their role in the Efimov effect". In: *Phys. Rev. A* 88 (2 2013), p. 023625. DOI: 10.1103/PhysRevA.88.023625. URL: https://link.aps.org/doi/10.1103/PhysRevA.88.023625.

[61] L. J. Wacker, N. B. Jørgensen, K. T. Skalmstang, M. G. Skou, A. G. Volosniev, and J. J. Arlt. "Temperature dependence of an Efimov resonance in ^{39}K". In: *Phys. Rev. A* 98 (5 2018), p. 052706. DOI: 10.1103/PhysRevA.98.052706. URL: https://link.aps.org/doi/10.1103/PhysRevA.98.052706.

[62] Roman Chapurin, Xin Xie, Michael J. Van de Graaff, Jared S. Popowski, José P. D'Incao, Paul S. Julienne, Jun Ye, and Eric A. Cornell. "Precision Test of the Limits to Universality in Few-Body Physics". In: *Phys. Rev. Lett.* 123 (23 2019), p. 233402. DOI: 10.1103/PhysRevLett.123.233402. URL: https://link.aps.org/doi/10.1103/PhysRevLett.123.233402.

[63] Jiří Etrych, Gevorg Martirosyan, Alec Cao, Jake A. P. Glidden, Lena H. Dogra, Jeremy M. Hutson, Zoran Hadzibabic, and Christoph Eigen. *Pinpointing Feshbach Resonances and Testing Efimov Universalities in ^{39}K*. 2022. DOI: 10.48550/ARXIV.2208.13766. URL: https://arxiv.org/abs/2208.13766.

[64] Bo Huang, Leonid A. Sidorenkov, Rudolf Grimm, and Jeremy M. Hutson. "Observation of the Second Triatomic Resonance in Efimov's Scenario". In: *Phys. Rev. Lett.* 112 (19 2014), p. 190401. DOI: 10.1103/PhysRevLett.112.190401. URL: https://link.aps.org/doi/10.1103/PhysRevLett.112.190401.

[65] Shih-Kuang Tung, Karina Jiménez-García, Jacob Johansen, Colin V. Parker, and Cheng Chin. "Geometric Scaling of Efimov States in a ^{6}Li–^{133}Cs Mixture". In: *Phys. Rev. Lett.* 113 (24 2014), p. 240402. DOI: 10.1103/PhysRevLett.113.240402. URL: https://link.aps.org/doi/10.1103/PhysRevLett.113.240402.

[66] R. Pires, J. Ulmanis, S. Häfner, M. Repp, A. Arias, E. D. Kuhnle, and M. Weidemüller. "Observation of Efimov Resonances in a Mixture with Extreme Mass Imbalance". In: *Phys. Rev. Lett.* 112 (25 2014), p. 250404. DOI: 10.1103/PhysRevLett.112.250404. URL: https://link.aps.org/doi/10.1103/PhysRevLett.112.250404.

[67] S. Knoop, F. Ferlaino, M. Mark, M. Berninger, H. Schöbel, H.-C. Nägerl, and R. Grimm. "Observation of an Efimov-like trimer resonance in ultracold atom–dimer scattering". In: *Nature Physics* 5.3 (2009), pp. 227–230. ISSN: 1745-2481. DOI: 10.1038/nphys1203. URL: https://doi.org/10.1038/nphys1203.

[68] Xin Xie, Michael J. Van de Graaff, Roman Chapurin, Matthew D. Frye, Jeremy M. Hutson, José P. D'Incao, Paul S. Julienne, Jun Ye, and Eric A. Cornell. "Observation of Efimov Universality across a Nonuniversal Feshbach Resonance in ^{39}K". In: *Phys. Rev. Lett.* 125 (24 2020), p. 243401. DOI: 10.1103/PhysRevLett.125.243401. URL: https://link.aps.org/doi/10.1103/PhysRevLett.125.243401.

[69] F. Ferlaino, S. Knoop, M. Berninger, W. Harm, J. P. D'Incao, H.-C. Nägerl, and R. Grimm. "Evidence for Universal Four-Body States Tied to an Efimov Trimer". In: *Phys. Rev. Lett.* 102 (14 2009), p. 140401. DOI: 10.1103/PhysRevLett.102.140401. URL: https://link.aps.org/doi/10.1103/PhysRevLett.102.140401.

[70] Thomas Lompe, Timo B. Ottenstein, Friedhelm Serwane, Andre N. Wenz, Gerhard Zürn, and Selim Jochim. "Radio-Frequency Association of Efimov Trimers". In: *Science* 330.6006 (2010), pp. 940–944. DOI: 10.1126/science.1193148. eprint: https://www.science.org/doi/pdf/10.1126/science.1193148. URL: https://www.science.org/doi/abs/10.1126/science.1193148.

[71] Olga Machtey, Zav Shotan, Noam Gross, and Lev Khaykovich. "Association of Efimov Trimers from a Three-Atom Continuum". In: *Phys. Rev. Lett.* 108 (21 2012), p. 210406. DOI: 10.1103/PhysRevLett.108.210406. URL: https://link.aps.org/doi/10.1103/PhysRevLett.108.210406.

[72] Maksim Kunitski, Stefan Zeller, Jörg Voigtsberger, Anton Kalinin, Lothar Ph. H. Schmidt, Markus Schöffler, Achim Czasch, Wieland Schöllkopf, Robert E. Grisenti, Till Jahnke, Dörte Blume, and Reinhard Dörner. "Observation of the Efimov state of the helium trimer". In: *Science* 348.6234 (2015), pp. 551–555. DOI: 10.1126/science.aaa5601. eprint: https://www.science.org/doi/pdf/10.1126/science.aaa5601. URL: https://www.science.org/doi/abs/10.1126/science.aaa5601.

[73] Noam Gross, Zav Shotan, Servaas Kokkelmans, and Lev Khaykovich. "Nuclear-Spin-Independent Short-Range Three-Body Physics in Ultracold Atoms". In: *Phys. Rev. Lett.* 105 (10 2010), p. 103203. DOI: 10.1103/PhysRevLett.105.103203. URL: https://link.aps.org/doi/10.1103/PhysRevLett.105.103203.

[74] Noam Gross, Zav Shotan, Olga Machtey, Servaas Kokkelmans, and Lev Khaykovich. "Study of Efimov physics in two nuclear-spin sublevels of 7Li". In: *Comptes Rendus Physique* 12.1 (2011). Few body problem, pp. 4–12. ISSN: 1631-0705. DOI: https://doi.org/10.1016/j.crhy.2010.10.004. URL: https://www.sciencedirect.com/science/article/pii/S1631070510001489.

[75] Maksim Kunitski, Qingze Guan, Holger Maschkiwitz, Jörg Hahnenbruch, Sebastian Eckart, Stefan Zeller, Anton Kalinin, Markus Schöffler, Lothar Ph. H. Schmidt, Till Jahnke, Dörte Blume, and Reinhard Dörner. "Ultrafast manipulation of the weakly bound helium dimer". In: *Nature Physics* 17.2 (2021), pp. 174–178. ISSN: 1745-2481. DOI: 10.1038/s41567-020-01081-3. URL: https://doi.org/10.1038/s41567-020-01081-3.

[76] Eric Braaten, Daekyoung Kang, and Lucas Platter. "Universal Relations for Identical Bosons from Three-Body Physics". In: *Phys. Rev. Lett.* 106 (15 2011), p. 153005. DOI: 10.1103/PhysRevLett.106.153005. URL: https://link.aps.org/doi/10.1103/PhysRevLett.106.153005.

[77] Marcus Barth and Johannes Hofmann. "Efimov correlations in strongly interacting Bose gases". In: *Phys. Rev. A* 92 (6 2015), p. 062716. DOI: 10.1103/PhysRevA.92.062716. URL: https://link.aps.org/doi/10.1103/PhysRevA.92.062716.

[78] Shina Tan. "Energetics of a strongly correlated Fermi gas". In: *Annals of Physics* 323.12 (2008), pp. 2952–2970. ISSN: 0003-4916. DOI: https://doi.org/10.1016/j.aop.2008.03.004. URL: https://www.sciencedirect.com/science/article/pii/S0003491608000456.

[79] Shina Tan. "Large momentum part of a strongly correlated Fermi gas". In: *Annals of Physics* 323.12 (2008), pp. 2971–2986. ISSN: 0003-4916. DOI: https://doi.org/10.1016/j.aop.2008.03.005. URL: https://www.sciencedirect.com/science/article/pii/S0003491608000432.

[80] Marcus Barth and Wilhelm Zwerger. "Tan relations in one dimension". In: *Annals of Physics* 326.10 (2011), pp. 2544–2565. ISSN: 0003-4916. DOI: https://doi.org/10.1016/j.aop.2011.05.010. URL: https://www.sciencedirect.com/science/article/pii/S0003491611001084.

[81] Shi-Guo Peng, Cai-Xia Zhang, Shina Tan, and Kaijun Jiang. "Contact Theory for Spin-Orbit-Coupled Fermi Gases". In: *Phys. Rev. Lett.* 120 (6 2018), p. 060408. DOI: 10.1103/PhysRevLett.120.060408. URL: https://link.aps.org/doi/10.1103/PhysRevLett.120.060408.

[82] Richard J. Fletcher, Alexander L. Gaunt, Nir Navon, Robert P. Smith, and Zoran Hadzibabic. "Stability of a Unitary Bose Gas". In: *Phys. Rev. Lett.* 111 (12 2013), p. 125303. DOI: 10.1103/PhysRevLett.111.125303. URL: https://link.aps.org/doi/10.1103/PhysRevLett.111.125303.

[83] Richard J. Fletcher, Raphael Lopes, Jay Man, Nir Navon, Robert P. Smith, Martin W. Zwierlein, and Zoran Hadzibabic. "Two- and three-body contacts in the unitary Bose gas". In: *Science* 355.6323 (2017), pp. 377–380. DOI: 10.1126/science.aai8195. eprint: https://www.science.org/doi/pdf/10.1126/science.aai8195. URL: https://www.science.org/doi/abs/10.1126/science.aai8195.

[84] Biswaroop Mukherjee, Parth B. Patel, Zhenjie Yan, Richard J. Fletcher, Julian Struck, and Martin W. Zwierlein. "Spectral Response and Contact of the Unitary Fermi Gas". In: *Phys. Rev. Lett.* 122 (20 2019), p. 203402. DOI: 10.1103/PhysRevLett.122.203402. URL: https://link.aps.org/doi/10.1103/PhysRevLett.122.203402.

[85] Y.-Q. Zou, B. Bakkali-Hassani, C. Maury, É Le Cerf, S. Nascimbene, J. Dalibard, and J. Beugnon. "Tan's two-body contact across the superfluid transition of a planar Bose gas". In: *Nature Communications* 12.1 (2021), p. 760. ISSN: 2041-1723. DOI: 10.1038/s41467-020-20647-6. URL: https://doi.org/10.1038/s41467-020-20647-6.

[86] F. Serwane, G. Zürn, T. Lompe, T. B. Ottenstein, A. N. Wenz, and S. Jochim. "Deterministic Preparation of a Tunable Few-Fermion System". In: *Science* 332.6027 (2011), pp. 336–338. DOI: 10.1126/science.1201351. eprint: https://www.science.org/doi/pdf/10.1126/science.1201351. URL: https://www.science.org/doi/abs/10.1126/science.1201351.

[87] A. N. Wenz, G. Zürn, S. Murmann, I. Brouzos, T. Lompe, and S. Jochim. "From Few to Many: Observing the Formation of a Fermi Sea One Atom at a Time". In: *Science* 342.6157 (2013), pp. 457–460. DOI: 10.1126/science.1240516. eprint: https://www.science.org/doi/pdf/10.1126/science.1240516. URL: https://www.science.org/doi/abs/10.1126/science.1240516.

[88] Luca Bayha, Marvin Holten, Ralf Klemt, Keerthan Subramanian, Johannes Bjerlin, Stephanie M. Reimann, Georg M. Bruun, Philipp M. Preiss, and Selim Jochim. "Observing the emergence of a quantum phase transition shell by shell". In: *Nature* 587.7835 (2020), pp. 583–587. ISSN: 1476-4687. DOI: 10.1038/s41586-020-2936-y. URL: https://doi.org/10.1038/s41586-020-2936-y.

[89] Marvin Holten, Luca Bayha, Keerthan Subramanian, Sandra Brandstetter, Carl Heintze, Philipp Lunt, Philipp M. Preiss, and Selim Jochim. "Observation of Cooper pairs in a mesoscopic two-dimensional Fermi gas". In: *Nature* 606.7913 (2022), pp. 287–291. ISSN: 1476-4687. DOI: 10.1038/s41586-022-04678-1. URL: https://doi.org/10.1038/s41586-022-04678-1.

[90] D. B. Hume, I. Stroescu, M. Joos, W. Muessel, H. Strobel, and M. K. Oberthaler. "Accurate Atom Counting in Mesoscopic Ensembles". In: *Phys. Rev. Lett.* 111 (25 2013), p. 253001. DOI: 10.1103/PhysRevLett.111.253001. URL: https://link.aps.org/doi/10.1103/PhysRevLett.111.253001.

[91] C. J. Picken, R. Legaie, and J. D. Pritchard. "Single atom imaging with an sCMOS camera". In: *Applied Physics Letters* 111.16 (2017), p. 164102. DOI: 10.1063/1.5003304. URL: https://doi.org/10.1063/1.5003304.

[92] Johannes Zeiher, Julian Wolf, Joshua A. Isaacs, Jonathan Kohler, and Dan M. Stamper-Kurn. "Tracking Evaporative Cooling of a Mesoscopic Atomic Quantum Gas in Real Time". In: *Phys. Rev. X* 11 (4 2021), p. 041017. DOI: 10.1103/PhysRevX.11.041017. URL: https://link.aps.org/doi/10.1103/PhysRevX.11.041017.

[93] R. Thomas, J.S. Otto, M. Chilcott, A.B. Deb, and N. Kjærgaard. "Reducing Number Fluctuations in an Ultracold Atomic Sample Using Faraday Rotation and Iterative Feedback". In: *Phys. Rev. Applied* 16 (6 2021), p. 064033. DOI: 10.1103/PhysRevApplied.16.064033. URL: https://link.aps.org/doi/10.1103/PhysRevApplied.16.064033.

[94] Martin Schlederer, Alexandra Mozdzen, Thomas Lompe, and Henning Moritz. "Single-atom counting in a two-color magneto-optical trap". In: *Phys. Rev. A* 103 (3 2021), p. 033308. DOI: 10.1103/PhysRevA.103.033308. URL: https://link.aps.org/doi/10.1103/PhysRevA.103.033308.

[95] A Hüper, C Pür, M Hetzel, J Geng, J Peise, I Kruse, M Kristensen, W Ertmer, J Arlt, and C Klempt. "Number-resolved preparation of mesoscopic atomic ensembles". In: *New Journal of Physics* 23.11 (2021), p. 113046. DOI: 10.1088/1367-2630/abd058. URL: https://doi.org/10.1088/1367-2630/abd058.

[96] Yaakov Yudkin and Lev Khaykovich. "Laser cooling at resonance". In: *Phys. Rev. A* 97 (5 2018), p. 053403. DOI: 10.1103/PhysRevA.97.053403. URL: https://link.aps.org/doi/10.1103/PhysRevA.97.053403.

[97] Ang Li, Yaakov Yudkin, Paul S. Julienne, and Lev Khaykovich. "Efimov resonance position near a narrow Feshbach resonance in a ^{6}Li$-^{133}$Cs mixture". In: *Phys. Rev. A* 105 (5 2022), p. 053304. DOI: 10.1103/PhysRevA.105.053304. URL: https://link.aps.org/doi/10.1103/PhysRevA.105.053304.

[98] Jacob Johansen, B. J. DeSalvo, Krutik Patel, and Cheng Chin. "Testing universality of Efimov physics across broad and narrow Feshbach resonances". In: *Nature Physics* 13.8 (2017), pp. 731–735. ISSN: 1745-2481. DOI: 10.1038/nphys4130. URL: https://doi.org/10.1038/nphys4130.

[99] P. Giannakeas, L. Khaykovich, Jan-Michael Rost, and Chris H. Greene. "Nonadiabatic Molecular Association in Thermal Gases Driven by Radio-Frequency Pulses". In: *Phys. Rev. Lett.* 123 (4 2019), p. 043204. DOI: 10.1103/PhysRevLett.123.043204. URL: https://link.aps.org/doi/10.1103/PhysRevLett.123.043204.

[100] Roy Elbaz, Yaakov Yudkin, P. Giannakeas, Jan-Michael Rost, Chris H. Greene, and Lev Khaykovich. "Observation of coherent oscillations in the association of dimers from a thermal gas of ultracold atoms". In: *Phys. Rev. A* 107 (3 2023), p. L031304. DOI: 10.1103/PhysRevA.107.L031304. URL: https://link.aps.org/doi/10.1103/PhysRevA.107.L031304.

[101] Peter Fulde and Richard A. Ferrell. "Superconductivity in a Strong Spin-Exchange Field". In: *Phys. Rev.* 135 (3A 1964), A550–A563. DOI: 10.1103/PhysRev.135.A550. URL: https://link.aps.org/doi/10.1103/PhysRev.135.A550.

[102] A. J. Larkin and Y. N. Ovchinnikov. In: *Zh. Eksp. Teor. Fiz.* 47 (1964), p. 1136.

[103] Martin W. Zwierlein, André Schirotzek, Christian H. Schunck, and Wolfgang Ketterle. "Fermionic Superfluidity with Imbalanced Spin Populations". In: *Science* 311.5760 (2006), pp. 492–496. DOI: 10.1126/science.1122318. eprint: https://www.science.org/doi/pdf/10.1126/science.1122318. URL: https://www.science.org/doi/abs/10.1126/science.1122318.

[104] Zhu-Xiong Ye, Alberto Canali, Elisa Soave, Marian Kreyer, Yaakov Yudkin, Cornelis Ravensbergen, Emil Kirilov, and Rudolf Grimm. "Observation of low-field Feshbach resonances between ^{161}Dy and ^{40}K". In: *Phys. Rev. A* 106 (4 2022), p. 043314. DOI: 10.1103/PhysRevA.106.043314. URL: https://link.aps.org/doi/10.1103/PhysRevA.106.043314.

משאב קוונטי בלתי מנוצל. יישמנו את הפרוטוקול הניסיוני בערכים שונים של אורך הפיזור וראינו את הטרימר המתקרב לסף הדימר-אטום. באופן מפתיע, במקום התקרבות הדרגתית ומיזוג אנו רואים את מפלס הטרימר חוצה אל הרצף. לאחר החצייה, נמצא שהטרימר יוצר מצב קשור לאורך זמן – לא תהודת פיזור – למרות שהוא מוטבע ברצף של מרכיביו.

בצד התיאורטי, בהשראת מבנה המפלס של ליתיום, ובפרט מערוץ הפיזור בו נעשה שימוש בניסוי, פיתחנו שני מודלים משלימים. הראשון מיועד לתהודות Feshbach חופפות ואילו השני משלב רצף כמעט מנוון. הם מתוכננים להיות פשוטים ככל האפשר תוך לכידת הפיזיקה המיקרוסקופית החיונית של אינטראקציות המחוזקות על ידי תהודה. אנו משתמשים במודלים אלה כדי לחקור את ההשפעות של תהודה קרובה או רצף קרוב על הפיזיקה הניתנת לצפייה של שניים ושלושה גופים. במקרה של רזוננסים חופפים, אנו מוצאים דחייה ברמת דימר-דימר ושהתכונות של Efimov נדחקות מהסונגולריות. השני נמצא בהסכמה כמותית עם תצפית של הטרימר ^{6}Li-Cs-Cs. רצף כמעט מנוון גורם לדימר להיות רדוד מהצפוי מפרמטר חוזק התהודה. בנוסף, בניגוד לתהודות חופפות, רצף כמעט מנוון אינו משפיע על נקודות הקצה של ספקטרום הEfimov אלא משנה את צורתו התפקודית במקום זאת. יחד, שני המודלים לוקחים בחשבון את התרומות העיקריות לפונקציית הגל האסימפטוטית. לפיכך, כל תכונה של שניים או שלושה גופים שאינה צפויה על ידי אף אחד מהמודלים נובעת כנראה מהפרטים קצרי הטווח של הפוטנציאל הבין-אטומי.

תקציר

פיזיקת מעט גופים ניסויית ותיאורטית באטומים אולטרה-קרים סיפקה תובנות רבות במהלך העשורים האחרונים.

בצד הניסוי, השליטה המעולה על אורך פיזור ה-*s*-גל של שני גופים באמצעות תהודות Feshbach אפשרה יצירת מערכות בעלות אינטראקציה חזקה ותצפית על מצבים גדולים הקשורים באופן רופף. טרימר Efimov בולט כמולקולת הילה מעניינת במיוחד, למשל, מכיוון שאין לו אנלוג קלאסי. הוא נמדד באמצעות התנגשויות לא קוהרנטיות ובלתי גמישות על פני מגוון מינים אטומיים ותהודות Feshbach. התוצאה הסוחפת הייתה שעבור תהודה רחבה, זנב van der Waals, המשותף לכל התנגשויות האטומים הניטרליים, אחראי לחוקי הטבע האוניברסליים. מצד שני, טרימרים של Efimov ליד תהודות צרות נשלטים על ידי חוזק התהודה. עם זאת, בליתיום בוזוני (^{7}Li), הכולל תהודה בינונית וצרה, רבות מהתצפיות הן יוצאות דופן והן מסמנות ביחד "פאזל ליתיום מעט-גופי".

בצד התיאורטי, מודלים מרובי-ערוצים מורכבים יותר ויותר מפותחים כדי להסביר את האופי המפותל של התנגשויות של מעט גופים. בעוד שערוצים מצמודים מלאים הוכחו כמדויקים בצורה יוצאת דופן עבור התנגשויות דו-גוף אלקליין, חישוב דומה עבור בעיית שלושה בוזונים יצטרך כוח חישוב רב יותר מהזמין כיום. לכן מודלים פשוטים הם בלתי נמנעים.

תזה זו מסמנת התקדמות ניכרת בשתי החזיתות.

בצד הניסוי אנו חוקרים את מצב הEfimov המעורר הראשון של ^{7}Li בקרבת סף הדימר-אטום. התצפיות שלנו מוסיפות לפאזל של מעט גופים. כדי לגשת למשטר התובעני הזה פיתחנו פרוטוקול שבאמצעותו נוצרת סופרפוזיציה של דימרים וטרמרים מגז תרמי. כלומר, האטומים נתונים לפולס קצר זמני, ולכן רחב מבחינה ספקטרלית, בתדר רדיו המגשר על הפרש האנרגיה מרצף האטום החופשי הן לדימר והן לטרימר. רצף פולסים כפול מאפשר מיצוי של הפאזה היחסית שנרכשה במהלך זמן הביניים של התפתחות חופשית, הכוללת מדידה מדויקת של אנרגיית הטרימר ביחס לאנרגיית הדימר. לפיכך אנו צופים בטרימר באמצעות האבולוציה הקוהרנטית שלו וההתאבכות עם הדימר. זה מסמן שינוי פרדיגמה בתחום הפיזיקה של מעט גופים. במקום לזהות מצב קשור באופן רופף כתכונת אובדן, כלומר לזהות את היעדרו, אנו מצליחים למנף אבולוציה קוהרנטית ולצפות בטרימר לפני שהוא מתפרק. במשך זמן רב מדי, בתחום הפיזיקה של הגוף, הקוהרנטיות נותרה

תוכן

עבודה זו נעשתה בהדרכתו של

פרופ' לב חייקוביץ

מן המחלקה לפיסיקה
של אוניברסיטת בר-אילן.

פיזיקה של גופים מעטים קוהרנטי

חיבור לשם קבלת התואר "דוקטור לפילוסופיה"

מאת:

יעקב יודקין

המחלקה לפיזיקה

הוגש לסנט של אוניברסיטת בר-אילן

רמת גן תמוז תשפ"ג